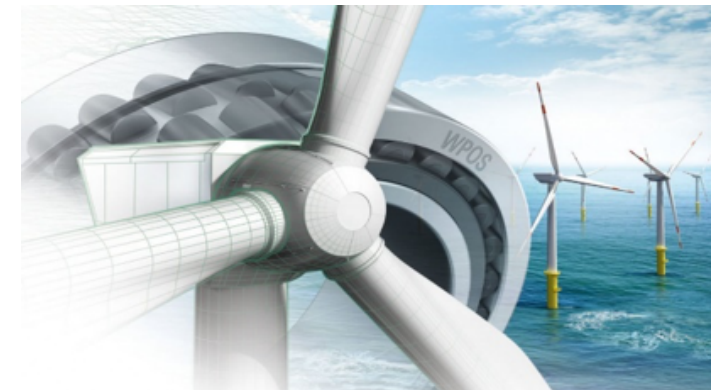Adrián Yagüe Martín

Prognosis and fault detection of drivetrains in medium-speed 10-MW
Floating Wind Turbines

June 2020

NTNU
Norwegian University of
Science and Technology

NTNU
Norwegian University of
Science and Technology

Prognosis and fault detection of drivetrains in medium-speed 10-MW Floating Wind Turbines

Adrián Yagüe Martín

Dedication

To Dani Gavilanes Martín.

You always put a smile on my face.

You continue to do so whenever I think of you.

Your joy & bliss is today my most cherished life lesson.
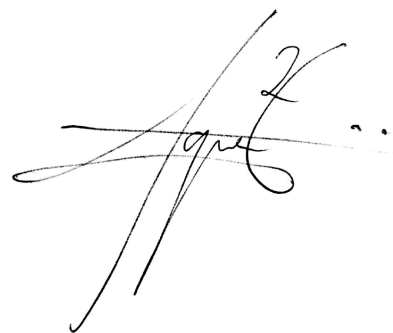
Your natural thrill lives on.

Acknowledgement

I would like to express my sincerest gratitude to Professor Amir R. Nejad for all his guidance, determination and for granting me the opportunity to participate in such a creative and thought-provoking project in a prominent field of offshore wind.

A special thank you to Pim van der Male and all the lecturers and researchers at DTU, TU Delft & NTNU for their knowledge and enthusiasm. Sharing your dedication to offshore wind and your zeal to build a sustainable future has made the journey all the more inspiring.

I would like to thank fellow students, who today I call friends, for all their genuine feedback which always inspired me to aim further.

Finally, I would like to express my gratitude to my parents, Raquel and Agustín, who never ceased to offer their unconditional support, patience, and love.
Without you, I wouldn't be who I am today.

Abstract

Premature failures in large offshore Wind Turbines are often attributed to bearing failure despite gearboxes being designed and developed using the best bearing design practices. Furthermore, as turbine size and rated power increase, bearings display an enhanced tendency to fail. Unscheduled bearing replacement at sea is a complex, costly, weather-dependent and time-consuming operation that results in high turbine downtimes. Market trends show an increase in turbine rated capacity and a noticeable shift towards deeper waters and far-off remote sites which further delays and complicates unscheduled maintenance activities and aggravates the cost penalties of idle turbines. Detecting an incipient bearing fault (diagnosis task) is therefore a major aspect to evaluate drivetrain and overall wind turbine reliability. Moreover, estimating the remaining useful life of bearings and predicting their operational state in the future (prognosis task) can achieve a breakthrough in optimising maintenance programs, improve wind farm operation and decrease wind turbine downtime which can bring about a significant cost reduction.

The purpose of this work is to investigate the health monitoring and prognostics possibilities of drivetrain bearings in a floating spar-buoy offshore wind turbine. The drivetrain concept considered in this work is based on DTU's 10-MW reference wind turbine. Specifically, this study targets the prognosis of four critical drivetrain bearings located in the main shaft and the high-speed shaft.

The absence of run-to-failure data of real wind farms, although inconvenient, is overcome by using model-generated degradation data. A high-fidelity numerical twin of a state-of-the-art drivetrain concept is used in this work and is established using a multi-body system (MBS) approach. The numerical twin models a medium-speed 10-MW gearbox that consists of 3 stages, 2 planetary stages and 1 parallel stage, supported in a 4-point configuration layout with two main bearings and two torque arms. The drivetrain concept studied in this work uses a novel selection of bearings which is currently gaining traction in large offshore wind turbines. The two main bearings that support the main shaft are tapered roller bearings (TRB) that carry both axial and radial loads as opposed to the main bearings used in traditional high-speed gearbox designs which typically use a cylindrical roller bearing to carry radial loads and a spherical roller bearing to carry axial loads.

Faults are applied on the main bearing and on the high-speed shaft bearings of the nu-

merical model. The model-generated degradation data, namely forces and acceleration measurements at several shafts and bearings, is used as input data for two independent prognosis models: a physics-based prognosis model and a data-driven prognosis model. The physics-based approach will culminate in a prediction of the remaining useful life (RUL) of several bearings under a range of faults. The fault detection and fault prognosis capabilities of the proposed prognosis methods is evaluated and compared. This work will also assess the merits and limitations of using model-generated degradation data for the development of prognosis models. Lastly, based on this study, the requirements to enable bearing prognosis from a purely data-driven approach, as opposed to a physics-based approach, is put forth.

Contents

List of Figures

List of Tables

Introduction

Motivation

The IEC standards establish that a WT gearbox must be designed to withstand a service life of 20 years; however accumulated experience consistently proves that a vast majority fail well before. Several studies found that WT's built as recently as 2008 presented 20-40% of gearboxes requiring a component replacement by 2012 and 5-10% complete gearbox failures [17]. There is widespread consensus on the fact that accurate and reliable condition monitoring systems (CMS) and prognosis models are an effective step to drastically cut down operational expenditure costs (OPEX) and overall project costs. The so-called OPEX costs are the funds allocated to the operation and maintenance (O&M) of the wind farm during its operational lifetime and typically represent around 30 to 20% of total project costs.

Well-aware on the major cost savings opportunities that arise with prognosis models, academia and industry are actively pursuing a wide range of techniques to incorporate 'intelligent' algorithms able to estimate the remaining useful life (RUL) of WT drivetrains whilst using a minimal number of sensors. Today, due to the improvement of modern Condition-Monitoring Systems (CMS) of wind turbine drivetrains, early fault detection and prognosis systems have become a reasonable short-term goal.

For three-stage gearbox used in offshore wind turbines, several large-scale reliability surveys have shown that the high-speed parallel stage is the least reliable gearbox module and failures appear to initiate in the bearings rather than in the gears. Furthermore, as turbine size and rated power increase, main shaft bearings in large turbines display an enhanced tendency to fail. Bearing replacement offshore is a complex, costly and time-consuming operation which requires the turbine to be disassembled by a specialized crew

and results in high downtimes. Unplanned maintenance in particular further exacerbates turbine downtime which is often the greatest cost penalty, exceeding the direct cost of component or system replacement.

Addressing wind turbine bearing vulnerability calls for an in-depth investigation on the prognosis possibilities and RUL estimation of wind turbine bearings. Furthermore, a robust bearing prognosis model can be an important contribution to optimise maintenance programs and decrease wind turbine downtime with significant benefits for cost-reduction.

Problem Statement

Wind turbines installed offshore must be designed to operate over 20 years in harsh environments under loading from wind and waves characterized by very stochastic processes. Since these environmental loads must be endured throughout the planned lifetime of the system, the harsh sea states and long service lifetime make periodic maintenance inevitable and a major cost driver. Market trends clearly show a shift into deeper waters and an increasing distance to shore of new wind farm projects which are being installed at remote locations. This is evermore true for floating offshore wind turbines (FOWT) which are expected to be deployed at far-off sites making access all the more challenging. Remote and inaccessible turbines complicate maintenance programs which require meticulous planning and proficient logistics management.

Maintenance offshore is complex and costly as it involves purpose-built vessels to transport spare parts and equipment, heavy duty floating cranes for major repairs and transfer of personnel, all of which are weather sensitive and difficult to plan under unpredictable environmental conditions. Unplanned maintenance causes delays, standby fees of expensive vessels and idle crews whilst increasing turbine downtime which is often the greatest cost penalty, exceeding the direct cost of component or system replacement.

A traditional approach to maintenance such as repairing failed components (corrective) or performing routine maintenance in order to minimize equipment failures (preventive) can quickly drive the operational expenditure costs (OPEX) up to as much as 20 to 30% of the overall project cost. Preventive maintenance often leads to excessive maintenance measures such as early preventive replacement of perfectly healthy components.

To optimise maintenance activities and bring down OPEX costs the wind industry has welcomed a new generation of prognosis health monitoring systems capable of enabling predictive maintenance as a cost-effective solution to the operation and maintenance (O&M). Prognosis systems rely on an optimal selection of sensors that monitor several physical quantities such as accelerations and temperatures. Through regular monitoring and measurements, and the subsequent analysis of these measurements, this data is used to detect changes in the normal operational behavior of electrical, structural and mechanical components such as generators, bearings and gears. The subset of sensors installed on a machine to monitor and collect a series of physical parameters is known as condition-based moni-

toring systems (CMS). Based on the collected data, operators gain valuable insight on the evolution of the operational state of vulnerable wind turbine components throughout their lifetime and are able to infer information on the structural integrity and performance level of these components. Maintenance based on state-of-the-art CMS allows early warning signs of incipient faults to be detected and addressed conveniently before a mechanical failure occurs.

Maintenance of wind turbines in general, and diagnosis and prognosis of drivetrains specifically is a very broad field of research. It is deemed important to explain the reasons why this area of study is so vast to duly justify that a scope reduction has been necessary.

To begin with, there is a large series of components within a WT drivetrain that are prone to failure. Faults can occur on the electrical components - generators, transformers or electrical motors driving yaw and pitch control-, faults can also occur on the mechanical components - bearings, gears and shafts- as well as on the hydraulic system and on the control system. Furthermore, the number, type and characteristics of these components varies significantly for different existing drivetrain designs and layouts.

Secondly, each component can fail according to more than one failure mode which altogether means a great number of different failure modes should be considered. Furthermore, certain failure modes can affect one or several subsystems of a WT. To complicate things even more, faults in different sub-assemblies and components generally involve very different degradation processes which follow distinct physical laws.

Thirdly, there is a wide range of available condition-monitoring systems (CMS) to choose from, each providing unique information on the evolution of distinct physical properties useful to track a variety of degradation processes. Implemented CMS techniques include vibration-based CMS -predominant in wind turbines today-, oil monitoring, acoustic emissions or thermography inspection to name a few. Naturally, depending on the primary CMS technique used to monitor the wind turbine, the approach to prognostics differs as does the data used as input for prognostics models.

Lastly, there is currently a large variety of drivetrain concepts deployed by the offshore wind industry. Design divergence in drivetrains makes it challenging to present a single maintenance scheme applicable to multiple drivetrain concepts. Different designs include geared and gearless drivetrains in combination with high-speed, medium speed and low-

speed generators as well as a variety of bearing configurations and internal drivetrain architectures. The proliferation and consolidation of several distinct gearbox designs means that different drivetrains will experience different types of faults and exhibit distinct faulty behavior. Additionally, different drivetrain designs require different types of sensors due to the difference of operating rotating speeds as well as different sensor placement due to the difference in the inner architecture of the drivetrain. A readily available example is the difference between measuring vibrations in geared drivetrains or direct drive concepts.

Scope

Due to the extensive and far-reaching nature of diagnosis and prognosis of wind turbine drivetrains, this thesis' scope needs to be considerably narrowed down which means certain compromises must be made.

The first limitation that this thesis must acknowledge is to narrow down the components which will be studied. Since modelling all the possible components in a WT is not possible this thesis shall only target a small number of specific components: bearings at the Main Shaft (MS) and bearings supporting the High-Speed Shaft (HSS). Moreover, these bearings may experience multiple failure modes such as faults in the rolling element, faults on the inner race or faults on the outer race. Replicating such faults requires a detailed high-fidelity bearing model which is not available for this thesis since the numerical drivetrain model includes bearings only in a simplified form with an associated stiffness. In this work, bearing damage will be replicated by intentionally reducing the bearing stiffness. A progressive reduction of bearing stiffness is assumed to be equivalent to a gradual increase of bearing damage. Although modelling damage in this fashion does come with its limitations, its an alternative and very convenient approach to simulate the behaviour of a faulty drivetrain.

The second compromise this thesis requires is to focus on a specific drivetrain design. This thesis alone cannot hope to address the wide range of drivetrain typologies and designs actively being used offshore today. For practical reasons a single type of drivetrain layout is considered of a 10-MW medium-speed design developed at NTNU by Wang *et. al.* in [3]. A high-fidelity numerical multibody model of this drivetrain concept has been made available and will therefore be used as the reference drivetrain design. The multibody model is presented in detail in .

Once a suitable drivetrain design and its corresponding numerical model has been selected, and a reduced number of drivetrain components where faults will be simulated has been chosen, this thesis must establish the type of data that will be used to establish a prognosis model.

Fault detection and prognosis approaches make use of data obtained from condition monitoring systems (CMS), SCADA data or a combination of both. SCADA data is available for existing wind farms only, is site-specific and has restricted access. Real CMS data is

also hard to access due to the competitive nature of the industry which makes operators reluctant to share this information. Academia is able to bypass the practical limitation of a lack of real CMS data by constructing numerical WT models to effectively replicate CMS data for both healthy and faulty WT behaviour. Generating simulated data is deemed a reasonable solution to overcome the lack of real CMS data. Specifically, vibration-based CMS will be simulated since it has been successfully used for prognosis across several industries, can be applied online in a continuous data acquisition set-up and is readily available data on all modern day WTs.

Therefore, the scope of this thesis will be the analysis of the behaviour under faulty bearing conditions of the 10-MW medium-speed drivetrain using simulated vibration CMS data. From the simulated faulty drivetrain behaviour this work will establish a method to diagnose specific faults in the gearbox and develop a model for RUL prediction for a WT gearbox with faulty components.

Objectives

This work has two main objectives. The first is to analyze and understand how the behavior of a WT drivetrain mounted on a floating offshore support structure is affected by different types of bearing faults originating at distinct locations. The faults that will be considered correspond to an equivalent radial and an equivalent axial damage in the main bearing at the Main Shaft (MS) as well as an equivalent radial damage originating at the High-speed shaft (HSS). To address this, loads and accelerations at both of these locations, as well as their evolution under increasing damage, will be thoroughly examined and compared to normal healthy operating conditions. Special attention will be paid to the potential redistribution of loads throughout several drivetrain components.

Based on these findings, the second purpose of this thesis is to investigate the health monitoring possibilities of drivetrain bearings. Specifically, this work targets four bearings prone to failure, the two main bearings supporting the MS located directly down-wind from the hub and two additional bearings supporting the HSS located at the gearbox side and the generator side.

The bearing health monitoring will be based on two independent approaches. A physics-based approach will see the implementation of bearing life calculations according the Lundberg-Palmgren hypothesis which is implicitly related to the physics-of-failure since the theory builds on S-N curves. This approach will be followed to estimate the life of the four bearings under different loading conditions associated with different types of faults and different degrees of damage intensity for each of these faults.

The second part will look into the simulated data to enable a data-driven approach. A step-by-step description of a common procedure to extract, identify and select several statistical and spectral quantities useful for the tasks of fault diagnosis and prognosis of bearings will be carried out. Based on these results, it will be argued whether a certain type of fault can readily be approached from a purely data-driven perspective or not. This part will culminate in the construction of health indicators and discuss their potential for prognosis.

Remarks on the merits and limitations of both approaches to prognostics will be put forth. Specific recommendations on how to improve prognostics capabilities of WT drivetrains using numerical models to generate simulated data will be summarized for future research.

Approach

A numerical model will be used to simulate the behaviour of a drivetrain operating with bearing damage. Simulations will replicate damage at two typically vulnerable locations, the main bearing supporting the high-speed shaft and a bearing at the high-speed shaft, which are historically prone to failure and lead to long turbine down-time.

The drivetrain behaviour will be analyzed for three different types of bearing faults simulated by three independent load cases. The first load case reflects an axial damage on this bearing and the second replicates radial damage on the main bearing. A third load case reproduces a radial damage at this high-speed bearing. Each of the three load cases will be further subdivided into five simulations of progressively increasing damage.

Although the numerical drivetrain model includes the geometry and mechanical properties of all the relevant drivetrain elements, the bearings themselves are modelled in a simplified manner with an associated stiffness and damping coefficients. Therefore to replicate bearing faults this thesis will modify the stiffness properties of each bearing in the numerical drivetrain model as a means to simulate bearing damage. Hence, bearing faults will be modeled by progressively reducing in five discrete steps the stiffness of the bearing where a fault is assumed.

The simulated faulty data will be used to establish a bearing damage prognosis model which will be developed further to enable a bearing remaining useful life (RUL) prediction. First, an analysis will be carried out based on comparing vibrations and loads measured at the main shaft and high-speed bearings when bearings are healthy as opposed to when bearings are simulated with a certain type and degree of damage. As damage severity increases the evolution of the accelerations and loads at different locations in the drivetrain will be investigated and signals which exhibit a noticeable deviation from healthy conditions will be identified to set the basis for a bearing prognosis model. This work will culminate in a qualitative comparison between two prognostics approaches, one based on the physical laws that describe the bearing degradation process and another based solely on the extraction of meaningful degradation indicators from the raw data obtained from the numerical model. For the data-driven approach, those measured signals that display a predictable trend as damage increases will be used as input for RUL prediction.

Research Questions

What is the detectability of each specific type of damage and how does the degree of detectability influence prognosis capabilities?

What are the requirements to enable prognosis from a purely data-driven approach as opposed to a physics-based approach?

Can the simulated data generated via a digital twin such as a numerical drivetrain model be used to effectively overcome the lack of "run-to-failure" and real condition-monitoring to establish a prognosis model?

Chapter 1

Background

1.1 Data acquisition

Prognosis of WT drivetrains can be constructed using a physics-based model, a data-driven method, an approach purely based signal processing and analysis or a hybrid approach. These approaches to predict the lifetime of a system are formally introduced and explained in detail in section 3.3. Regardless of the implemented approach, the fundamental prerequisite to enable a prognostics model is that sufficient and appropriate data must be available. Reliability data, historical failures or CMS databases of WTs is an essential input to establish a prognosis model. In fact, most prognosis tools, physics-based models , signal-analysis approaches and data-driven methods, explained in subsection 3.3.1, subsection 3.3.2 and subsection 3.3.3 respectively are generally constructed using run-to-failure data or alternatively lifetime data collected throughout the operational lifetime of a machine.

For some specific applications and certain types of machines however run-to-failure data is not always abundant. This is particularly true for long-life systems with high reliability such as WT or aircrafts [18]. Furthermore, even if run-to-failure data exists it may not be accessible to the general public. Such is the case for offshore WTs. Due to the competitive nature of the industry, manufacturers and operators tend to be protective of their data and are generally reluctant to openly share reliability information of their wind farms or component failure rates.

The access to CMS data from real wind farms is even more restricted for large offshore wind farms than for their onshore counterparts. As a consequence, having enough run-to-failure

data to establish prognosis model should not be taken for granted.

The absence of run-to-failure data, although inconvenient, can be mitigated by using degradation data instead. Hence, to build a prognosis method for drivetrain RUL estimation of WT drivetrain bearings rather than using limited, or sometimes non-existent, run-to-failure data the alternative is to use degradation as the main source of input data. Nowdays, it is common practice for a WT operator to collect data during the service life of the offshore wind farm. Degradation data is therefore abundant, and is extensively used to optimise operation and monitor the system. Degradation data is typically collected continuously by several purpose-built sensors prior to halting a turbine that begins to exhibit unacceptable or faulty behaviour.

Even though the degradation indicators corresponding to system failure are unknown since the machine was halted to prevent further damage, the data collected throughout the operational lifetime does provide valuable information on the degradation processes that lead to stopping the machine [18]. Degradation data can either be collected by sensors or simulated and it is obtained according to one of the following three ways:

- Degradation data obtained directly from a set of sensors installed on real WTs offshore, collected either by SCADA or by sensors purposely built-in for condition monitoring;

- Experimental degradation data obtained from a test rig and acquired by placing a set of sensors on a down-scaled version of a WT drivetrain. Such test rigs are designed to replicate real operating conditions of drivetrains. To simulate faulty conditions, certain components of the test rig can be modified to alter their behavior and mimic the expected conditions that lead to faults;

- Experimental degradation data obtained from numerical models implemented on specific software and simulation tools. The degree of detail of these numerical models may vary significantly as some high-fidelity models accurately reflect an entire wind turbine system interacting with a stochastic environment whilst others approaches focus on a simplified model that only replicates a certain specific physical process reliably. Furthermore, the scope of the models also varies, some models include the entire wind turbine system, ranging from the support structure and the mooring lines to the tower and the rotor to enable an aero-elastic-hydro-servo dynamic analysis

whilst others focus in greater detail on a subset of components and on a particular physical domain such as a an electromagnetic model of the generator, a simplified mechanic model of a gearbox, a lumped thermodynamic model of an oil lubrication system or a coupled combination of models to replicate an operational drivetrain. To simulate faulty conditions, numerical models will be tweaked such that the desired fault can be replicated and the faulty behavior can be modelled and studied.

Needless to say, real-life degradation data obtained from an offshore wind farm is by far the best data source when it comes to constructing a reliable prognosis model from realistic data. That being said, experimental data obtained from test rigs and/or numerical models present some interesting advantages such as low cost and greater flexibility to model and analyze a wider range of drivetrain concepts. As the industry continues to deploy several different types of concepts -geared and gearless drivetrains in combination with high-speed, medium speed and low-speed generators- the modelling flexibility made possible by numerical models becomes convenient to rapidly assess the healthy and faulty behavior of different drivetrain designs. This is important because different drivetrain concepts may experience different types of faults and exhibit distinct faulty behavior.

1.2 Preliminary concepts

Since obtaining data is an indispensable step prior to constructing a prognosis model, generating data with the help of a numerical model is necessary. The following section will introduce the preliminary concepts prior to formally introducing the numerical model in chapter 2. This section will first introduce the concept of *decoupled approach* implemented to obtain drivetrain data which actually corresponds to a realistic offshore wind-wave climate obtained from a global analysis. Then, this section will look into the reference turbine design on which the numerical model is based as well as the reference floater concept of a floating offshore wind support structure for which the global analysis is carried out.

1.2.1 Decoupled Approach - Global Model & Local Model

This academic work is based on a decoupled approach which combines two different models applied consecutively. First an aero-hydro-servo-elastic simulation is performed using SIMA which replicates the response of DTU's 10-MW reference WT mounted on an up-scaled version of OC3 spar-buoy floating support structure. This is refered to as the global

analysis and it is used to obtain the behavior of the entire offshore wind turbine system for a specific wind-wave climate. Subsequently, the output results, namely forces and motions at the nacelle, are used as input for a detailed mechanical drivetrain model of the drivetrain proposed by *Wang* in *et. al* in [3] and described in greater detail in [16]. This second step is performed using a multi-body simulation software on which the drivetrain model has been constructed: SIMPACK. This thesis focuses on the output variables obtained from this second step, and primarily consists of the analysis of the accelerations at several key locations of the drivetrain.

The decoupled approach is necessary because the external dynamic excitation forces of the wind turbine such as the tower shadow, wind and waves are in the low frequency range often lower than 2 Hz whereas the drivetrain internal excitation forces are significantly higher [1]. For instance, gear meshing frequencies which are susceptible to induce internal excitation in the drivetrain are normally in the high-frequency range above 20 Hz. Therefore, in order to capture external resonance induced by wind and waves a time step of 0.1 s is usually sufficient for the global analysis. On the contrary, to capture internal resonance within the drivetrain a significantly smaller time step in the range of 0.005 s is required. Specifically, the simulations concerning the drivetrain model on SIMPACK have been executed using a time step of $\Delta t = \frac{1}{600} \approx 0.00167$ seconds.

The global analysis is used to estimate the motions and load effects in the structural member's such as the tower, nacelle, blades and the support structure or foundation. In the global model the tower and blades are typically modelled as flexible members whereas the drivetrain is modelled in a simplified manner since the primary goal is to evaluate the behaviour of the overall system under the simultaneous effects of wind, waves and currents [1]. In the present work, for the global analysis the drivetrain is modelled in its simplest form shown in Figure 1 as a two-mass model torsional spring of an equivalent torsional stiffness k_{teq} to account for the first torsional mode of the drivetrain.

In Figure 1 the two mass-model with a gear system shown in the left-hand of the figure is first modelled by taking into account the gear ratio as seen in the middle illustration in Figure 1. The parameters J_r is the rotor inertia including shaft, hub and blades and J_g is the inertia of the generator about the low-speed shaft. The equivalent torsional stiffness k_{teq} is calculated according to Equation 1.1 where k_{tr} is the torsional stiffness of the main shaft, k_{tg} is the torsional stiffness of the generator and n is the generator speed over the
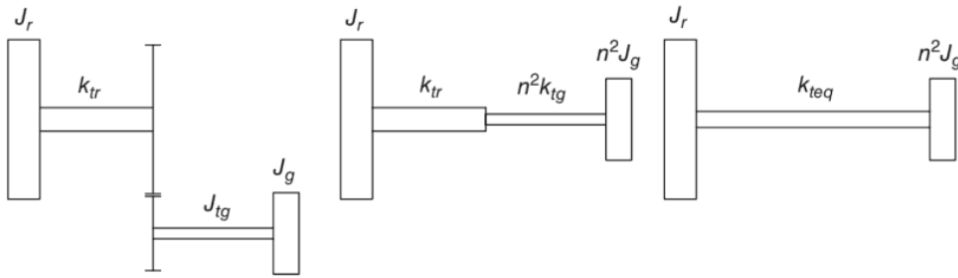
Figure 1: Simplified two-mass model of drivetrain used in the global analysis [1]

rotor speed which is the inverse of the gearbox ratio.

$$k_{teq} = \frac{k_{tr} n^2 k_{tg}}{k_{tr} + n^2 k_{tg}} \tag{1.1}$$

The simplified drivetrain model used in the global analysis is valid as long as the range of natural frequencies of the drivetrain is above the overall wind turbine excitation excitation frequencies. A detailed discussion on the state-of-the-art of drivetrain modelling and analysis as well as the implementation of a decoupled approach is provided in the work of Amir Rasekhi Nejad in *Chapter 3: Modelling and Analysis of Drivetrains in Offshore Wind Turbines* published in [1].

1.2.2 DTU 10-MW reference Wind Turbine

The 10-MW DTU reference turbine and its reference document [14] was published by DTU in 2013. The idea behind the 10-MW DTU reference turbine is to set in place a reference wind turbine to compare future designs against and its reference document. This reference turbine is intended to set the design basis for next-generation large-scale wind turbines, particularly relevant to offshore projects.

In the reference document, the design prioritises good aerodynamic performance and emphasizes on fairly low weight design. That being said, [14] underlines that its main goal isn't to design a rotor pushed to the limit with lowest possible weight. Also, the purpose of the reference document isn't to provide a design of a complete wind turbine and the focus is mainly on the rotor. The 10-MW DTU reference turbine does however provide a sufficiently detailed design to allow for a comprehensive comparison of simulation results

from aerodynamic and structural tools.

Accordingly, [14] only presents limited properties of the 10-MW turbine design shown in Table 1. This grants turbine designers and researchers a flexibility concerning the turbine such as drivetrain layout and gearbox design, selection of gear type and number of gears or the choice of bearings.

Parameter	Value
Rated rotor speed (rpm)	9.6
Rated generator speed (rpm)	480
Gearbox ratio	01:50
Electrical generator efficiency (%)	94
Generator inertia about high-Speed shaft (kgm2)	1500.5
Equivalent drive-shaft torsional-spring constant (Nm/rad)	2317025352
Equivalent drive-shaft torsional-damping constant (Nm/(rad/s))	9240560

Table 1: 10-MW Drivetrain properties provided by DTU [14]

The 10-MW DTU reference turbine is pitch-regulated with an active control system that varies the pitch angle of the blades. Above rated speed, the pitch-angle is increased to control the aerodynamic torque acting on the rotor and to decrease the rotational speed of the blades as wind speed increases. Beyond rated wind speed, the rotational speed is reduced such that the torque transferred to the shaft is kept constant below a set threshold. Hence, the turbine will produce increasing power up until the rated wind speed, beyond which it sees constant power P_{rated} due to the pitch actuator up until cut–out speed.

1.2.3   Floater concept

The reference 10-MW drivetrain is mounted on a state-of-the-art commercial-scale FOWT type floater. The floater chosen in this work is a new spar-buoy concept based on up-scaling the "OC3-Hywind" concept developed by NREL. Rather than supporting NREL's 5-MW reference WT, this spar-buoy concept was designed to support the DTU 10-MW reference WT. The up-scaled platform concept satisfies all the relevant design criteria, namely buoyancy, stability, hydrodynamic and strength criteria.

The floating structure is cylindrical and made of steel with a total draft of 120 meters below SWL. More specifically, the spar-buoy consists of two cylindrical regions connected by a linearly tapered conical region. The top of the upper cylinder is at 10 m above SWL and has a diameter of 8.3 m, the tapper region extends from 4 m to 12 m below SWL and

connects to the lower cylinder which has a diameter of 12 m and extends all the way to 120 m below SWL.

The spar-buoy is anchored to the seabed to prevent it from drifting away. To do this a 3-point catenary spread mooring system is used for station-keeping. The restoring force are obtained by by lifting and lowering the weight of the mooring lines. In a spread mooring system, several pre-tension anchor lines are arrayed around the structure to keep it in the wanted location [15]. For the 10-MW WT support structure a large part of the anchor line lies on the sea bed to ensure anchors are kept in position. Moreover, mooring lines must provide sufficient breaking strength to resist the maximum tension with adequate safety margins.

Due to its large top mass comprised of the rotor and nacelle, the presence of the wind turbine will raise the center of gravity of the whole structure above sea level. This poses a challenge for the stability of the spar-buoy. To address, spar designs typically have very large drafts and are ballasted at the bottom to significantly lower the center of gravity. For the up-scaled 10-MW "OC3-Hywind" spar-buoy, the structure is filled with a ballast of concrete. The heavy ballast will provide stability and restoring stiffness, thus limiting the platforms' motions in pitch and roll under the action of wind and waves.

Buoyancy requirements are that the floater should provide enough displacement to support the weight of the floater, the tower and the WT at the design draft level of 120 m. An appropriate amount of ballast design is important to achieve the design draf

One of the most critical aspects of floater design are the natural periods as they will determine motion characteristics in the platform's degrees of freedom. According to wave spectrum analysis for different locations and sea states, ocean waves contain major energy within the range 5 to 25s. Therefore, the floater's natural periods should be kept away from these exciting frequencies such that resonant behaviour can be minimized or avoided altogether if possible. For spar-buoy floaters used for WTs it is common to have a natural period of around 20 to 25s in heave motion and a natural period around 30s in pitch and roll motion. As for yaw and horizontal motions, namely sway and surge, the natural periods are governed by the mooring system.

In [15] several free decays tests were performed using the SIMO-RIFLEX simulation tool. The aim of decay analysis is to obtain the natural periods and damping ratios - both the

linear and quadratic damping ratio- for the spar-floater equipped with the DTU 10MW reference WT.

To perform a free decay an initial displacement is introduced in a given degree of freedom. The structure is then released so it can oscillate freely around the initial equilibrium position with a damped natural period until it comes to a rest and reaches equilibrium. From the damped natural period T_d obtained from the free decay tests, and if the damping ratio ζ_n is known, the undamped natural period T_n can be obtained.

In [15] a logarithmic decrement was used to estimate the system damping ratio according. First a decrementation δ is calculated according to expression Equation 1.2, where x_0 is the initial amplitude and x_n is the amplitude of n peaks away.

$$\delta = \frac{1}{n} \ln \left(\frac{x_0}{x_n} \right) \tag{1.2}$$

The damping ratio ζ is then found as:

$$\zeta = \frac{1}{\sqrt{1 + (2\pi/\delta)^2}} \tag{1.3}$$

When the damping ratio is known, the undamped natural period can be calculated simply as:

$$\omega_n = \frac{\omega_d}{\sqrt{1 - \zeta^2}} \tag{1.4}$$

Due to symmetry of the spar, only surge, heave, pitch and yaw were considered for the decay tests. Results of the free decay tests of the platform are shown in Table 1.2.3. As can be seen, the damping ratios are small which means that the damped and undamped frequencies ω_d, ω_n are almost equal. Hence, the undamped natural period is $T_n \approx T_d$.

Degree of freedom	Damped natural period [s]	Damping ratio [-]
Surge	103.3	0.024
Heave	31.3	0.0032
Pitch	35.5	0.0033
Yaw	7.61	0.0031

Table 2: Results for decay tests corresponding to spar floater supporting the DTU 10-MW WT according to [15]

1.3 Design codes & standards for WT CMS

In the same way design codes and standards are used to set the basis of design calculations of wind turbines, and aid engineers in the modelling, simulation and validation of new designs, a range of standards and guidelines exist to correctly design condition monitoring systems.

Several reference standards are used in offshore wind turbine condition monitoring that specify the number, the location and the characteristics of sensors that enable an appropriate monitoring system.

There is a very broad spectrum of documents and ongoing initiatives related to the condition monitoring of machines, some guidelines are specific to the CMS of wind turbines, some go further into detail establishing recommendations for the condition monitoring of specific WT components such as WT drivetrains and other documents provide generic guidelines for condition monitoring and diagnostics of rotating machines. In [5] a comprehensive list of commonly used standards and guidelines on CMS was presented. The most relevant standards and guidelines related to the progress of work this work are provided below including wind-specific documents for CMS in Table 3 and general design standards for CMS in Table 4.

Furthermore, some standards focus on specific CMS methods such as vibrations. The selection of documents shown in Table 5 focus on vibration-based CMS systems of rotating machinery and Table 6 collects other relevant documents concerning CMS such as the ISO standards for oil monitoring or other useful documents put forth by industry players.

Issued by	Reference	Title
DNVGL	GL-IV-4	*Rules and Guidelines – IV Industrial Services – Part 4: Guideline for the Certification of Condition Monitoring Systems for Wind Turbines*
DNVGL	DNVGL-SE-0439	*Certification of condition monitoring*
IEC	IEC61400-25	*Wind Turbines – Part 25: Communications for monitoring and control of wind power plants*
IEC	IEC61400-25-6	*Wind turbines - Logical node classes and data classes for CM*
ISO	ISO 10816-21	*Mechanical vibration - Evaluation of machine vibration by measurements on non-rotating parts - Part 21: Horizontal axis wind turbines with gearbox; based on VDI 3834*
ISO	ISO 16079-1	*Condition monitoring and diagnostics of wind turbines-Part 1: General guidelines drivetrain*
ISO	ISO 16079-2	*Condition monitoring and diagnostics of wind turbines-Part 2: Monitoring the drivetrain*
VDI	VDI 3834-1	*Measurement and evaluation of the mechanical vibration of wind energy turbines and their components – Part 1: Onshore wind energy turbines with gears (Note: not for condition monitoring, but vibration assessment)*
VDI	VDI 3834-2	*Measurement and evaluation of the mechanical vibration of wind energy turbines and their components – Onshore wind energy turbines with gearless drive (in preparation)*

Table 3: Wind-specific guidelines and standards for condition monitoring

Issued by	Reference	Title
ISO	ISO 13372	*Condition monitoring and diagnostics of machines - vocabulary*
ISO	ISO 13379-2	*Condition monitoring and diagnostics - General procedures*
ISO	ISO 13379-2	*Condition monitoring and diagnostics of machines - Data interpretation and diagnostics techniques - Part 2: Data-driven applications*
ISO	ISO 13381-1: 2004-11	*Condition monitoring and diagnostics of machines - Prognostics - Part 1: General guidelines*
ISO	ISO 17359:2011-09	*Condition monitoring and diagnostics of machines - General guidelines*

Table 4: Non wind-specific guidelines and standards for condition monitoring

Issued by	Reference	Title
ISO	ISO 10816-1	*Mechanical vibration - Evaluation of machine vibration by measurements on non-rotating parts*
ISO	ISO 10816-2	*Mechanical vibration - Industrial machines with nominal power above 15 kW and nominal speeds between 120 r/min and 15 000 r/min when measured in situ*
ISO	ISO 13373-1	*Condition monitoring and diagnostics of machines - General procedures*
ISO	ISO 13373-2	*Condition monitoring and diagnostics of machines - Vibration condition monitoring - Part 2: Processing, analysis and presentation of vibration data*
VDI	VDI 3839-1	*Instructions on measuring and interpreting the vibration of machines – General principles*
VDI	VDI 3839-2	*Vibration patterns for excitation arising from unbalance, incorrect assembly, bearing faults and damage to rotating components.*
VDI	VDI 3839-5	*Typical vibration patterns with electrical machines*
VDI	VDI 3841	*Vibration monitoring of machinery - Necessary measurements*

Table 5: Documents, standards & guidelines regarding vibration condition monitoring

Issued by	Reference	Title
ISO	ISO 4406	*Hydraulic fluid power – Fluids – Method for coding the level of contamination by solid particles*
VDI	VDI 3832	*Measurement of structure-borne sound of rolling element bearings in machines and plants for evaluation of state condition.*
DIN	DIN 31051	*Fundamentals of maintenance*
Allianz	AZT	*Anforderungen an Condition Monitoring Systeme für Windenergieanlagen Requirements for condition monitoring systems for wind turbines*

Table 6: Other relevant documents & guidelines for the condition monitoring of wind turbines

Chapter 2

Methodology

This work has chosen to use a vibration-based approach for fault detection and fault prognosis in WT bearings. The state-of-the-art of vibration-based condition-monitoring in WT drivetrains is discussed in detail in subsection 3.2.1. Vibrations have been used successfully used for fault detection across a wide range of industries and has proven to be a reliable method for early detection of incipient faults. Another method which is also commonly used is monitoring the lubrication-oil, explained in subsection 3.2.2. Alternative methods exist such as acoustic emissions or thermography analysis using infrared cameras which are typically used to compliment and reinforce existing condition-monitoring systems. An overview of these methods is presented in subsection 3.2.3.

Vibration-based maintenance is the preferred method since it can be performed online remotely without the need to travel to the offshore site. Furthermore, as seen in Figure 2
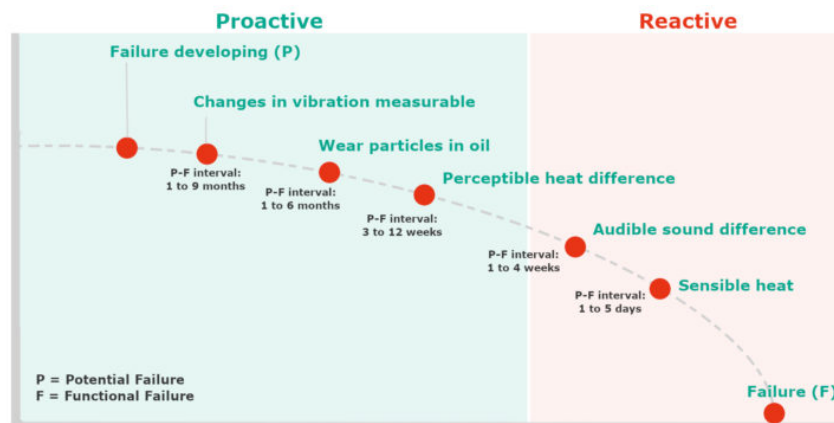
Figure 2: Various condition-monitoring methods to track changes in machine behavior [2]

vibration-based condition monitoring has been found to enable early fault detection compared to other methods which enhances diagnostics and prognostics capabilities. These advantages are well-known by wind farm operators and it is customary that all offshore wind turbines deployed today are equipped with vibration-based condition monitoring systems.

Due to the lack of CMS vibration data of real offshore wind farms, a numerical model to simulate the vibrations of a healthy and faulty drivetrain is necessary. Previously in subsection 1.2.1 the concept of decoupled approach was introduced and in the present section the steps that have been followed to obtain the simulated data are discussed. First, the numerical model that will be used in this thesis is described, then the approach that has been used to replicate bearing damage based on a gradual decrease of bearing stiffness is explained before the Load Cases (LC) are formally presented.

2.1 Numerical 10-MW medium-speed gearbox model

The numerical model of the 10-MW medium-speed drivetrain used in this study was constructed on SIMPACK, a multibody system (MBS) simulation software. It was developed by Shuaishuai Wang *et. al.* in [3]. The model is based on a concept of a reference 10-MW wind turbine proposed by the Technical University of Denmark (DTU) in 2013 introduced in subsection 1.2.2 and extensively described in [14]. The 10-MW reference wind turbine developed in [3] is mounted on a spar-buoy type floater. The modelled WT drivetrain has a four-point support configuration with two main bearings and two torque arms as shown in Figure 3.
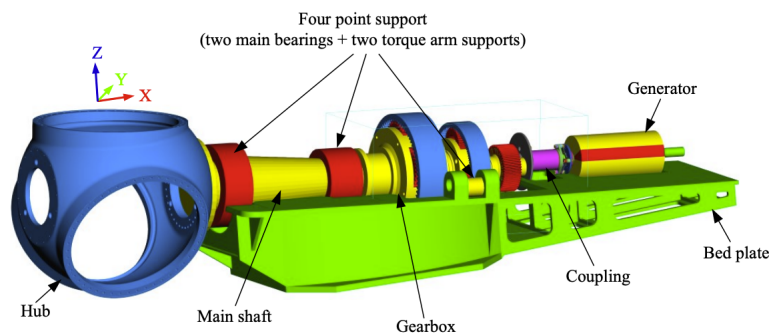
Figure 3: 3D view of the 10-MW drivetrain MBS model with 4 point configuration -two main bearings and two torque arms- as constructed on SIMPACK in [3]

Medium-speed drivetrains are a compromise between conventional high-speed drivetrains, which are historically prone to failures, and direct drive drivetrains which often result in large generators. Hence, a medium-speed drivetrain is a promising design for large scale offshore wind turbines since they yield a lower failure probability compared to a high-speed drivetrain whilst effectively reducing generator size and weight compared to the direct drive drivetrain.

The DTU reference document [14] only presents limited properties of the 10-MW turbine design shown in Table 1. This allows a degree of design flexibility in terms of drivetrain layout and gearbox design, selection of gear type and number of gears and the choice of bearings. The DTU reference document [14] does specify a 1:50 gearbox ratio as can be seen from Table 1. In order to achieve this gearbox ratio Wang *et. al.* proposed a gearbox configuration consisting of two planetary stages and one parallel stage.

Several designs were proposed and a schematic overview of the gearbox design process is represented by the flowchart shown in Figure 4. The selection of the most suitable design was done based on three design criteria: weight, volume and load sharing performance. The design principle was to minimize the weight and volume of the gearbox whilst being able to safely carry the input loads applied to gearbox. Optimizing the design for minimum weight and volume is seen as an effective way to reduce transportation and lifting costs.

The best design according to these criteria is shown in Figure 5 and resulted in a total dry weight 60.43 tones. The 4 point support configuration can be clearly seen in both Figure 5a and 5b. This final gearbox design is equipped with five planets in the first planetary stage and three planets in the second planetary stage. The downwind bearing is designed to withstand huge non-torque loads transmitted from the hub center and consists of two identical bearings as can be seen in Figure 5b. Also visible on the schematic layout of the model, it can be each planet in the gearbox first stage is supported by four bearings in order to resist the huge loads input from the planet carrier. The remaining drivetrain specifications of the final design are listed in Table 2.1.

Once the final design was set in place the parameters of the SIMPACK numerical model were defined to match the ones given by DTU. The natural frequency for the shaft torsion mode were obtained for the numerical model via modal analysis. The SIMPACK models' eigenfrequencies were seen to be in close agreement with the natural frequency values pre-
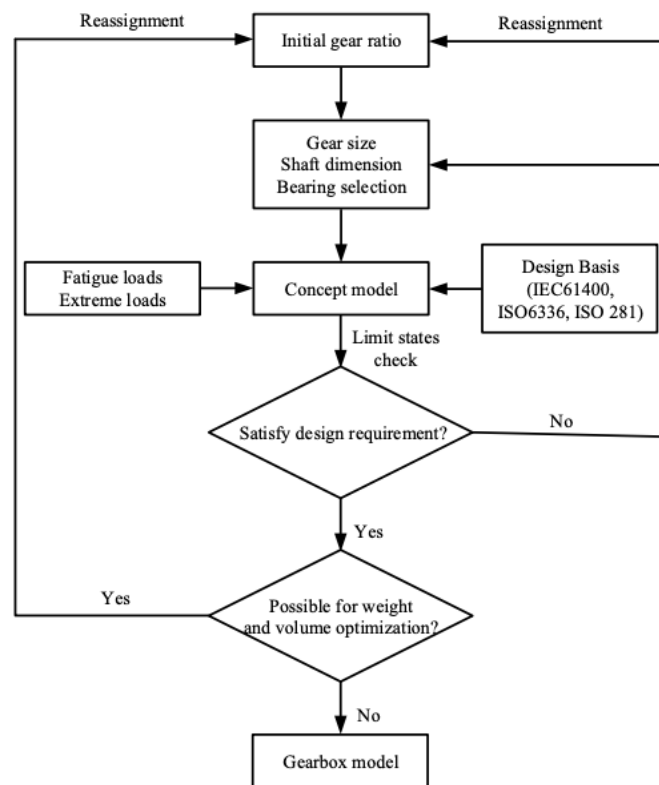
Figure 4: Flowchart of gearbox design [3]

Parameter	Value
Drivetrain type	4-point supports
Gearbox type	Two planetary + one parallel
First stage gear ratio	1:4.423
Second stage gear ratio	1:5.192
Third stage gear ratio	1:2.179
Total gear ratio	1:50.039
Designed power (kw)	10000
Rated input shaft speed (rpm)	9.6
Rated generator shaft speed (rpm)	480.374
Total gearbox dry weight ($\times$ 1000 kg)	60.43
Maximum gearbox outer diameter (m)	3.098
Service life (year)	20

Table 7: 10-MW reference wind turbine drivetrain specifications [3]

sented in the DTU wind energy report. The results indicate the first order eigenfrequencies, which are critical drivetrain properties, in the two drivetrain models match well.

(a)

(b)
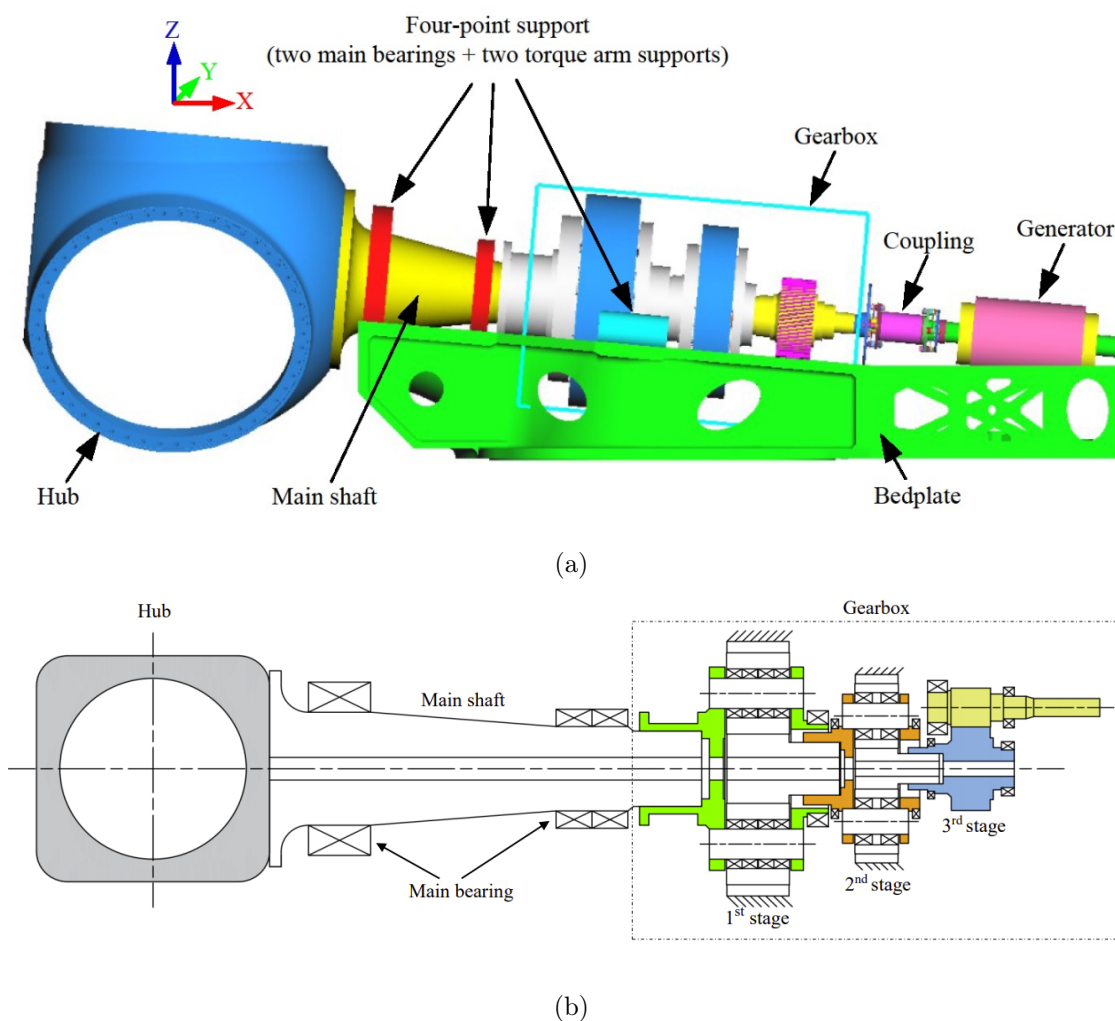
Figure 5: Most lightweight design of 10-MW medium-speed WT drivetrain model as designed by Wang *et. al.* with (a) side view of the SIMPACK 10-MW WT model and (b) schematic view of layout [3]

2.2 Approach to model damage

To enable a prognosis model, the prerequisite is to generate data corresponding to a drivetrain operating with healthy bearings and damaged data corresponding to a certain type and degree of damage in one of the bearings at the MS or at the HSS. In order to do this an approach to artificially introduce bearing damage in the numerical model must be set in place. This section discusses such an approach.

The bearings in a WT drivetrain may experience multiple failure modes such as faults in the rolling element, faults on the inner race or faults on the outer race. When a rolling element in a bearing passes over a given defect, for instance on the inner or outer race,

the contact generates an impact that repeats each time the rolling element hits that same defect. This impact is associated to a specific frequency which provides unique information on the location of the defect.

Accordingly, faults in bearings can be seen to excite a series of distinct characteristic fault frequencies which correspond to relevant impulse frequencies. It is important to note that these characteristic frequencies vary with shaft speed, which in turn varies with the wind speed. Therefore, bearing characteristic frequencies encompass a frequency range that depends on shaft and wind speed.

The rolling element damage feature frequency f_{RE}, the inner race damage feature frequency f_{BPFI}, the outer race damage feature frequency f_{BPFO} and the fundamental train damage feature frequency f_{FTF} are given by expressions Equation 2.1-2.4

- Ball spin frequency:

$$f_{\mathrm{RE}} = \frac{D}{2d} \left(1 - \frac{d}{D} \cos \alpha \right) \left(1 + \frac{d}{D} \cos \alpha \right) f_{\mathrm{shaft}} \tag{2.1}$$

- Ball passing inner race frequency:

$$f_{\mathrm{BPFI}} = \frac{n}{2} \left(1 + \frac{d}{D} \cos \alpha \right) f_{\mathrm{shaft}} \tag{2.2}$$

- Ball passing outer race frequency:

$$f_{\mathrm{BPFO}} = \frac{n}{2} \left(1 - \frac{d}{D} \cos \alpha \right) f_{\mathrm{shaft}} \tag{2.3}$$

- Fundamental train frequency:

$$f_{\mathrm{FTF}} = \frac{1}{2} \left(1 - \frac{d}{\mathrm{D}} \cos \alpha \right) f_{\mathrm{shaft}} \tag{2.4}$$

where, as shown ,D and d is the pitch diameter and the roller element diameter as shown in Figure 6, n is the number of rollers and α is the roller contact angle.

Since each type of bearing failure has an associated "signature" frequency, the characteristic fault frequencies for a given bearing can be calculated beforehand in order to detect the presence of faults.
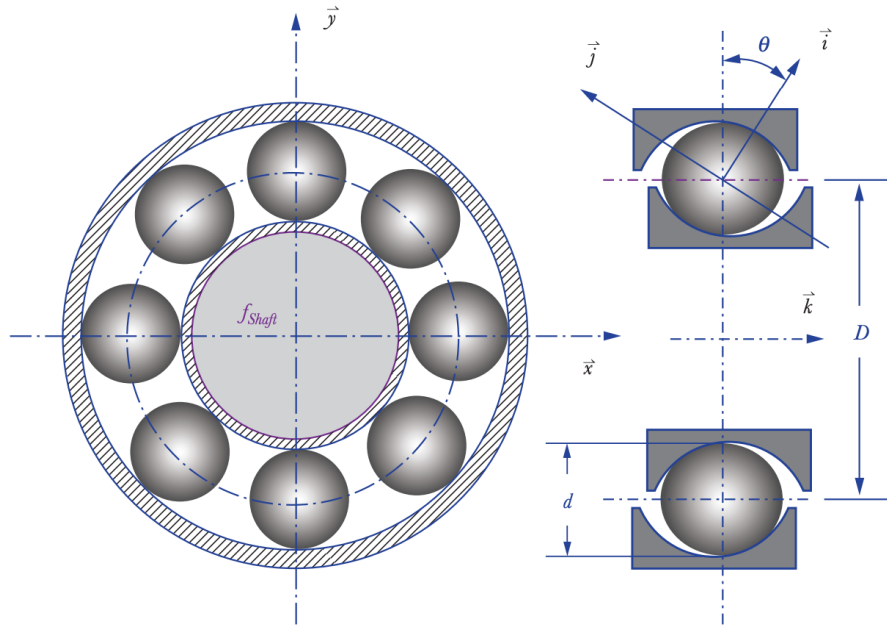
Figure 6: Schematics of a ball bearing

Although this is a very common and valuable approach to fault detection and can be further manipulated to set the basis for prognosis models, to implement it a detailed model of the bearing itself is indispensable. Only if all the elements that constitute the bearing are fully modelled does it make sense to identify these characteristic fault frequencies and track whether they get excited.

Such a detailed model of the bearings is not available for this thesis. Although the numerical model constructed on SIMPACK does include the geometry and mechanical properties of all the relevant drivetrain elements, the bearings themselves are modelled in a simplified manner with an associated stiffness and damping coefficients.

Hence, rather than focusing on specific bearing faults by establishing a high-fidelity numerical model of each bearing, this thesis will directly modify the stiffness properties of each bearing to simulate bearing damage. Bearing faults will therefore be replicated artificially by progressively reducing the stiffness of the bearing where a fault is assumed.

Although modelling damage in this fashion does come with its limitations, its an alternative and very convenient approach to simulate the behaviour of a faulty drivetrain.

From hereon, bearing stiffness reduction is assumed to be equivalent to an increase of bearing damage.

2.3 Load Cases

The methodology followed in this thesis follows a decoupled approach. As explained in subsection 1.2.1 first a global analysis was performed using a fully coupled aero-hydro-servo-elastic model in the time-domain implemented on software *SIMA*. Then, once the response of the spar buoy WT exposed to a realistic wind-wave climate is obtained from the global analysis it is used as input for the numerical drivetrain model.

Environmental Parameters for the Global Analysis

For the global analysis a single representative sea-state was considered. In particular, the selected environmental parameters correspond to **LC3** in Figure 7. These parameters were chosen because the behaviour of the drivetrain for a wind speed close to the turbines rated speed wind speed is of interest. Furthermore, this environmental load case has a high probability of occurrence during the turbines operational lifetime as seen from the probability distribution function in Figure 7. This high probability makes this environmental load case particularly representative when verifying the behaviour of the drivetrain operating with a bearing damage. Hence, the wind speed u for the global analysis is selected such that $u = 12 \; m/s$. The sea-state parameters H_s and T_p corresponding to this wind speed are obtained from the long-term joint distributions of wind and wave data. Specifically, these environmental parameters have been obtained from joint distributions of wind and wave data measured at the Northern North Sea and presented by Li *et. al.* in [4].

Load Cases simulated on the numerical drivetrain model

Once a single environmental load case has been defined in terms of all the relevant environmental parameters, the high-fidelity multi-body numerical drivetrain model will be run to simulate a series of fault cases. Simulations will focus on two essential bearings of the drivetrain. These bearings are:

1. The first main bearing, directly downwind from the rotor, labelled as **INP-A**

2. The high-speed bearing on the generator side, labelled as **HS-B**

The choice of these bearings is the fruit of an educated selection based on reliability and downtime data collected at offshore wind farms. Bearings in the HSS have always been

Load case	LC1	LC2	LC3	LC4	LC5
u (m/s)	5	8	12	16	24
H_s (m)	1.6	1.9	2.5	3.3	5.4
T_p (s)	9.4	9.7	10.1	10.7	11.9
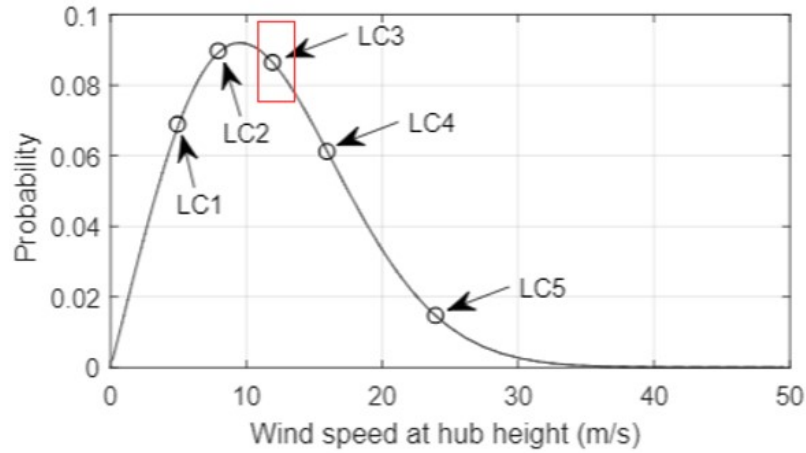
Figure 7: Load cases in normal operational conditions (top) and probability distribution of wind speed at hub height [4]

susceptible to failure. Bearings in the MS show an increasing tendency to fail as turbine size and rated power continuous to grow. Furthermore, replacement of bearings is a complex and location of both of these bearings **INP-A** and **HS-B** are marked in red in the schematic overview of the numerical drivetrain model shown in Figure 8.
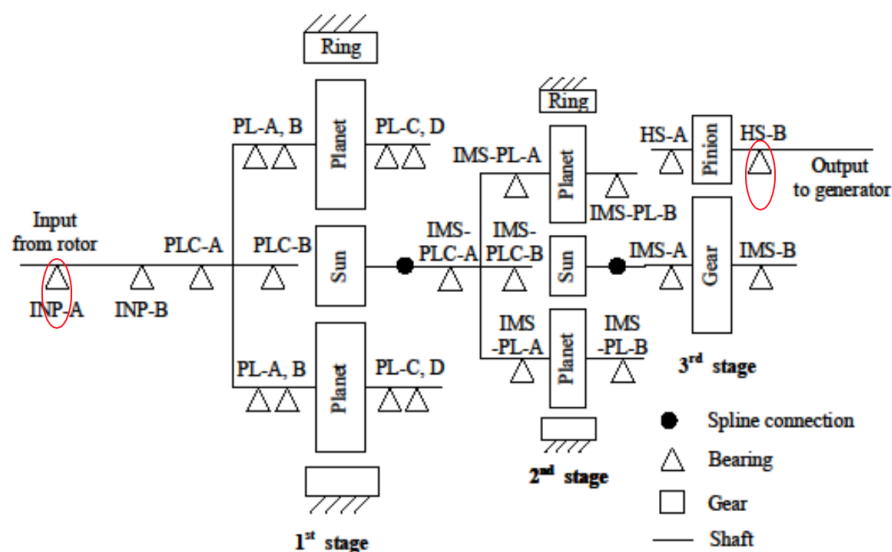
Figure 8: Caption

A total of three distinct load cases (LC) have been considered, each reflecting a specific type of bearing damage. The first 2 cases, *LC1* and *LC2* concern different types of damage on the MS bearing **INP-A** whereas *LC3* models a fault occurring at the HSS bearing **HS-B**. Each LC can be further subdivided into 6 simulations, a first simulation, referred to as *Baseline*, which considers the bearing stiffness equal to its original healthy value and 5 simulations which gradually decrease the bearing stiffness 15%, 30%, 50%, 70%, and 90% of its initial healthy-state stiffness.

LC1 and *LC2* correspond to an axial and radial damage of **INP-A**, respectively. Axial damage is replicated by gradually decreasing the axial stiffness of bearing **INP-A** K_x^{INPA} according to the approach described in section 2.2. The values of the bearing stiffness for healthy *Baseline* case and for the 5 subsequent simulations of increasing damage are presented in Table 8.

	LOAD CASE 1	
	Damage	**value [N/m²]**
Baseline	K_x^{INPA}(healthy)	3.52E+09
LC1_1	$0.85 \cdot K_x^{\text{INPA}}$	3.00E+09
LC1_2	$0.75 \cdot K_x^{\text{INPA}}$	2.47E+09
LC1_3	$0.50 \cdot K_x^{\text{INPA}}$	1.76E+09
LC1_4	$0.30 \cdot K_x^{\text{INPA}}$	1.06E+09
LC1_5	$0.10 \cdot K_x^{\text{INPA}}$	3.52E+08

Table 8: Evolution of the axial bearing stiffness of **INP-A** for each simulation for *LC1*

For the radial damage of **INP-A** a similar approach is followed by modifying the bearing stiffness K_y^{INPA} and K_z^{INPA} within the numerical model. The values of the bearing stiffness K_y^{INPA} and K_z^{INPA} for healthy and faulty conditions are provided by Table 9.

	LOAD CASE 2			
	Damage	**value [N/m²]**	**Damage**	**value [N/m²]**
Baseline	K_y^{INPA}(healthy)	8.92E+09	K_z^{INPA}(healthy)	1.25E+10
LC2_1	$0.85 \cdot K_y^{\text{INPA}}$	7.59E+09	$0.85 \cdot K_z^{\text{INPA}}$	1.06E+10
LC2_2	$0.75 \cdot K_y^{\text{INPA}}$	6.25E+09	$0.75 \cdot K_z^{\text{INPA}}$	8.76E+09
LC2_3	$0.50 \cdot K_y^{\text{INPA}}$	4.46E+09	$0.50 \cdot K_z^{\text{INPA}}$	6.26E+09
LC2_4	$0.30 \cdot K_y^{\text{INPA}}$	2.68E+09	$0.30 \cdot K_z^{\text{INPA}}$	3.76E+09
LC2_5	$0.10 \cdot K_y^{\text{INPA}}$	8.92E+08	$0.10 \cdot K_z^{\text{INPA}}$	1.25E+09

Table 9: Evolution of the radial bearing stiffness of **INP-A** for each simulation for *LC2*

Similarly to *LC2*, the final load case considered in this work *LC3* also replicates a radial damage only this time the radial damage affects a bearing of the HSS **HS-B**.

According to the approach to model damage described previously in section 2.2 the bearing stiffness will be progressively decreased to model incremental bearing damage. This is achieved by modifying K_y^{HSB} and K_z^{HSB} in the numerical drivetrain model. The bearing stiffness values corresponding to *LC3* for healthy and increasing damage are presented in Table 10.

	LOAD CASE 3			
	Damage	**value [N/m^2]**	**Damage**	**value [N/m^2]**
Baseline	K_x^{HSB}(healthy)	7.42E+09	K_z^{HSB}(healthy)	8.54E+09
LC3_1	$0.85 \cdot K_y^{\text{HSB}}$	6.31E+09	$0.85 \cdot K_z^{\text{HSB}}$	7.26E+09
LC3_2	$0.75 \cdot K_y^{\text{HSB}}$	5.19E+09	$0.75 \cdot K_z^{\text{HSB}}$	5.98E+09
LC3_3	$0.50 \cdot K_y^{\text{HSB}}$	3.71E+09	$0.50 \cdot K_z^{\text{HSB}}$	4.27E+09
LC3_4	$0.30 \cdot K_y^{\text{HSB}}$	2.23E+09	$0.30 \cdot K_z^{\text{HSB}}$	2.56E+09
LC3_5	$0.10 \cdot K_y^{\text{HSB}}$	7.42E+08	$0.10 \cdot K_z^{\text{HSB}}$	8.54E+08

Table 10: Evolution of the radial bearing stiffness of **HS-B** for each simulation for *LC3*

2.4 Simulated data

The high-fidelity numerical model of the WT drivetrain has been described and the three LC considered in this work have been formally defined. The numerical model is constructed on SIMPACK, a multibody software package. The LCs are used to generate data corresponding to a variety of bearing faults. SIMPACK provides a very large amount of variables for each LC related to the loads, motions, velocities and accelerations in the six-degrees of freedom of virtually every single body that comprises the drivetrain model. This section aims at highlighting which of SIMPACK's multiple outputs will be used as input for the prognosis model.

2.4.1 Equivalent sensor layout concept

The numerical model provides abundant data for the main shaft, the gearbox and the high-speed shaft as well as the generator, the housing and the bed-plate. Real-life condition monitoring systems (CMS) however collect a far more limited amount of information. In fact, commercial CMS implemented on offshore wind turbines today mobilize a minimal number of sensors. A large number of sensors results in higher costs. A greater amount of sensors also requires more computational power to collect, store and process larger amount of data. Furthermore, adding more sensors than necessary will not always result in a substantial improvement of monitoring capability and may result in redundant data which

hardly justifies an increase in costs.

Since this thesis wishes to present itself as a realistic approach to RUL prediction of drivetrain bearings, it's fundamental constraint is to achieve this goal whilst mobilizing a minimal number of sensors. Therefore, rather than using an unrestricted number of SIMPACK's output variables for RUL prediction this thesis has selected those output variables that most closely match the data collected by real-life CMS used in the wind industry today.

Vibration-based CMS make use of a variety of sensors which include accelerometers, velocity transducers and displacement transducers, Accelerometers remain by far the most widely used sensors in the monitoring of drivetrains. Sensors built-in into WT drivetrains follow

Specific standards such as *IEC 61400-25-6* [13] and*ISO 13373-1* [19] provide guidelines and recommendations for sensor type and frequency range, the number of sensors, sensor positioning and orientation and other characteristics depending on sensor location. As stated in [5], it is critical to ensure vibrations are transmitted to the sensor as directly as possible by mounting sensors in such a way that allows reliably measuring all relevant frequencies.

Figure 9 and Figure 10 illustrate two standard layouts for accelerometers for WT drivetrains. Specifically, Figure 9 corresponds to publicly available documentation of SKF's *WindCon* commercial vibration-based CM system.

The sensor notations listed below and illustrated in Figure 10 shows a typical sensor set-up on a WT drivetrain comprised of **eight accelerometers**.

2 sensors on the main bearing

1. AN1 in the radial direction

2. AN2 in the axial direction

4 sensors on the gearbox

3. AN3 or AN4 in the radial direction of the planetary gear
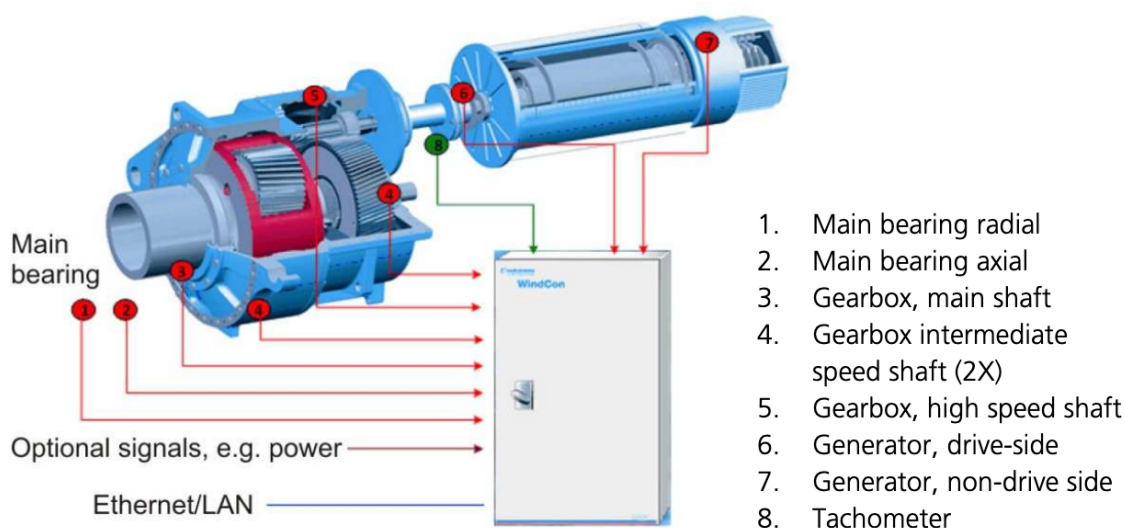
Figure 9: Example of sensor positioning for vibration-based CM applied in the SKF Wind-Con system [5]

4. AN5 on the LSS in the radial direction

5. AN6 on the ISS in the radial direction

6. AN7 on the HSS in the radial direction

2 sensors on the generator

7. AN11 in the radial direction on the drive end

8. AN12 in the radial direction on the non-drive end

This academic work will therefore make use of a numerical model to reproduce data which is comparable to the real degradation data gathered by a typical state-of-the-art condition monitoring sensor layout scheme by only examining a limited number of sensors. The equivalent sensor layout that will be considered in the numerical model is chosen such that it satisfies ISO 10816-21:2015 [7] requirements. For a drivetrain with two main bearings the sensor placement scheme put forth by the standards in Annex B and is shown in Figure 11.

2.4.2   Overview of variables used

Selecting those variables from the numerical model that would otherwise be fairly easy to collect by a standard CMS of a real turbine will benefit the applicability of the prognosis model to real-life data.
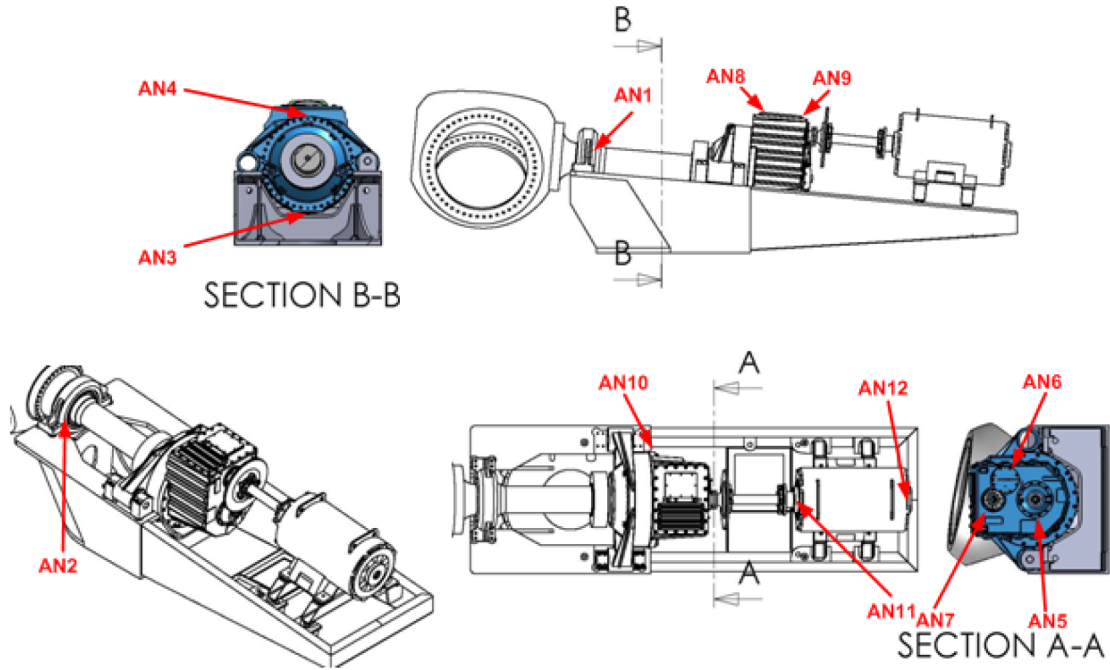
Figure 10: Sensor deployment strategy for vibration-based CM systems on wind turbine drivetrains [6]

Monitoring accelerations is common practice in vibration-based condition monitoring. Accordingly, most WTs today carry several accelerometers mounted in the drivetrain.

This thesis will incorporate the acceleration signals which are likely to be measured by real-life accelerometers according to the standard sensor set-up illustrated by Figure 9 and Figure 10. The reference standard ISO 10816-21:2015 [7] specifies that gearboxes comprising planetary stages should be equipped with one sensor per stage in the area of the ring gear and at the level of the sun.

Although several sensors at each stage are recommended by the standards, this work wishes to study the fault detection capabilities with a minimal number of sensors. Since load cases *LC1* and *LC2* replicate a damage originating on the main bearing at the Mains Shaft whereas *LC3* replicates a damage originating on a high-speed shaft bearing, it has been deemed interesting to see if it is possible to detect an incipient damage on the MS using the furthest sensor recommended in the standards corresponding to B3 in Figure 11.

Hence, the equivalent sensor layout considered in this work is chosen such that it corresponds to A1 and B3 according to the notation in Figure 11. This layout effectively satisfies standards [7] whilst mobilizing a minimum number of sensors.
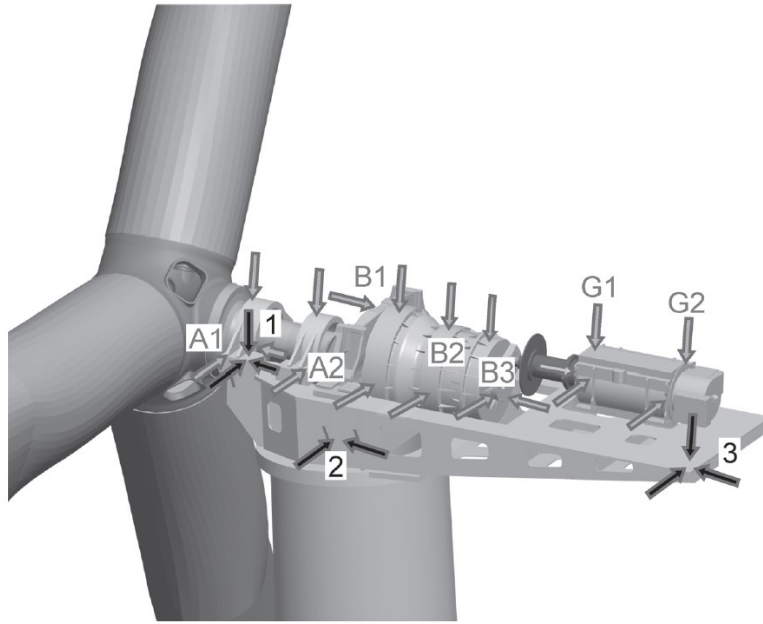
Figure 11: View of a wind turbine with two main bearings and the relevant measuring positions for accelerometer sensors [7]

Accordingly, the corresponding SIMPACK variables that will be used are:

- Translation and radial accelerations measured at the Main Shaft (location A1 in Figure 11);

- Translation and radial accelerations measured at the High-Speed Shaft (location B3 in Figure 11);

The above-mentioned translational and rotational accelerations will be collected in all three directions x, y, and z and their value is obtained in a fixed coordinate system.

In total, 12 acceleration signals are extracted from the numerical model for each LC. Six accelerations at each shaft -three translational accelerations and three rotational- for both the M and the HSS. Therefore, **36** different acceleration signals will be used for the prognosis model.

Besides accelerometers, special sensors exist to measure loads at specific locations. This is done with a strain gauge, a type of electrical sensor with a resistance that changes when force is applied which results in a variation of the electrical output. This allows strain gauges to effectively measure pressure, force, weight and tension. That being said, force-measuring sensors such as strain gauges are not present in condition-based monitoring

systems for offshore WTs. In fact, the equipment used to monitor drivetrains is typically consists of accelerometers only .

This work will, however, will use the numerical drivetrain model to extract forces at relevant locations. The purpose of collecting force and force variation on the bearings is to understand how damage affects the load path within the bearings. Furthermore, the prognosis of bearing lifetime according to the physics-based model implemented in chapter 5 requires the forces as input. Accordingly, the forces at all 4 bearings under study are assumed to be measurable. Hence, this thesis will also incorporate the following force signals:

- F_x, F_y and F_z measured at **INP-A** the main up-wind bearing supporting the Main Shaft;

- F_x, F_y and F_z measured at **INP-B** the main down-wind bearing supporting the Main Shaft;

- F_x, F_y and F_z measured at **HS-A** the bearing on the High-Speed Shaft on the gearbox side;

- F_x, F_y and F_z measured at **HS-B** the bearing on the High-Speed Shaft on the generator side .

Hence, 12 force signals are extracted from the numerical model for each LC which adds up to **36** different force time series for all three load cases.

Chapter 3

Literature Review

3.1 Fundamentals of Maintenance

3.1.1 Maintenance Strategies

An effective maintenance program is a crucial aspect in just about every industry. As mentioned extensively throughout the literature and synthesized particularly well in [20] maintenance strategies can be reactive, preventive or predictive:

Reactive maintenance

Also known as corrective maintenance or run-to-failure maintenance, reactive maintenance is perhaps the traditional approach to maintenance and is essentially repairing a machine or component when failure has occurred. Reactive maintenance gives the longest time between shutdowns and therefore yields a major cost in form of production loss. Repairing upon failure has another potential disadvantage: machines comprised of many components can fail in a catastrophic manner due to the failure of components other than the ones that initially failed in caused by chain-reaction of consequential damage.

Preventive maintenance

Preventive maintenance or scheduled maintenance is a time-based approach that sees the replacement of certain critical components at scheduled interventions. It is common to undertake these interventions at regular intervals which are shorter than the estimated time between failures. The advantage of such an approach is that the (1) probability

of catastrophic failure is significantly reduced and (2) a vast majority of the maintenance activities can be planned ahead easing logistics and ensuring a good control of productivity.

The main disadvantages are that (1) the time to failure of a component must be accurately predictable; (2) a number of 'healthy' components are replaced systematically which yields an excessive consumption of unnecessary resources; (3) the frequency of maintenance activities is high to ensure success which results in a large number of maintenance and that (4) a number of unforeseen failures can still occur. Furthermore, an additional consequence of (2) is that excessive number of unneeded maintenance activities can give introduce new faults in machinery which otherwise would have been avoided thus increasing 'infant mortality' of the components. This phenomenon is associated to the morale of that maintenance workers that knowingly and repetitively replace fully-working components as pointed out in [20].

Predictive maintenance

Predictive maintenance is the strategy that seeks to carry out maintenance activities at the optimum time, nor too late after a component has already failed, nor excessively early when a component still has a significant useful life remaining. The goal is to predict potential breakdown of a component through regular condition monitoring. Condition monitoring (CM) is defined as the process of monitoring a parameter or a set of parameters measured in the machinery such that a significant change observed in the monitored parameter(s) is useful in identifying the development of failure. The main advantages of CM are (1) failures can be detected early thereby reducing catastrophic failures; (2) the health of components can accurately evaluated which allows more cost-effective maintenance activities; and (3) the collection, evolution and subsequent analysis of parameters can provide valuable insight on root causes of failures as well as reliable input for component design and improved operation of machinery.

Of these three maintenance strategies, CM based maintenance is by far the best suited for large offshore wind farms located at remote locations which can be difficult to access throughout the year. As such CM based maintenance has been chosen as the main targeted maintenance approach of this study.

Theoretically, it is possible to monitor relevant parameters to assess the behaviour of almost all the major elements that comprise a utility-scale wind turbine. Therefore it is typically

possible to monitor the rotor blades, the nacelle, the drivetrain, the tower, or even the foundation if the appropriate sensors are put in place. From a practical perspective, it is not cost-effective to monitor all components and compromises need to be met.

3.1.2   Definition of Condition Monitoring

Condition monitoring (CM) is simply using equipment installed on a machine to monitor a series of physical parameters measured on the machine's components. CM is based on regular monitoring and measurements and the subsequent analysis of these measurements to detect changes in the normal operational behaviour of mechanical components such as bearings or gears. By analyzing deviations in the measurements the development of faults can be identified and located within the mechanical system of components.

A CM system can be classified as either an on-line system or an off-line system. CM carried out by permanently monitoring the components with the help of monitoring equipment continuously transmitting measurements to a data server located in a control center is considered to be on-line. If on the other hand a posterior laboratory analysis is needed to process measurements and yield results the CM system is known as an off-line CM.

Broadly speaking, any given CM system can be broken down into three sequential steps listed below and illustrated in Figure 12:

1. **Data acquisition** covers the collection and storage of raw data of all the monitored components. Data can be a scalar value, an array of scalar values or a data file, such as a picture or a thermographic data file.

2. **Data processing** to reduce raw data, extract suitable features, relate the observations in the data to certain components and detect faults. It is a key-step to transform large amount of collected data into meaningful indicators that can be interpreted for fault detection.

3. **Prognosis of the remaining useful life**. After having identified that a fault is developing and its location the last natural step in the utilization of CMS data is to estimate how soon and how likely failure will occur. It is a critical step to maintenance planning.
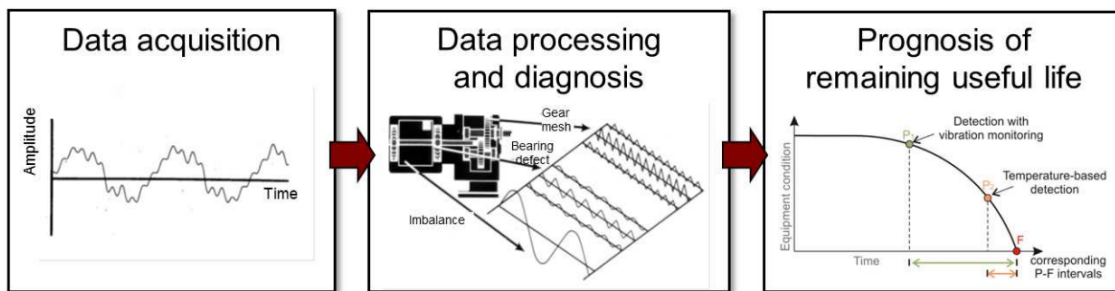
Figure 12: Three-step process of a CM system [5]

The benefits of CM include [10]: 1) detecting incipient failures early, thereby reducing the chances of catastrophic failures; 2) accurately evaluating component health conditions, which has the potential to enable more cost-effective O&M; and 3) analyzing root causes, which may provide the inputs for improved turbine operation, control strategy, and component design. Although the economics of deploying CM for a wind park are case dependent [11], some studies have shown the estimated return on assumed cost being better than 10:1 [12], with total return on investment achieved in less than three years [13]. These benefits will be even more dramatic if turbines are installed offshore where accessibility is a huge challenge. In a broad sense, CM of an onshore utility-scale wind turbine can target almost all of its major subsystems, including the blades, nacelle, drivetrain, tower, and foundation. However, the CM discussed in this report is focused solely on the wind turbine drivetrain.

3.1.3 SCADA data & purpose-designed CMS

As of today, it is clear that an accurate and reliable condition monitoring system is a good method to increase availability and decrease the cost of energy from wind. Challenges related to O&M are enhanced for offshore wind farms (OWF) since they may not be accessible for several periods of the year. This means OWF will benefit substantially from a proactive maintenance strategy which can be delivered by effective wind turbine condition Monitoring Systems (WTCMS).

Condition monitoring can make use of two potential sources of data used for condition monitoring of wind turbines available to industry.

1. **Supervisory Control and Data Acquisition (SCADA) systems** SCADA systems are initially designed for operating purposes only, making it possible for opera-

tors to supervise and control wind farms remotely. They have gained an overwhelming popularity amidst operators and they are present today in almost every OWF. The parameters monitored by a SCADA system are related to power production, wind farm efficiency and safety. The monitored signals include active and reactive power output, generator currents and voltages, turbine and generator shaft speeds and temperatures of several sub-components, such as temperature of both the gearbox and generator bearings, lubrication oil temperature or the average nacelle temperature. Measurements are usually done at 10 min intervals

2. **Purpose-designed CMS**, based upon experience of monitoring conventional rotating machines in other industries, mainly vibration-based systems, although some are used in combination with oil particle counters and fibre-optic strain gauges. They comprise an integral part of this work and are discussed in detail in section 3.2

The suitability of SCADA systems for wind farm control has lead to these systems being installed by default hence providing an available data source at no additional cost. In turn, this has sparked interest on how measurements from SCADA data can be used for performance monitoring systems which would potentially make CM very cheap with little to no additional instrumentation required. Currently, efforts are being made to assess the viability of using SCADA-based CM such as the EU FP7 ReliaWind project [21]. Although their added values needs to be explored in more detail, as of today few operators expect SCADA to significantly reinforce CMS because of its low 10 min sampling rate has been considered too low for accurate fault diagnosis in wind turbien drivetrains. As summarized in [22] SCADA-based CM is cheap and informs the operator the approximate WT condition but cannot replace a professional purpose-designed WTCMS.

3.2   Condition monitoring techniques

The capability of a condition monitoring system (CMS) relies upon two basic elements: the number and type of sensors, and the associated signal processing and simplification methods utilized to extract important information from the various signals. This section aims at explaining the most common types of sensors currently used for WTCMS. A variety of CM techniques are used throughout the industry to monitor the different wind turbine components. The most relevant are:

Vibration analysis is the most popular technology employed in WT, especially for rotating equipment requiring different sensors for different frequencies. It is appropriate for monitoring the gearbox, the bearings as well as the blades

Acoustic emission when the structure of a metal is altered a rapid release of strain energy takes place and elastic waves are generated which can be analysed by acoustic emissions. The primary source of AE in WTs is the generation and propagation of cracks. AE sensors have been used successfully not only in the monitoring of bearings and gearboxes but also for damage detection in blades of a WT

Ultrasonic testing techniques for the detection of surface and subsurface structural defects of wind turbine towers and blades. Applied to blades, ultrasound techniques exist to visualize and inspect the multi-layered structure of the WT blade and to find defects like delaminations or lack of glue.

Oil analysis involves monitoring oil temperature, contamination and moisture. Useful to detect early warnings of excessive wear in WT gearbox by oil contamination and characterization of the particulates. Although on-line oil analysis is gradually becoming more important with several on-going pilot projects today it is mostly executed off-line by taking samples.

Strain measurement

Electrical effects

Shock pulse method (SPM)

Performance monitoring by using relationship between parameters such as power, wind speed, blade angle and rotor speed can be used for the early detection of faults. An example is the power and voltage flicker analysis with variable wind speed and turbulence.

Process parameters

Radiographic inspection using X-rays, although only rarely used, provides useful information regarding the structural condition of components. the main advantage of X-ray inspection is its accuracy of this technique and a transportable radiographic system for WT blades has been recently demonstrated.

Thermography a technique currently only applied off-line which involves visual interpretation of hot spots that arise due to bad contact or a system fault often used for monitoring electronic and electric components. Pulsed thermography can be employed for the structural evaluation of blades but due to the bulky equipment involved this is not a standard methodology amongst wind turbine operators.

Out of the above mentioned methods of condition monitoring, vibration based and lubricant oil based CMS are by far the most common techniques and are currently widely implemented by manufacturers and operators to monitor wind turbine drivetrains. Both vibration-based and oil-based CMS are be discussed in greater detail in subsection 3.2.1 and subsection 3.2.2 respectively.

However, as of today, ongoing R&D is exploring suitable complementary methods to improve the fault detection capabilities in wind-turbine drivetrain components. Alternative approaches actively been pursued by the include acoustic emissions, thermography using infrared (IR) cameras as well as the analysis of different electrical and mechanical quantities measured in wind turbines. These alternative methods to compliment and reinforce existing CMS techniques are discussed in subsection 3.2.3

3.2.1   Vibration-based CMS

The working principle of a vibration-based CMS is based on the fact that when rotating machinery presents damage excessive vibrations begin to take place within the drivetrain. Since damage on any given component can be associated to a unique vibration pattern, the CMS is used to monitor and register vibration patterns which can then be decomposed into spectral components. In the resulting spectrum characteristic frequencies are identified which can then be related to machine components.

In wind turbine CM, vibration analysis is extensively used to monitor several drivetrain components such as the gearbox and gearbox bearings, the main bearing(s), and generator. Typically, vibration-based CM systems use several standard accelerometers sensors located across the drivetrain. Different types of accelerometers are used from the very low-frequency range to the high frequency range.

Data acquisition

Besides the sensors, a CMS requires a data acquisition system (DAS), commonly housed in

the nacelle, and a data server. The DAS transmits the data to a data server via Ethernet or fiber optic cables when the data server is located at the offshore wind park, or transmits the data wirelessly to a server located onshore in the monitoring center.

Instrumentation

Vibration-based CMS make use of a variety of sensors which include accelerometers, velocity transducers and displacement transducers, although accelerometers are by far the most widely used sensors in the monitoring of drivetrains. The correct selection of sensors is crucial to the quality of the CMS and should follow the recommendations of ISO 13373-1 [19], where the types and frequency range of sensors are outlined.

The main difference between different vibration-based CM systems is the number and the location where these sensors are installed within the drivetrain. Furthermore, due to the wide variety of drivetrain designs currently deployed in the wind industry an increasing number of different sensor lay-outs are being considered. An obvious example is the difference between measuring vibrations in geared drivetrains or direct drive concepts as illustrated in Figure 13. These two drivetrain designs require different types of sensors due to the difference of operating rotating speeds as well as different sensor placement due to the difference in the inner architecture of the drivetrain.

(a) (b)
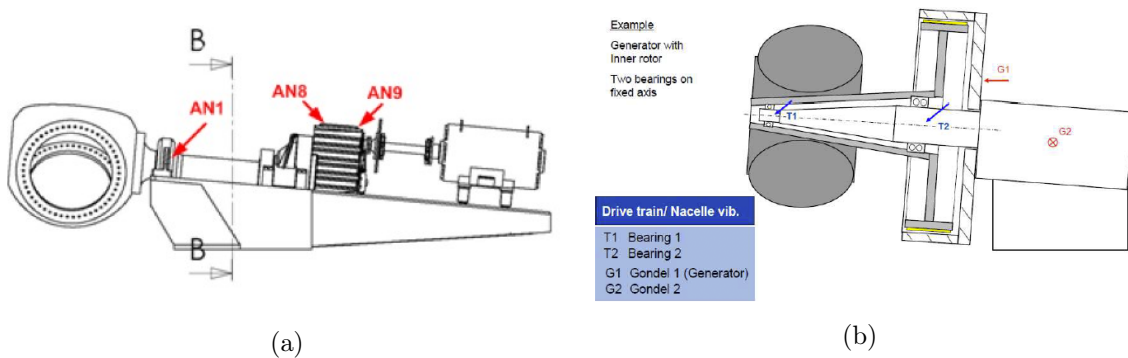
Figure 13: Sensor deployment strategy for vibration-based CM for (a) conventional geared drivetrain [6] and (b) for a direct drive turbine [5]

Analysis of CMS vibration signals

In terms of analysis algorithms, vibration signal analysis is commonly done by performing the well-known fast Fourier transform (FFT) or envelope analysis to display the presence of defect frequencies and detect a fault signature. However, since practically all WTs today are variable speed machines, their non-stationary nature due to speed variation makes it

difficult to extract meaningful information with FFT and similar approaches. Furthermore, conventional rotating machinery CMS is well established for for components that rotate relatively fast, however vibration analysis for faults in medium and low-speed components is lagging and often does not lead to satisfactory results due to complex gearbox and variable speed designs [23]. An extensive overview of these and additional signal analysis tools commonly used to process and interpret vibration signals is provided in subsection 3.3.2

Limitations & challenges in vibration-based CM

A fundamental challenge in vibration-based CM is the disparity of drivetrain designs currently deployed in the wind industry which makes it difficult to standardize sensor placement strategies. For example vibrations in geared drivetrains and direct drive trains require different types of sensors due to the difference of operating rotating speeds as well as different sensor placement due to the difference in the inner architecture of drivetrain.

The vibration monitoring for the slow rotating stage comprised of planetary gears is particularly challenging as it becomes a difficult task to track all the components and their evolution. Due to their challenging nature and fault detection complexity, planetary slow rotating stages are actively being targeted by researchers. Nonetheless, it is equally critical to accurately evaluate defects in the high-speed stages typically comprised of parallel gears.

A particular challenge in typical gearboxed drivetrains which use epicyclic gearboxes (EG), a concept widely adopted by the wind industry, is the influence of the sensor arrangement on the measured vibrations. In a comprehensive work [8] it is pointed out that the deficient results of failure detection on EG using vibration analysis is due to:

- The lack of understanding on the complex characteristics of the vibrations generated in EG caused by the fact that each planet gear meshes with the sun gear and ring gear simultaneously making the number of meshing processes double to the number of planet gears

- The location of the sources of vibrations varies continually whilst the sensor location remains fixed. This is due to the fact that the contact between the meshing gears, where vibrations occur, rotate around their own axis and revolve around the sun gear whereas the sensors remains steady. This implies that the distance between the sensor and the points of generation of vibrations changes continuously.

3.2.2 Oil-based CMS

Lubricating oil plays a crucial role in ensuring the ability of wind turbine to perform conveniently by guaranteeing the adequate functioning of gearboxes. In machinery, a lubricant has 3 primary functions:

1. Physically separate component surfaces with an oil film. If film thickness is sufficient, metal-to-metal contact can be avoided reducing the friction between the surfaces of components. Reducing friction effectively reduces wear as well as the amount of energy required to perform the work.

2. Controlling component temperature by absorbing heat generated at the friction surface and dispersing it.

3. Transport dirt and other debris away from the friction surface with some oil additives including agents that break up contaminants to either make them settle in the reservoir or hold them in suspension until they are filtered out.

The ability of the lubrication oil to perform these functions will reveal if it provides adequate protection to the gearbox and whether the wind turbine will continue to operate in a reliable way.

When considering oil-based monitoring it is important to distinguish between two different targets that can be achieved through the analysis of oil. Firstly, examining the quality of the lubricant oil itself to determine if the lubricant oil needs to be replaced. Indirectly, this also provides information of the effectiveness of the filter system. Secondly, oil CM can also be used to monitor the gearbox by analyzing wear debris found in the oil which can indicate developing faults of mechanical components. Therefore oil analysis is also a valuable technique to achieve gearbox gear and bearing monitoring.

Simply stated oil monitoring serves a double function: (1) its an effective way to assess the useful life of the lubricant oil itself and (2) its a reliable method to detect machine wear as unhealthy components release wear particles.

It is equally important to distinguish between the online and offline analysis of oil condition monitoring. Online oil CM is performed by Oil particle-counter sensors which are low-cost and well-proven. In contrast, regular oil sampling also used for gearbox gears and bearing

monitoring is done offline in a laboratory where the composition and shapes of lubrication oil metal particles can be analyzed which is far more complicated and requires accessing the actual offshore turbine

Instrumentation

The quality of oil is a reliable method to evaluate the degree of protection offered to mechanical components. Oil-based CM can use a variety of sensors to assess the quality of the lubricant. These sensors are used to measure parameters such as the water content, particles concentration, wear-debris production, viscosity and oil quality, some of which can be implemented in a real-time oil CM, for example the total count of particles. Oil temperature and pressure are also commonly measured and are usually part of the data collected by turbine SCADA systems. However, most oil CMS have been developed in other industries and their applicability to wind turbine CM still remains to be demonstrated. In fact, a majority of the most common sensors used in oil CMS are still at research stage for wind turbine drivetrain monitoring and several sensor manufacturers are currently proving their capabilities to the industry. Figure 14 shows sensors readily available at commercial level and their current maturity in wind energy applications. Characteristics of each of these sensors is provided in [5].

Since oil-based condition monitoring is still at an early stage for WTCM, from sensor technology and validation to fault detection and diagnosis capabilities, online oil-based CM for wind turbine drivetrains mainly refers to particle-counters systems. These sensors are the only ones currently implemented by several wind turbine manufacturers

3.2.3   Other methods for CMS

Besides the two most common condition-monitoring practices - vibration-based and oil analysis CMS- alternative methods to monitor the condition of wind-turbine drivetrain components are being pursued by the industry. These alternative methods are not necessarily novel techniques as they exist in other industries, their applicability to wind turbines however remains relatively new and is yet to be demonstrated. Alternative methods are currently at different development level, some are at R&D level, while others are in the pilot phase with a few being implemented by manufacturers to demonstrate their functionality. The most relevant and promising are presented in this section.

Type of sensor	Output signal	Status of implementation in wind turbines
Water-content sensors	Water saturation (%)	Only laboratory tests, validation for wind turbines required
Particles-concentration sensors	Particles size distribution according to ISO 4406	Laboratory tests and experimental test in a wind turbine
Wear-debris sensors	Quantity of particles per unit of time and size	Part of standard CMS of some wind turbine manufactures
Dielectric constant sensors	Dielectric constant	Laboratory tests for several industry applications
Viscosity sensors	Kinematic viscosity	Laboratory tests for wind turbine applications
Oil-properties sensors	Viscosity, temperature, density, dielectric constant	Experimental test in some wind turbines
Oil-quality sensors	Color code, quality index	Laboratory tests for wind turbine applications

Figure 14: Overview of commercially available sensors for oil condition monitoring [5]

3.2.3.1 Acoustic Emissions

Using acoustic emissions (AE) as a tool for the condition monitoring is not new, however it is only in the last years it has expanded [8]. As of today, fault detection based on AE is considered a promising approach to monitor several components of wind turbines, such as drivetrain components -namely bearings and gearboxes-, as well as the rotor blades.

When a crack is generated and propagates on the surface of a material a sudden release of energy occurs in the form high-frequency transient elastic waves. These waves are solid-borne rather than airborne acoustic signals [20] and they appear due to bursts of stress waves being emitted as cracks initiate and grow. Therefore, detecting and analyzing these acoustic emissions can lead to identifying and locating cracks. This is done by installing surface-mounted piezoelectric sensors that have the ability to detecting these waves and locating their origin.

However, AE are not only present in the event of cracks. Impacts, friction, turbulence or leakage are also common sources of AE. Asperity in between two surfaces such as the
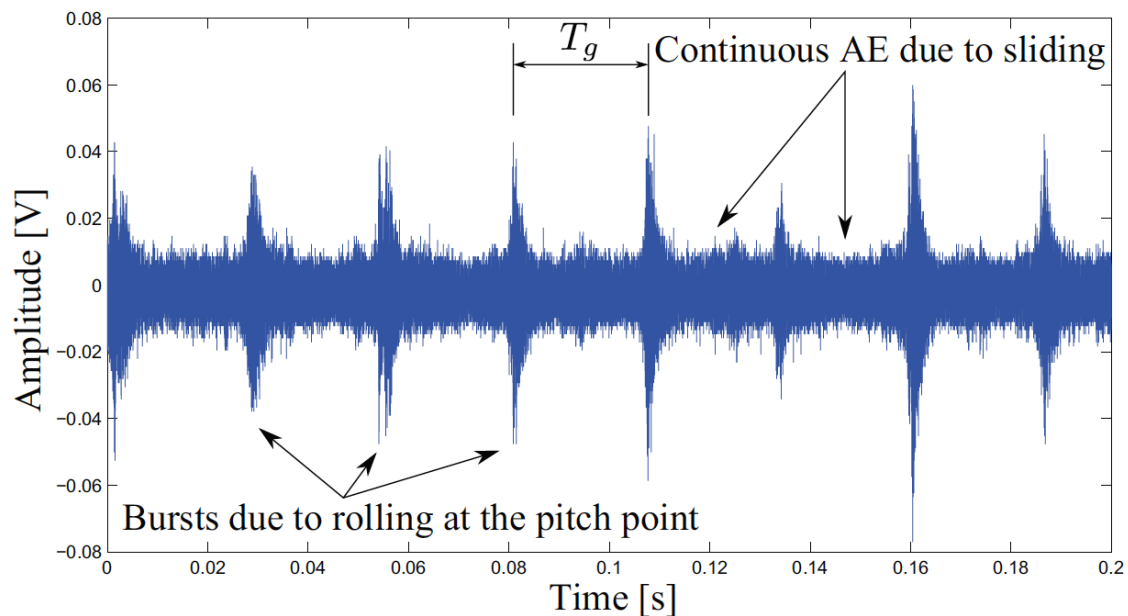
Figure 15: Typical time history of AE signal measured on a spur gearbox [8]

meshing process of two gears also generates AE.

Analysis of AE has received increasing attention in bearing and gearbox diagnosis. For instance, the signals generated during the meshing of two spur gears reveals a train of bursts over a continuous background noise. The bursts are thought to be produced at the pure rolling portion of the meshing period, whereas the continuous noise is produced in the portion where a combination of rolling and sliding occur [8]. A time history of a typical AE signal measured on a gearbox shows the presence of burst at the gear mesh period T_g with a continuous background corresponding to sliding is seen in Figure 15.

In the case of meshing processes, the AE were seen to be influenced by the characteristics of the gear tooth surfaces and the lubricant film thickness. A high roughness of the tooth surfaces increases the asperity contact and results in higher AE. Parameters influencing the film thickness such as temperature and load will also influence AE. For instance, a higher temperature or an increase in the load both result in a decrease in the film thickness which increases the asperity contact, triggering higher AE levels.

The advantages of AE-based CM are discussed in [8]. The main advantage is that even micro physical phenomena will generate some degree of AE which makes it a great indicator for early-stage failure detection. Also, in the typical range of AE frequencies the mechanical noise has a low amplitude, offering a high signal-to-noise ratio for AE signals. Furthermore,

AE waves travel from the source in all directions, they are hence non-directional signals that require a single sensor. Finally, the frequency of the AE signals depends on material properties rather than on the rotational speed of the machine which in turn may be an advantage to monitor low-speed rotating machinery.

However, attenuation of the signal is inconvenient: the AE wave amplitude decreases as its distance from the source increases. For this reason it is good practice to install sensors as near to the AE source. Additionally, noise from other equipment can reduce the quality in the output signals. Also, it is important to note that AE are sensitive to interfaces and changes in the propagation medium such as changes of material, where one part of the AE wave will be transmitted and the other part will be reflected. This should also be considered when selecting an appropriate location to place the sensor.

In the same way vibrations measured on an epicyclic gearbox are intimately linked to the sensor location, the sources of generation of AE such as the contact point between teeth revolve around the sun gear which will influence the AE measured by the sensor.

Although the frequency range associated to AE differs in literature, for metallic components, the range is typically 100 kHz to 1 MHz according to [20]. It is important to underline the estimated suitability of AE to effectively detect faults in low speed rotating parts.

3.2.3.2 Thermography

Thermography is based on obtaining a heat distribution at the surface of a component and relies on infra-red (IR) cameras to produce heat zone images of components in order to detect thermal anomalies. Degeneration of components or a bad contact may lead to hot spots which can be identified visually by analyzing thermal images.

It is a estimated to be particularly suitable for monitoring and failure identification of electronic and electric components. As a general rule, these components will have a range of normal operating temperatures which is suitable to use as a baseline for detecting thermal changes and variations.

As of today, thermography is mainly applied offline. For wind turbines, this would involve manually carrying out a visual inspection of the mechanical or electrical component which is problematic due to safety reasons. Although thermography is a non-intrusive technique

which may be a suitable complementary method to improve the fault detection capabilities and although some studies have shown the feasibility of using IR-technology for wind turbine condition monitoring, it is unlikely thermography will be used for online CM of wind turbines on the short term due to the high costs of IR cameras [5]. This may change on the longer term, as IR-cameras and diagnostic software suitable for on-line monitoring enter the market at a competitive cost [24]

3.3   Approaches to detection, diagnosis & fault prognosis

To evaluate the health of a WT drivetrain during its operational life a suitable health monitoring system must be put in place in the form of a prognosis.

There are several accepted ways to classify health monitoring systems for diagnosis and prognosis. A common classification for prognostic methods which is illustrated schematically in Figure 16 distinguishes methods into three distinct families: physics-based models, data-drive models and hybrid models. Other classifications include signal analysis methods as a distinct independent group given the prominent role signal processing plays in current fault detection and prognosis approaches. All of these methods can make use of CMS signals, SCADA data or a combination of both
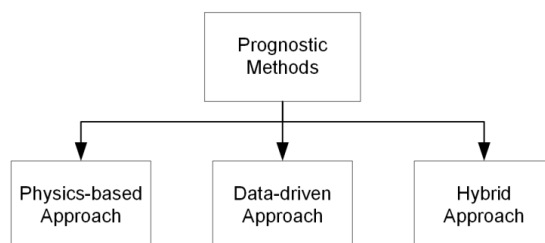
Figure 16: Main Prognostics Approaches [9]

Physics-based models rely on an understanding of the physics that govern the system and its degradation mechanics. Sufficient knowledge on the system, its operational behaviour, abnormal functioning and failure modes must be available to derive explicit mathematical relations that describe the degradation processes.

To formalize a physics-based model the understanding of the physics of failure is indispensable. This can be considered both as a drawback and as an opportunity. The disadvantage is that each failure mode has to be analysed independently and for many relevant failure

modes a clear degradation mechanism is not present. Even if a given failure mode can be associated to a specific degradation mechanism fitting a physical degradation model to this mechanism is not always possible. Furthermore, even if a degradation process for a given failure mode is modelled successfully the inputs of such models may not be readily available nor provided by CMS techniques reducing their applicability. A relevant advantage of physics-based models is that they establish synergies with the design process and can help optimize future designs by understanding the degradation mechanisms. Additionally, physics based models are easily certified since the principles behind the algorithm are justified by proven physical principles. Another important advantage, particularly relevant for academic research, is that a physics-based algorithm can be implemented with short data sets.

Data-driven models generally refer to a broad category of methods that combine statistics and historical failure data of WT components with pattern recognition algorithms. Prognosis based on data-driven methods are capable of establishing complex models exclusively from available historical data. Within data-driven methods literature shows an increasing interest to incorporate 'intelligent' algorithms based on artificial intelligence (AI) and Machine Learning (ML) techniques in particular. ML is used to identify underlying patterns in data by training an algorithm with large datasets. Artificial neural networks (ANN) and clustering/classification techniques belong to this category of methods.

Data-driven methods make no use of the underlying physics that govern the system. Therefore an in-depth understanding of the physics of the system under study is not necessary to implement a data-driven approach. Despite the lack of underlying physical basis, data-driven methods have proven successful for fault detection, prognosis tasks and RUL estimation. This is particularly useful when the system under study and the damage mechanisms that it experiences are complex. The physics-of-failure associated to WT drivetrains are often complicated to model and poorly understood. Sometimes physical models that capture the relevant degradation processes are simply not available. This highlights the advantage of using a data-driven method to overcome the limitations inherent to the lack of knowledge. Data-driven methods are preferred when evaluating the health of complex systems which typically present complicated, and sometimes unavailable, physics of failure.

Signal analysis and signal processing methods are based on time and frequency domain analysis. Signal processing operations usually have a strong mathematical basis but their

application in fault detection and prognosis tasks does not require an explicit mathematical relation with the monitored system. These methods cover the range of classic and more advanced techniques used to analyse, synthesize and extract meaningful data from measurements.

Although some prognosis approaches are based exclusively on the implementation of signal analysis to obtain results, in reality all of the prognosis methods illustrated in Figure 16 will mobilize signal processing tools to a certain extent. For instance, a physics-based model or a data-driven approach may use signal analysis to reduce signal noise, extract characteristics of the system or capture degradation patterns.

Since processing a raw signal is a prerequisite of almost any prognosis method regardless of the approach, and this is done with Signal analysis tools, prognosis methods which are either based solely on signal analysis or rely to a certain degree on signal analysis are the most prevalent.

Hybrid models is a term used to define any given combination of the previously described methods to incorporate the strengths of two or more of these approaches and define a robust model for fault prognosis.

In conclusion, physic-based models assess the degree of degradation through degradation models which theoretically make physics-based models particularly suitable for prognostics. As such they should be preferred over purely data-driven methods when reasonably accurate. On the other hand, data-driven methods are preferred when evaluating the health of complex systems which typically present complicated, and sometimes unavailable, physics of failure.

The following section provides a comprehensive overview of each of these approaches: several aspects of physics-based models and their limitations are examined in subsection 3.3.1, signal analysis based methods are discussed in subsection 3.3.2 and an introduction to data-driven models is carried out in subsection 3.3.3. This section culminates with a qualitative comparison between physics-based models and data-driven methods presented in subsection 3.3.4.

3.3.1 Physics-based Models

Physics-based models rely on an understanding of the physics that govern the system and its degradation mechanics. Sufficient knowledge on the system, its operational behaviour, abnormal functioning and failure modes allows the health monitoring to be formalized by mathematical relations describing the underlying physics that drive the process. A PHM system can then be set-up by solving equations derived from engineering and science knowledge and used for diagnostics, prognostics or both of these purposes.

Cubillo *et al.* present in their work *Physics of failure for prognostics of gears and bearings of rotating machinery* a selection of the most appropriate physic-based models to represent the degradation mechanisms of typical components of rotating machinery. Cubillo *et al.* point out that some of the necessary inputs of these models are largely unknown and will not be provided by CMS systems even if a convenient degradation mechanism for a particular failure mode is put forth and modelled. This work [25] is still deemed of interest to understand the existing physics-based approaches to monitoring the health of the main rotating machinery, namely rolling bearings and gears, and understand the limitation of these models. In [25] the most common failure modes of gears and rolling bearings are analysed and potentially relevant degradation mechanism models are presented for each failure mode. The degradation mechanisms investigated are:

Creep Known to affect the inner raceway of roller bearings, creep consists of a permanent deformation that can be caused by low loads under high temperature. Its a time and temperature dependent phenomenon.

Fatigue Known to cause micropitting, macropitting and spalling of gears, fatigue causes damage in the form of small scattered holes in rolling and sliding contacts. Association of these small defects into bigger ones can lead to further damage and trigger component failure. Estimating the fatigue life of a component and the modelling of the phenomenon of fatigue is an important field for research. In fact the majority of the most developed physics-based models for prognostics are based on fatigue principles [25]

Cracks Excessive load, assembly errors such as misalignment, contaminants in the lubrication oil, deficient material or excessive cycles triggering fatigue damage can all lead

to crack growth on gear teeth and roller bearings. Furthermore crack is the degradation mechanism that ultimately leads to failure due to fracture of the component. As such, finding suitable degradation models that describe the length of cracks, their propagation mechanisms and severity an important target of physics-based models

Wear Common bearing and gear failure mechanisms involving metal-to-metal contact such as abrasion and scuffing are caused by wearing of the material which makes wear monitoring an important degradation mechanism to consider.

Modelling of Creep

A physics-related model that is commonly used to represent creep behaviour is the Norton creep law shown in Equation 3.1 where σ is the stress level; T is the temperature; and A, n and p are material constants.

$$\text{Creep rate } = AT^n\sigma^m \tag{3.1}$$

Prognostic methods implementing physics-based creep models have been developed by [26] for hot section component degradation in engines. Although some creep-models have been investigated for the purpose of health monitoring WT blades, no method targeting the drivetrain and its components using creep models ha been found in the literature.

Modelling of Fatigue

Several degradation mechanisms leading to permanent deformation are caused by fatigue. Modelling and implementing fatigue based on the CMS would therefore be beneficial to estimating the RUL of drivetrain components. First its important to distinguish between two fatigue-driven failure mechanisms: Low Cycle Fatigue and High Cycle Fatigue. Excessive load can cause the accumulation of permanent deformations which are typically governed by a deformation mechanism consisting of low cycle fatigue (LCF). This mechanism is characterized by a stress level above the yield stress of the material and the plastic deformation $\Delta\epsilon$ -the strain range- is the main factor that controls the degradation and the failure mechanism. Cyclic stresses acting on gears is also very common, leading to high cycle fatigue (HCF), characterized by removal of material such as pitting and spalling. HCF stresses are below the yield stresses and its the stress range $\Delta\sigma$ that controls the degradation mechanism. Physics of Failure will thus lead to different models to represent the

LCF and HCF degradation mechanisms. For HCF, Wohler proposed an approach extensively used today based on experimental fatigue data initially obtained from railroad axles although today analytical equations for a very wide range of metallic structure exist and are available in well-accepted standards. The Wohler approach to model the degradation process is based on the stress range $\Delta\sigma$ correlated to the number of cycles at that characteristic stress level in the so-called S-N curves. Basquin's law shown in Equation 3.2 is another common approach to account for HCF damage in gears based on the experimental work of Wohler.

$$\sigma_a = \frac{\Delta\sigma}{2} = \sigma'_f \left(2N_f\right)^b \tag{3.2}$$

Where where N_f refers to the number of cycles, σ_a is the stress amplitude, ${\sigma_a}'$ is the fatigue strength coefficient and b is the fatigue strength exponent. Concerning the magnitude in plastic deformations in HCF situations it should be noted that discontinuities in the material or a poor quality of the contact surface negatively affect the life of the component and these effects are further exacerbated under high temperatures which are common in gears.

For LCF, plastic deformation is the main factor that controls the failure mechanism. A common approach to physically model degradation due to LCF is the so-called Manson–Coffin shown in Equation 3.3 which uses a power law to describe the dependency of the cyclic life with deformation. In Equation 3.3 $\Delta\varepsilon_p$ is the plastic strain range and c and ε_f are experimental constants. A more accurate modifed model capable of representing both LCF and HCF degradation mechanisms is the Manson and Halford model which accounts for the elastic and plastic component of the strain [25].

$$\Delta\varepsilon_a = \frac{\Delta\varepsilon_p}{2} = \varepsilon_f \left(2N_f\right)^c \tag{3.3}$$

Modelling of Crack growth

Cracks due to fatigue have been found to be a critical degradation mechanism affecting gears and bearing alike. The most common crack growth degradation model is based on Paris' law, a crack growth equation that gives the rate of growth of a fatigue crack as shown in Equation 3.4.

$$\frac{da}{dN} = m\Delta K^b \tag{3.4}$$

Where a is the crack length, $\frac{da}{dN}$ is the fatigue crack growth for a load cycle and N the number of cycles; m and b are material parameters and intensity coefficient K depends on type of crack and geometry.

Although Paris' Law does not account for the initially slow crack growth nor the initial crack length it has proven to model component degradation in a sufficiently accurate manner. Although Paris' Law is widely accepted, several modifications and corrections have improved its ability to improve crack modelling such as the inclusion of thermal effects. Furthemore, a range of methods have been put forth which combine Paris' Law with other techniques to improve degradation estimation or model specific situations and components. One specific bearings degradation model was proposed by Hoepric in [27]. The joining of fatigue cracks can lead to macropitting and spalling. Hoepric presented an alternative equation inspired on Paris' formulation adjusted to represent the growth of the spall area in bearings:

$$\frac{dD}{dN} = C_0 D^n \tag{3.5}$$

Where D is the defect area, nd C_0 and n are material parameters. This spall degradation formula prsented in Equation 3.5 was succesfully applied for RUL estimation of rolling bearings by Orsagh *et al* in [28] in the context of prognostics for gas turbine engine bearings

Finally, it is worth mentioning that crack growth modelling is a prominent research area which is demonstrated by the appearance of increasingly sophisticated models. Methods have formalized such as in [29] that combine Paris' Law with support vector machine (SVM) algorithm based on machine learning techniques to estimate crack length. As such this method is not strictly a physics-based approach but rather a hybrid method.

Modelling of Wear

Physics based Models for PHM based on degradation caused by wear are limited [25]. However, several methods have been proposed. The Archard wear equation is a simple model shown in Equation 3.6 is used to describe sliding wear and is based on the theory of asperity contact. It states that the volume of the removed debris due to wear V_{wear} is proportional to the work done by friction forces.

$$V_{\text{wear}} = K \left(\frac{WL}{3H} \right) \tag{3.6}$$

Where H is the material hardness, W is the load, L is the sliding distance and K is the wear coefficient. By modifying the value of K, more complex wear models based on Archard's Law can be formalized to model adhesive, abrasive and corrosive wear.

Another degradation mechanism based on fracture mechanics was specifically intended to model wear caused by subsurface fatigue and proposed by Ghosh *et al.* in [30]. Equation 3.7 provides a correlation between wear and crack propagation as a function of the surface shear stress

$$\log(N) = a \cdot \log(Q) + b \tag{3.7}$$

where N is the number of cycles to failure, a and b are empirical constants determined in [30] and Q is shear stress at the contact which depends on the friction coefficient and on the applied load.

3.3.2   Signal analysis based methods

Signal analysis and signal processing methods are based on time and frequency domain analysis and do not require any explicit mathematical model. Within the available literature on fault detection, fault diagnosis and prognosis systems for WT drivetrains, methods based on signal analysis and processing are the most prevalent health monitoring systems. Any signal analysis method is based on the underlying prerequisite of processing a raw signal and transform it into meaningful information which amounts to reducing noise, extracting characteristics of the system and capturing degradation patterns. For instance, in the case where the inner race of a bearing has a small local defect, every time a rolling element passes over this defect an impulse is generated which will repeat itself every time it passes creating a distinctive signature in the vibration pattern. The vibration signals are then analysed either in the time or frequency domain to extract characteristic statistical features which reveal these distinctive signatures and can then ultimately be related to a fault case. Signal processing methods can be conveniently divided into time-domain and frequency-domain analysis techniques and will hence be treated separately in the following section. Most of the signal analysis methods that will be introduced are based on complex concepts involving intense mathematical manipulation which will not be looked into in detail unless deemed relevant to the progress of this work.

3.3.2.1   Time-domain analysis methods

Signal processing methods based on time-domain analysis commonly focus on statistical features such as minimum and maximum value, the peak-to-peak value, crest factor value, root mean square (RMS) as well as on statistical moments including the mean, mean, variance, kurtosis and other statistical parameters such as the skewness, the wave factor, the impulse factor or the margin factor are also used [24]. These values are often used as the basis of more advanced analysis such as Trend analysis, Time synchronous averaging (TSA) techniques or Amplitude demodulation. Trend Analysis is a powerful method capable not only of identifying faults but also assessing their evolution and severity in time. TSA is used to resample vibration data synchronously with a shaft rotation so as to extract a periodic signal from noisy data; it is extensively used to monitor rotating components such as gears, rotating bearing and other defects within the gearbox. Amplitude demodulation facilitates the extraction of frequencies that are hidden by higher energy vibrations, for example to

enable a good visualization of bearing defects frequencies without the interference of gear mesh frequencies [5].

3.3.2.2   Frequency-domain analysis methods

Fast Fourier Transform (FFT)

Fast Fourier Transform (FFT) is the most common method to transform a signal in the time domain into a spectrum in the frequency domain, used extensively in vibration and AE signals. With an understanding of the fundamental kinematic and geometric characteristics of monitored the component it is possible to distinguish in a spectrum healthy rotation frequencies corresponding to normal operational conditions from defect frequencies. Optimally, a vibration spectrum reveals valuable diagnostic information on location of a fault. which makes it particularly powerful to evaluate the health of complex systems containing a variety of bearings, shafts and gears such as a wind-turbine gearbox [5]. A vast majority of commercially available CMS, including those targeting gearbox and generator monitoring, use FFT of vibration signals for fault diagnosis

Power density spectrum

Other more advanced methods in the frequency-domain are analysis of the overall spectral energy by means of the RMS value which results in a power density spectrum. The analysis of the energy in the sidebands can indicate degradation. An example of the advantages of spectral analysis is illustrated in Figure 17 where the vibration spectrum of a signal obtained by an accelerometer monitoring the HSS is shown for a healthy and damaged gearbox. The study was performed by NREL in and the comparison of both frequency spectra shows the gear mesh frequency peak which is similar the healthy and the damaged gearbox but the spectra corresponding to the latter reveals some additional side bands indicating damage. These sidebands are in fact spaced at 30 Hz which matches the rotational speed of HSS and serve as an indicator of the gearbox bearing and gear damage.

Envelope Analysis

Envelope analysis is accepted as one of the most effective techniques to monitor bearing condition monitoring because it allows signatures that may be hidden in a narrow frequency band with a small amplitude to be separated from vibration components with higher
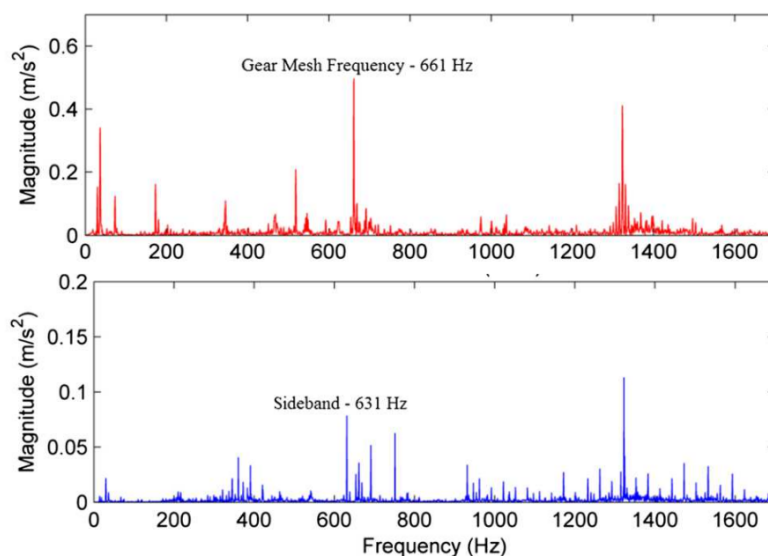
Figure 17: Frequency spectrum from a HSS gear in a wind-turbine gearbox in healthy (top) and degraded condition (bottom) [5]

amplitude in a wide frequency bands such as the mesh frequency. A frequency spectrum of bearing vibrations with a damage on the rolling element is likely to not reveal important frequency peaks corresponding to faults, however in an envelope spectrum these are easier to distinguish. To perform an envelope analysis, several steps are required; first a band-pass filter is applied around an excited natural frequency, then the Hilbert transform is used to extract the envelope signal and finally this envelope can be further analyzed in the frequency domain.
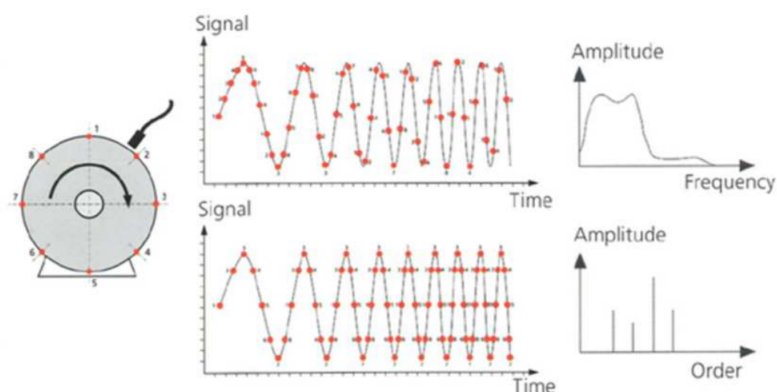
Figure 18: Sample recording at equidistant rotation angles rather than at equidistant times improving clarity [5]

Order Analysis

Given the variable-speed nature of WT the continuously changing speed of the rotor makes

it difficult to collect data in a consistent and meaningful way. In order to approach fault detection via vibration spectrum analysis some signal processing techniques must be applied. One such of these techniques is order analysis based on synchronous sampling which enables for example to collect samples at equidistant rotation angles rather than equidistant sampling times which improves clarity as seen in Figure 18. Order analysis is particularly important for extraction of fault features detection in WT drivetrains.

Cepstrum analysis

Cepstrum analysis is another widely used tool among frequency domain analysis methods which is suitable to detect periodicity in a spectrum, for example families of harmonics with uniform spacing [31]. Mathematically, a cepstrum is defined as a spectrum of a logarithmic spectrum and it has the advantage that the logarithmic amplitude scale emphasizes the harmonic structure of the spectrum whilst reducing the influence of noise. The type of periodic features considered when assessing gearbox vibrations are the families of sidebands spaced at a given shaft speed which typically indicate several types of faults. Peaks in a cepstrum can then be related to a specific frequency identifying the affected shaft. An example of cepstrum analysis is provided in Figure 19 where peaks easily help identify a family of harmonics at 7.5 Hz which corresponds to the ISS rotational speed for both the healthy and damaged gearbox. However, in the cesptrum of the faulty gearbox is observed at 30 Hz which matches the HSS frequency which indicates damage in the gear wheel.
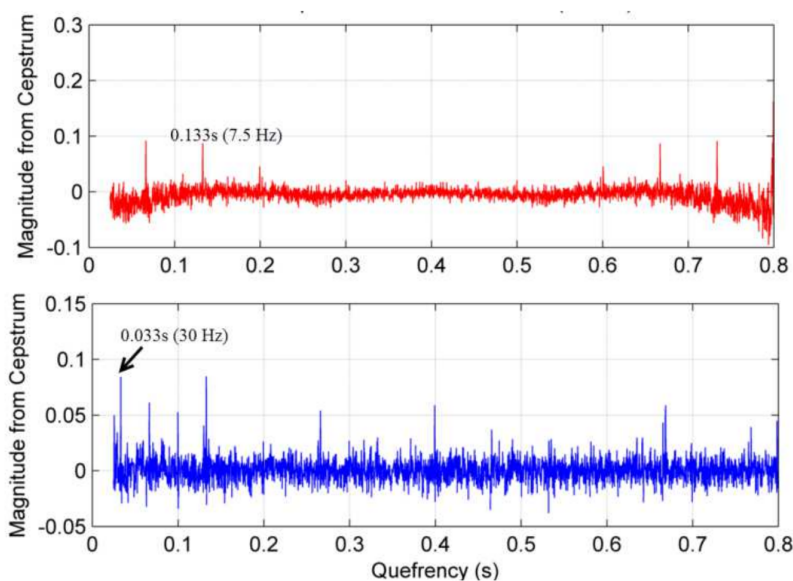
Figure 19: Real cepstrum from a HSS gear in a wind-turbine gearbox in healthy (top) and degraded condition (bottom) [5]

3.3.3   Data-driven methods

Literature shows an increasing interest to incorporate 'intelligent' algorithms to existing CMS. Data-driven models generally refer to a broad category of methods that make no use of the underlying physics that govern the system to construct a PHM system but instead combine machine learning techniques with statistics and historical failure data of WT components or similar machines to estimate the operating state of the system in the future. Within data-driven methods, AI methods occupy a prominent role as they are capable of establishing complex models exclusively from available historical data.

In a particularly outstanding work Stetco *et al.* [10] screened 144 papers, from 2011 on-wards, and they produced a comprehensive summary of the proposed methods that use machine learning for wind turbine CM. Given the number of papers analyzed, their relevance and how up-to-date the gathered information is, the reader is referred to [10] for further considerations of data-driven prognostics models.

3.3.3.1   Introduction to machine learning

Given the prevalence of machine learning (ML) techniques in an increasing wider set of CMS prognosis proposals this section aims at introducing the main concepts related to this field and establish several key definitions. Firstly, its important to briefly distinguish what is meant by Artificial Intelligence, Machine Learning, Neural Networks and Deep Learning. A comprehensive schematic view is shown in Figure 20 and the following fundamental definitions are put forth:
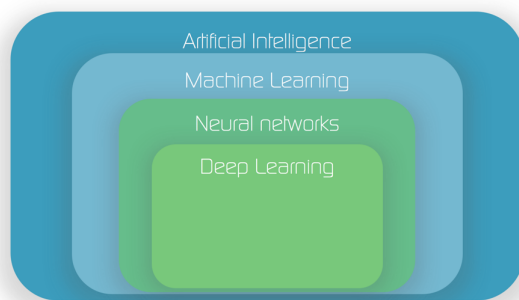
Figure 20: Schematic overview of A.I. and its subsets

Artificial Intelligence: is the broader concept within computer science encompassing any technique that enables computers to mimic human intelligence to solve cognitive

problems, recognise patterns, construct logic-trees, learn from past experience and address other complex tasks commonly associated with human intelligence;

Machine Learning: is a subset of AI and is essentially a technique for realizing AI. The core idea behind ML is that the machine itself learns from its experience and improves at performing a given task without human intervention making increasingly accurate predictions. A fundamental step in ML is the training phase which entails feeding data to the machine's algorithm;

Neural Networks: is a subset of ML which is inspired on the architecture of interconnected brain cells to recognize patterns and make human-like decisions, hence the name Artificial Neural Networks (ANN). Such a conceptual mimic of the functioning of the human brain makes it possible for an algorithm to learn without being explicitly programmed to do so. A simple ANN is generally limited to a maximum number of 3 layers consisting of an input layer, a single hidden layer of neurons and an output layer. Due to their relatively simple architecture based on a limited (or shallow) number of layers, ANN typically present a high degree of interpretability. Interpretability is the potential for a human to explain or understand how results, decisions and conclusions are reached;

Deep Learning: also known as Deep Neural Networks is essentially a network structure consisting of multiple layers of ANN. Each successive layer of neurons uses the output from the previous layer as input. Due to its enhanced and more complex multi-layer structure Deep Learning can be more accurate at predicting and decision making than a simpler ANN but the learning process is comparatively more time consuming and requires large amounts of data. Deep Learning is often described as a black box because the learning process is difficult to explain even if it provides valid results. As the depth of a Deep Learning algorithm, that is an increase in the number of layers, the interpretability typically diminishes

Conceptually, Machine learning is perhaps the most thought provoking and abstract term since it is difficult to define precisely and covers a broad range of processes. A good starting point is a comprehensive and simple example, like that provided in [32]:

"When the performance of a speech-recognition machine improves after hearing several

samples of a person's speech, we feel quite justified in that case to say that the machine has learned."

There are two major settings within ML that a learning process can be established, *supervised learning* and *unsupervised learning* In *supervised learning* the relation between the input and the output variables is known, sometimes only approximately, in which case the input data is said to be labeled. In other words, prior knowledge is available of what the output values are for specific "labeled" input. The goal of supervised learning is to learn a function that best approximates the relationship between input and output based on sample data and desired outputs. *Unsupervised learning* draws inferences from data without labeled inputs thus finding all kind of unknown patterns in data. Clustering algorithms are an essential concept when it comes to unsupervised learning and they deal with the processing of a collection of uncategorized data and find natural clusters or groups if they exist in the data.

Supervised learning can be further subdivided into models that predict a numeric variable -regression models- or a categorical variable, known as classifiers. The choice obviously depending on the type of problem and the desired output. As of today, almost two-thirds of methods use classification and the rest rely on regression [10]. Figure 21 provides a comprehensive schematic overview of the two main types of *supervised learning* models.

In Figure 21 the fundamental steps for classification and Regression-based models are listed and include data pre-processing for both approaches, and a series of specific steps for each type of approach. Regardless of the type of *supervised learning* approach, feature selection and feature extraction are a key step to enable a robust ML-based PHM system and they will be discussed briefly in subsubsection 3.3.3.3.

3.3.3.2   Regression & Classification models

Regression models

Regression models have been developed to identify how signals and features relate to different outputs within a series of WT components. Component behaviour can be captured through regressions of different complexities, from a simple linear model to a complex nonlinear one. Based on inputs, which are time series or sensor signals, regression models are built which predict the numeric output when a given component is assumed to be per-
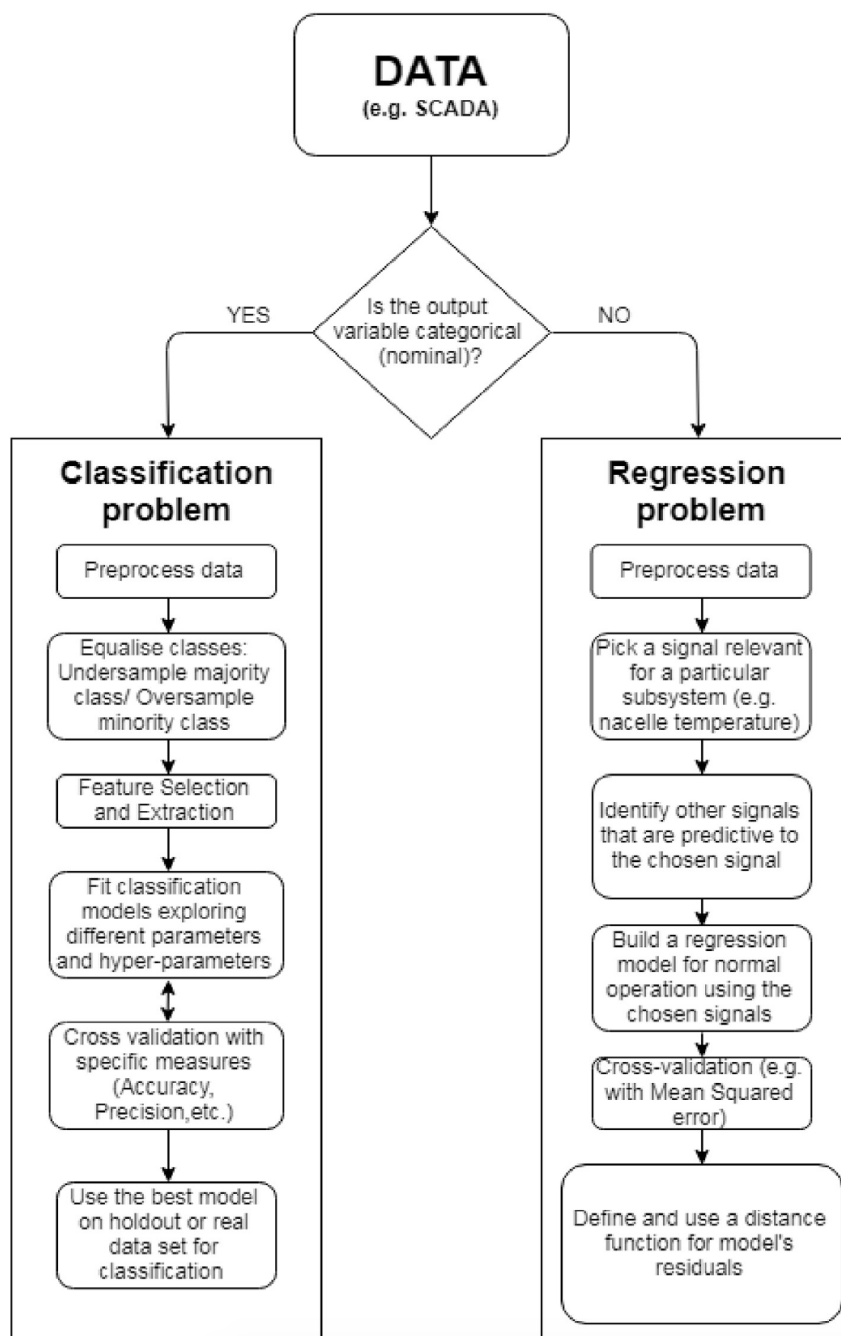
Figure 21: Two main approaches to learning from data in *supervised machine learning* [10]

forming at its optimum. Once the relationship between multiple input variables and the dependent output variables for a healthy system have been captured by fitting regression models, the model is ready to receive new data and detect deviations from this healthy state if they exist. If this deviation persists for several consecutive time intervals an alarm will be triggered.

Regression models may perform at various levels of complexity also referred to granularity:

at the most granular level regression models can target relationships between signals of turbine sub-components or between sub-assemblies, and at the uppermost level a WT can be considered or even an entire farm. A regression built at the highest conceptual level that treats the entire WT as a black box may for instance fit the generated power numerically in terms of the observed wind speed. This application may be advantageous because the power curves made available by manufacturers differ from the power production characteristics at the installed site. In this way, by constructing a regression model the real power curves can be modelled empirically which is useful to asses and predict the wind energy potential at specific site, make better wind turbine choices, or enable predictive control and optimization applications. Since this work focuses on detection, diagnosis and predictive methods for WT drivetrain components, Table 11 summarizes a set of methods that use regression ML to predict generator bearing failure, monitor generator temperature and lubricant pressure as well as diagnose faults related to drivetrain components. The methods reviewed here all use SCADA data as their main input data to establish relations with the state of the system or sub-assembly under study.

Year	Data	Task	Title
2011	SCADA	Generator bearing failure prediction	*Comparative analysis of neural network and regression based condition monitoring approaches for wind turbine fault detection*
2012	SCADA	Generator temperature monitoring	*Wind turbine generator condition-monitoring using temperature trend analysis*
2017	SCADA	Lubricant pressure monitoring	*Wind turbine gearbox failure identification with deep neural networks*
2018	SCADA	Gearbox	*Diagnostic models for wind turbine gearbox components using SCADA time series data preprint*

Table 11: Regression based ML methods for faults related to drivetrain components

In the context developing a reliable fault Detection System for a Nuclear Plant with a significant amount of available data, Gross *et al.* [33] developed a method that examines the totality of accumulated information available from the array of sensors and compares all the data as a whole to similar sets of data collected at various instances in the past. This comparison of the current condition of the system with it's past history allows an optimal estimate of the current state of the system. To achieve this a Multivariate State Estimation Technique (MSET) was developed which used advanced pattern recognition and was capable of estimating the state of a system even in the presence of errors in the data

currently due to sensor malfunction or other. A regression model for generator faults based on this state estimate technique method (MSET) was built by Guo *et al.* [34]. Out of 47 available SCADA signals, 5 variables were selected to predict generator temperature. These variables, namely power, ambient temperature, nacelle temperature, generator cooling air and stator winding temperature were grouped in an input vector. For each input vector at any time step the output of the model is a linear combination of historical observations stored in the so-called memory matrix. Anomaly detection was based on residual analysis using a moving average window which detected statistically significant changes: if either the residual mean value remained zero or the standard deviation increased significantly and these parameters exceeded predefined thresholds, an incipient failure was flagged. The method achieves better modelling accuracy than a standard NN and proved useful to detect dangerous generator over temperature before damage occurred and was validated with SCADA data from a wind farm located at Zhangjiakou in northern China.

Wang *et al.* [35] in their work *Wind Turbine Gearbox Failure Identification With Deep Neural Networks* used a multi-layer deep neural network (DNN) to build regression models of lubricant pressure based on SCADA data from six wind farms. This work served as a comparative analysis of data-driven models by comparing the performance of several ML methods. The DNN model was found to be the most accurate and superior to other models including Lasso, Ridge, k-NN, SVMs and NNs. MAPE and SDAPE (standard deviation of the absolute error) were used as an accuracy measure to compare the performance of the different models. To identify failures Exponentially Weighted Moving Average (EWMA) charts were used to track shifts in absolute percentage errors which may indicate failure. The effectiveness of the proposed monitoring approach was demonstrated by examining real cases from wind farms in China.

The last ML regression model that will be reviewed in this section was proposed by Orozco *et al.* [36] that used SCADA data corresponding to 614 turbines from 7 farms to fit a regression model for normal temperature behaviour. Given that the size of the dataset was particularly large and involved as much as 948 GB of measurements [10] Orozco *et al.* made use of novel distributed processing frameworks to agilize the process. To train the model independent variables such as ambient temperature and power output were used to learn the existing causal relationships with dependent variables such as component temperature. This work was particularly interesting because multiple types of regression

models were built including linear and polynomial regression, random forests and NNs to find the best model fit. The quality of the fit was measured via Root mean squared error (RMSE). Abnormal spikes in component temperature were detected through a model that adjusted temperature data to account for the effects caused by ambient temperature and normal temperature increases when loaded.

Classification models

Classification models rely on predefined categories identified by labels and relate different independent input variables grouped in a vector to one of these categories.

These predefined categories may indicate several states concerning a specific WT component, such as the state of a WT generator that may have several categories. Like the examples presented in [10] a ML classification algorithm targeting the generator could have "healthy", "winding failure", "brush failure" categories and other relevant failures for different specific components. On the other hand, the input vectors typically consist of features extracted from pre-processed sensor signals relevant to the component being monitored. Several CM using ML classification methods have been explored to perform detection, diagnosis, and prediction tasks of a number of components and a variety of failures including blade faults related to rotor imbalance and misalignment, structural vibrations errors, generator brush failure as well as several gearbox-related faults. A review of such methods is done in [10] and Table 12 summarizes those classification methods that target WT drivetrain components which are the primary focus of this work.

Year	Data	Task	Title
2012	SCADA	Generator Brush Failure prediction	*Fault monitoring of wind turbine generator brushes: a data-mining approach*
2014	SCADA	Transmission system fault diagnosis	*Fault diagnosis for a wind turbine transmission system based on manifold learning and Shannon wavelet support vector machine*
2016	Sim./Exp.	Mechanical fault detection	*Neural Networks for Wind Turbine Fault Detection via Current Signature Analysis*
2018	Sim./Exp.	wind turbine gearbox fault detection	*Multiscale convolutional neural networks for fault diagnosis of wind turbine gearbox*
2018	SCADA	Detection, diagnosis & prediction of generator faults	*Diagnosing and predicting wind turbine faults from SCADA data using support vector machines*

Table 12: Classification based ML methods for faults related to drivetrain components

Since classification methods fall under supervised ML methodology, as mentioned previously classification requires labelled input, that is labels assigned specifying the category to which training instances belong [10]. However most ML classification algorithms work best when the number of instances in each class is similar which can become a problem when there is a disproportionate ratio of observations in one class and very few in another class. For example, when there is a significant difference in the distribution of different failures or between healthy and faulyy conditions. This unequal distribution of classes means that the resulting model is biased. This unbalance of classes is a common problem which needs to be addressed and several techniques called class equalization exist. For instance under-sampling and over-sampling which entails either removing instances belonging to the majority class or sampling more instances from the minority class, or doing both; or Tomek-links which eliminate points in the majority class considered redundant or borderline. The purpose is to distribute classes evenly and class equalization has been shown to increase accuracy.

A generator brush failure classification model based on SCADA was put forth by Verma *et al.* [15], for example, developed sampled every 10 min. The signal selection step was performed through a combination of the three methods mentioned in subsubsection 3.3.3.3 including the chi-square filter technique, a wrapper method and a boosting tree which is a type of embedded method. In total 10 signals were found to be predictive of generator brush failure including nacelle revolution, drive train acceleration and others. They addressed the class imbalance problem using Tomek-links and their results show that brush failures can be predicted with reasonable accuracy 12 h before they occur.

Leahy *et al.* [37] in an outstanding work also considered faults in the generator and formalized a method based on classification capable of fault detection, diagnosis & prognosis using SCADA data from a 3MW wind turbine situated in Ireland. Three levels of fault classification were were investigated: fault detection, distinguishing between faulty and fault-free operation; fault diagnosis, whenever faulty operation was identified the nature of the fault was diagnosed and classified according to four types of fault categories and fifth category "others"; and, fault prediction, where a specific fault was identified as being likely to occur in advance of the fault actually occurring. In total 29 features from the SCADA system were selected and used in the classification. Unbalanced class data was solved via undersampling and oversampling procedures were used when training SVM classifiers. This

work concluded that the precision was low for all three classification problems -detection, diagnosis & prognosis- was low although the recall was high. Although the results lacked the desired accuracy of a robust prediction model the framework and workflow proposed by Leahy *et al.* will be looked into in greater detail because the methodology that was developed is relevant to this thesis.

The last classification method that will be reviewed in this section used NN together with a general model of a variable speed WT to investigate mechanical fault detection related to rotor eccentricity by using the generator current signal. Ibrahim *et al.* [38] trained multiple NNs for a series of rotational speed ranges and trained the NN associated to each range on simulated healthy & faulty current signals coming at different speeds. The classification results were promising for the detection of transient faults data but achieved a lower accuracy when predicting linearly increasing faults. The model was trained and validated using a WT model constructed on Matlab/SIMULINK and the authors stated further work is required to validate the model using real data.

3.3.3.3   Feature extraction & Feature seletion

Prior to feature selection and feature extraction the dataset needs to be cleared of nonphysical and/or unreasonable values. However implementing outlier filtering methods -used to identify and remove extreme or unlikely values, or measurement errors- should be done carefully. Marti-Puig *et al.* warned in [39] that removing outliers using common filtering methods for WT-specific diagnosis may initially decrease the error on the training data set but can also potentially increase the error in the test data. This means that many outliers removed automatically by certain filtering methods were in fact failure states of the turbine which were ignored and therefore worsened detection capabilities. To address this expert input to predefine variable's absolute and relative ranges is recommended [39] rather than automatic outlier filtering methods. An example of poor outlier filtering was provided in [10] concerning the monitoring of generator temperature. Spikes in generator temperature may be treated as outliers an removed from the dataset whereas this increase in generator temperature may be simply due to an increase in ambient temperature and not due to an internal malfunction of the generator. Once outliers have been removed in a reliable way feature selection and extraction are the next critical steps in building an ML model.

Feature extraction

For classification problems feature extraction is one of the most important steps and it involves selecting suitable time series signals collected by sensors either by either SCADA or CMS that best relate to the outcome that we wish to predict. For instance, when studying generator faults feature extraction may consist on keeping data from the generator vibration sensor and discard acoustic sensors in the tower [10]. Feature selection can performed automatically or semi-automatically by several methods, some of the most common are:

- **Filter methods** are based on the statistical significance between every available signal and the desired outcome to establish a ranking based on how suitable they are to predict this outcome. The user can then select among these features those offering best results.

- **Wrapper methods** which feed the algorithm with different subsets of features (signals) and the relative usefulness of each signal is determined based on the prediction performance. Two common approaches to wrapper methods are starting off with very few signals and gradually add more signals if they result in a better performance or doing the opposite, a backward selection that begins with all the available signals and removes them as long as it increases performance;

Other methods for feature selection such as the so-called embedded methods that have integrated feature selection as part of their training of the ML model by progressively learning the relative importance of each feature for a specific prediction. They have been found to be very successful when used in combination with filters [10].

Feature selection

After appropriate feature selection has been performed, feature extraction from the raw data must follow. Feature extraction refers to all the operations that permit discarding noise from the selected features whilst keeping their main characteristics intact significantly reducing the size and the computational expense in treating the data. This step greatly contributes in speeding up the training phase of the model and results in better outcomes than if the algorithm is directly applied on the original data. In time series, feature extraction techniques include: (1) **extracting statistical parameters** from the signal (mean, standard, deviation, maximum, minimum, skewness, kurtosis, peak-to-peak,crest

factor, wave factor, impulse factor, margin factor, root mean square); (2) **extracting time-Frequency domain properties** by transforming signals into frequency domain and storing relevant characteristics such as the largest coefficients of the Discrete Fourier transform, Empirical Mode Decomposition (EMD), coefficients of the Wavelet transform and several other variations of the Wavelet transform; or (3) **storing coefficients of models that are fitted to time series data** such as coefficients of ARIMA models or fitted stochastic processes such as Hidden Markov to name a few.

In wind turbine CM applications, feature extraction is commonly done through time-frequency strategies, however it is important to note that classic frequency-domain methods that may work well on stationary lab-generated signals may not be suitable for non-stationary signals that do not have the same mean in the time domain space such as signals produced from variable-speed rotating machines like a WT gearbox or generator. For instance, the more typical Fourier transform is not particularly efficient to capture the non-stationary nature of real-world WT signals and the Wavelet transform is preferred because it is capable of representing non-stationary and non-linear signals efficiently and can provide both time and frequency localization.

The underlying idea of Wavelet transform is to deconstruct a signal into a number of wavelets -short 'burst' of waves that quickly die away- added together whereas the Fourier Transform decomposes a time signal by adding infinitely long sin and cos. Unlike sinusoidal functions, wavelets are limited in time and frequency and can model a signal through a number of finite waves that can 'slide' along to time domain giving a more accurate representation of the signal and therefore a better resolution in time. Several "mother" Wavelet functions are used can be used to transform a signal from the time-domain to the frequency domain and are shown in Figure 22. A practical application of the Wavelet Transform is illustrated in Figure 23 showing a non-stationary hourly WT power production signal and how the original signal can be approximated using only a few significant coefficients stored in the so-called Wavelet Spectrum.

3.3.4 Qualitative comparison between physics-based and data-driven models

Data-driven methods methods in general, and machine-learning (ML) techniques specifically are not built on any explicit mathematical model and do not rely on the knowledge of
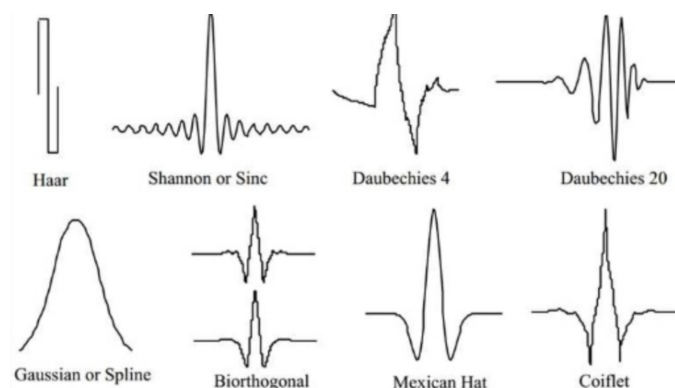
Figure 22: Most common "mother" Wavelet functions
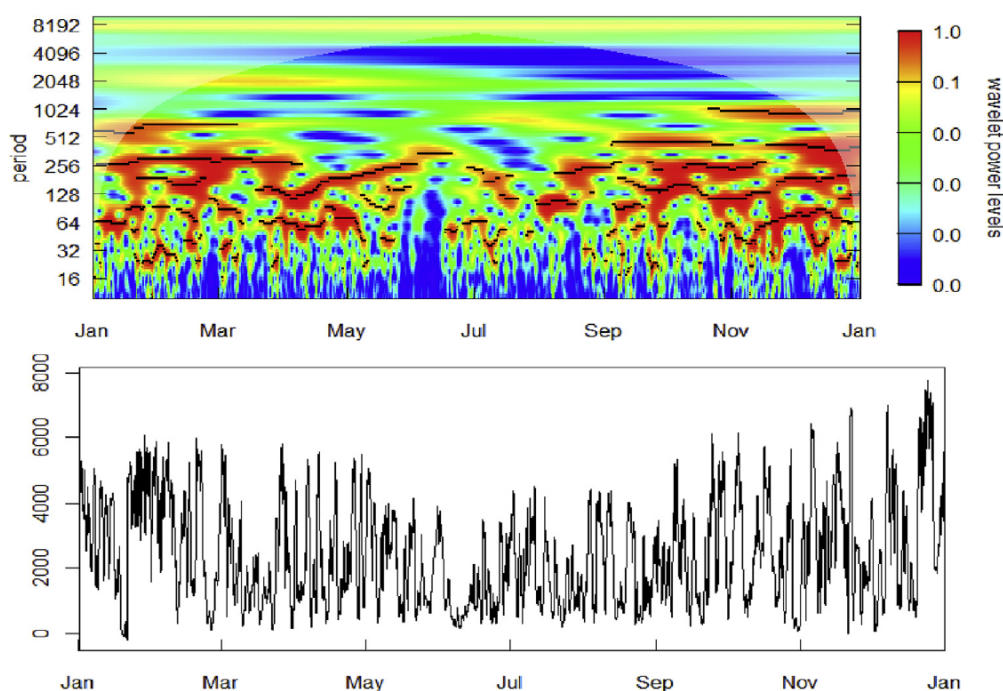
Figure 23: Wavelet Transform power Spectrum showing the most relevant coefficients shown in red and marked with a black line and below the reconstruction of the original signal filtered of noise using these significant coefficients [10]

the physics that govern the system nor do they seek to model relevant degradation mechanisms. ML techniques have however proven successful for fault detection, classification and RUL estimation. One of the main advantages of data-driven methods is that they do not require an in-depth understanding of the physics of the system under study. Hence, if a process is too complex or poorly understood data-driven approaches can be used to overcome the limitations inherent to the lack of knowledge. On the other hand, to formalize a physics-based model the understanding of the physics of failure is indispensable. This can be considered both as a drawback and as an opportunity. The disadvantage of

physics-based models based on the physics of failure is that each failure mode has to be analysed independently and for many relevant failure modes this is not possible. Overall, few failure modes are actually suitable for a physics-base approach. Furthermore, even if a degradation process for a given failure mode is modelled successfully the inputs of such models may not be readily available nor provided by CMS techniques reducing their applicability in fault diagnosis. In addition, physics-based algorithms may not be transferable nor scalable between different WTs due to the system-specific model parameters.

However, physics-based models where possible provide several relevant advantages. Firstly, physics of failure has synergies with the design process and can help optimize future designs by understanding the degradation mechanisms. When it comes to data-driven models, these provide little to no insight that may contribute to improve designs. Also physics-based models are easily certified since the principles behind the algorithm are justified by proven physical principles. Another important advantage is a physics-based algorithm can be modelled with shorter data sets than data-driven methods since data is only needed to adjust the parameters and validate the model, whereas data-driven models, particularly those based on artificial intelligence, require significant large data sets of healthy and faulty conditions which are not always available. A majority of PbMs for prognostics are based on fatigue principles, either using HCF and LCF models or modelling the crack growth. Therefore, failure modes mainly caused by fatigue are ideal candidates for PbM approaches due to the extensive literature and options available.

In conclusion, using physic-based models to assess the degree of degradation is done through degradation models which theoretically make physics-based models particularly suitable for prognostics. As such they should be preferred over purely data-driven methods when reasonably accurate. However, since some failure modes do not have a clear associated degradation mechanism and some degradation mechanisms, even if they exist, cannot be modelled or CMS signals fail to provide the necessary input for these models, relying solely on physics-based models will remain a challenge. As Artificial intelligence (AI) is actively making its way into the wind energy industry it promises to bring about a revolutionary change in existing condition monitoring techniques and early fault detection capabilities as long as sufficient data be available and the models are validated. Furthermore, since data-driven allow diagnostics and prognostics without further analysis of the physics of failure, this permits these methods to be scaled to other WTs which can be expected to

present similar failure modes and correlations between measured variables and the health of the system.

Chapter 4

Discussion of results

The numerical model constructed on SIMPACK provides a very large amount of variables related corresponding to the accelerations and rotational accelerations in the MS and the HSS as well as the loads experienced by the 4 bearings under study.

The selected accelerations are:

- Translational accelerations a_x, a_y and a_z measured at the Main Shaft (MS);

- Rotational or angular accelerations measured on the MS;

- Translational accelerations a_x, a_y and a_z on the High-Speed Shaft (HSS);

- Rotational accelerations a_x, a_y and a_z on the HSS;

The selected forces that will be used analyzed are:

- Forces F_x, F_y and F_z acting on the up-wind main bearing which supports the MS, designated as **INP-A** in Figure 24;

- Forces F_x, F_y and F_z acting on the down-wind main bearing labelled as **INP-B** in Figure 24. The bearing **INP-B**, together with **INP-A**, also supports the MS;

- Forces F_x, F_y and F_z acting on a bearing located on the high-speed stage which supports the high-speed shaft connecting gearbox and generator. This bearing is labelled **HS-A** according to Figure 24 and is located on the gearbox side;
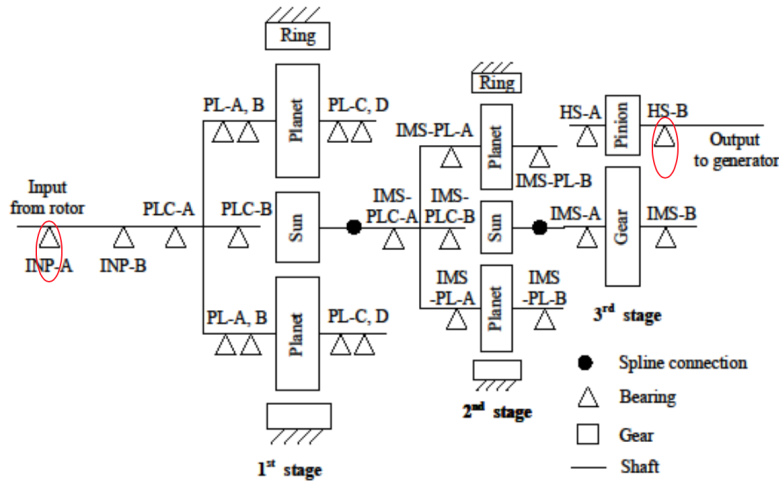
Figure 24: Caption

- Forces F_x, F_y and F_z acting on bearing that supports the HSS on the generator side and designated as **HS-B** in Figure 24;

4.1 Analysis of results in time-domain

A first sensible step is to plot the evolution of several physical quantities in the time-domain, specifically accelerations, angular accelerations measured at two distinct locations: the main-shaft (MS) and the High-speed shaft (HSS) and loads acting on the 4 bearings under study, **INP-A** and **INP-B** supporting the MS as well as **HS-A** and **HS-B** supporting the HSS.

4.1.1 LC-1 - Forces on bearings and accelerations at the MS and HSS

The damage simulated in *LC1* represents a progressive decrease in the axial stiffness of the up-wind bearing supporting the MS **INP-A**. Figure 25 shows the evolution of the forces in x, y and z directions as damage progresses. The blue line represents the baseline load case in which the drivetrain is operating in a healthy state where the stiffness of bearing stiffness is equal to $K_{\text{x,INP-A}}$. The remaining colour scheme represents 5 different degrees of increasing fault severity ranging from yellow to red, corresponding to a damage of $0.85 \cdot K_{\text{x,INP-A}}$ and $0.10 \cdot K_{\text{x,INP-A}}$ respectively. From Figure 25 it can be clearly seen that as damage increases the axial force F_x acting on bearing **INP-A** gradually decreases as the depletion of axial bearing stiffness directly leads to a reduction in its axial load carrying capacity. For *LC1*, the loads acting on **INP-A** in y and z direction remain unchanged and

independent of the decrease in axial stiffness of the bearing.
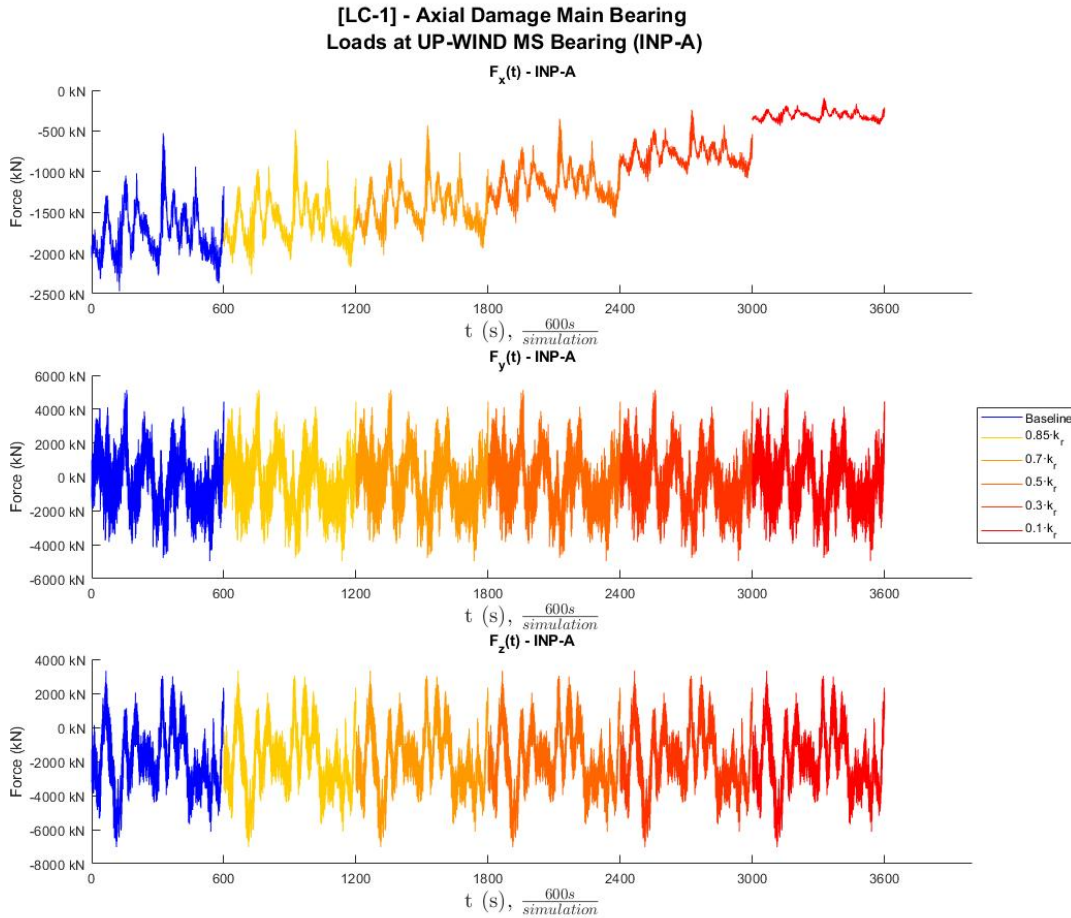
Figure 25: Evolution of F_x, F_y and F_z experienced at **INP-A** for a an axial damage occurring at bearing **INP-A** (*LC1*)

On the other hand, the axial loads acting on **INP-B**, located directly down-wind of **INP-A** display an increasing trend as damage increases. This can be observed in Figure 26 which shows that as the stiffness in axial bearing stiffness of **INP-A** deteriorates and its load carrying capacity decreases the loads transferred to the next bearing increase significantly. This behaviour clearly illustrates that a faulty up-wind bearing **INP-A** in the MS will transmit axial loads through the MS to other components of the drivetrain, including the other MS bearing **INP-B**. Although not plotted in Figure 26, as opposed to F_x, forces F_y and F_z at bearing **INP-B** do no vary.

Figure 27 represents the evolution of the forces in x direction at the HSS, at bearings HS-A and HS-B as axial damage in the bearing at the MS increases. These results indicate that although the MS bearing **INP-B** experiences a greater axial load, this load transfer
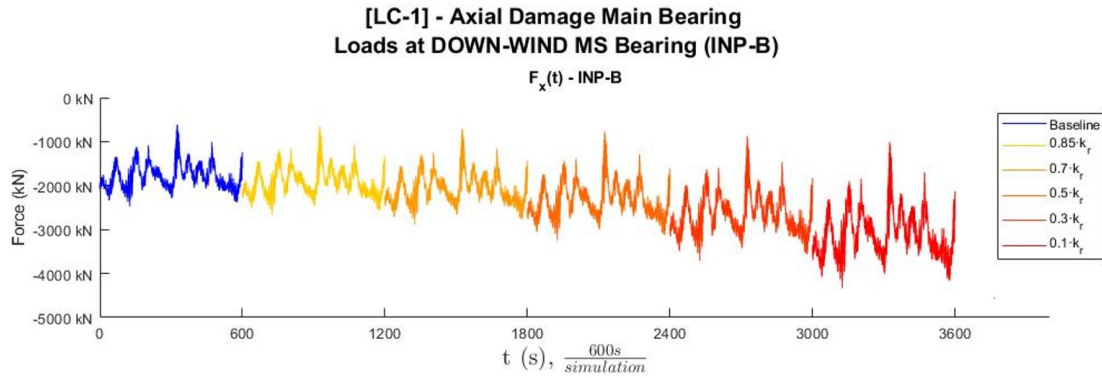
Figure 26: Evolution of F_x measured at **INP-B** for a an axial damage occurring at bearing **INP-A** ($LC1$)

continues to propagate through the drivetrain and reaches the HSS. Figure 27 illustrates that due to a decrease of the axial stiffness of the main bearing in the MS the HSS will also experience an increased axial load. Although not plotted in Figure 27, as opposed to F_x, the forces F_y and F_z at both bearings in the HSS do no see display significant variation as severity of axial damage in the MS increases. Physically speaking, these results are in close agreement with the simulated damage in axial direction.

The evolution of force time-series has been analyzed at each individual bearing. Figure 28 summarizes well the variation of forces in x, y and z for $LC1$. Figure 28a shows the evolution under increasing damage of the mean force component and Figure 28b shows the evolution of the standard deviation of force components in all three directions for each bearing. Figure 28a clearly indicates that a gradual decrease in the axial bearing stiffness results mainly in a response in x direction with no significant effect on x and y force components at any of the bearigs. The response in x leads to an increase of the mean F_x as well as an increase in the standard deviation σ_{F_x} in **INP-B**, the non-damaged bearing of the MS. This increase in loads is proportional to the decrease of axial load carrying capacity experienced by the damaged **INP-A** which accordingly experiences a decrease mean load and σ_{F_x} as damage becomes more severe.

The results of $LC1$ clearly reflect how a local damage in the up-wind MS bearing will directly affect the down-wind MS bearing. Furthermore, as seen in Figure 27, a damage at the MS also induces a response at the HSS which although the impact is small. This highlights that the gearbox does have a certain degree of transfer capability of axial loads. This is somewhat expected since mechanical components in the gearbox are designed to
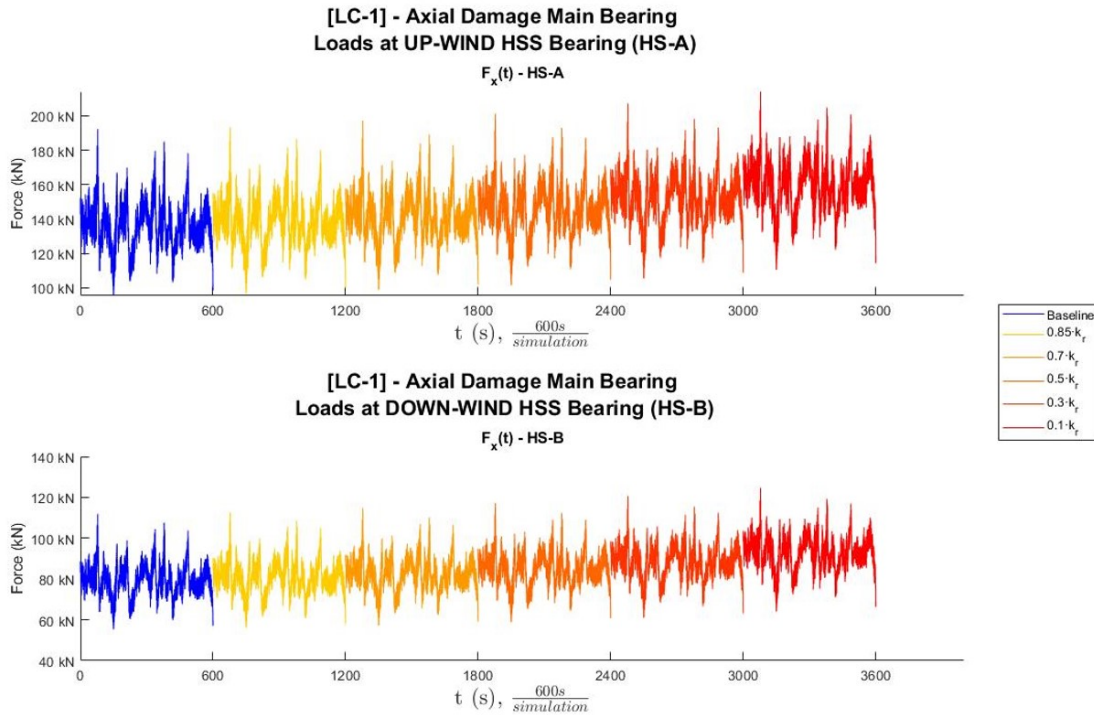
Figure 27: Evolution of F_x at **HS-A** (top) and **HS-B** for a an axial damage occurring at bearing **INP-A** (*LC1*)

carry mainly torque loads and have limited resistance to axial loads which facilitates the transfer path of axial loads across the gearbox towards the HSS and generator bearings.

4.1.2   LC-2 - Forces on bearings and accelerations at the MS and HSS

Load case *LC2* also considers a damage originating at **INP-A**, the up-wind bearing supporting the MS. However this set of simulations replicates a radial damage in the bearing rather than an axial damage. In a similar manner, the radial stiffness of **INP-A** is progressively decreased. Once again the behaviour of all 4 bearings will be evaluated as fault severity increases. Presumably, a radial defect will result in a modified share of the radial loads F_r at each bearing. It is therefore important to keep in mind that $F_r = \sqrt{F_y^2 + F_z^2}$

Figure 29 shows the evolution of mean and standard deviation of forces at all 4 bearings for *LC2* and for increasing damage. As was to be expected, a gradual decrease of the radial stiffness of **INP-A** results in variations of the mean F_y and F_z this bearing perceives as well as on the values of σ_{F_y} and σ_{F_z} seen in Figure 29a. This confirms that a radial damage in **INP-A** leads to a progressive decrease of its radial load carrying capacity. However, the main bearing **INP-A** is not the only bearing that experiences a significant variation in
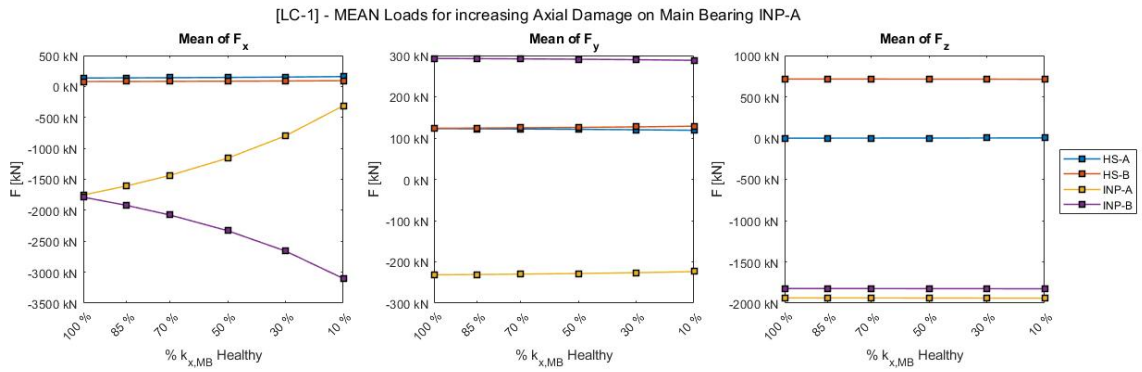
(a) Evolution of the mean value of forces for decreasing axial stiffness of MS bearing
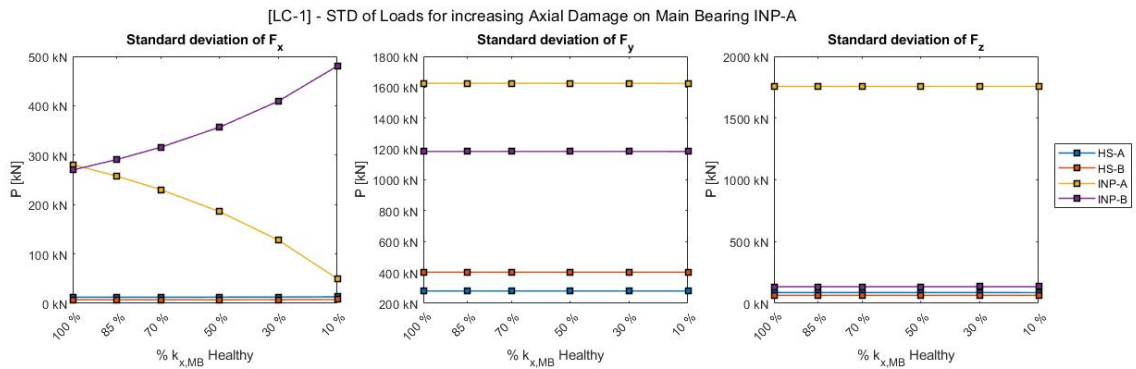
(b) Evolution of the standard deviation of forces for decreasing axial stiffness of MS bearing

Figure 28: Evolution of mean and standard deviation of forces in x, y, z directions at all 4 bearings for *LC1*

loads. In fact, all four bearings experience a significant modification of their load sharing behaviour compared to healthy conditions. This is readily observed in Figure 29a which clearly shows that a gradual damage of **INP-A** induces a decrease in the loads experienced by **INP-B** and **HS-B** and and increase of loads acting on **HS-A** in terms of mean F_y and F_z load components.

A critical observation that must be highlighted is that a radial damage on the MS bearing **INP-A** triggers a redistribution of loads throughout the entire drivetrain affecting both mS bearings and HSS bearings. Furthermore, this load transmission effect begins to take place for relatively low damage of **INP-A**. Figure 29 clearly shows that for a damage at **INP-A** of approximately $0.85 \cdot K_r^{\text{INP-A}}$ the HSS bearings **HS-A** and **HS-B** already begin to suffer a variation in loads. The transfer of loads from the MS bearings towards the HSS becomes all the more evident as radial bearing stiffness continues to decrease.

Figure 30 indicates that radial damage on the MS up-wind bearing significantly reduces its load carrying capacity as F_y and F_z steadily decrease. This triggers a load transmission

(a) Evolution of the mean value of forces for decreasing radial stiffness of MS bearing
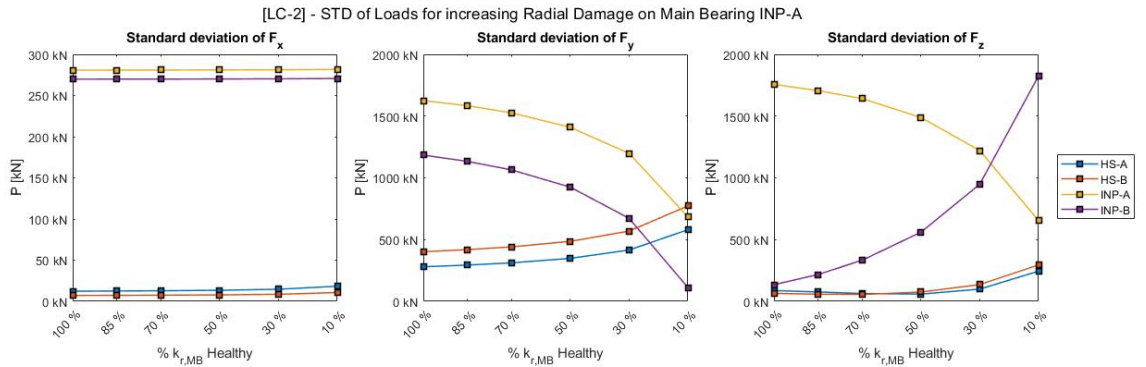
(b) Evolution of the standard deviation of forces for decreasing radial stiffness of MS bearing

Figure 29: Evolution of mean and standard deviation of forces in x, y, z directions at all 4 bearings for *LC2*

through the MS to the down-wind MS bearing, **INP-B** seen in Figure 31. The induced behaviour in **INP-B** is particularly prominent in the variation in the vertical load F_z, which sees a significant increase from a mean load of $2000kN$ under healthy conditions corresponding to baseline and shown in blue in Figure 31 to a peak value approximately four times higher.

Its worth noting from Figure 31 how the F_y forces decrease drastically when the radial damage in **INP-A** progresses from $0.3 \cdot K_r^{\text{INP-A}}$ to $0.1 \cdot K_r^{\text{INP-A}}$. This drastic decrease in forces is a direct result from the large displacements that take place within the drivetrain. As the radial stiffness of **INP-A** decrease the displacements become too large which triggers a loss of contact between the bearing and the shaft. The decrease in contact between components leads to a significant decrease of loads F_y acting on the bearing.

Although not shown in Figure 31, similarly to what can be observed in Figure 30, a radial damage does not trigger a significant effect on the forces along x direction, F_x.

As mentioned, a decrease in the radial stiffness of **INP-A** also triggers a noticeable differ-
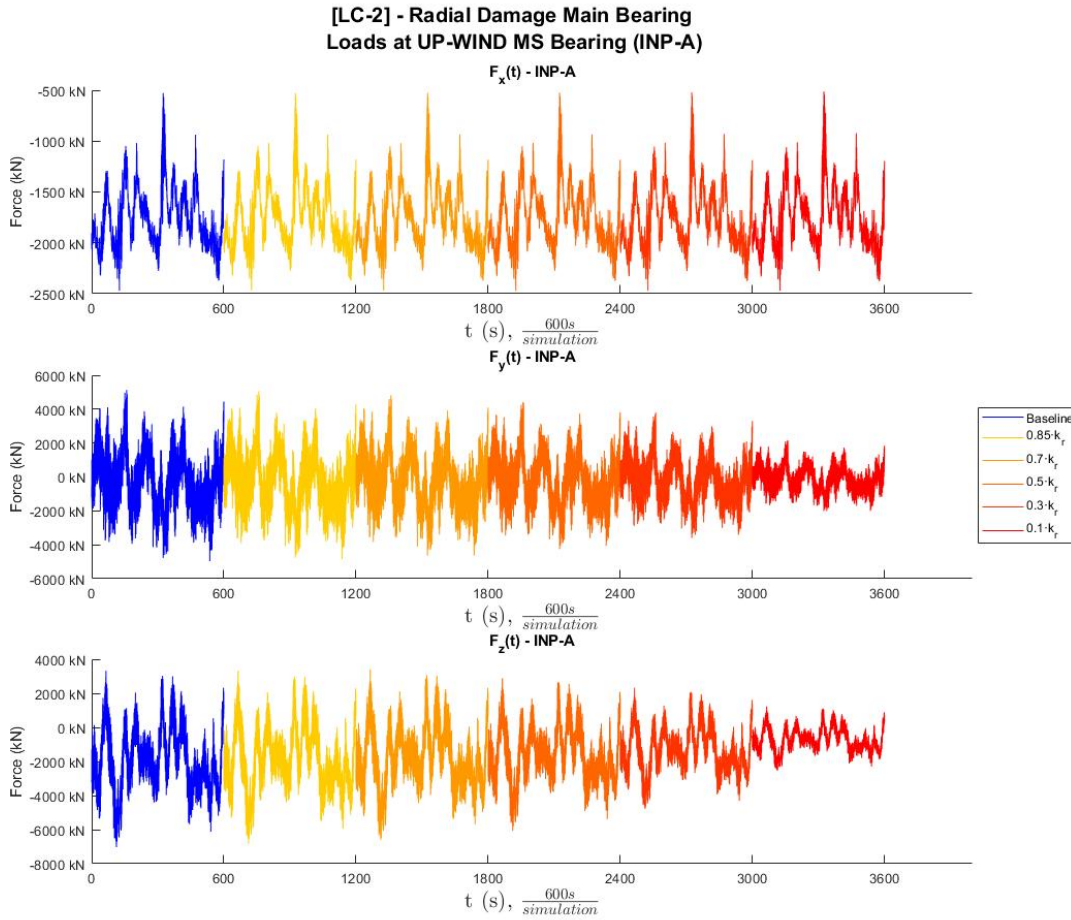
Figure 30: Evolution of F_x, F_y and F_z experienced at **INP-A** for a radial damage occurring at bearing **INP-A** (*LC2*)

ence in the loads acting on both bearings at the HSS. This effect is illustrated in Figure 32. This increase is particularly acute in the evolution of F_z experienced by **HS-A** and **HS-B** as radial damage increases beyond $0.3 \cdot K_r^{\text{INP-A}}$.

From the analysis of results corresponding to *LC2* several important remarks can be put forth. Firstly, changes in the radial stiffness of at the MS will trigger a response that affects all the considered drivetrain bearings both in the MS and in the HSS. This response is in the form of a redistribution of radial loads. This redistribution is caused by the fact that the radial damage of **INP-A** depletes its ability to carry radial loads which must then be transferred to other drivetrain components such as bearings. Furthermore, the transmission of these loads is noticeable from an early damage stage. This means that when the bearing radial stiffness is decreased only slightly the up-wind bearings such as **INP-B**, **HS-A** and **HS-B** already begin to exhibit a modified load carrying capacity.
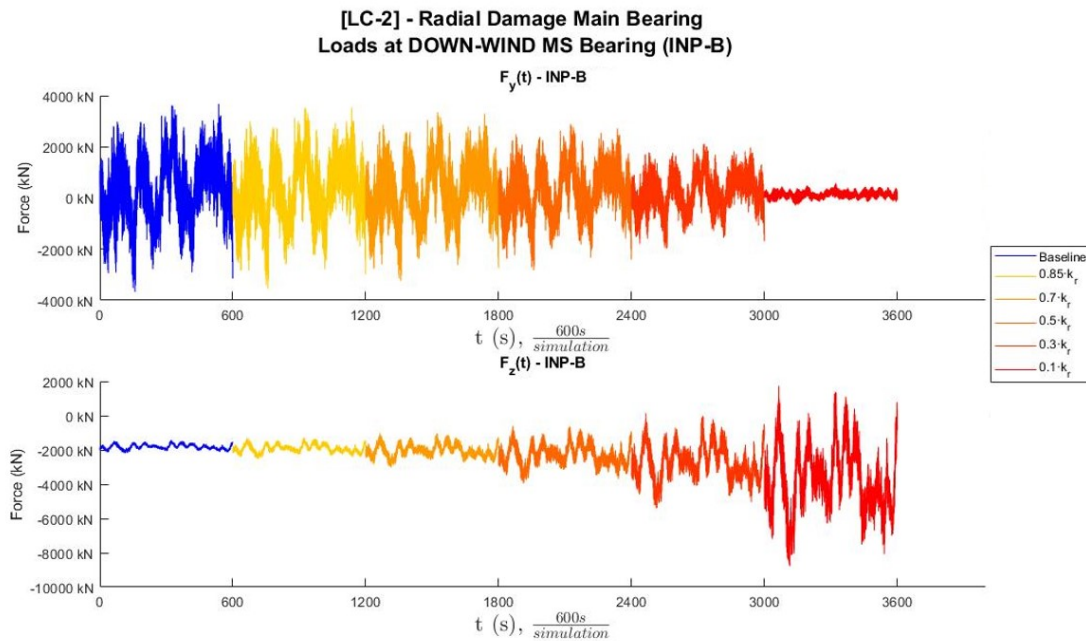
Figure 31: Evolution of F_y and F_z experienced at **INP-B** for a radial damage occurring at bearing **INP-A** (*LC2*)
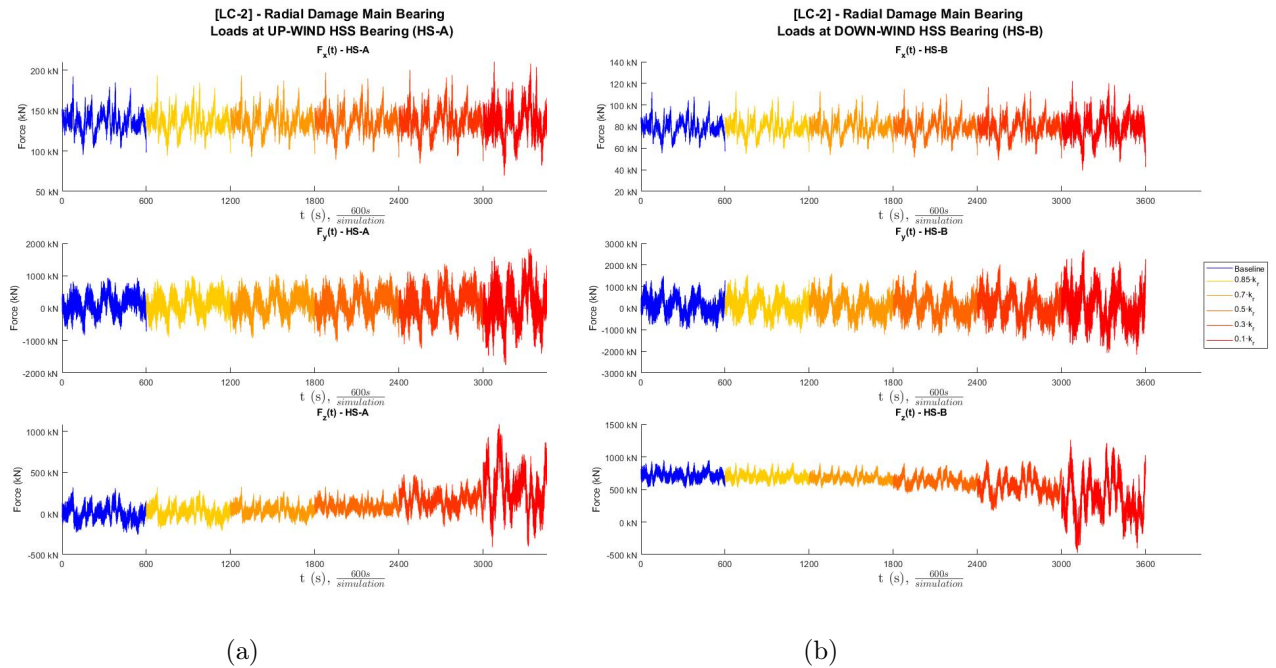
Figure 32: Evolution of F_x, F_y and F_z (a) at **HS-A** and (b) at **HS-B** for a radial damage occurring at bearing **INP-A** (*LC2*)

It is also important to note that since the HSS bearings are significantly affected by a radial defect originating at the MS, it straightforwardly implies that other bearings in the drivetrain which have not been studied, such as gearbox bearings in the intermediate speed

shaft (ISS), will also be affected.

Results of *LC2* indicate that the health of MS bearings is critical to overall drivetrain health. Load case *LC2* proves that a radial defect in the MS can be detrimental to drivetrain health and is likely to influence the behaviour of gearbox and generator bearings.

Finally, it is interesting to compare the behaviour of the drivetrain corresponding to *LC1* as opposed to *LC2*. The first assumed an axial damage on the MS bearing **INP-A** whereas the latter modelled a radial damage occurring at that same bearing. *LC1* did show that the gearbox can transfer axial loads to a certain extent. *LC2*, however, proves that the gearbox model exacerbates the transmission of radial loads far more intensely than for axial loads. This reveals that the gearbox highly facilitates the transfer path of radial loads.

4.1.3 LC-3 - Forces on bearings and accelerations at the MS and HSS

The final load case considered in this work involves a damage on a bearing in the HSS, specifically **HS-B** located on the generator side. Similarly to *LC2*, the numerical model of the drivetrain is run for 5 different fault levels of increasing severity which progressively decrease the radial stiffness of **HS-B** from a mild damage corresponding to $0.85 \cdot K_r^{\text{HS-B}}$ to a severe damage of $0.10 \cdot K_r^{\text{HS-B}}$ where $K_r^{\text{HS-B}}$ is the radial stiffness of **HS-B** under healthy conditions. This is done by simultaneously decreasing $K_y^{\text{HS-B}}$ and $K_z^{\text{HS-B}}$ in the numerical drivetrain model.

By looking at the evolution of loads at **HS-B** seen in Figure 34a the decrease of radial stiffness is seen to decrease in F_y and F_z loads. Since the radial F_r is $F_r = \sqrt{F_y^2 + F_z^2}$ the progressive reduction of F_y and F_z clearly indicate a decrease in radial load carrying capacity due to the evolution of the bearing's stiffness. A considerable shift in the mean vertical load carried as radial stiffness decreases can be seen from Figure 33a.

For a high damage severity $K < 0.30 \cdot K_r^{\text{HS-B}}$ radial stiffness approaches $0.10 \cdot K_r^{\text{HS-B}}$ the vertical loads carried by **HS-B** decrease substantially and approach a mean value of $F_z = 100 \ kN$, an eight fold reduction when compared to baseline-healthy conditions. Furthermore, bearing $HS-B$ exhibits a clear reduction of mean F_y load to practically 0 as radial damage increases. Again, this decrease becomes particularly apparent in Figure 33a as radial stiffness approaches $0.10 \cdot K_r^{\text{HS-B}}$.

Figure 34 shows the variation of loads at the HSS bearings for increasing radial damage
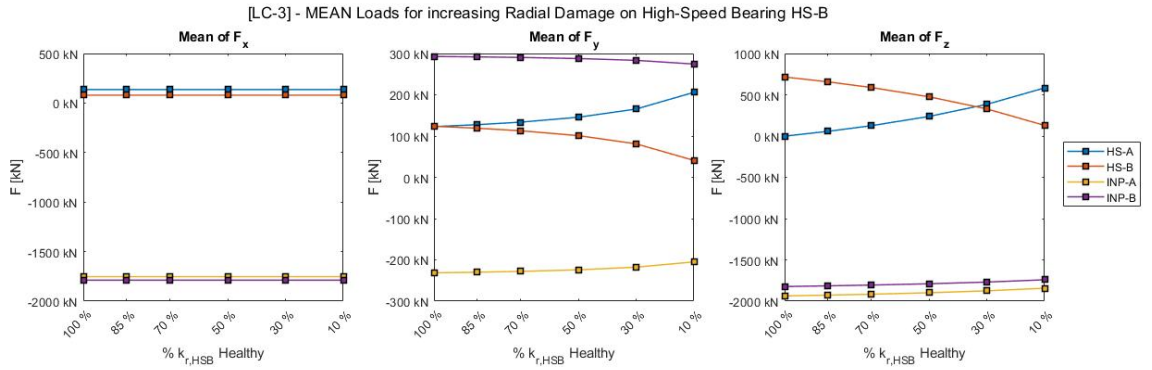
(a) Evolution of the mean value of forces for decreasing radial stiffness of HSS bearing
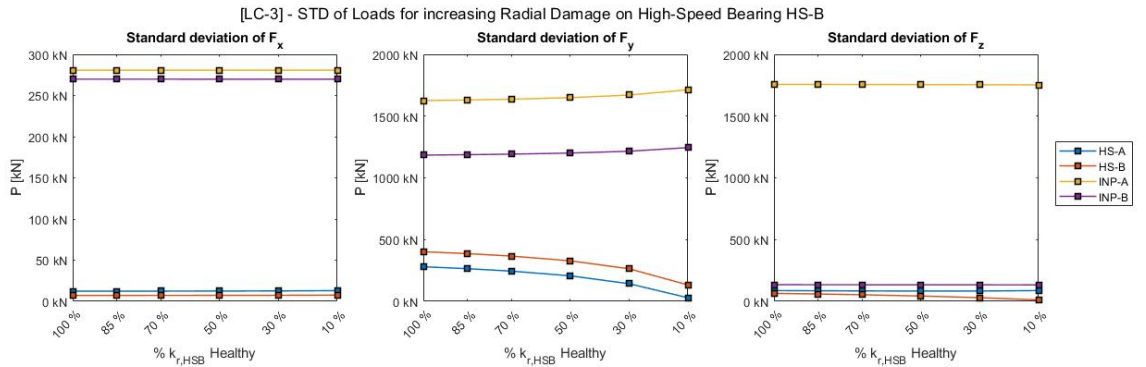
(b) Evolution of the standard deviation of forces for decreasing radial stiffness of HSS bearing
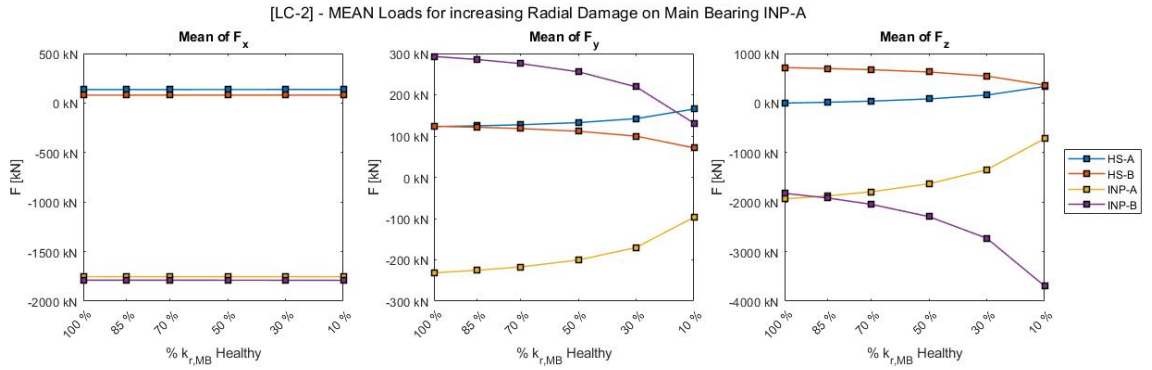
Figure 33: Evolution of mean and standard deviation of forces in x, y, z directions at all 4 bearings for *LC3*

of **HS-B**. The loads acting on **HS-B** and **HS-A** are given by Figure 34a and Figure 34b respectively. The damaged bearing, plotted on the left side, clearly carries a lower radial load. Load carrying capacity reduction is particularly drastic for vertical forces as F_z shifts from a mean value of approximately $800 \ kN$ for healthy conditions to as low as $100 \ kN$ when radial stiffness approaches $0.10 \cdot K_r^{\text{HS-B}}$. The reduction in loads carried by **HS-B** is taken up by **HS-A**, seen in Figure 34b, located up-stream from **HS-B**.

The evolution of loads at MS bearings for *LC3* is presented in Figure 35. The time-series do not reveal significant variations in the loads acting on **INP-A** and **INP-B** compared to a healthy HSS bearing. However, the evolution of the mean force and standard deviation presented in Figure 33 did reveal a slight shift of average F_y and F_z loads acting on both bearings. Specifically a slight decrease in the mean F_y and mean F_z loads acting on **INP-A** and **INP-B** was observed.

Although not visible in the time-domain, these signals are good candidates for a frequency domain analysis to establish whether a defect at the HSS does induce a response in the
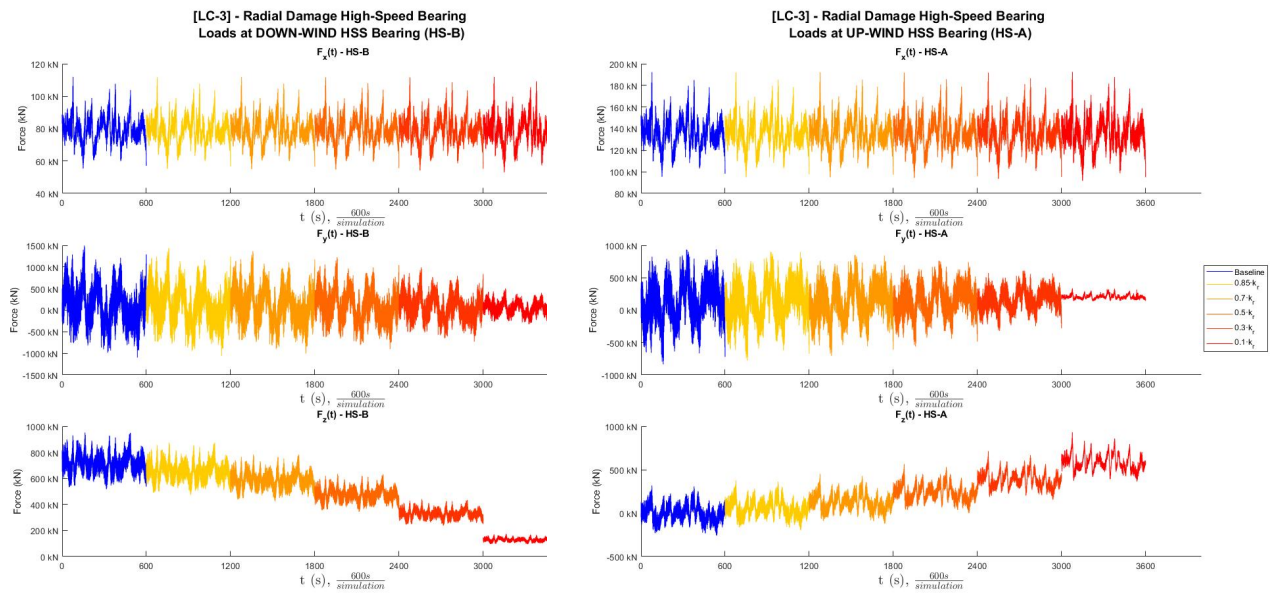
(a)   (b)

Figure 34: Evolution of F_x, F_y and F_z (a) at **HS-B** and (b) at **HS-A** for a radial damage occurring at HSS bearing **HS-B** (*LC3*)

MS and the frequency components that may be excited as a result.
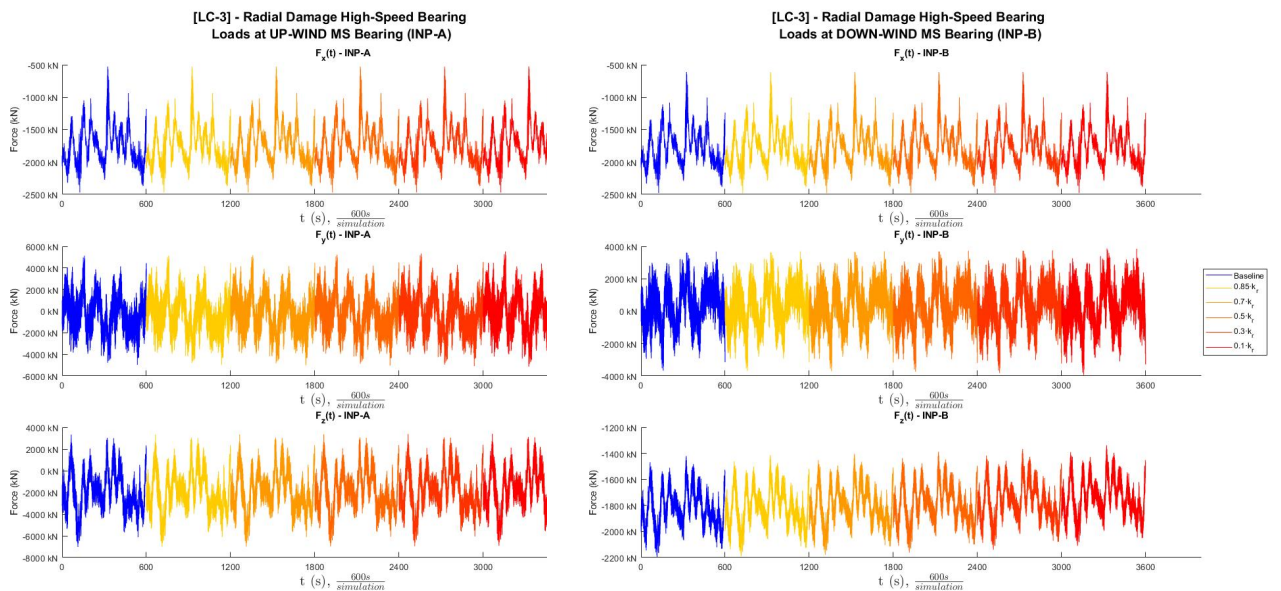
(a)   (b)

Figure 35: Evolution of F_x, F_y and F_z (a) at **INP-A** and (b) at **INP-B** for a radial damage occurring at HSS bearing **HS-B** (*LC3*)

Analysis of forces

Visualizing time-series of accelerations is a simple preliminary approach to identify which accelerations vary significantly for each LC and detect potential trends. In this step several accelerations are examined at the MS and the HSS. At both of these locations translation accelerations $[\frac{m}{s^2}]$ and angular accelerations $[\frac{rad}{s^2}]$ have been obtained in x, y, z directions.

4.2   Analysis of results in frequency-domain

Understanding the frequency distribution of a signal is a very powerful tool to reveal information that may not be readily visible in the time series. In vibration analysis, the *Power Spectral Density* (PSD) of a signal is extensively used to detect incipient faults and can help locate the origin of a fault.

The *power* in *Power Spectral Density* refers to the fact that the magnitude of the PSD is calculated as the mean-square value of the signal and does not refer to the physical quantity power. The mean-square value of any quantity has become known as the power of that quantity. The term *spectral* indicates that the PSD is a function of frequency since it represents the distribution of a signal over a spectrum of frequencies. Lastly, the term *density* refers to the fact that the magnitude of the PSD is normalized to a single hertz bandwidth. when performing a PSD of an acceleration signal the PSD will hence have units of $\left[\frac{m^2/s^4}{Hz}\right] \equiv \left[\frac{g^2}{Hz}\right]$. Accordingly, the PSD of angular acceleration will have units of $\left[\frac{rad^2/s^4}{Hz}\right]$.

The present section will present the PSD plots of the accelerations measured at the MS and the HSS for several LC. The main advantage of carrying out of a PSD of the accelerations is to visualize relevant resonant behaviour otherwise hidden in the signal.

A first set of relevant frequencies to look for in PSD plots are the shaft-related frequencies corresponding to the drivetrain shafts presented in Table 13. These include but are not limited to the speed of the MS and the HSS, labelled **MS_spd** and **HSShaft** in Table 13. Additionally, its recommendable to evaluate the frequency content in the surrounding of the frequencies corresponding to the rotational speed of the shafts found inside the gearbox, namely the low-speed intermediate shaft **ILSShaft** and the high-speed intermediate shaft **IHSShaft** as well as the emshing frequencies of the first, second and third stage, **Mesh_ST1**, **Mesh_ST2** and **Mesh_ST3**. Furthermore, higher-order harmonics of the shaft-related frequencies may also be excited under faulty conditions. Therefore, it is good
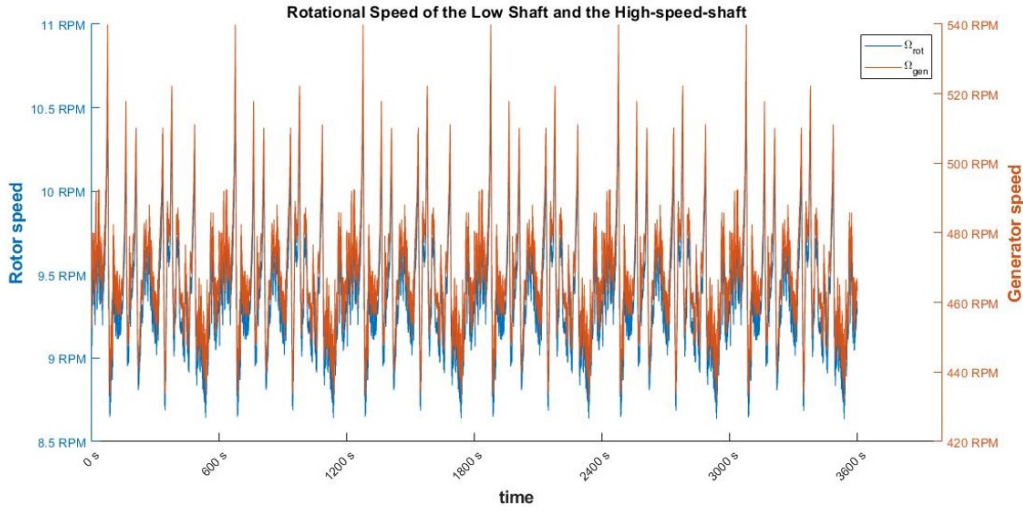
Figure 36: Rotational speeds corresponding to the Main Shaft (rotor) and the high-speed shaft (generator) as obtained from SIMPACK

	MS_spd	ILSShaft	IHSShaft	HSShaft	Mesh_ST1	Mesh_ST2	Mesh_ST3
P=1	0.15614	0.69064	3.5858	7.8134	13.897	75.275	218.78
P=2	0.31229	1.3813	7.1716	15.627	27.794	150.55	437.55
P=3	0.46843	2.0719	10.757	23.44	41.69	225.82	656.33
P=4	0.62458	2.7625	14.343	31.254	55.587	301.1	875.1
P=5	0.78072	3.4532	17.929	39.067	69.484	376.37	1093.9
P=6	0.93686	4.1438	21.515	46.881	83.381	451.65	1312.7

Table 13: Shaft speeds and gear meshing frequencies in [Hz] for a number of harmonics P={1,2,...,6} assuming a MS speed $f_{MS} \approx 0.156$ Hz

practice to verify the energy content and the evolution of the side-bands at several harmonics of these speeds. Table 13 shows up to the sixth harmonic of each shaft and gear mesh related frequency. All the values presented in Table 13 have been computed based on the average Main Shaft rotational speed obtained from SIMPACK and seen in Figure 36 labelled as rotor speed Ω_{rot}. Accordingly, the average shaft speed $\bar{\Omega}_{\mathrm{rot}} = 9.369$ RPM obtained from SIMPACK was used which corresponds to a main shaft speed $f_{rot} \equiv f_{MS} \approx 0.156$ Hz. This average main shaft rotational frequency was assumed when calculating the remaining shaft and gear meshing frequencies.

The meshing frequency of the first planetary stage is calculated as

$$f_{\mathrm{mesh,ST1}} = f_s \cdot z_r \tag{4.1}$$

The speed of the intermediate low-speed shaft **ILSShaft** corresponds to the rotating speed of the sun gear of the first planetary stage $f_{\text{sun},1}$ calculated as:

$$f_{\text{ILSS}} = f_{\text{sun},1} = f_{\text{mesh,ST1}} \cdot \frac{z_{r,1} + z_{s,1}}{z_{r,1} \cdot z_{s,1}}; \tag{4.2}$$

Where $z_{\text{r},1}$ and $z_{\text{s},1}$ are the number of teeth in the ring gear and the sun gear of the first planetary stage provided in Table 14.

The speed of the intermediate high-speed shaft **IHSShaft** and the high-speed shaft **HSShaft**, f_{IHSS} and f_{HSS} are calculated according to:

$$f_{\text{IHSS}} = f_{\text{sun},1} \cdot N_2 \tag{4.3}$$

$$f_{\text{HSS}} = f_{\text{IHSS}} \cdot N_3 \tag{4.4}$$

The meshing frequencies of the second planetary stage $f_{\text{mesh,ST2}}$ and the third parallel stage $f_{\text{mesh,ST3}}$ are calculated as

$$f_{\text{mesh,ST2}} = f_{\text{IHSS}} \cdot \frac{z_{r,2} + z_{s,2}}{z_{r,2} \cdot z_{s,2}}; \tag{4.5}$$

$$f_{\text{mesh,ST3}} = f_{\text{HSS}} \cdot z_{\text{pinion}} \tag{4.6}$$

Where $z_{\text{r},2}$ and $z_{\text{s},2}$ are the number of teeth in the ring gear and the sun gear of the second planetary stage given in Table 14 and $z_{\text{pinion}} = 28$ is the number of teeth in the pinion gear of the parallel stage.

Besides the shaft-related frequencies there are a series of characteristic fault frequencies susceptible to be excited. In the equations below z_r, z_s and z_p are the number of teeth in the ring gear, sun gear and planetary gears, K is the number of planets and N is the gear ratio according to the notation introduced in Table 14. All the relevant gear characteristics are available in [16] where a detailed design of the drivetrain analyzed in this work was presented.

		Stage 1	Stage 2	Stage 3
type		Planetary	Planetary	Planetary
num. of teeth ring gear	z_r	89	109	-
num. of teeth sun/pinion	z_s	26	26	26
num. of teeth planet/gear	z_p	31	41	51
number of planets	K	5	3	-
gear ratio	N	4.423	5.192	2.179

Table 14: Relevant gear characteristics for the calculation of characteristic fault frequencies as published in [16]

Gear Meshing Frequency

$$f_m = f_s \cdot z_r = \frac{z_r z_s}{z_r + z_s} \cdot f_s \tag{4.7}$$

Characteristic Frequency of Sun Gear with Distributed Fault

$$f_{\text{csd}} = f_s^H = \frac{f_m}{z_s} = \frac{z_r}{z_r + z_s} \cdot f_s \tag{4.8}$$

Characteristic Frequency of Sun Gear with Local Fault

$$f_{\text{csl}} = K \cdot f_s^H = K \cdot \frac{f_m}{z_s} = K \cdot \frac{z_r}{z_r + z_s} \cdot f_s \tag{4.9}$$

	Sun_Distrib	Sun_Local	Plnt_Distrib	Plnt_Local	Ring_Distrib	Ring_Local
P=1	0.53449	2.6725	0.44828	0.44828	0.15614	0.78072
P=2	1.069	5.3449	0.89657	0.89657	0.31229	1.5614
P=3	1.6035	8.0174	1.3449	1.3449	0.46843	2.3422
P=4	2.138	10.69	1.7931	1.7931	0.62458	3.1229
P=5	2.6725	13.362	2.2414	2.2414	0.78072	3.9036
P=6	3.207	16.035	2.6897	2.6897	0.93686	4.6843

Table 15: Characteristic fault frequencies of the drivetrain assuming a MS speed $f_{MS} \approx 0.156$ Hz

First it is interesting to notice the large difference in frequency content for accelerations corresponding to the MS and those measured at the HSS, seen in Figure 37a and Figure 37b respectively.

Spectral Analysis of LC2

As was seen in the preliminary time-domain analysis, the load case *LC2* which replicates

(a) Evolution of PSD of $\ddot{x}$ at the MS

(b) Evolution of PSD of $\ddot{x}$ at the HSS
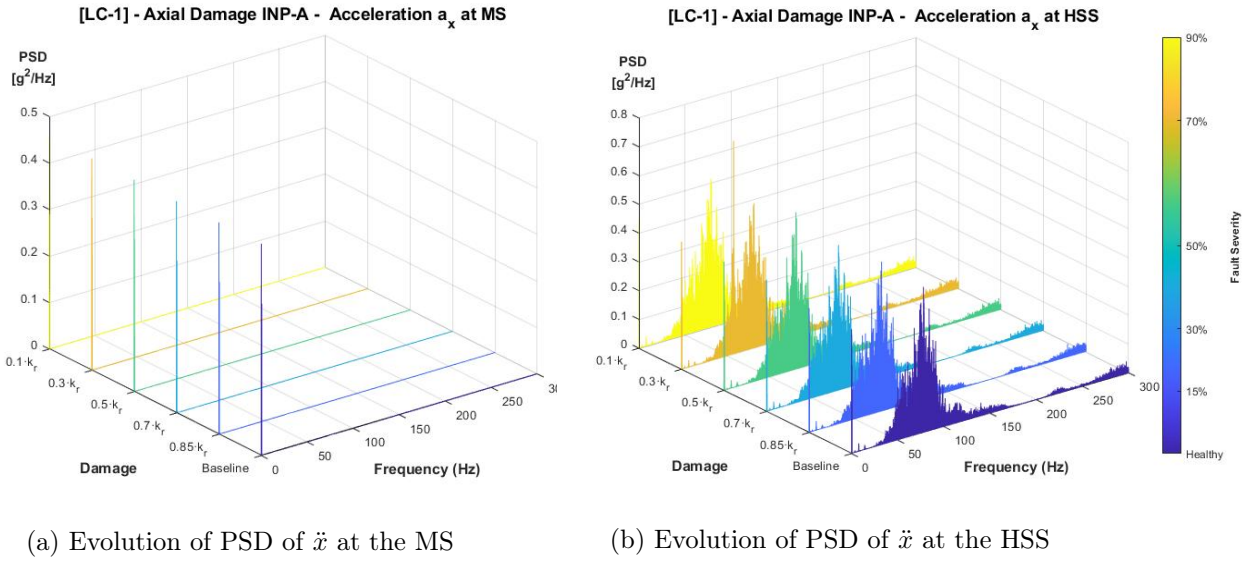
Figure 37: Evolution of the translational acceleration in x for *LC1*

a radial damage on the MS bearing **INP-A** resulted in a significant response at several other bearings in the drivetrain, both at the MS and HSS. Presumably, inspection of the acceleration signals in the frequency domain is likely to reveal how accelerations vary for increasing radial damage. Figure 38 shows the frequency content surrounding several relevant frequencies, specifically f_{HSS}, $f_{\mathrm{mesh,ST1}}$ and f_{ISS}. The peaks in the frequency spectrum show resonance frequencies and the magnitude of the peaks the degree of resonance. Any consistent variation in the location, number and magnitude of these peaks will indicate the appearance of a fault. Furthermore, the size and characteristics of the side-bands are also fault indicators. Figure 38 clearly illustrates abnormal behaviour in MS acceleration $\ddot{y}$ as damage increases. Firstly all three figures, Figure 38a, Figure 38b and Figure 38c show that the peak value increases as the radial damage at **INP-A** increases. This means the energy content at the specific frequencies is higher when damage is present as compared to healthy conditions (PSD shown in blue). The increase in energy content escalates dramatically at around f_{ISS} shown in Figure 38c from a peak value of approximately $5 \cdot 10^{-4}$ $\left[\frac{g^2}{Hz} \right]$ for healthy conditions to a peak value over $2 \cdot 10^{-2} \left[\frac{g^2}{Hz} \right]$ when radial bearing stiffness decreases to $0.1 \cdot K_r^{\mathrm{INPA}}$. Furthermore, Figure 38a shows not only an increase in peak magnitude but also a consistent shift in peak location towards lower order frequencies. These observations clearly highlight the relation between a radial damage at the bearing and the resulting accelerations $\ddot{y}$ of the MS.

Now that variations in the acceleration signals of the MS where the actual bearing damage

(a)   (b)

(c)
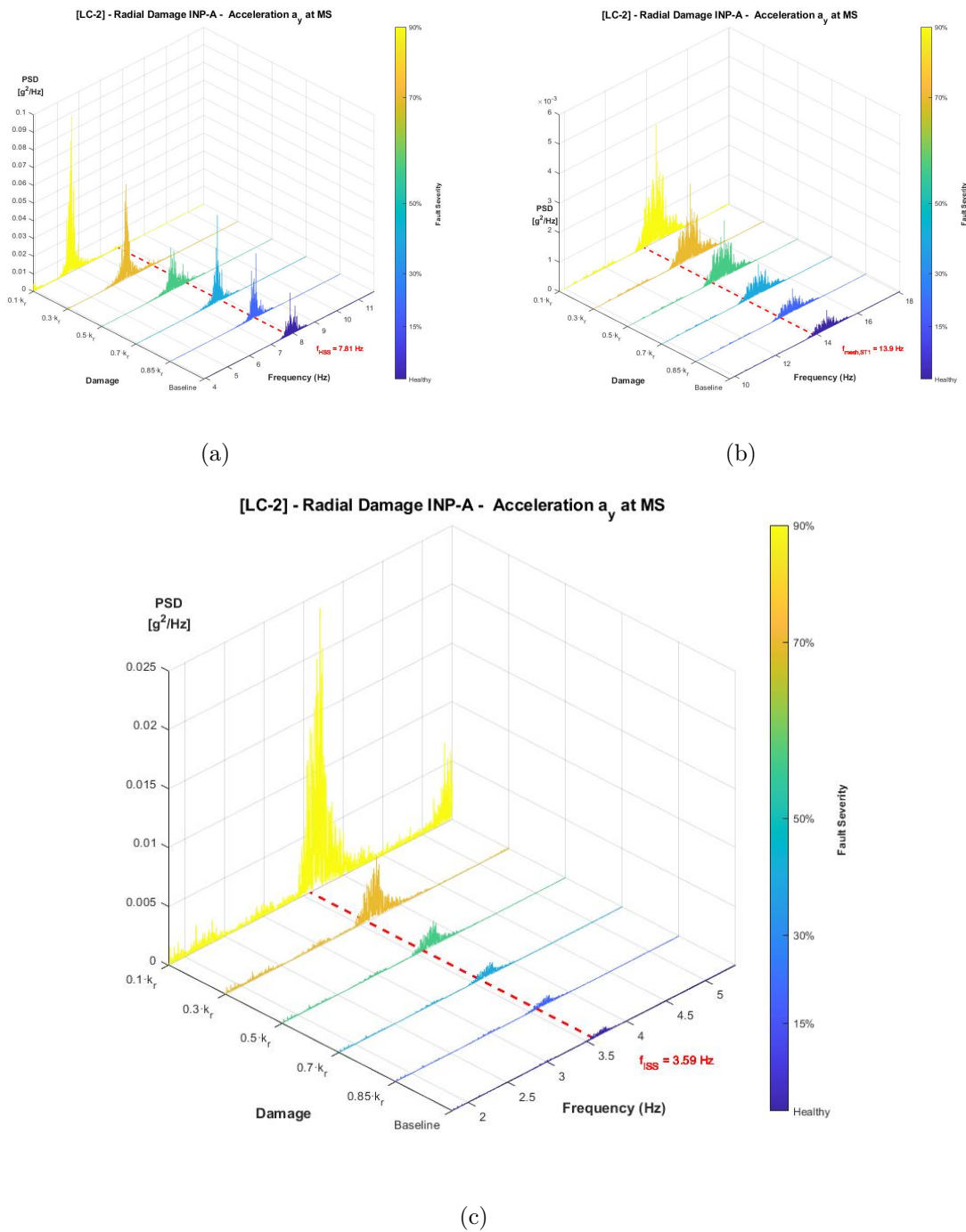
Figure 38: Evolution of PSD of MS $\ddot{y}$ for LC2 inspected at several relevant frequency ranges: (a) for the frequency range surrounding f_{HSS}, (b) surrounding the meshing frequency of the first planetary stage frequency $f_{\mathrm{mesh,ST1}}$ and (c) for the range in the vicinity of f_{ISS}

originates, it is interesting to explore whether a similar abnormal behaviour can be detected for accelerations of the HSS. In the prior analysis of $LC2$ in the time-domain it was clear that a fault at the MS resulted in a transfer of loads towards the HSS bearings. Presumably, this is the result of a deviation in the normal accelerations at the HSS which should be

possible to detect in the frequency-domain.

Figure 39 presents the PSD of $\ddot{y}$ of the HSS for *LC2* and clearly illustrate that the acceleration signal at the HSS is excited by the meshing frequency of the first and second planetary stage, $f_{\mathrm{mesh,ST1}}$ and $f_{\mathrm{mesh,ST2}}$ respectively. Despite the resonant behaviour observed at these frequencies, however, there is no remarkable differences in the energy content for increasing radial damage Both in Figure 39a and Figure 39b the location and magnitude of the peaks, as well as the shape of the side-bands remain approximately identical for the six simulations of incremental radial damage at **INP-A**

(a)   (b)
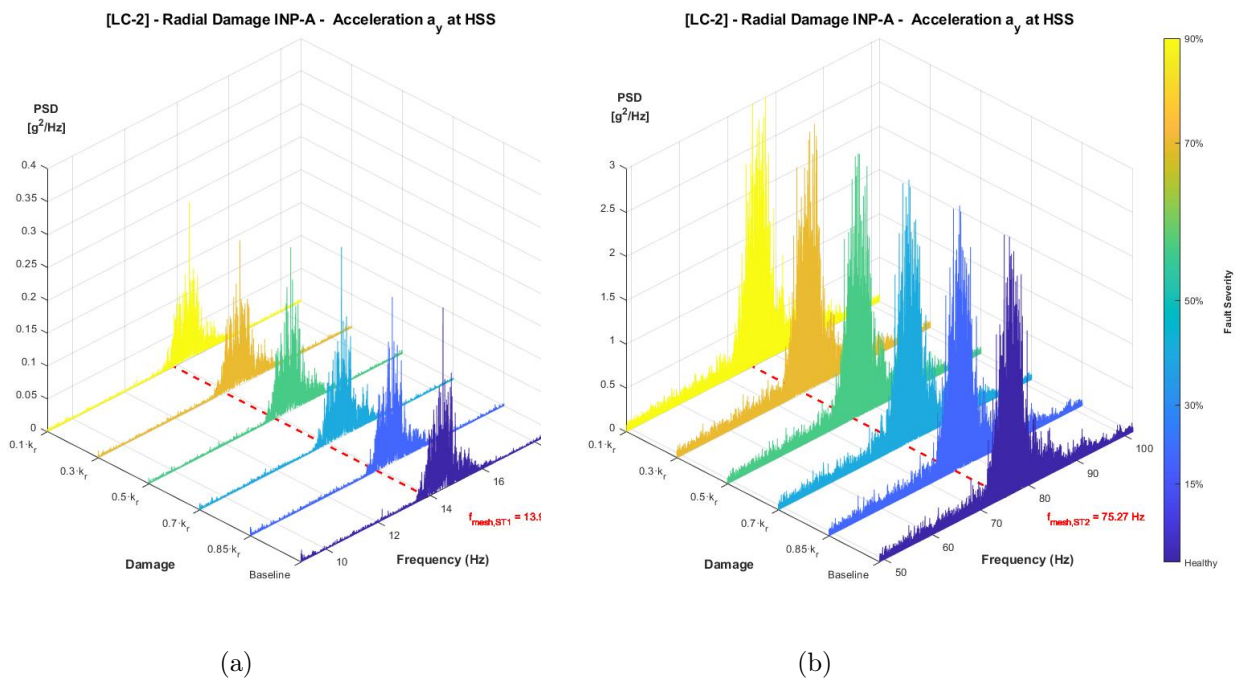
Figure 39: PSD of the acceleration signal a_y of the HSS showing resonance at the gear meshing frequency of (a) the first planetary stage $f_{\mathrm{mesh,ST1}}$ and (b) the second planetary stage $f_{\mathrm{mesh,ST2}}$ for *LC2*

On the other hand, a potential indication of a developing fault is clearly seen from the PSD spectra in Figure 40. This figure illustrates the energy content in the vicinity of the frequencies corresponding to the rotational speed of the intermediate high-speed shaft (IHSS) f_{IHSS} and the high-speed shaft (HSS) f_{HSS}.

Figure 40a shows the energy content of $\ddot{y}$ of the HSS in the frequency range surrounding the characteristic frequency f_{IHSS} whereas Figure 40b shows the PSD of the same acceleration signal centered at f_{HSS}. Both of these figures highlight an abnormal behaviour. Figure 40a exposes the increase of the energy content as the radial damage becomes more severe. This

is seen by peaks which increase consecutively although the location of these peaks remains approximately constant. Further indication of damage is provided by Figure 40b which shows not only a reduction in the magnitude of the peaks but also a remarkable shift towards a lower frequency range.

(a)   (b)
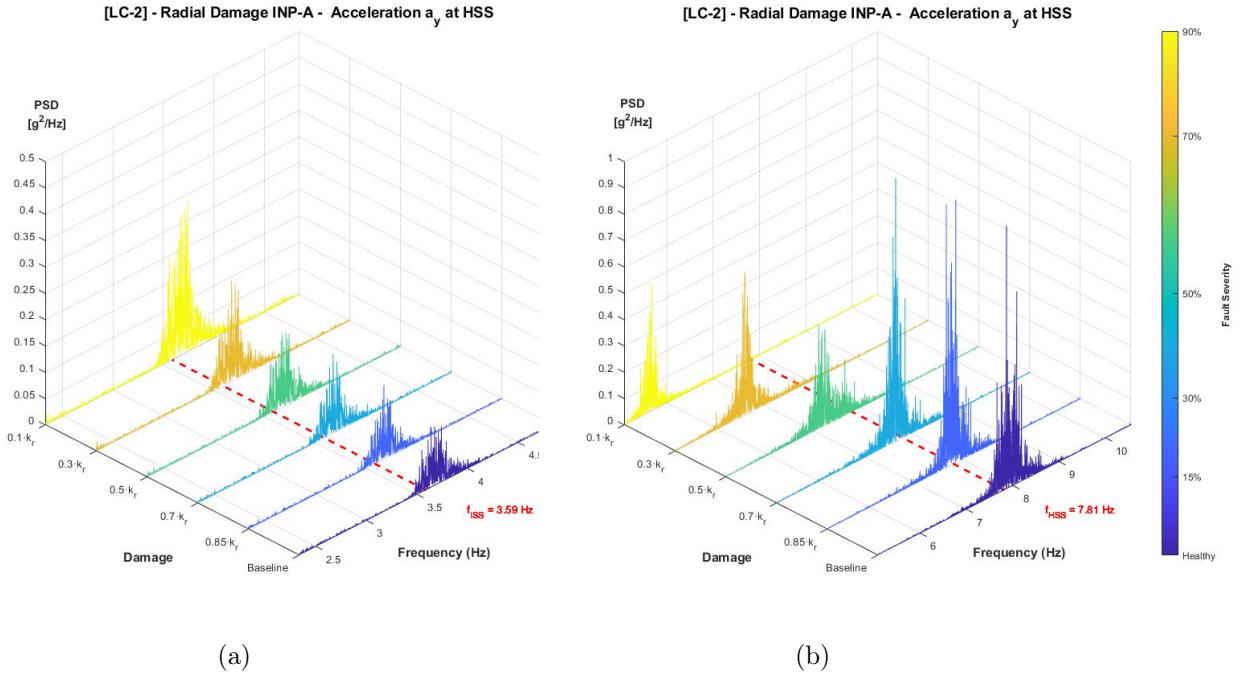
Figure 40: PSD of the acceleration signal $\ddot{y}$ of the HSS showing (a) an increase of the energy content at f_{IHSS} and (b) a variation of the magnitude and location of the energy content at f_{HSS} for *LC2*

Furthermore, it is important to select accurately the frequency ranges in order to detect shifts. As an example, Figure 41 shows the PSD of $\ddot{x}$ of the HSS for *LC2*. Whereas Figure 41a covers a wide frequency range some changes in the frequency content indicating an incipient fault may not be readily visible. On the other hand, Figure 41b represents the PSD of the same signal but closes-in on the frequency range surrounding the characteristic frequency of rotation of the HSS, $f_{\mathrm{HSS}} = 7.81$ Hz $\approx 468,6$ RPM. Figure 41b clearly shows that a radial damage at **INP-A** influences the translational acceleration $\ddot{x}$ at the HSS. Specifically, for increasing damage there is a noticeable shift of energy moving away from the characteristic frequency f_{HSS} under healthy conditions. This progressive shift was hard to identify in Figure 41a but can be identified swiftly by analyzing an adequate frequency range.

Spectral Analysis of LC1 & LC3

(a)

(b)
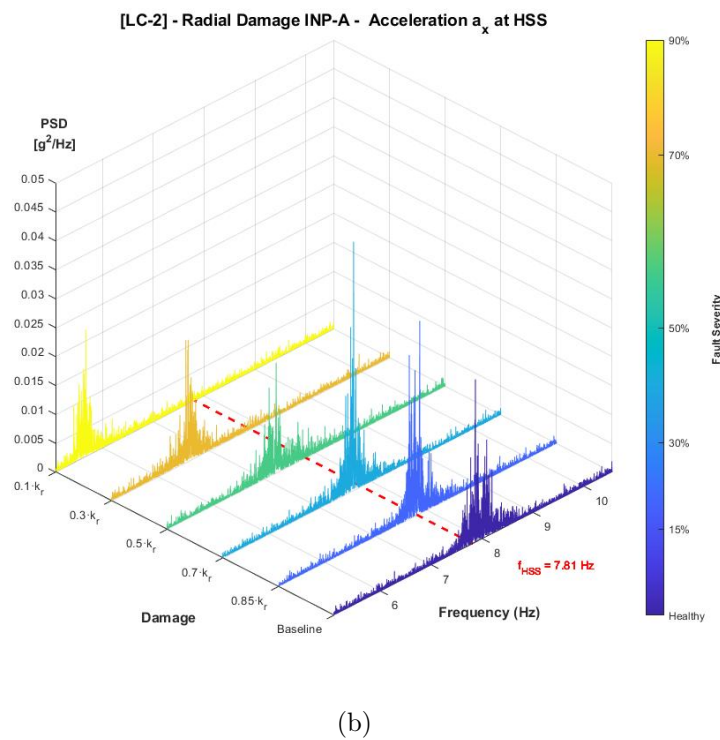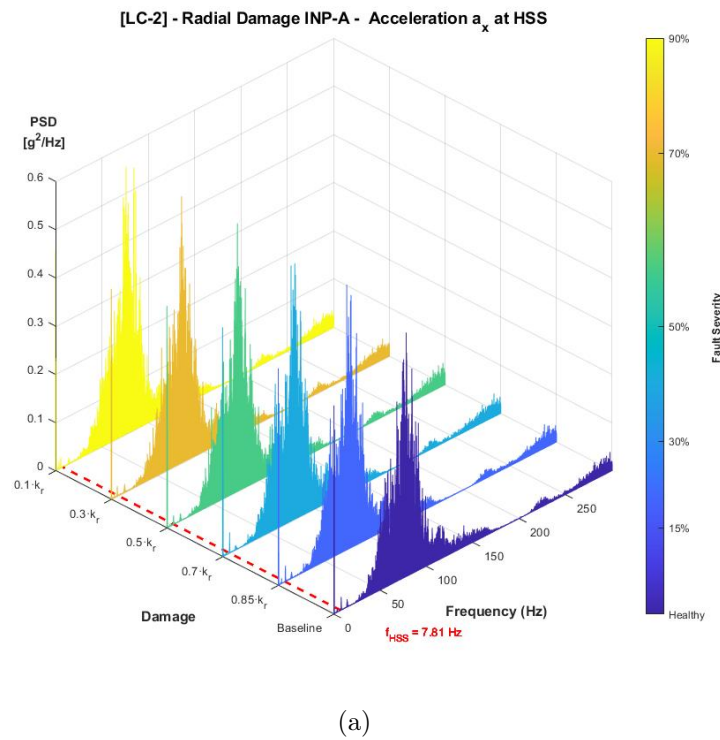
Figure 41: Evolution of PSD of $\ddot{x}$ of HSS for LC2. (a) for a large frequency range and (b) for a frequency range in the surroundings of the HSS frequency f_{HSS}

The goal of spectral analysis is to be able to identify peaks and resonant behaviour which may be relevant for fault detection. Faulty behaviour in the frequency-domain which may

otherwise be hidden in the time-domain can aid the prognosis of these faults. However, the spectral analysis of the load cases *LC1* and *LC3* was significantly less fruitful than that of *LC2*. In fact, no anomalies in the frequency content for increasing damage was observed in the spectral analysis of the accelerations for either of these load cases.

The correct visualization of spectral information depends on the sampling rate f_s, also known as sampling frequency. Hence, in the absence of fault evidence in the frequency domain, the first verification should be to evaluate if the selected sampling rate is adequate. Essentially f_s refers to the number of data points acquired per second. In this work, a sampling rate of $f_s = 600$ Hz = 600 samples/second. The minimum requirements to select f_s are different for the time-domain and the frequency-domain.

To obtain correct peak amplitude in the time domain, f_s should be such that it is at least $\times 10$ times faster than the highest frequency of interest. In practice, sampling even higher than $\times 10$ improves measuring the amplitude correctly in the time domain. The frequency domain only requires sampling $\times 2$ the highest frequency of interest. This optimal sampling frequency rate such that the data in the signal is neither lost nor over-lapped is known as the Nyquist rate. In practice a slightly higher value of $\times 2.5$ is sometimes preferred.

Generally speaking, monitoring machine bearings requires high frequency-rate in the kHz range. In a study of WT bearing diagnosis [40] with a shaft rotational frequency $f_r = 12$ Hz and a fault characteristic frequency of inner race $f_{\text{FCFI}} = 57$ Hz the resonant frequency of rolling bearing $f_n = 4000$ HZ. Furthermore, it is generally agreed that to capture bearing signals at initial defect stage which favours early fault detection, sampling frequency must be very high since this defect typically generate vibrations at high frequency in the proximity of 10 kHZ as seen in Figure 42. For a large size bearing rotating at slow speed, defect frequency can be in ranges as high as 15 kHz and higher [11].

Although the sampling frequency is lower than the recommended sampling frequency to detect specific bearing faults as seen in Figure 42, it is important to keep in mind that the bearings in the numerical are modelled in a simplified manner with an associated stiffness and damping coefficients. Therefore, the high-frequency ball bearing passing frequency will not be present in the acceleration signals.

Accordingly, the highest frequency is the meshing frequency in the third parallel stage $f_{\text{mesh,ST3}}$ as seen in Table 13
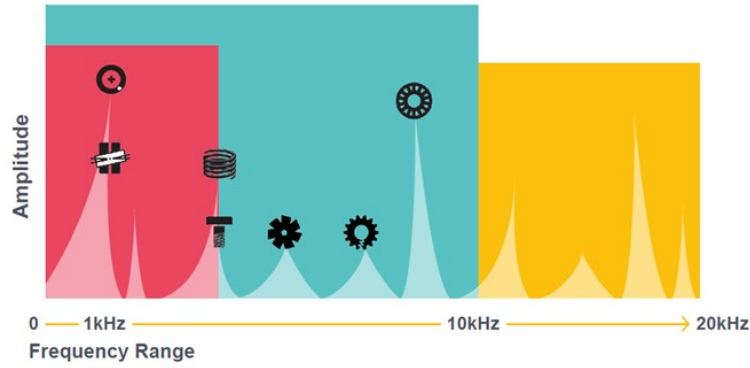
Figure 42: Schematic representation of typical frequency ranges corresponding to different types of faults [11]

$$2,5 \times f_{\mathrm{mesh,ST3}} = 2,5 \times 218,78 \approx 547 < 600 \ \mathrm{Hz} \tag{4.10}$$

Hence, according to Equation 4.10, the sampling frequency selected in this work satisfies the Nyquist Rate sampling criterion and is sufficiently large to capture useful information in the high-frequency range. Therefore the sampling frequency should not be an obstacle to establish the right diagnostic.

Since the sampling frequency was found to be adequate, the little evidence of faulty behaviour in the frequency domain may mean that the load cases *LC1* and *LC3* do not result in abnormal accelerations in the main shaft or the high-speed shaft. However, load cases *LC1* and *LC3* represent faults originating at distinct locations which means that the fact that no variation in PSD plots was observed may be associated to radically different reasons. At this point, it is safe to say that the preliminary frequency-domain analysis of these two load cases in terms of PSD was inconclusive.

In practice, this means that fault detection of a radial damage originating at the main shaft (*LC2*) based on spectral analysis is possible. The same cannot be said for an axial fault originating on the main shaft bearing (*LC1*) or for a radial fault propagating from the high-speed shaft bearing (*LC3*) since spectral analysis provided no signs of fault progression which makes it an unreliable source for fault detection. Although no significant variation in the frequency content of the acceleration signals for these load cases was found, it is important to note that an in-depth spectral analysis has not been performed and that a

more detailed analysis might be necessary.

Chapter 5

Physics-Based Approach

5.1 Bearing life

Premature failures in large offshore WTS are often attributed to bearing fatigue despite gearboxes being designed and developed using the best bearing-design practices available according to NREL as cited by [41]. Hence, the ability to estimate bearing life is a major aspect to evaluate overall WT reliability. Accordingly, prediction of bearing life is the cornerstone of this thesis.

Bearing life calculation is the single most common approach to assess the behaviour, reliability, damage and remaining useful lifetime (RUL) of bearings. Additionally, bearing life calculation can be used as a tool to estimate the future operational state of a bearing under specific loading conditions. This in turn can contribute to the prognosis and RUL estimation of several other components in the WT drivetrain.

Present day standards consider bearing life calculation according to Equation 5.1. The established procedure to estimate the life of a bearing based on the work of Gustaf Lundberg and Arvid Palmgren. Lundberg and Palmgren combined the Weibull probability distribution of metal fatigue to establish the basic theory of the stochastic dispersion of bearing lives. In its final and simplest form, the bearing life is calculated as:

$$L_{10} = \left(\frac{C}{P}\right)^a \tag{5.1}$$

L_{10} is formally defined as the number of cycles when in an identical group of bearings, 90% bearings operate normally without any fatigue damage while only the remaining 10% of the bearings incur pitting damage.

In Equation 5.1:

- C in $[kN]$ is the bearing basic dynamic load rating corresponding to the dynamic load that the bearing can withstand if the basic rating life is exactly 10^6 revolutions. C is a factor that depends on the bearing geometry;

- P in $[kN]$ is the equivalent dynamic bearing load;

- a is the exponent for the bearing life equation. For ball bearings $a = 3$ and for roller bearings $a = \frac{10}{3}$.

Equation 5.1 has been adopted by ISO standards over time and is integrated in the standard used today: ISO 281 .

The bearing equivalent dynamic load P in Equation 5.1 is calculated according to Equation 5.2 from the values of the axial loads F_a and radial loads F_r acting on the bearing.

$$P = X \cdot F_r + Y \cdot F_a \tag{5.2}$$

where X and Y are the radial and axial load bearing factors, respectively. For a given bearing, these values are constant factors obtained from the bearing manufacturer. In terms of the SIMPACK values, axial and radial loads F_a F_r are equivalent to:

$$F_a \equiv F_x$$
$$F_r = \sqrt{F_y{}^2 + F_z{}^2}$$

The values of the bearing basic dynamic load rating C in Equation 5.1 and the radial and axial load bearing factors X and Y from Equation 5.2 are given in the last three columns of Table 16. These values are provided by the manufacturer and presented in [16].

Note that in Table 16 MS and HSS represent Main Shaft and High-Speed Shaft and **TRB** and **CRB** represent tapered roller bearing and cylindrical roller bearing respec-

	Location	Type	Provider	Designation	OD	ID	B	C	X	Y
INP-A	MS (Up-Wind)	TRB	Koyo	2TR1450	1770	1450	145	5.6431	1	0
INP-B	MS (Down-Wind)	TRB	Koyo	2TR950B	1250	950	136	4.5774	1	0
HS-A	HSS (gearbox side)	CRB	SKF	NNCF4980BV	540	400	140	2.16	1	0
HS-B	HSS (generator side)	TRB	Koyo	45T605729	570	300	290	3.79	1	1.24

Table 16: Bearing provider, designation, geometrical properties and constant factors for the calculation of bearing life. Provided by the manufacturer as presented in [16]

tively. **OD/ID** is the outer/inner diameter of the bearing and **B** is bearing thickness. All dimensions are given in millimetres.

Equivalent force for time-varying loads

For the application of Equation 5.2 it is important to note that for all three load cases considered in this work in reality $F_a \equiv F_a(t)$ and $F_r \equiv F_r(t)$. Hence, for time-varying loading, an equivalent steady load P_{eq} must be defined in order to calculate the bearing life L_{10}.

Here, the load duration distribution method is used to obtain an expression for P_{eq}. This approach is suggested by ISO 6336-6 and used in [12]. The method is shown schematically in Figure 43.

In practical terms, the load is divided into a number i of bins, and the duration and speed associated with each bin is calculated. It is a rather conservative approach since it assumes the upper level of the load each bi is in fact the maximum stress range level for that bin.

The equivalent steady load P_{eq} as implemented by Nejad *et. al.* in [12] is obtained according to Equation 5.3.

$$P_{eq} = \left(\frac{\sum n_i t_i P_i^a}{\sum n_i t_i} \right)^{\left(\frac{1}{a} \right)} \tag{5.3}$$

In Equation 5.3, n_i is the rotational speed in bin i, t_i is the bin duration, and P_i is the maximum load in that bin obtained from Equation 5.2.

5.2   Evolution of bearing dynamic equivalent loads

Now that a methodology has been put in place to compute an bearing dynamic equivalent load P_{eq} for time-varying loading this section will examine the evolution of these loads for
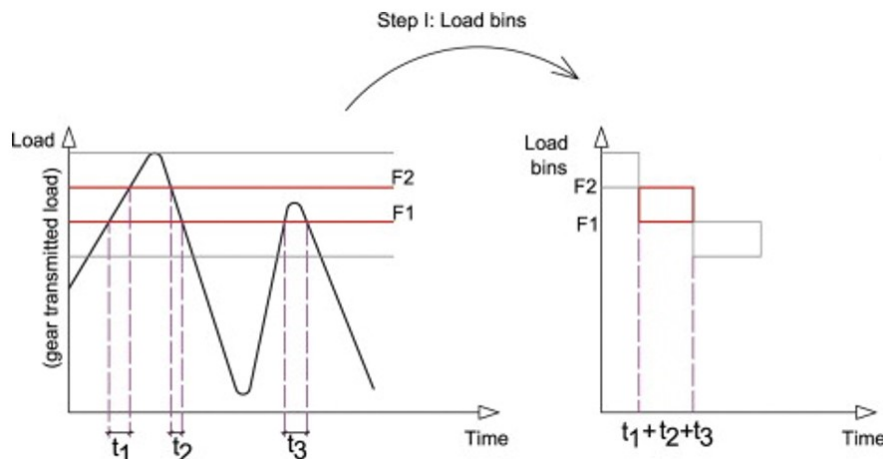
Figure 43: Creating load bins from a load time series [12]

increasing damage.

P_{eq} has been calculated according to Equation 5.3 using 100 bins. P_{eq} has been calculated for each bearing under baseline-healthy conditions, and for 5 consecutively increasing damage severity. This has been carried out for all 3 LCs.

Figure 44 and Figure 45 show the evolution of bearing dynamic equivalent load P_{eq} for time-varying loading corresponding to *LC1* and *LC2* respectively, whereas Figure 46 corresponds to *LC3*.

LC 1

Figure 44 shows that P_{eq} remains constant at all 4 bearings despite the gradual decrease in the axial stiffness of the MS bearing **INP-A**. This means that *LC1* has no effect on the bearing dynamic equivalent load, even when damage severity is high.

These results are in close agreement with the characteristics of *LC1* since this load case primarily induces an increase in non-torque loads and has little effect on the radial loads transferred from the MS to the gearbox bearings. This damage, by its very nature, has a negligible effect on the dynamic equivalent radial load perceived by all 4 bearings under study.

LC 2

Figure 45 corresponds to the evolution of P_{eq} as a progressive radial damage develops at **INP-A**. As damage increases, **INP-A** can no longer accommodate radial loads which
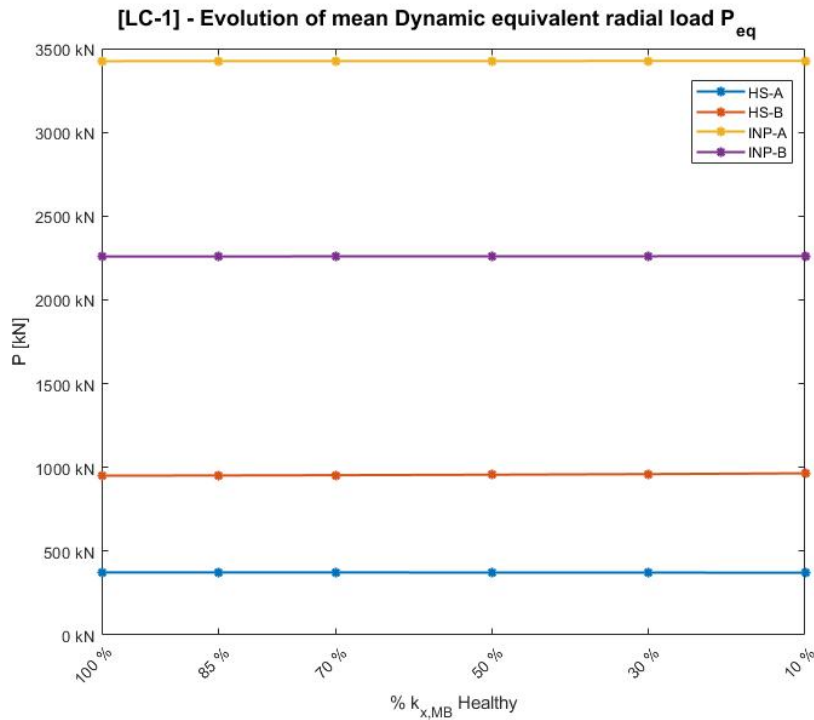
Figure 44: Evolution of P_{eq} at all 4 bearings for decreasing axial stiffness of MS bearing **INP-A** (*LC1*)

results in a significant decrease of P_{eq} in this bearing. This reduction in P_{eq} is higher than 60% given that when the radial stiffness of **INP-A** reaches 10% $K_{\text{r,MB}}$ $P_{\text{eq}} = 1320\ kN$ as opposed to healthy conditions, when radial stiffness of the bearing is 100% $K_{\text{r,MB}}$ and $P_{\text{eq}} \approx 3500\ kN$. Figure 45 clearly shows a transfer of radial loads to the remaining bearings as P_{eq} increases at **INP-B**, **HS-A** and **HS-B**. The increase in the P_{eq} is as high as 100% for **INP-B** compared to its healthy operational state. It is interesting to point out that the decrease of P_{eq} at **INP-A** leads to an increase at **INP-B** at a very early stage which can already be detected during the first faulty simulation when radial bearing stiffness is 85% $K_{\text{r,MB}}$.

In the HSS, under healthy conditions $P_{\text{eq}} = 373\ kN$ for **HS-A** and $P_{\text{eq}} = 950\ kN$ for **HS-B** which increase up to 817 kN and 1122 kN representing an increase of 118% and 18% respectively. Therefore, the increase in P_{eq} is highest at the HSS at the **HS-A** bearing.

It can be seen from Figure 45 that the performance of the main bearing **INP-A** has a crucial impact on the behaviour of the remaining bearings, both on the MS bearing **INP-B** and the gearbox bearings at the HSS **HS-A** and **HS-B**. The radial load enters the gearbox and is effectively propagated to the HSS where the bearing **HS-A** displays
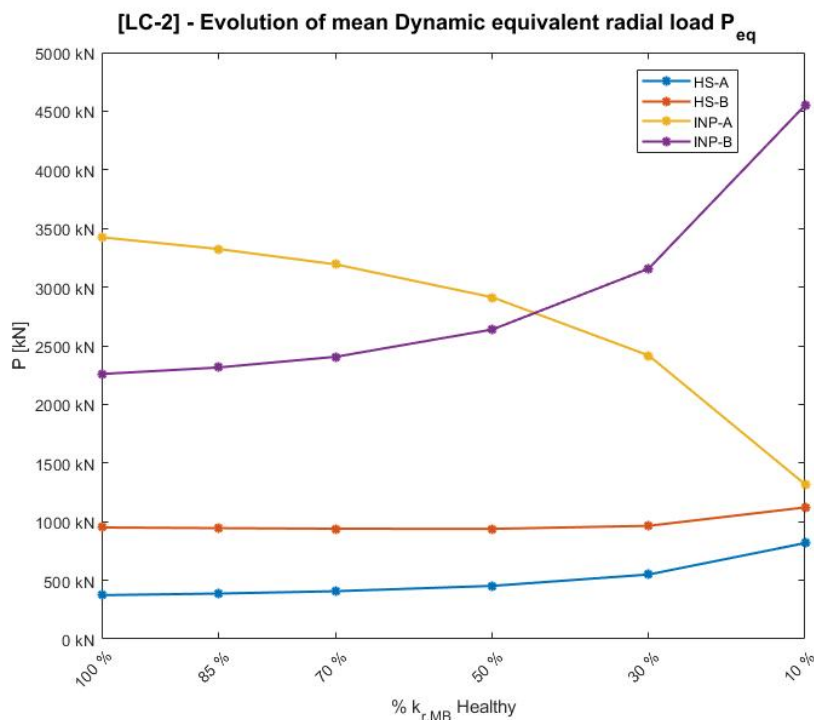
Figure 45: Evolution of P_{eq} at all 4 bearings for decreasing radial stiffness of MS bearing **INP-A** (*LC2*)

an increase of 118% of the the dynamic equivalent radial load compared to the healthy no-damage case.

LC 3

Figure 46 corresponds to *LC3* and shows the evolution of P_{eq} as a progressive radial damage develops at **HS-B**. Whereas the equivalent load P_{eq} remains approximately unchanged at the MS bearings a noticeable change is observed at the HSS bearings. As radial stiffness of **HS-B** decreases, this bearing can no longer accommodate radial loads which results in a decrease of up to 68% of P_{eq} when the fault severity approaches 10% $K_{\text{r,HSB}}$. This reduction in P_{eq} leads to a direct increase of the dynamic equivalent load at **HS-A** highlighting a transfer of loads between the two bearings supporting the HSS. When operating in healthy conditions, **HS-A** sees an equivalent load $P_{\text{eq}} = 373\ kN$ whereas for the most severe damage considered $P_{\text{eq}} > 635\ kN$, an increase of more than 70%. Its interesting to note that the increase in P_{eq} increases rapidly as radial bearing stiffness at **HS-B** falls bellow 50% $K_{\text{r,HSB}}$.

Based on Figure 45 and Figure 46 which illustrate the evolution of P_{eq} for radial damage in the MS and in the HSS respectively. It is interesting to realise that whereas a radial

damage in the MS leads to a greater share of radial loads in the gearbox bearings as can be seen from Figure 45. However, when the radial damage originates at the HSS, specifically at the **HS-B** bearing on the generator side, although a greater share of radial loads is experienced by the bearing on the gearbox side, **HS-A**, radial loads do not propagate towards the MS. This is readily seen in Figure 46 which clearly shows the increase in P_{eq} at **HS-A** as radial stiffness decreases but no noticeable changes in the equivalent load P_{eq} in the MS.

This indicates that the gearbox may act as an amplifier of radial loads when the loads propagate in downwind direction, from the MS to the HSS. On the other hand, a different the gearbox exhibits a different behaviour in terms of radial load transfer in upwind direction, when a radial damage originates in the HSS. A possible explanation for this phenomenon is the gear ratio which increases...
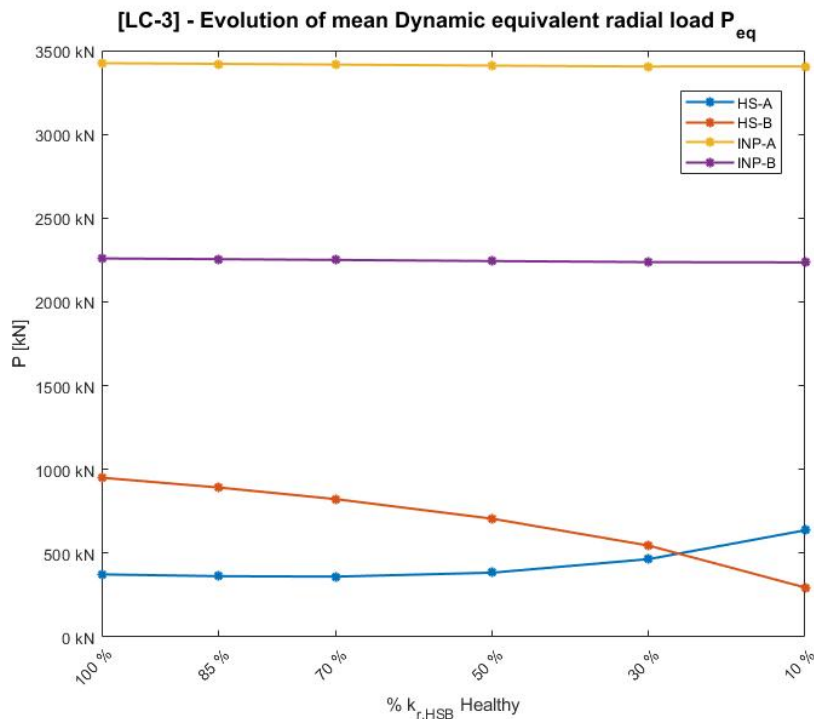
Figure 46: Evolution of P_{eq} at all 4 bearings for decreasing radial stiffness of HSS bearing **HS-B** (*LC3*)

5.3   Comparative analysis of bearing life

In the present work, the lifetime calculation in the four separate bearings is computed via comparison with the healthy state of each bearing. This approach will suffice because

it permits a straightforward comparison between the bearing life $L_{10,i}$ corresponding to a certain damage intensity i with respect to the bearing life $L_{10,i=0}$ when the bearing is fully healthy. Naturally, the no-damage healthy lifetime $L_{10,i=0}$ corresponds to the baseline case. This is expressed in terms of percentage by introducing the factor χ for each bearing:

$$\chi_i = \frac{L_{10,i} - L_{10,i=0}}{L_{10,i=0}} \times 100 \qquad \text{with} \qquad i = \{0, 1, 2, 3, 4, 5\} \tag{5.4}$$

In Equation 5.4, index i is the damage intensity where $i = 0$ denotes healthy conditions obtained from the baseline simulation and $i = \{1, 2, ..., 5\}$ represents increasing damage. Hence, χ_i is the expected variation of the lifetime L_i for damage intensity i with respect to the lifetime when that same bearing operates with no damage $L_{10,i=0}$.

The sign of χ will effectively highlight whether a certain bearing experiences and increase or a decrease of its expected lifetime compared in comparison to no-damage conditions.

- Negative values of the numerator will result a negative value of χ. This means $L_i < L_0$ which represents a **decrease** in the lifetime of a bearing for damage intensity i compared to the no-damage situation.

- Positive values of χ indicate that $L_i > L_0$ which means the estimated lifetime of that specific bearing for that specific damage intensity i sees an **increase** compared to the lifetime L_0 of that same bearing when no damage occurs.

Since in the previous section an equivalent steady load P_{eq} was computed according to Equation 5.3, assuming $P_i(t) \equiv P_{i,\text{eq}}$, the bearing life for a damage intensity i can be obtained according to Equation 5.5

$$L_{10,i} = \left(\frac{C}{P_{\text{eq},i}} \right)^a \tag{5.5}$$

According, to Equation 5.5, for a given bearing, the lifetime corresponding to healthy conditions $L_{10,i=0}$ with no damage can be expressed as:

$$L_{10,i=0} = \left(\frac{C}{P_{\text{eq},0}} \right)^a \tag{5.6}$$

By substituting the expressions for the bearing life under i damage $L_{10,i}$ in Equation 5.5 and the expression for the bearing life with no damage $L_{10,i=0}$ from Equation 5.6 into the expression of χ given by Equation 5.4, we can obtain the following simplified relation:

$$\chi_i = \frac{L_{10,i} - L_{10,i=0}}{L_{10,i=0}} = \left(\frac{P_{eq,0}}{P_{eq,i}}\right)^a - 1 \tag{5.7}$$

Equation 5.7 is applied to all 4 bearings, **INP-A**, **INP-B**, **HS-A** and **HS-B**, for every damage intensity $i = \{1, 2, ..., 5\}$ and for all 3 load cases.

5.4   Results of physics-based model

The comparative analysis of the bearing life calculation carried out in the previous section gives the evolution of the life of **INP-A**, **INP-B**, **HS-A** and **HS-B** for all three load cases through the non-dimensional factor χ.

Results corresponding to *LC1*, *LC2* and *LC3* are given in Table 17, Table 18 and Table 19, respectively. Shown in grey is the bearing affected by the damage for *LC1*, results highlighted in red depict a **decrease** in bearing life time with regard to healthy conditions whereas results highlighted in green correspond to an **increase** in bearing lifetime compared to the baseline simulation where the bearing is fully healthy.

Its important to note from Equation 5.7 that factor χ_i is computed directly from the bearing life calculation $L_{10,i}$ which is based on the load $P_{eq,i}$. Since χ_i is inversely proportional to $P_{eq,i}$, a decrease of the latter will result in an increase of χ_i value. t According to the established damage modelling procedure, damage is introduced by decreasing the stiffness of the bearing were damage is assumed, which in turn reduces the load $P_{eq,i}$ experienced by that bearing. Hence, the lifetime of the actual damaged bearing will increase disproportionately which is unrealistic. For this reason the lifetime results corresponding to the damaged bearing should be treated with care. Accordingly, the lifetime bearing results highlighted in grey Table 17, Table 18 and Table 19 are non-physical and should not be misinterpreted.

Results corresponding to *LC1* illustrate that an axial damage at a MS bearing leads to a decrease in the lifetime of bearings at the MS and the HSS. The down-wind MS bearing

INP-B experiences a consistent decrease of its lifetime as damage increases in the upwind bearing although the impact is limited to 0.26% decrease compared to its healthy state lifetime. The decrease of lifetime is significantly more severe for the HSS bearing on the generator side, **HS-B** which is as high as 4.88%.

	LC1			
	HS_A	**HS_B**	**INP_A**	**INP_B**
healthy	0.00%	0.00%	0.00%	0.00%
χ_1	0.17%	-0.51%	-0.02%	-0.03%
χ_2	0.37%	-1.10%	-0.03%	-0.06%
χ_3	0.71%	-2.04%	-0.06%	-0.11%
χ_4	1.12%	-3.28%	-0.10%	-0.17%
χ_5	1.70%	-4.88%	-0.15%	-0.26%

Table 17: Variation of χ at every bearing for increasing damage of *LC1*

Results corresponding to *LC2* illustrate the drastic decrease of lifetime caused by a radal damage on the MS bearing. A significant reduction in lifetime is seen for all the considered bearings of both the MS and HSS. Bearing **INP-B**, directly down-wind from the damaged bearing experiences a very harsh impact on its lifetime, as decrease as high as 90.31% compared to its healthy state. Both bearings of the HSS also suffer a severe depletion of their lifetime of 92.66% and 42.43% for **HS-A** and **HS-B**, respectively. Out of all the bearings under study, the HSS bearing **HS-A** is the most affected by a radial damage originating in a MS bearing.

	LC2			
	HS_A	**HS_B**	**INP_A**	**INP_B**
healthy	0.00%	0.00%	0.00%	0.00%
χ_1	-11.37%	1.99%	10.41%	-7.81%
χ_2	-25.07%	3.83%	26.25%	-18.99%
χ_3	-47.38%	4.25%	71.51%	-40.41%
χ_4	-72.44%	-4.85%	219.52%	-67.26%
χ_5	-92.66%	-42.43%	2305.94%	-90.31%

Table 18: Variation of χ at every bearing for increasing damage of *LC2*

The evolution of the lifetime of the 4 bearings for *LC3* are presented in Table 19. The obtained results clearly indicate that the bearing **HS-A** is most affected by a radial damage occurring at **HS-B**. The transfer of loads to the neighbouring bearing leads to a severe decrease of the lifetime of **HS-A** which is as high as 92.66% compared to its healthy state. Both bearings of the MS experience an increase in their expected lifetime of 1.89% and

			LC3	
	HS_A	**HS_B**	**INP_A**	**INP_B**
healthy	0.00%	0.00%	0.00%	0.00%
χ_1	10.23%	23.61%	0.40%	0.63%
χ_2	12.82%	62.01%	0.83%	1.33%
χ_3	-8.66%	169.89%	1.44%	2.33%
χ_4	-51.72%	537.77%	1.97%	3.29%
χ_5	-83.10%	4824.28%	1.89%	3.55%

Table 19: Variation of χ at every bearing for increasing damage of *LC3*

3.55% for **INP-A** and **INP-B**, respectively. According to Equation 5.7, this apparent increase of their lifetime compared to the no-damage situation is a direct consequence of a lower amount of loads applied to these bearings. The underlying reason for this decrease in the loads experienced on the MS may be due to the fact that bearings within the gearbox are suffering from a severe increase of loads coming from the HSS.

The framework followed to obtain these results is based on physical phenomena associated to fatigue through the $S - N$ curves, obtained experimentally. Furthermore, this approach to bearing fatigue life estimation is fully accepted in relevant standards used today. Effectively, the progressive degradation of bearings has been modelled according to the underlying physics which helps validate the method.

In order to actually enable an RUL estimation it is necessary to establish a relation between the simulated faulty conditions and the number of years these bearings are able to operate under these faulty conditions.

Note that three considered damage cases that have been simulated on the numerical drivetrain model are representative of one sea state characterized by a single unique combination of environmental parameters $u - H_s - T_s$ such that $u = 12 \ m/s$, $H_s = 2.5 \ m$ and $T_p = 10.1 \ s$ This means that the behaviour of the drivetrain has been simulated operating for three different faults but for one wind-wave climate. Naturally, given the stochastic nature of the offshore environment this unique combination of environmental parameters occurs only during a small fraction of the turbines intended lifetime. In order to ascertain the amount of hours the turbine operates at this particular combination $u - H_s - T_s$ the joint probability of occurrence of these parameters must be determined.

The process of obtaining the joint distribution of environmental parameters $H_s \ T_p$ and

Figure 47: Location of the eighteen potential offshore sites studied in [4]

U_w is not straightforward and finding a relationship for the combined distribution of these parameters is complex. A simplified method to obtain the joint distribution of H_s, T_p and U_w is given by Equation 5.8 as presented in [4]. To simplify the joint probability distribution a marginal distribution of the wind speed U_w was assumed, as well as a probability distribution of H_s that only depends on wind-speed and a probability distribution of T_p that is only dependent on H_s.

$$f_{U_w,H_s,T_p}(u,h,t) \approx f_{U_w}(u) \cdot f_{H_s|U_w}(h|u) \cdot f_{T_p|H_s}(t|h) \tag{5.8}$$

In Equation 5.8 $f_{U_w}(u)$ is the marginal distribution of wind speed U_w, the conditional distribution of H_s for given U_w is given by $f_{H_s|U_w}(h|u)$ and $f_{T_p|H_s}(t|h)$ is the conditional distribution of T_p for given H_s.

Parametric expressions for $f_{U_w}(u)$, $f_{H_s|U_w}(h|u)$ and $f_{T_p|H_s}(t|h)$ are provided in [4]. The parameters are site-specific and those corresponding to *Site No. 14* as shown in Figure 47 are used.

Therefore, using the parameters corresponding *Site No. 14* an explicit expression of the

marginal distribution of wind speed $f_{U_w}(u)$ can be found. The probability corresponding to $u = 12\ m/s$ is obtained from this probability distribution. Then the conditional distribution of H_s for a given wind speed $f_{H_s|U_w}(h|u)$ was determined for $U_w = 12\ m/s$. The probability corresponding to a wave height H_s was obtained. Similarly, the conditional distribution of T_p for a wave height H_s at *Site No. 14* was calculated such that $f_{T_p|H_s}(t|h = 2.5\ m)$. Finally, the probability for $T_p = 10.1\ s$ was determined. This calculation process is illustrated in Figure 48.

According to this procedure, the parameters shown in Figure 48 can be introduced in Equation 5.8 which yields:

$$f_{U_w,H_s,T_p}(u,h,t) \approx f_{U_w}(u) \cdot f_{H_s|U_w}(h|u) \cdot f_{T_p|H_s}(t|h) \tag{5.9}$$

$$\approx 0.05383 \ \cdot \ 0.24980 \ \cdot \ 0.16276 = 0.0022 \tag{5.10}$$

Hence, the joint probability of occurrence p of environmental parameters $u \ - H_s \ - T_s$ such that $u = 12\ m/s$, $H_s = 2.5\ m$ and $T_p = 10.1\ s$ is p=**0.0022**. Determining the amount of hours the turbine can be expected to operate at this particular sea-state is then straightforward. Assuming the wind turbines design lifetime is **20 years**:

$$T\left(u, H_s, T_p\right) = p \cdot 20 \text{ years } \cdot 8760 \ \frac{\text{hours}}{\text{year}} = 385.44 \text{ hours} \approx 16 \text{ days} \tag{5.11}$$

Therefore the drivetrain bearings in a healthy state should theoretically be able to withstand a minimum of 386 hours.

The lifetime in hours for a given bearing can be calculated according to Equation 5.12. Where C_j is the basic dynamic load rating in $[N]$ for bearing j, Ω_j is the shaft speed in RPM for bearing j as given in Table 16, $P_{eq0,j}$ in $[N]$ is obtained according to Equation 5.3 and corresponds to the steadystate equivalent dynamic bearing load for healthy conditions
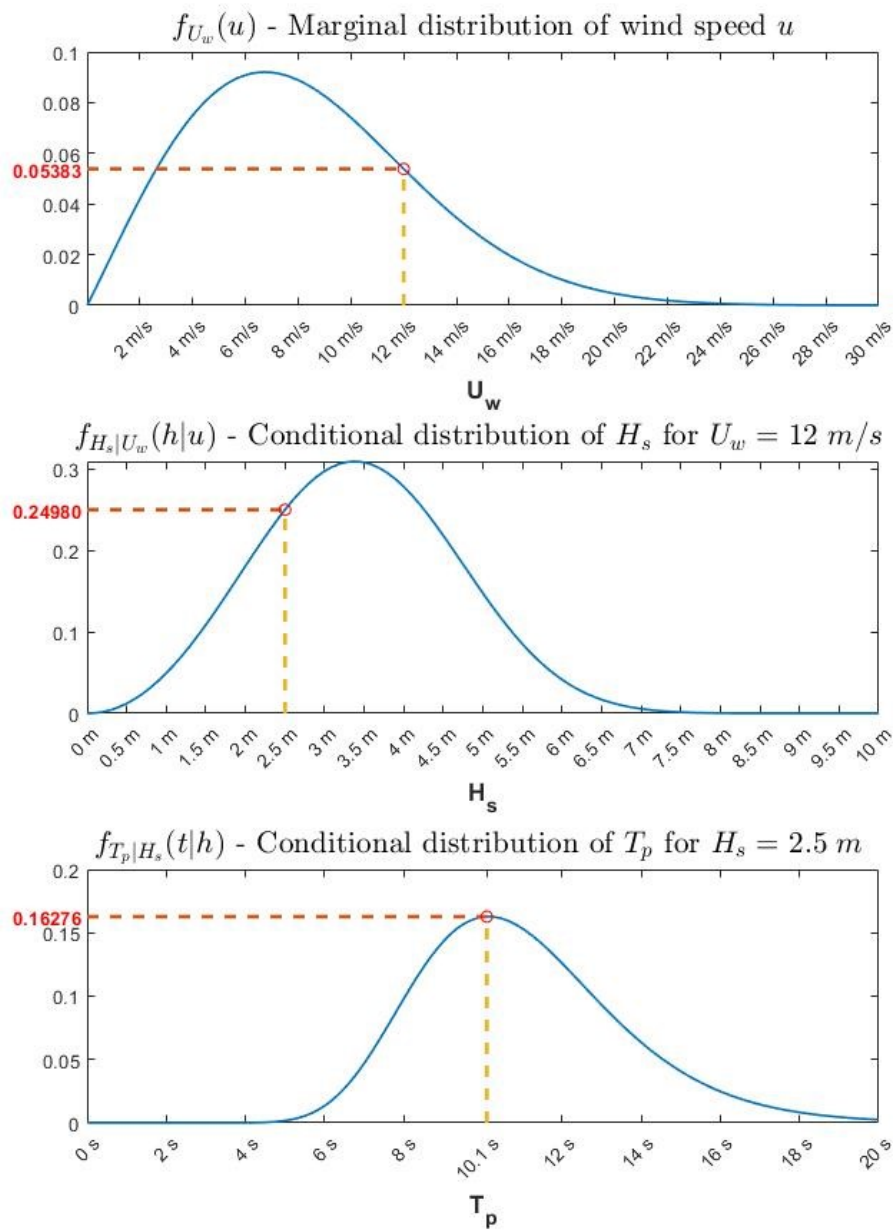
Figure 48: Computation of the joint probability distribution of $u - H_s - T_s$. for $U_w = 12\ m/s$, $H_s = 2.5\ m$ and $T_p = 10.1\ s$

	HS_A	HS_B	INP_A	INP_B
hours	11578	3351	8809	17545
days	482.41	139.62	367.03	731.04

Table 20: Bearing lifetime for the baseline simulation for which bearings are fully healthy

and $a = 10/3$

$$L_{10} = \frac{10^6}{60 \cdot \Omega_j} \left(\frac{C_j}{P_{eq0,j}} \right)^a \tag{5.12}$$

The results of bearing lifetime for healthy conditions are presented in Table 20. The first remark from these results is that the lifetime of all bearings is significantly higher than the duration of the wind-wave climate which has been considered which amounts to approximately 385.44 hours $\approx$ 16 days.

From Table 20 it can be seen that the bearing with the shortest lifetime when in healthy conditions is **HS-B** which has a lifetime $\approx$ 139 days $>>$ 16 days.

This in turn means that for the environmental conditions assumed in this work these bearings will operate safely. This does not mean that the bearings are exempt from failure throughout their lifetime. This simply confirms that these bearings can easily withstand the considered wind-wave climate. However, bearings will be subject to a large number of different $u - H_s - T_s$ combinations and the lifetime of every bearing in the drivetrain must be verified for each combination that is likely to occur. This verification is commonly performed through a fatigue analysis. The assessment of the Fatigue Limit State (FLS) is however not the goal of this work.

By applying Equation 5.13, the lifetime in hours for a given bearing j can be calculated for every damage intensity i nad for each load case.

$$L_{10,i} = \frac{10^6}{60 \cdot \Omega_j} \left(\frac{C_j}{P_{eqi,j}} \right)^a \tag{5.13}$$

Where C_j is the basic dynamic load rating in $[N]$ for bearing j, Ω_j is the shaft speed in RPM for bearing j as given in Table 16, $P_{eqi,j}$ in $[N]$ is obtained according to Equation 5.3 and corresponds to the steadystate equivalent dynamic bearing load for damage intensity i for bearing j. Again, $a = 10/3$.

As determined in Equation 5.11, for a sea-state such that $u = 12\ m/s$, $H_s = 2.5\ m$ and $T_p = 10.1\ s$ and with a joint probability $p = 0.0022$ the bearings need to withstand a minimum of 385.44 hours ≈ 16 days. Hence, failure is assumed to occur when the remaining useful life RUL is such that $RUL < t_{\lim}$, where $t_{\lim} = 16$ days.

In reality, offshore maintenance requires additional time to adequately respond to component failure. Preparations are required such as chartering the appropriate offshore vessel for the task, hiring crew members & technicians, purchasing transporting parts and ferrying components to the offshore site.

For optimal maintenance planning threshold should be selected so as to start preparing for OM well ahead of bearing failure. Naturally, the threshold must therefore be selected higher than 16 days for caution. Two different thresholds are considered to estimate the RUL of bearings, $t_{f,1}$ and $t_{f,2}$ such that $t_{f,2} > t_{f,1}$. Both thresholds are multiples of $t_{\lim} = 16$ days and are defined as follows:

- $t_{f,1} = 4 \cdot t_{\lim} = 4 \cdot 16 = 64$ days;

- $t_{f,2} = 8 \cdot t_{\lim} = 8 \cdot 16 = 128$ days;

The first threshold, $t_{f,1}$ corresponds to approximately one month and a half before the bearing fails whereas $t_{f,2}$ corresponds to over 3.5 months before failure occurs. It is assumed that for minor repairs setting the threshold to a value $t_{f,1}$ is sufficient. For major O&M operations which require extended preparation time or more delicate repairs where the turbine needs to be disassembled a greater threshold may be reasonable such as $t_{f,2}$. Naturally, assuming a lower threshold is less conservative and yields a greater risk. Setting the threshold to a value $t_{f,2}$ is therefore more conservative than selecting a lower $t_{f,1}$ threshold.

In reality, setting an appropriate threshold will require a case-by-case study, should be defined uniquely for different critical parts [42] and taking several factors into account. Some considerations for threshold selection are:

- Estimated transport and bearing replacement time including onshore and offshore logistics;

- Estimated fault severity and/or possibility of further damage to other drivetrain components;

- Distance-to-shore from port to the offshore wind farm, including accessibility study to offshore site and seasonal weather windows;

- Ease of access to appropriate vessels for ferrying components and enabling repair;

- Availability of spare parts or ease to purchase necessary replacements;

- Uncertainties in the RUL model;

For simplicity, this work will assume two distinct thresholds, a first threshold $t_{\mathrm{f},1} = 64$ days and a second more conservative threshold value $t_{\mathrm{f},2} = 128$ days.

The evolution of the bearings RUL for increasing damage is shown in Figure 49, Figure 50 and Figure 51 for *LC1* , *LC2* and *LC3*, respectively. Note that in these figures only the behaviour of the non-damaged bearings are shown. Hence, for *LC1* and *LC2* which replicate a damage in bearing **INP-A**, only the variation in RUL for **INP-B**, **HS-A** and **HS-B** is shown. Similarly, for *LC3* which considers a damage occurring at **HS-B** bearing, the RUL is shown for **HS-A**, **INP-A** and **INP-B**.

The reason behind this was explained previously. According to the established procedure to model damage by decreasing the stiffness of the bearing where damage is assumed, a disproportionate increase of this bearing's lifetime occurs which is unrealistic and non-physical. Therefore, the lifetime of the bearings where the actual simulated damage originates is not considered in Figure 49, Figure 50 and Figure 51.

Figure 49 shows the evolution of the RUL for the three remaining bearings for increasing damage intensity of *LC1*. The behaviour is in accordance with the tabulated χ_i values in Table 17. An axial damage occurring in the MS does not induce a significant decrease in bearing lifetime for any of the considered bearings. In fact, the most conservative failure threshold $t_{\mathrm{f},2} = 128$ days is not breached by any of the bearings even when damage is most severe. This means that for the axial damage occurring at MS bearing **INP-A**, no predictable failure will occur on any of the bearings according to the physics-based model.

The load case *LC2* which replicates a radial damage on the up-wind MS bearing was previously seen to have a large impact on the entire drivetrain. This becomes evident
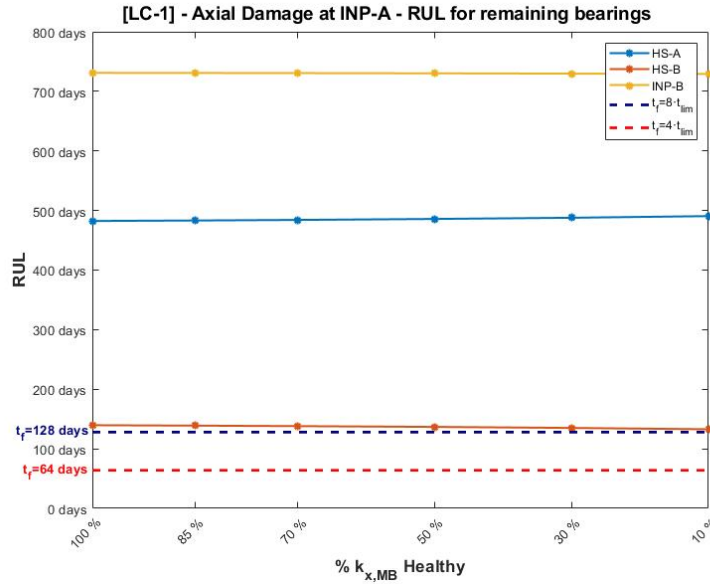
Figure 49: Evolution of RUL of bearings **INP-B**, **HS-A** and **HS-B** for increasing axial damage at **INP-B** ($LC1$)

from Figure 50 which shows that all three bearings will experiment a decrease in their expected lifetime. The down-wind MS bearing **INP-B** experiences a severe depletion of lifetime. The lifetime of this bearing plummets from 731.04 days when healthy according to Figure 50 and the value in Table 20 to just over 70 days when bearing stiffness reaches $0.10 \cdot K_r^{\text{INP-A}}$. This corresponds to a decrease of lifetime of 90.31% as given by the corresponding χ_i factor in Table 18.

The decline of lifetime is also remarkable for **HS-A** which decreases from 482.4 days to approximately 35 days for a damage corresponding to $0.10 \cdot K_r^{\text{INP-A}}$ In fact, the lifetime of **HS-A** drops below both threshold values $t_{f,1}$ and $t_{f,2}$ during the last damage branch $[0.30 - 0.10] \cdot K_r^{\text{INP-A}}$.

It is interesting to note from Figure 50 that at early damage stage, the HSS bearing on the generator side (**HS-B**) is relatively unaffected by the increasing radial damage propagating from the MS. However, as the up-wind HSS bearing **HS-A** lifetime collapses the down-wind HSS bearing begins to deteriorate until it effectively crosses the most conservative failure threshold $t_{f,2}$ when damage exceeds $0.30 \cdot K_r^{\text{INP-A}}$.

These results are equivalent to the non-dimensional χ_i factor summarized in Table 18 which reflected a decrease of lifetime of -92.66% for **HS-A**, -90.31% for **INP-B** and -42.43% for **HS-B**.
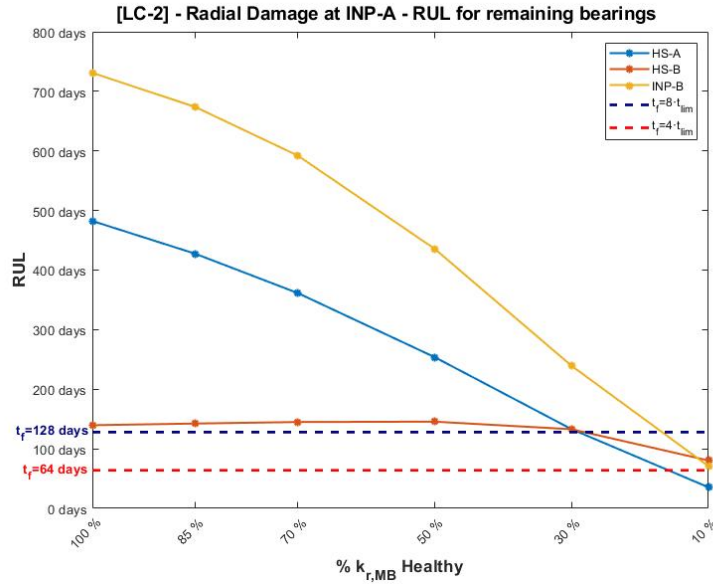
Figure 50: Evolution of RUL of bearings **INP-B**, **HS-A** and **HS-B** for increasing radial damage at **INP-B** (*LC2*)

Hence, according to the physics-based model, all three bearings **INP-B**, **HS-A** and **HS-B** are predicted to fail for a radial damage originating at the MS. The most severe failure is that of **HS-A** since it plunges below the threshold $t_{f,2} = 128$ days and shortly after below $t_{f,1} = 64$ days. The other two bearings, **INP-B** and **HS-B** also fail according to the model as they breach $t_{f,2} = 128$ days, although only predicted failure is according to the more conservative failure threshold.

Bearing lifetime results corresponding to *LC3* are provided graphically in Figure 51. In this load cases, a radial damage originating in the HSS down-wind bearing **HS-B** leads to a failure of the up-wind HSS bearing **HS-B**. Bearings of the MS seem to be unaffected by this damage load case and their expected lifetime is in fact seen to increase compared to the no-damage situation by 1.89% for **INP-A** and 3.55% for **INP-B** according to the tabulated values of χ_i presented in Table 19. Hence, according to the physics model, only **HS-A** deteriorates and precipitates to failure. From the results in Figure 51 the lifetime of this bearing breaches only the most conservative of the two thresholds: $t_{f,2} = 128$ days. However, it is crucial to note that for the most severe damage case corresponding to $0.10 \cdot K_r^{HS-B}$ the predicted lifetime of **HS-A** is approximately 80 days, hence very close to the critical failure threshold $t_{f,1} = 64$ days.

The above failure results for *LC2*, *LC3* and *LC1* according to the implemented physics-
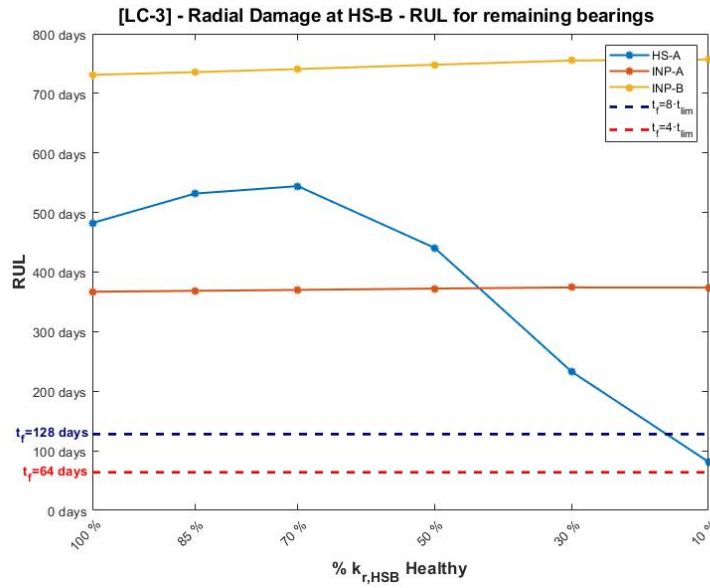
Figure 51: Evolution of RUL of bearings **INP-A**, **INP-B** and **HS-A** for increasing radial damage at **HS-B** (*LC3*)

based model are summarized in Table 21.

	HS-A	HS-B	INP-A	INP-B
LC1	No failure	No failure		No failure
LC2	Severe Failure	Failure		Severe Failure
LC3	Failure		No failure	No failure

Table 21: Failed bearings according to physics-based model.
Failure (=RUL $< t_{\mathbf{f,2}} = 128$ days) and **Severe Failure (=RUL $< t_{\mathbf{f,1}} = 64$ days)**

The final step is to find the actual RUL (in days) for each of the bearings that fails according to the physics prognostics model. That can be obtained from geometry by finding the intersection between the failure thresholds $t_{\mathrm{f},1}$ and $t_{\mathrm{f},2}$ and the corresponding RUL curve.

Figure 52 shows the evolution of RUL of **INP-B**, **HS-A** and **HS-B** for increasing radial damage at **INP-A** corresponding to *LC2*. The x-axis shows the RUL in days and the y-axis shows the time the bearing has been operating (in days). The maximum value in the y-axis corresponds to the maximum operational time without failure which will naturally corresponds to $L_{10,\mathrm{i}=0}$, the expected lifetime of the bearing of the no-damage situation ($i = 0$). The maximum values of lifetime for all bearings are given in Table 20.

Each line represents the bearing RUL for a specific damage intensity. The dark blue

line corresponds to the RUL baseline case. According to the healthy bearing lifetime values provided in Table 20, when the drivetrain is healthy, bearing **HS-A** has a lifetime of 482.41 days which means the predicted RUL is $\mathrm{RUL}_{\mathrm{healthy}}^{\mathrm{HS-A}} = L_{10,\mathrm{i}=0} = 482.41$ days. Similarly, $\mathrm{RUL}_{\mathrm{healthy}}^{\mathrm{HS-B}} = 139.62$ days and $\mathrm{RUL}_{\mathrm{healthy}}^{\mathrm{INP-B}} = 731.04$ days. Hence, the RUL curve corresponding to Baseline in Figure 52 shown in dark blue is a decreasing line which will always have a slope -1.

Figure 52a and Figure 52b show the predicted RUL of several bearings for *LC2* corresponding to failure thresholds $t_{\mathrm{f},2} = 128$ days and $t_{\mathrm{f},1} = 64$ days, respectively.
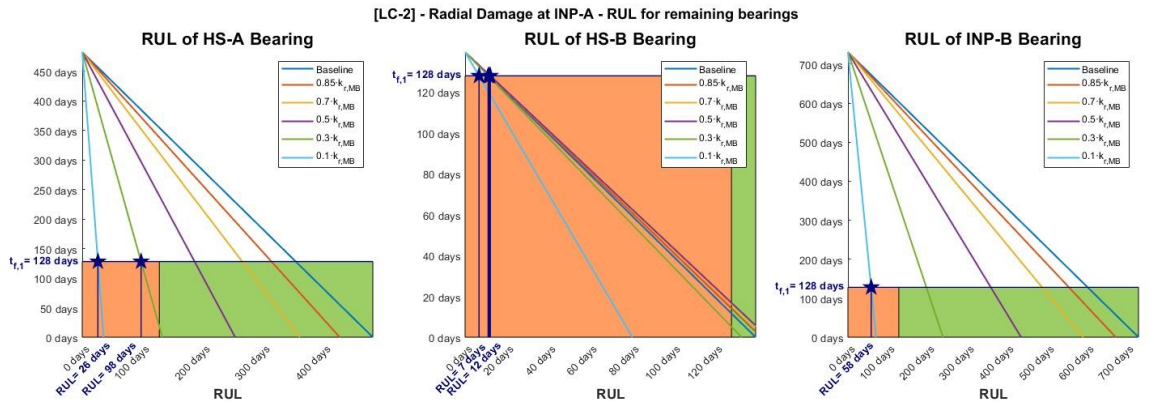
(a) Predicted RUL of **INB-B** for $t_{\mathrm{f},2} = 128$ days
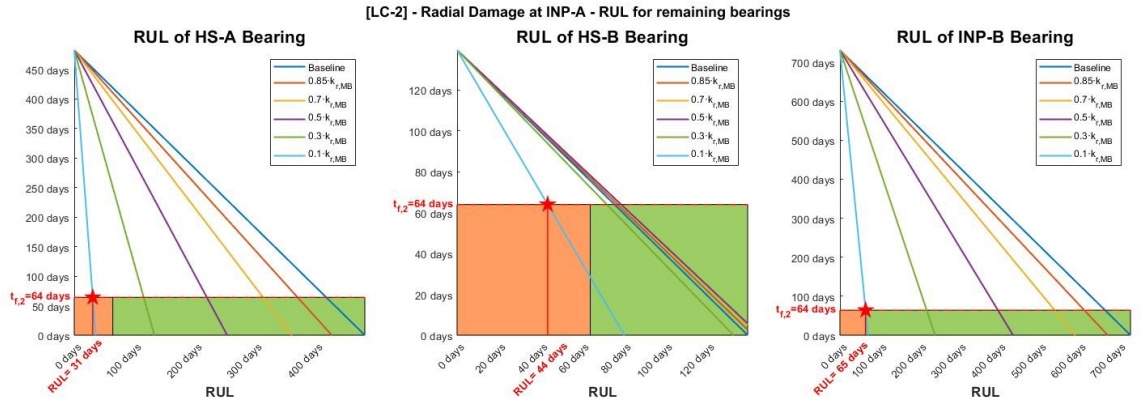
(b) Predicted RUL of **INP-B** for $t_{\mathrm{f},1} = 64$ days

Figure 52: Predicted RUL of **INP-B**, **HS-A** and **HS-B** according to physics-based model for both failure thresholds for load case *LC2*

Figure 52a shows that the conservative failure threshold $t_{\mathrm{f},2}$ is breached for all bearings. It is reached for bearing **HS-A** for two consecutive damage cases and first hits the threshold for the damage case corresponding to $K = 0.30 \cdot K_{\mathrm{r}}^{\mathrm{INP-A}}$. Similarly, Figure 52b shows that **HS-A** crosses the critical failure threshold $t_{\mathrm{f},1} = 64$ but only when damage increases to $K = 0.10 \cdot K_{\mathrm{r}}^{\mathrm{INP-A}}$ critical.

Hence, the RUL of bearing **HS-A** is:

$$\text{RUL}^{\text{HS-A}}\left(t_{\text{f},2} = 128 \text{ days}\right) = 98 \text{ days} \qquad \text{RUL}^{\text{HS-A}}\left(t_{\text{f},1} = 64 \text{ days}\right) = 31 \text{ days}$$

For **INP-B**, by looking at Figure 52a we find the RUL corresponding threshold $t_{\text{f},1}$ and Figure 52b gives the RUL corresponding to $t_{\text{f},2}$. Graphically, these correspond to:

$$\text{RUL}^{\text{INP-B}}\left(t_{\text{f},2} = 128 \text{ days}\right) = 58 \text{ days} \qquad \text{RUL}^{\text{INP-B}}\left(t_{\text{f},1} = 64 \text{ days}\right) = 65 \text{ days}$$

Notice that according to the physics-based RUL model, the bearing **INP-B** is very close to failure if failure is assumed at $t_{\text{f},1}$ since $\text{RUL}^{\text{INP-B}}\left(t_{\text{f},1} = 64 \text{ days}\right) \approx 64$ days.

Notice that the predicted RUL for **HS-B** yields almost immediate failure according to the selected threshold values. The reason being that the healthy lifetime of **HS-B** is approximately 140 days, significantly lower than the other two. This strongly implies that the selected threshold values are an inappropriate choice to evaluate the health of this bearing. This further enforces the idea that the threshold must be defined uniquely for different critical parts.

$$\text{RUL}^{\text{INP-B}}\left(t_{\text{f},2} = 128 \text{ days}\right) = 58 \text{ days} \qquad \text{RUL}^{\text{INP-B}}\left(t_{\text{f},1} = 64 \text{ days}\right) = 65 \text{ days}$$

Figure 53 shows the evolution of the RUL of several bearings for LC3 evaluated at the conservative threshold $t_{\text{f},2}$ for Figure 53a and at the critical threshold $t_{\text{f},1}$ for Figure 53b. According to the physics-based model, *LC3* only leads to noticeable damage on the the up-wind HSS bearing HS-A which is readily seen from Figure 53a that illustrates that only this bearing's lifetime crosses the threshold $t_{\text{f},2}$. The remaining bearings of the MS, **INP-A** and **INP-B** experience no variation in their lifetime which explains why the RUL of these bearings for different damage intensities are all superposed and collapse in a single line approximately equal to the curve corresponding to baseline-healthy conditions, with a slope -1. Hence, for *LC3* we only have potential failure in bearing **HS-A** and the corresponding RUL values at the two thresholds are:

$$\text{RUL}^{\text{HS-A}}\left(t_{\text{f},2} = 128 \text{ days}\right) = 60 \text{ days} \qquad \text{RUL}^{\text{HS-A}}\left(t_{\text{f},1} = 64 \text{ days}\right) = 71 \text{ days}$$

From Figure 53b it is clear that the bearing **HS-A** almost crosses the critical threshold $t_{f,1}$ but remains within the theoretical acceptable RUL. According to the physics-based model this bearing can be expected to fail when the radial stiffness K_r of bearing **HS-B** approaches to $K_r = 0.10 \cdot K_r^{\text{HS-B}}$
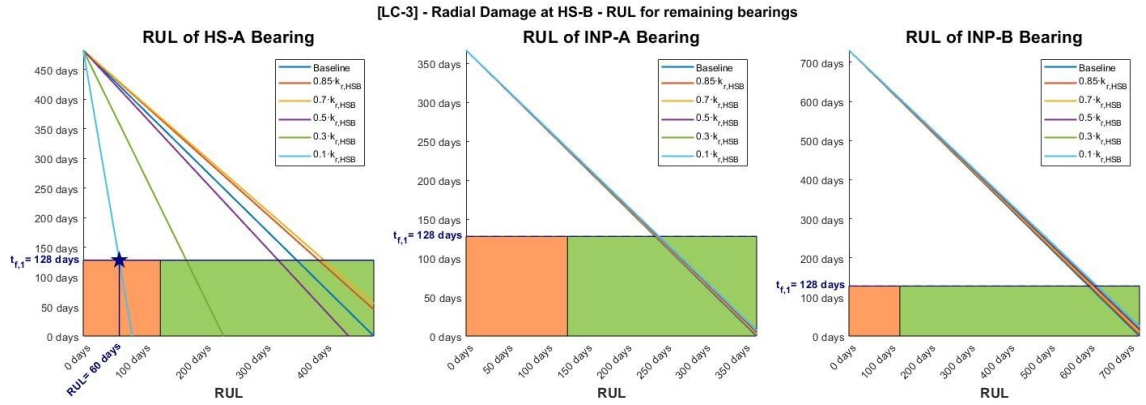
(a) Predicted RULs for $t_{f,2} = 128$ days
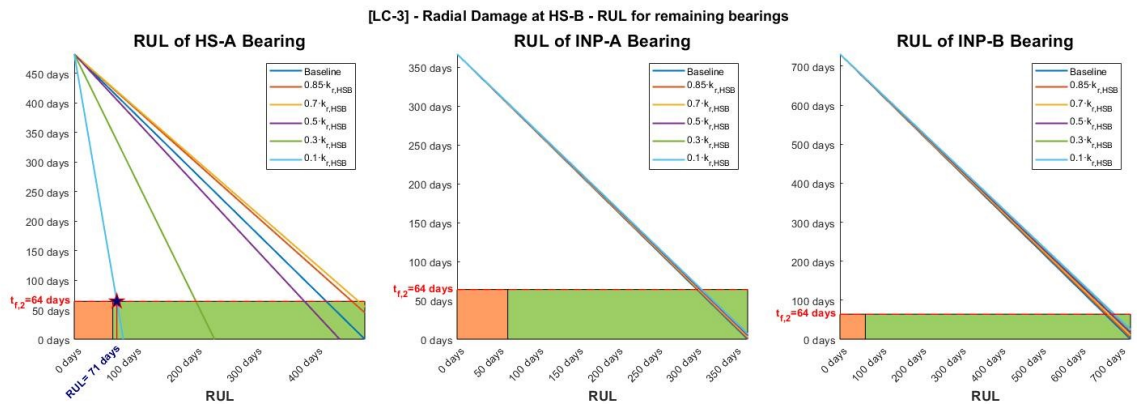
(b) Predicted RULs for $t_{f,1} = 64$ days

Figure 53: Predicted RUL of **HS-A**, **INP-A** and **INP-B** according to physics-based model for both failure thresholds for load case *LC3*

The axial damage occurring at the MS bearing **INP-A** was previously seen to have a mild effect in terms of redistribution of loads withing the drivetrain. This resulted in practically no impact on the RUL of the remaining bearings. According to the results presented in Table 21 and shown in Figure 54, the physics-based model does not reflect any significant influence of axial MS damage on the remaining bearings considered in this work.
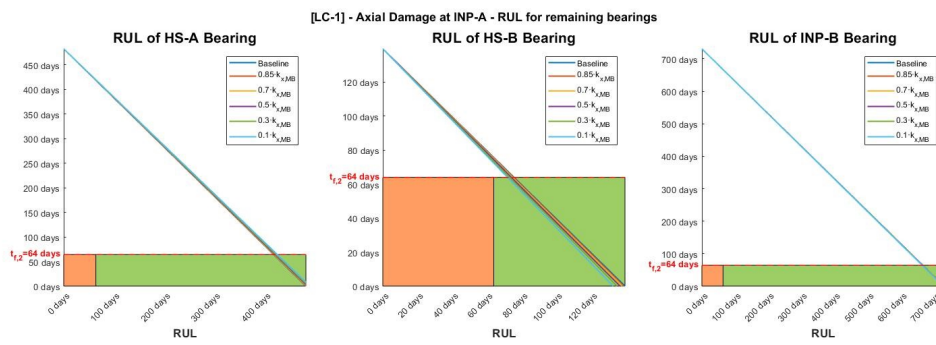
Figure 54: Predicted RUL of **INP-B**, **HS-A** and **HS-B** according to physics-based model for $t_{\mathrm{f},2} = 64$ days for load case *LC1*

Chapter 6

Data-driven Approach

6.1   Introduction to Data-driven method

Despite the lack of run-to-failure data, this section will discuss a data-driven approach based solely on degradation data obtained from simulations.

The design load cases have been introduced in section 2.3 and analyzed in the time domain in section 4.1 and in the frequency domain in section 4.2. Since these load cases replicate different types of faults at different locations of the drivetrain it should come as no surprise that different approaches to RUL estimation will need to be put forward concerning for different types of faults occurring at different locations. The primary difference is perhaps that *LC1* and *LC2* reproduce faults in the Main Bearing located on the Main Shaft whereas *LC3* replicates a fault on a bearing located on the high-speed shaft. Since the rotational speed of the high-speed shaft bearing is higher by a factor of 50 than the rotational speed experienced by the bearings at the Main Shaft it is very likely that the RUL estimation at these distinct locations will require a different approach.

In the first part of this section the first steps to enable a data-driven approach will be presented with a general procedure to extract k potential degradation indicators. Since not all the potential indicators will provide useful information on the degradation process a methodology will be presented in order to identify and select those indicators which are deemed suitable to track the degradation process. A number k of potential indicators will be narrowed down to chose only n high-quality indicators which display a consistent and predictable behaviour as fault severity increases. Naturally, $n < k$.

Once a set of n reliable degradation indicators has been selected, a dimension reduction based on Principal Component Analysis (PCA) will be performed. The goal of dimension reduction is to effectively merge n suitable indicators into a single improved indicator. This improved indicator will be constructed as an optimal combination of n indicators and will be referred to Health Indicator (H.I). Ideally Health Indicators will be obtained for all 4 bearings under study, **INP-A** and **INP-B** supporting the MS and **HS-A** and **HS-B** supporting the HSS. Furthermore, the same bearing may have more than one associated indicator depending on the considered fault. For instance, H.I$_{HS-B}^{LC1}$ and H.I$_{HS-B}^{LC3}$ are 2 different Health Indicators that track damage on the HSS bearing **HS-B** but for two different types of damages, H.I$_{HS-B}^{LC1}$ will be used to track the damage due to a decrease in axial stiffness originating in the main shaft (see definition of $LC1$) whereas H.I$_{HS-B}^{LC3}$ will be used to monitor the damage at **HS-B** caused by a decrease of bearing radial stiffness at the HSS (see definition of $LC3$).

The ability to construct health indicators associated to each bearing for all three LCs will be investigated. The merits and limitations of using health indicators to estimate the different types of damage associated to $LC1$, $LC2$ and $LC3$ will be evaluated. If necessary, some specific recommendations will ensue for the prognosis of each load case in terms of its potential to be eligible for a purely data-driven approach.

In the second part of this section the methodology will be refined for each load case in order to improve the prediction capabilities for each specific type of damage.

6.2 Feature extraction

Condition indicators, also known as simply indicators or features are a series of values extracted from the time-varying acceleration signals. The first 100 s of all acceleration signals have been discarded in order to bypass transient effects. De-noising the signal .... has not been necessary.

Abundant references in literature provide an extensive list of potential features that can prove useful when tracking the damage process from vibration signals. Tracking the damage process means a feature capable of representing the trends related to the degradation from normal to failure conditions. A suitable and sensitive feature extraction method to identify potential indicators is highly valuable both for bearing fault diagnosis and prediction.

Broadly speaking, methods used in this work to extract potential features for vibration signals fall under one of the following three categories:

- extraction of time-domain features, particularly statistical properties of the signal;

- extraction of frequency-domain features such as spectral quantities and characteristic fault frequencies;

- Non-dimensional features;

Among these categories, the time-domain features are found to be the most dominant feature extraction method for rolling element bearings.

6.2.1 Statistical Features

Each mechanical failure has an associated "signature" that can be found in the frequency or time domain representations of vibration signals.

Root Mean Square (RMS)

The root mean square (RMS) value describes the energy content of a vibration signal. This can be readily seen by comparing the RMS value of the velocity vibration signal v_{rms} Equation 6.1 to the definition of kinetic energy E_K, seen in Equation 6.2.

$$v_{\mathrm{rms}} = \sqrt{\frac{1}{T} \int_T v^2(t)\mathrm{d}t} \tag{6.1}$$

$$E_K = \frac{1}{2}mv^2(t) \tag{6.2}$$

In Equation 6.1 T is the integration time and $v(t)$ is the velocity and m is the weight of the moving object in Equation 6.2. From the above, it is clear that the RMS value reflects the energy content in a given the signal.

Today, more often than not, digital signals are used and the RMS calculation for a discrete signal is obtained according to Equation 6.3. For a vibration signal of sample size N, the

RMS value is calculated according to:

$$\text{RMS} = \sqrt{\frac{1}{N}\sum_{i=1}^{N} x_i^2} \tag{6.3}$$

Where x_i is the i-th sample vibration amplitude.

The RMS value is a weak method to detect a failure at its early stage because of the relatively small energy generated by an incipient defect which results in a small difference in the RMS value. Despite that RMS is not a very sensitive indicator for incipient faults it does capture the general fault progression as severity increases. Hence, RMS is a capable indicator to describe the overall increase of the vibration energy as the fault progresses.

RMS is one of the most common used statistical parameter that describe the change in the dynamic of the machine [9]. When used as a prediction indicator, an approach that is receiving increasing attention in literature is to extrapolate the trajectory of RMS values for RUL prediction.

Variance and standard deviation

The variance, typically denoted as σ^2, measures the dispersion of a signal around its reference mean value. The standard deviation is simply the square root of the variance.

$$Var = \sigma^2 = \frac{\sum_{i=1}^{N}(x_i - \mu)^2}{N} \tag{6.4}$$

$$Std = \sigma = \sqrt{\frac{\sum_{i=1}^{N}(x_i - \mu)^2}{N}} \tag{6.5}$$

Kurtosis

Kurtosis refers to the fourth statistical moment of a given signal and describes the shape of the amplitude distribution of the signal. Specifically, Kurtosis describes how peaked or flat a distribution or the histogram of a vibration signal is.

A kurtosis value close to 3 indicates a Gaussian-like signal. A kurtosis value smaller than 3 indicates vibration signals with relatively flat peaks whereas a kurtosis greater than 3 is typical in Signals with sharp peaks. It is generally accepted that the kurtosis value of a

vibration signal from a healthy bearing is approximately three and the skewness value is approximately zero.

The Kurtosis of a random signal with N number of samples and a mean sample amplitude μ is computed as:

$$KU = \frac{\frac{1}{N} \sum_{i=1}^{N} (xi - \mu)^4}{\left[\frac{1}{N} \sum_{i=1}^{N} (xi - \mu)^2 \right]^2} \tag{6.6}$$

Where x_i is the i-th sample amplitude.

In some vibration signals the presence of background noise and other vibration sources may hide changes in the kurtosis and undermine the detection of bearing faults. To address this issue instead of computing the kurtosis of the overall signal it may be beneficial to obtain the kurtosis values across different frequency bands [9].

Skewness

Skewness describes how symmetric the probability density function (PDF) of a vibration amplitude signal is. If the PDF is shifted to the left or to the right, it is said to be skewed. On the other hand, a time series with a similar number of large and small amplitude values will have a skewness closer to zero. Accordingly, skewness provides a measure of the size of the tails of a distribution.

$$\text{Sk} = \frac{\sum_{i=1}^{N} (x_i - m)^3}{(N-1)\sigma^3} \tag{6.7}$$

Peak to Peak

The Peak to peak value is simply the distance between the maximum amplitude and the minimum amplitude of the signal. Peak to peak is a measurement of spread in the signal

Shape Factor

The Shape factor (SF) is defined as the RMS divided by mean value of a vibration signal.

that is affected by an object's shape but is independent of its dimensions

$$\text{SF} = \frac{\sqrt{\frac{1}{N} \sum_{i=1}^{N} x_i^2}}{\frac{1}{N} \sum_{i=1}^{N} |x_i|} \tag{6.8}$$

Crest Factor

The Crest factor (CF) quanitfies how much impact occurs throughout a vibration signal. It is commonly taken as the ratio of the maximum (or minimum) value of the signal to the RMS level and is obtained according to Equation 6.9. Alternative definitions exist which consider the numerator as the mean of the maximum and minimum of the signal instead.

$$\text{CF} = \frac{\max |x_i|}{\sqrt{\frac{1}{N} \sum_{i=1}^{N} x_i^2}} \tag{6.9}$$

The CF value is normally between 2 to 6 with values over 6 indicating possible component failure. This parameter has proved to successfully indicate damage at an early stage, particularly for faults related to gears. This is because the CF feature is useful to detect changes in the signal pattern caused by impulsive vibration sources such as a gear tooth fracture.

Impulse Factor

The Impulse factor (IF) can be used to track how much impact occurs in the vibration signal due to a defect such as that which originates at a faulty bearing. This feature is similar to the CF. However, whereas the CF measures the impact by dividing the maximum absolute value of vibration signal and RMS value (seen in Equation 6.9), the IF divides the maximum absolute value by the mean of the absolute value instead as seen in Equation 6.10.

$$\text{IF} = \frac{\max |x_i|}{\frac{1}{N} \sum_{i=1}^{N} |x_i|} \tag{6.10}$$

Margin Factor

The Margin factor (MF), similarly to the CF and IF values, also measures the level of impact between rolling element and raceway. The MF is obtained as the ratio of the maximum absolute value of the vibration signal to the RMS of the absolute value of the vibration signal.

$$\text{MF} = \frac{\max |x_i|}{\left(\frac{1}{N} \sum_{i=1}^{N} \sqrt{|x_i|}\right)^2} \tag{6.11}$$

The above statistical time-domain features are extensively used in condition-monitoring of WT vibration signals. Additionally, statistical features can also be used to describe and evaluate the quality of the result of a specific algorithm to analyze vibration signal analysis.

6.2.2   Frequency-domain Features

The frequency domain features make use of properties obtained from the vibration data based on frequency. This field of mathematics is also commonly referred as spectral analysis.

The most well-known spectral analysis tools are those based on the discrete Fourier transform (DFT) which have consolidated thanks to the fast Fourier transform (FFT) algorithm which significantly speeds up calculations.

Spectral Skewness & Spectral Kurtosis

The work of Antoni and Randall [43] demonstrated the high potential of using advanced statistical measures in the vibration-based condition monitoring of rotating machine to efficiently detect faults. Specifically, Randall *et. al.* proposed the use of spectral skewness (SS) and spectral kurtosis (SK) to detect faults. These features were found to be robust even in the presence of noise. Furthermore, SS and SK yielded good results for non-stationary signals.

The SS measures the symmetry of the distribution of the spectral magnitude values around its mean [44].

$$\text{SS}(n) = \frac{2 \sum_{k=0}^{B_L/2-1} \left(|X(k,n)| - \mu_{|X|}\right)^3}{B_L \cdot \sigma_{|X|}^3} \tag{6.12}$$

The SK feature measures the distribution of the spectral magnitude values and compare these values with a Gaussian distribution. Furthermore, the SK is an powerful tool to locate the frequency bands with a high amount of impulsiveness. It is defined as;

$$\text{SK}(n) = \frac{2\sum_{k=0}^{\text{B}_L/2-1} \left(|X(k,n)| - \mu_{|X|}\right)^4}{\text{B}_L \cdot \sigma_{|X|}^4} - 3 \tag{6.13}$$

SK has shown good results to detect incipient faults even when a relatively high amount of noise is present in the signal. This is made possible by the fact that SK analyzes the entire frequency band and selects the sensitive frequency band correspond to the bearings' characteristics frequencies [44].

6.3   Feature Selection

Once a number of potential features has been computed the so-called feature selection phase can begin. Feature selection essentially means evaluating all the candidate features mentioned above and searching for the those that are appropriate for RUL prediction. Identifying one or several suitable indicators greatly simplifies the degradation assessment and prognostics task.

A suitable indicator is a certain feature that effectively reflects a degradation pattern by consistently increasing or decreasing as damage progresses. Since the bearing fault degradation is considered to be an irreversible process [9] some features can be expected to increase/decrease persistently.

The present section focuses on establishing a methodology to evaluate feature performance. First, several metrics used to quantify the prognostics capability of a given indicator are presented. In this thesis 2 metrics known as *monotonicity*, and *trendability* are used. Once the technique to measure the performance of features has been introduced the following step is to apply the performance algorithms on all the features. Feature performance will be examined for all acceleration signals, namely the accelerations and the rotational accelerations in the MS and the HSS. This will be carried out for the accelerations and rotational accelerations obtained from all thee LCs.

6.3.1   Feature Performance metrics

Monotonicity

Monotonicity is the metric that describes the positive or negative trend of an indicator. This is an important metric since a degradation process involves a certain degree of accumulation which can be tracked.

The monotonicity performance metric will be appointed a score between 0 and 1. A monotonicity value equal to one means that the feature is perfectly monotonic. In practice, a monotonicity close to unity, for instance higher than 0.6, will imply that a given feature may be a reasonable choice for RUL prediction. On the contrary, a low monotonicity value, for instance lower than 0.4, indicates that a feature is non-monotonic and a poor choice to describe and track the damage process.

Mathematically, the monotonicity of a data-series can be expressed as the average difference between the positive and negative derivatives for each time sequence. In other words, if the curve never reverses direction it can be said to be monotonic. This is equivalent to the derivative of the transfer function never changing sign. It can be calculated according to Equation 6.14.

$$\text{Monotonicity} = \text{mean}\left(\left|\frac{\#\text{pos}\frac{d}{dx} - \#\text{neg}\frac{d}{dx}}{n-1}\right|\right) \tag{6.14}$$

Where $\#\text{pos}\frac{d}{dx}$ and $\#\text{neg}\frac{d}{dx}$ are the number of positive derivatives and negatives derivatives respectively. Here $n = 6$ is the number of measurements since 6 different time series of 6 distinct damage intensities are considered, one baseline case with no damage and 5 faulty cases.

Trendability

Trendability quantifies the degree to which a given indicator has the same fundamental shape and can be described by using a similar function form [9]. Hence, a feature is considered trendable if all the parameters can be modelled by the same function. Trendability essentially measures the similarity between the trajectories of a feature for different time intervals. A more trendable feature displays trajectories with the same underlying shape.

Mathematically, trendability is determined by the minimum absolute correlation calculated among all the con

$$\text{trendability} \ = \min_{j,k} |\text{corr}\,(x_j, x_k)|\,, \quad j, k = 1, \dots, M \qquad (6.15)$$

where x_j represents the vector of measurements of a feature on the j-th system and the variable M is the number of machines considered. Since data is only available for one drivetrain, monotonicity will be used to compare a feature in different time instances.

Similarly to monotonicity, the trendability metric will have a value of 1 if a given feature is perfectly trendable and a value of 0 if it is non-trendable.

6.3.2 Results from feature selection

The feature performance metrics that will be used now been introduced. Now, based on these metrics, feature selection may be carried out by applying the feature performance algorithms.

For illustration purposes, Figure 55 shows the evolution for increasing fault severity of 15 potential features extracted from two acceleration signals, accelerations $\ddot{y}$ measured at the MS and at the HSS. Figure 55a shows these features at the MS and Figure 55b shows the same features but for the HSS. From Figure 55a it can be clearly seen that the RMS, the standard deviation Std, $Peak2Peak$ and $Energy$ are high quality features that display an persistent increasing trend as the damage progresses which makes them good indicators which can be predicted. On the other hand, notice that the $Kurtosis$, $ShapeFactor$ or $SpectralKurtosis$ values to name a few do not behave in a predictable manner for increasing damage severity. The latter are therefore not suitable indicators and should be discarded in the feature selection phase. Now, by observing Figure 55b it is interesting to note that for the same load case $LC2$ and for acceleration along the y direction $\ddot{y}$ in the HSS a different set of features are predictable. For example, the $ShapeFactor$, that was a considered a poor damage indicator in the MS becomes in fact a reasonably good indicator for the HSS.

The underlying idea that must be derived from Figure 55 is that feature selection for each

acceleration signal at either the MS or the HSS needs to be done on one-by-one basis since each signal is likely to present a different number of suitable features and the suitable features may differ significantly.
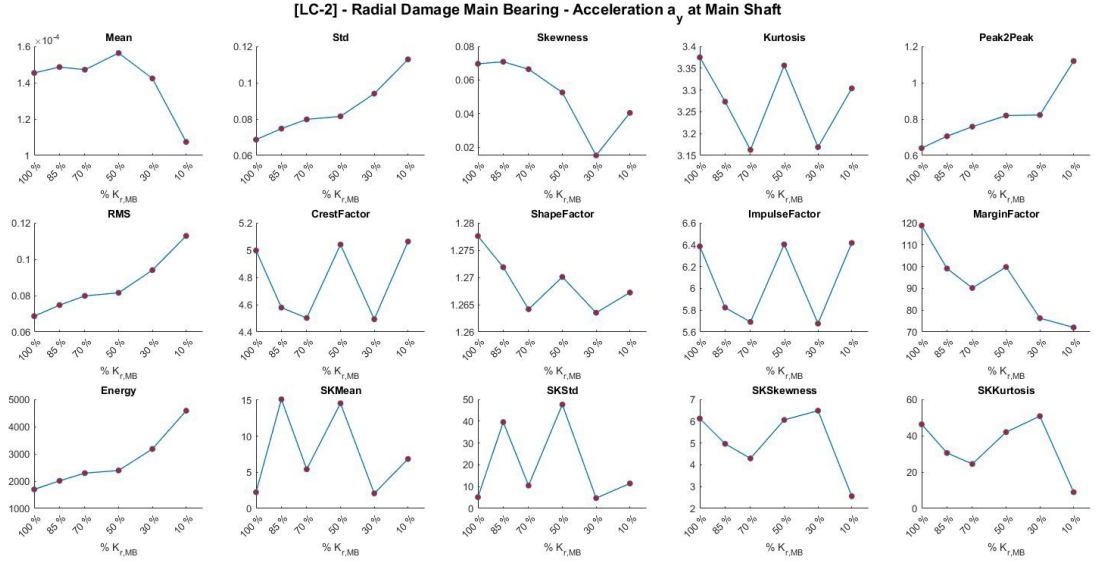
(a) Evolution of statistical and spectral features of the acceleration y at the MS for decreasing radial stiffness of MS bearing
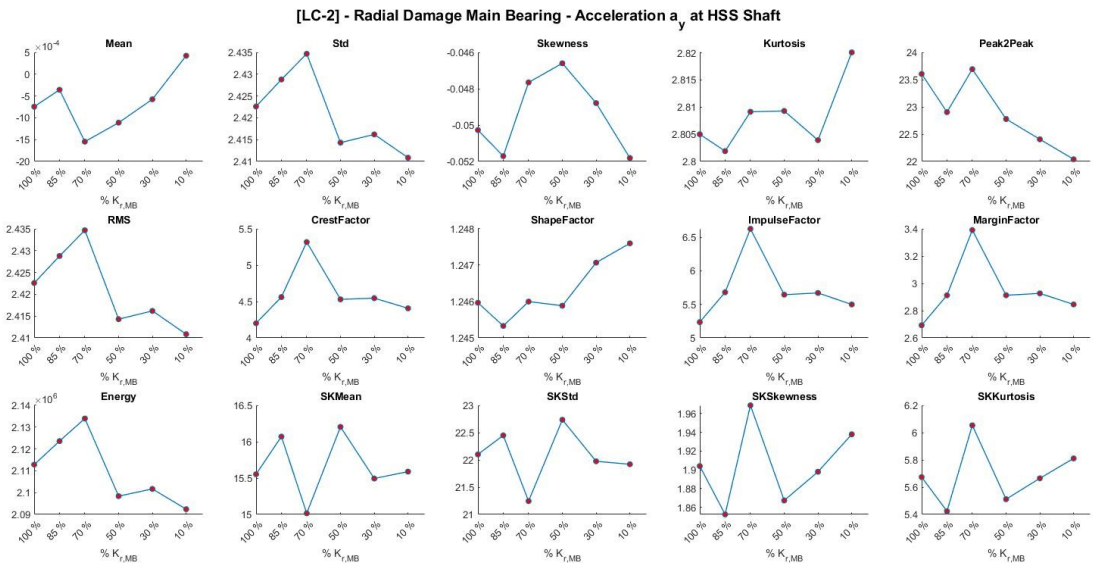
(b) Evolution of statistical and spectral features of the acceleration in y at the HSS for decreasing radial stiffness of MS bearing

Figure 55: Features of the acceleration in y at the MS and HSS for load case $LC2$

Figure 56 shows the result of the application of the feature performance metric for the same two acceleration signals shown in Figure 55 corresponding to $LC2$. It can be seen that each feature receives a score such that $Monotonicity \in \{0, 1\}$. Features with a high-score

approaching unity are those that behave monotonically and ideal for RUL predictions. By comparing the results in Figure 56 with the evolution of the features for increasing damage Figure 55 it can be clearly seen that only those features that vary in a predictable manner obtain a high result in the monotonic metric. Features in the acceleration $\ddot{y}$ measured at the MS such as Std, $Peak2peak$, RMS and $Energy$ which exhibit a continuous increase as seen in Figure 55a accordingly result in a value of monotonicity of 1 as seen in Figure 56. Similarly, the $MarginFactor$ which gradually decreases but only 4 out of the 5 different damage branches as observed in Figure 55a receives a lower monotonicity score equal to 0.6. The remaining features corresponding to $\ddot{y}$ of the MS do not display any persistent trend and accordingly the feature performance metric ranks low with values of 0.2.
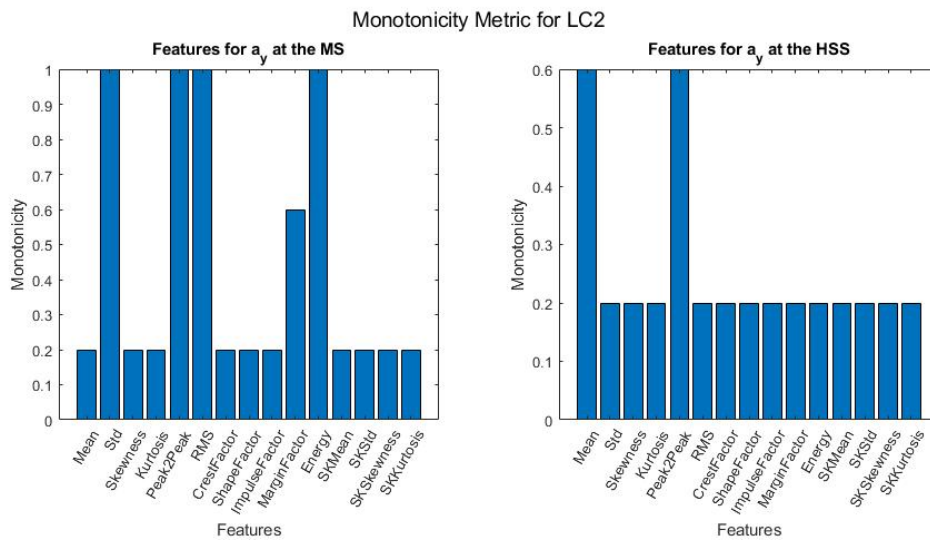
Figure 56: Feature performance for accelerations in y at the MS and HSS for $LC2$

When evaluating the quality of a features two additional important aspects need to be pointed out:

1. How monotonic the evolution of a given feature for increasing damage is. For instance, a feature that continuously increases or decreases as damage intensity increases.

2. How early the feature begins to exhibit a monotonic behaviour. For instance, a feature that begins to display a trend for an early damage of $0.85 \cdot K$ will be more valuable than a feature that behaves monotonically at a later stage for a higher damage.

An example of the second consideration mentioned above can be readily illustrated in Figure 57. Here two different features are shown, *Kurtosis* and *SKKurtosis*, extracted from acceleration $\ddot{z}$ at the HSS for *LC3*. Although both features have a similar shape and increase as damage progresses, the value of *Kurtosis* displays a trend at a very early stage when damage is low and radial bearing stiffness is $85\% \cdot K_r^{\mathrm{HSB}}$. On the other hand, the trend reflecting damage begins at a later stage for *SKKurtosis* which only initiates at damage values beyond $70\% \cdot K_r^{\mathrm{HSB}}$. Hence, for these two features corresponding to HSS vertical accelerations and for *LC3*, *Kurtosis* would provide an earlier indicator of damage which makes it a more suitable indicator in terms of early detection.
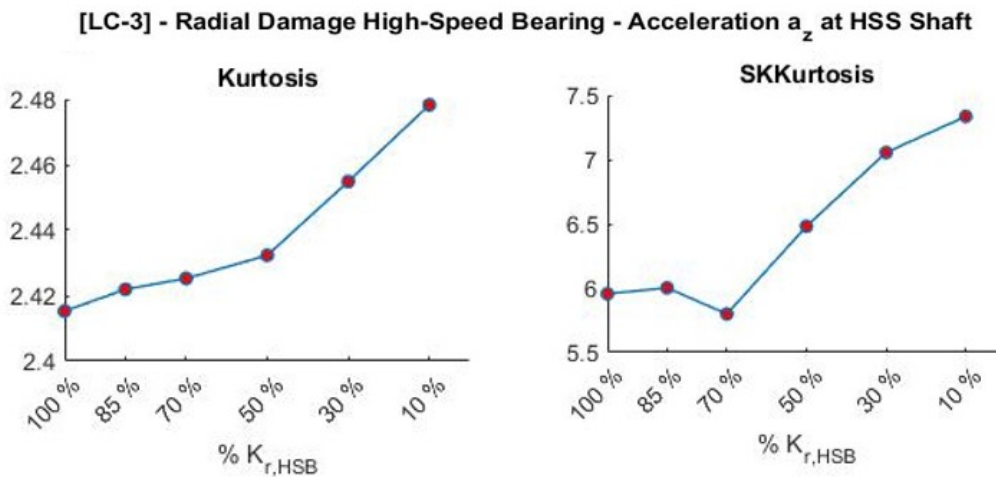
Figure 57: Comparison of 2 features corresponding to accelerations in z at the HSS for *LC3*.

6.3.3 Automated feature selection

As mentioned in the previous section, each acceleration signal is susceptible to present a unique set of suitable features. Feature selection must then be performed on a signal-by-signal basis. Furthermore, some acceleration signals may contain a large number of features that can be used as damage indicators whereas other signals may contain only a reduced number or none at all.

For agility, feature performance evaluation and the subsequent feature selection process has been automated. A routine was coded on Matlab that evaluates the monotonicity algorithm for each feature of all the considered acceleration signals and for all three load cases.

The results of the feature selection phase are shown for LC2 and LC3 in Tables 22. Results corresponding to LC1 are not provided given the very small amount of features that fulfilled the minimal monotonicity requirements. The color scheme used in Tables 22 is defined numerically in Table 23 in terms of monotonicity values.

From these results some meaningful remarks may already be put forth:

- The design load case *LC3* is particularly abundant in the amount of features that display a consistent and predictable evolution as damage progresses;

- The design load case *LC3* can be detected by all 4 of the considered sensors enabling the construction of Health Indicators for both the axial and rotational acceleration, at both the MS and HSS;

The abundance and quality of the features that characterize *LC3* make it a particularly suitable scenario for a purely data-driven approach.

On the other hand, for *LC1* and *LC2* a compromise has to be made in order to enable sufficient features to construct a health indicator and apply a similar data driven method. These two compromises are:

1. Decrease the feature quality requirements such that features with an average score of 0.4 in the monotonicity metric are deemed sufficiently good. This results in a lower overall quality of the H.I.

2. Decrease the range over which monotonicity is evaluated to fewer points. This implies searching for monotonicity at higher damage intensities and when the bearing is approaching failure. This approach undermines the ability to detect a fault at an early stage.

Pre-selection of features according to feature performance metrics such as monotonicity is known to improve the prognosis capabilities. Hence, signals with a wider range of good quality features can be expected to outperform signals characterized by fewer features of good quality .

LC2

	Main Shaft						High-Speed Shaft					
	accel			ang. acc.			accel			ang. acc.		
	x	y	z	x	y	z	x	y	z	x	y	z
'Mean'								P				
'Std'		G			P							
'Skewness'												
'Kurtosis'												
'Peak2Peak'	Y	G	G	G				P				P
'RMS'		G			P							
'CrestFactor'												
'ShapeFactor'										P	P	
'ImpulseFactor'												
'MarginFactor'						P						
'Energy'		G		P								
'SKMean'												
'SKStd'												
'SKSkewness'												
'SKKurtosis'												

LC3

	Main Shaft						High-Speed Shaft					
	accel.			ang. acc.			accel			ang. acc		
	x	y	z	x	y	z	x	y	z	x	y	z
'Mean'												
'Std'	G	G	G	G	G	G		G	G	G	G	G
'Skewness'	G	G		G	G	G		G	G	G	G	G
'Kurtosis'	G	G	G	G	G	G	G			G	G	
'Peak2Peak'	G		G	G		G	G	G	G		G	
'RMS'	G	G	G	G	G		G	G	G	G	G	G
'CrestFactor'	G	G	G	G		G	G	G		G	G	G
'ShapeFactor'	G	G	G	G		G		G	G	G	G	G
'ImpulseFactor'	G	G	G	G	G		G	G		G	G	G
'MarginFactor'	G		G	G	G		G			G	G	
'Energy'	G	G	G	G	G		G	G	G		G	G
'SKMean'	G			G	G		G	G		G	G	G
SKStd'	G		G	G	G		G			G	G	G
'SKSkewness'												G
'SKKurtosis'												

Table 22: Feature selection results for *LC2* (top) and *LC3* (bottom) for translational and angular accelerations atthe MS and at the HSS

Number of features	Monotonicity value
ALL	>0.8
Last 5	>0.8
Last 4	>0.8

Table 23: Color scheme corresponding to the feature performance evaluation criteria according to the monotonicity value

6.3.4 Enhanced approach to feature selection

Feature selection is a key step in narrowing-down the number of features that can be useful for the prognosis task. An enhanced approach to feature selection is presented in this section based on the concept of active power bin, introduced in the standard *IEC 61400-25-6* [13].

Active power bins build on the idea that the measure vibration level and the stress on components of the drivetrain are found to be closely related to the active power production of the WT. A schematic representation of the active power bin concept is illustrated for 5 bins in Figure 58. Specifically, this figure bins the vibration data of the generator Drive End (DE) according to the bin of active power measured at the generator. This concept can be implemented in several different tasks related to drivetrain behaviour analysis. In particular, the standards suggest that active power levels should be used to adapt the monitoring techniques to the specific power generation situation of the WT. Generally speaking, using power as the binning criteria is seen as more reliable than using wind speed due to the strong correlation between power and mechanical vibrations. In practice, active power bins can be implemented to set different individual triggers for each bin as shown in Figure 58 which illustrates individual vibration thresholds for each bin shown in yellow and red. Introducing these individual triggers is convenient to track and compare the evolution of mechanical vibrations over time within a specific bin, which reduces the risk of false alarms. Naturally, it also guarantees that vibration measurements are only recorded when the WT is actually producing power.

The concept of active power bin is deemed useful not only for adaptive condition monitoring but also to enhance the feature extraction and feature selection phases.

As an example Figure 59a shows the implementation of the active bin concept for the ac-
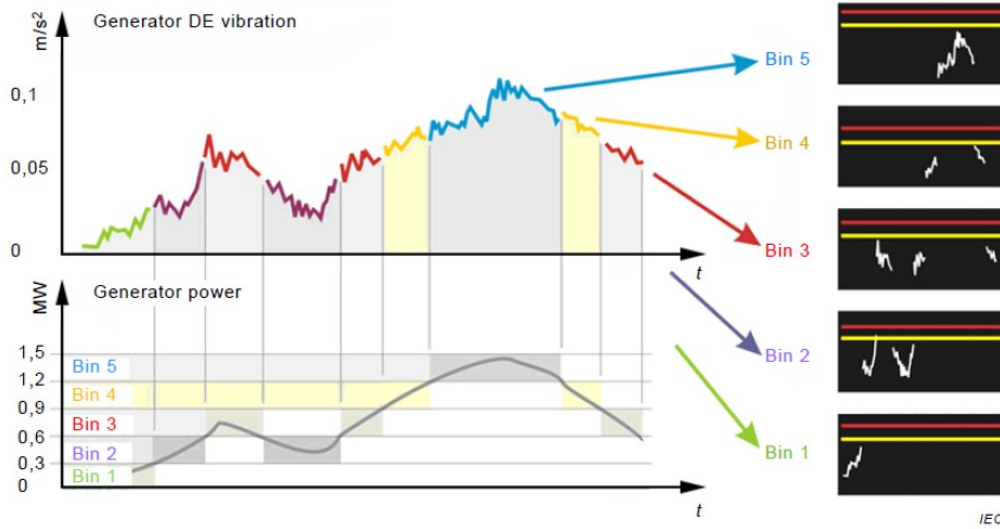
Figure 58: Concept of active power bin as introduced by the standard *IEC 61400-25-6* [13]

celeration signal corresponding to LC1. To implement the power bin concept rather than using the electrical power the mechanical power P_{mech} has been used by considering the mechanical torque T_{gen} in $[N \cdot m]$ and the rotational speed at the generator shaft $\Omega_{gen.}$ in [RPM] according to Equation 6.16. Both $T_{\text{gen}}(t)$ and $\Omega_{gen.}(t)$ are readily available quantities provided by SIMPACK. The average value was used when applying Equation 6.16.

$$P_{\text{mech}} = \Omega_{\text{gen.}} \cdot T_{\text{gen}} \tag{6.16}$$

To the right of Figure 59a the corresponding bin labels are shown. In total, 20 discrete bins of a range $\Delta P = 0.5\ MW$ have been used such that $Bin\ \#1 = [5 - 5.5]$ MW and $Bin\ \#20 = [15 - 15.5]$ MW . Figure 59a illustrates the binning process of the acceleration $\ddot{y}$ measured at the MS and the horizontal lines indicate the upper and lower limits of each bin.

It is interesting to note that each bin contains an uneven number of measurements. Figure 59b shows the histogram of the distribution of the number of measurements that fall into each power bin. The distribution clearly indicates that the greatest share of measurements is located at $Bin\ \#6 = [8 - 8.5]$ MW and the surrounding bins. In fact, a reduced number of bins concentrates well-over 90% of all vibration measurements.

Once the acceleration signal has been binned according to the power bins the same feature
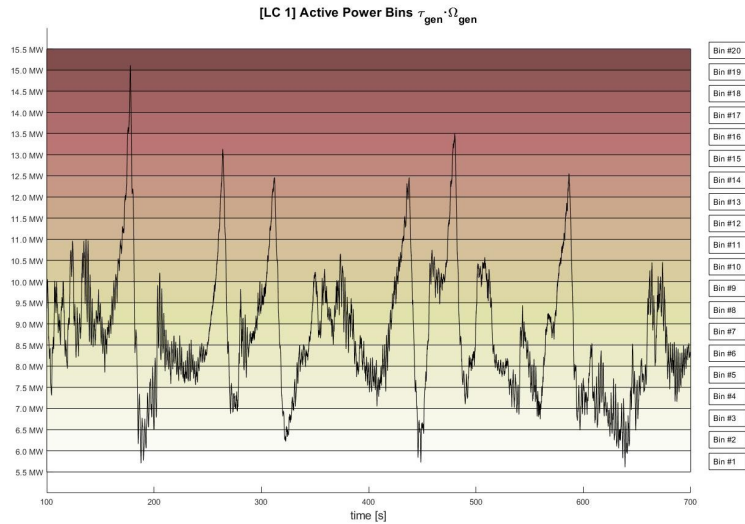
(a) Binning of MS acceleration $\ddot{y}$ using the Active power bin concept using n=20 bins
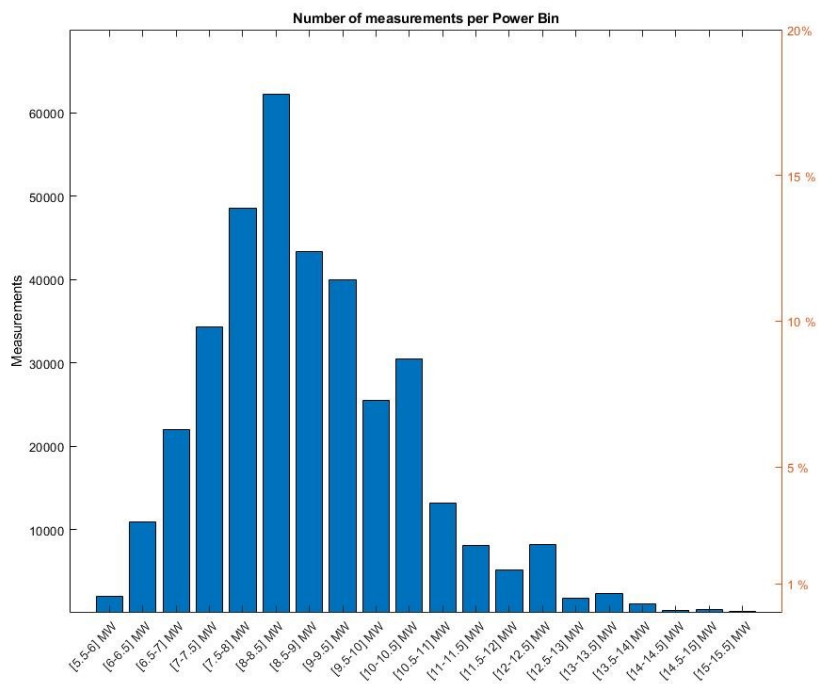
(b) Distribution of the number of measurements for each considered power bin

Figure 59: Features of the acceleration in y at the MS and HSS for load case $LC2$

extraction phase as introduced in section 6.2 is followed. A total of 15 potential features which are a combination of time-domain and frequency-domain statistical properties are computed for the accelerations of each bin. The results of the feature extraction phase combining the power bin concept is shown graphically in Figure 60. Notice from these figures that now rather than computing a unique set of 15 features for the entire acceleration signal 15 features are obtained for each unique power bin.

Figure 60a shows the feature extraction for all the considered power bins $n = 20$. For clarity, Figure 60b shows the same feature extraction but only for the most populous bins according to uneven distribution of measurements shown in Figure 59b. Specifically, $n = 10$ most populated bins are shown in Figure 60b which amount to approximately to 91.8% of all recorded acceleration measurements.

The power bin concept in the context of feature selection is not intended to replace the previously explained feature extraction method and feature selection phase but rather to complement it. Hence, rather then extracting features from the entire acceleration signal it is good practice to pre-process the acceleration signal into n number of shorter acceleration signals corresponding to each power bin and consequently extract features for these n signals according to the method introduced in section 6.2. Then feature selection can be carried out similarly to the method explained in section 6.3 by evaluating the *monotonicity* according to Equation 6.14 of each feature for each power bin.

The idea of binning the acceleration based on mechanical power to enhance feature selection is to ascertain the trendability of a given feature across several bins which allows for a greater confidence in the choice of features. Additionally, the consistency of the trend of a given feature can be compared for multiple bins and allows for an improved visualization of potential trends in the features as damage increases.
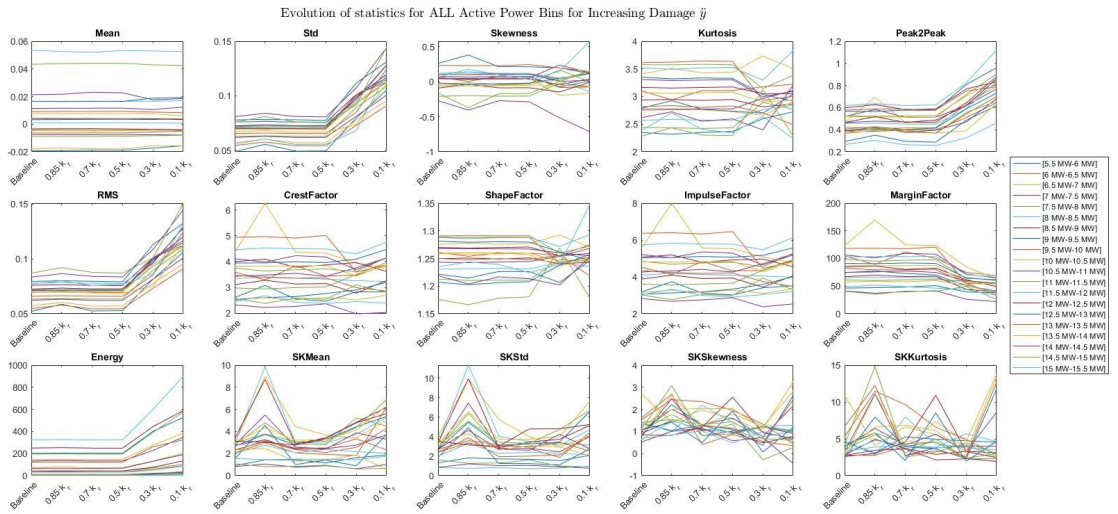
(a)
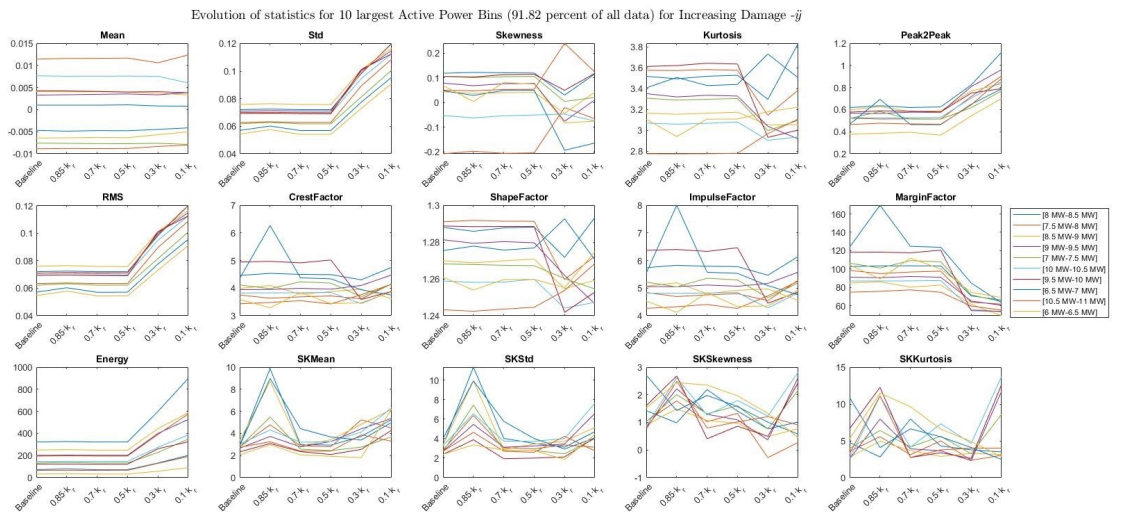
(b)

Figure 60: Evolution of statistical and spectral features of the MS acceleration ÿ for load case *LC1* shown (a) for all 20 power bins and (b) for 10 most populous power bins representing 91.8% of all measurements

6.4 Health Indicators

In the previous sections a methodology for feature extraction and feature selection has been discussed and implemented. By doing so, the most promising features for RUL prediction have been selected for each acceleration signal and for each load case, whereas the remaining non-monotonic features have been discarded. Now that a number of suitable features has been identified and pre-selected, the final step of the proposed data-driven approach can

be formalized: constructing health indicators.

6.4.1   Principal Component Analysis

In order to construct the health indicator a data dimensionality reduction is deemed convenient. Since some signals have a large number of associated features which can be used for the task of prognosis, it is unpractical to look at each of these predictable features individually. Instead, an algorithm will be implemented to merge all the suitable features whilst preserving the information of each individual feature. This is commonly referred to as data dimensionality reduction.

Principal component analysis (PCA) is one such data dimensionality reduction algorithm extensively used in computational statistics in a variety of fields. To name a few, PCA has been implemented in image processing tasks, fault diagnosis, pattern recognition, neural network, data compression, wavelet transform [45]. PCA is a convenient approach to reduce the dimension of data and extract meaningful information from a set comprised of several variables.

Mathematically, the PCA is determined as follows. Imagine m random vectors with each vector containing n samples written in matrix form $[\boldsymbol{X}]_{\boldsymbol{m} \times \boldsymbol{n}}$.

$$\mathbf{X} = \begin{bmatrix} x_{11} & x_{12} & \cdots & x_{1n} \\ x_{21} & x_{22} & \cdots & x_{2n} \\ \vdots & \vdots & & \vdots \\ x_{m1} & x_{m2} & \cdots & x_{mn} \end{bmatrix} \tag{6.17}$$

Each vector $x_1, x_2, ... x_m$ represent m different features such as those obtained from the feature selection phase.

The covariance matrix of $[\boldsymbol{X}]_{\boldsymbol{m} \times \boldsymbol{n}}$ can be computed and is expressed as follows:

$$\mathbf{C} = \begin{bmatrix} \text{cov}\,(\mathbf{x}_1, \mathbf{x}_1) & \text{cov}\,(\mathbf{x}_1, \mathbf{x}_2) & \cdots & \text{cov}\,(\mathbf{x}_1, \mathbf{x}_m) \\ \text{cov}\,(\mathbf{x}_2, \mathbf{x}_1) & \text{cov}\,(\mathbf{x}_2, \mathbf{x}_2) & \cdots & \text{cov}\,(\mathbf{x}_2, \mathbf{x}_m) \\ \vdots & \vdots & & \vdots \\ \text{cov}\,(\mathbf{x}_m, \mathbf{x}_1) & \text{cov}\,(\mathbf{x}_m, \mathbf{x}_2) & \cdots & \text{cov}\,(\mathbf{x}_m, \mathbf{x}_m) \end{bmatrix} \tag{6.18}$$

The characteristic equation of the covariance matrix $\boldsymbol{C}$ in Equation 6.18 can be expressed as:

$$\mathbf{C}\boldsymbol{\alpha}_i = \lambda_i\boldsymbol{\alpha}_i \tag{6.19}$$

In Equation 6.19, λ_i are eigenvalues of the covariance matrix and α_i are eigenvectors corresponding to λ_i. Naturally, the eigenvectors α_i must satisfy condition Equation 6.20

$$\begin{aligned} \boldsymbol{\alpha}_i^{\mathrm{T}}\boldsymbol{\alpha}_j = 1 \quad i = j \\ \boldsymbol{\alpha}_i^{\mathrm{T}}\boldsymbol{\alpha}_j = 0 \quad i \neq j \end{aligned} \tag{6.20}$$

Once the eigenvalues λ_i of the covariance matrix have been calculated, using a cumulative contribution rate L_l, an effective number of eigenvalues l can be determined out of the total number of eigenvalues m, where $l < m$. The cumulative contribution of l eigenvalues is defined as:

$$L_l = \frac{\sum_{i=1}^{l} \lambda_i}{\sum_{j=1}^{m} \lambda_j} \tag{6.21}$$

Where $\lambda_j \in 1, 2, ..., m$ and $\lambda_i \in 1, 2, ..., l$. By setting a cumulative contribution rate L_l greater than a certain value, typically 80% - 95%, the number l of effective eigenvalues can be decided.

Finally, the data can be reduced from m variables to l new variables by using an l number of eigenvectors α_i with $i \in= \{1, 2, ..., l\}$ corresponding to $\lambda_1, \lambda_2, ..., \lambda_l$ as follows

$$\mathbf{y}_i = \alpha_{i1}\mathbf{x}_1 + \alpha_{i2}\mathbf{x}_2 + \cdots + \alpha_{im}\mathbf{x}_m = \boldsymbol{\alpha}_i^{\mathrm{T}}\mathbf{X} \tag{6.22}$$

Where m vectors $X = [x_1, x_2, ...x_m] \in \mathbb{R}^{1\times n}$ corresponding to m different features have been reduced to l new vectors $Y = [y_1, y_2, ...y_l] \in \mathbb{R}^{1\times n}$. The vectors y_i are known as the Principal Components. The principal components can be used to express the reconstructed

approximate matrix $\widehat{\boldsymbol{X}}$ according to Equation 6.23.

$$\widehat{\mathbf{X}} = \sum_{i=1}^{l} \alpha_i \mathbf{y}_i \tag{6.23}$$

The reconstructed approximate matrix $\widehat{\boldsymbol{X}}$ comprises most of the information of the original dataset X but excludes a number of redundant features that bring little new information and effectively reduces data dimension from m to l.

6.4.2   Constructing Health Indicators

The PCA algorithm as described above has been implemented in this work. It is used to reduce the number of selected features extracted from each acceleration signals.

Here it is important to keep in mind that from the previous sections, although the same 15 features were computed for each acceleration signal -translational and rotational acceleration at the MS and at the HSS, for all 3 load cases- the feature selection phase culminated in very different results. Whereas the feature selection phase provided a large amount of quality features for *LC3*, a reduced number of suitable features was found for *LC2* and of lower quality for RUL prediction. For load case *LC1* feature selection was even more difficult with hardly any relevant features fulfilling the requirement of the monotonicity performance metric adequately.

Naturally, in the absence of appropriate features, applying the PCA algorithm for feature fusion and reducing the dimension of data is not possible. Following from the results of the feature selection phase prsented in subsection 6.3.3, no health indicators were possible to construct for LC1 which makes this load case not suited to be approached through a purely data-driven model. For *LC2* only the acceleration signal corresponding to $\ddot{y}$ in the MS was sufficiently monotonic to enable the construction of a Health Indicator. Lastly, the load case replicating damage at the HSS, *LC3*, was abundant in monotonic features which subsequently allowed the construction of Health Indicators for all four signals in all three directions x, y, z: accelerations and translational accelerations of the MS as well as accelerations and translational accelerations of the HSS

The results of PCA are commonly visualized in principal component space. Since PCA components are obtained in descending order of component variance, the first two will have

(a) Results of PCA merging 8 features

(b) Results of PCA merging 11 features

(c) Results of PCA merging 3 features

(d) Results of PCA merging 8 features

Figure 61: PCA analysis for acceleration $\ddot{x}$ and rotational acceleration $\ddot{\alpha}_x$ in the MS (top figures) and HSS (bottom figures) corresponding to *LC3*

the lowest variance and are therefore of greater interest. Hence, the principal components are plotted in the space of the first two principal components. As stated, feature selection for *LC3* culminated in a large group of variables corresponding to acceleration and rotational acceleration signals in the MS and the HSS. Accordingly, Figure 61, Figure 62 and Figure 63 present the results of the PCA analysis for the angular and rotational accelerations at both shafts. Figure 61 illustrates the results of the acceleration $\ddot{x}$ and the rotational acceleration $\ddot{\alpha}_x$, whereas Figure 62 and Figure 63 present the equivalent results for the accelerations in y and z respectively. For all figures, the top two figures are the first 2 principal components for translational and rotational accelerations at the MS and the bottom two figures correspond to the first 2 principal components for translational and rotational accelerations signals of the HSS. The number of features that were fused for each signal is specified for each signal.

These plots show two principal components for each signal. The goal is to determine a single one of the two components and preferably select the one that displays an increasing trend for increasing damage. For instance, Figure 61c shows that the first principal component

(a) Results of PCA merging 6 features

(b) Results of PCA merging 5 features

(c) Results of PCA merging 3 features

(d) Results of PCA merging 6 features
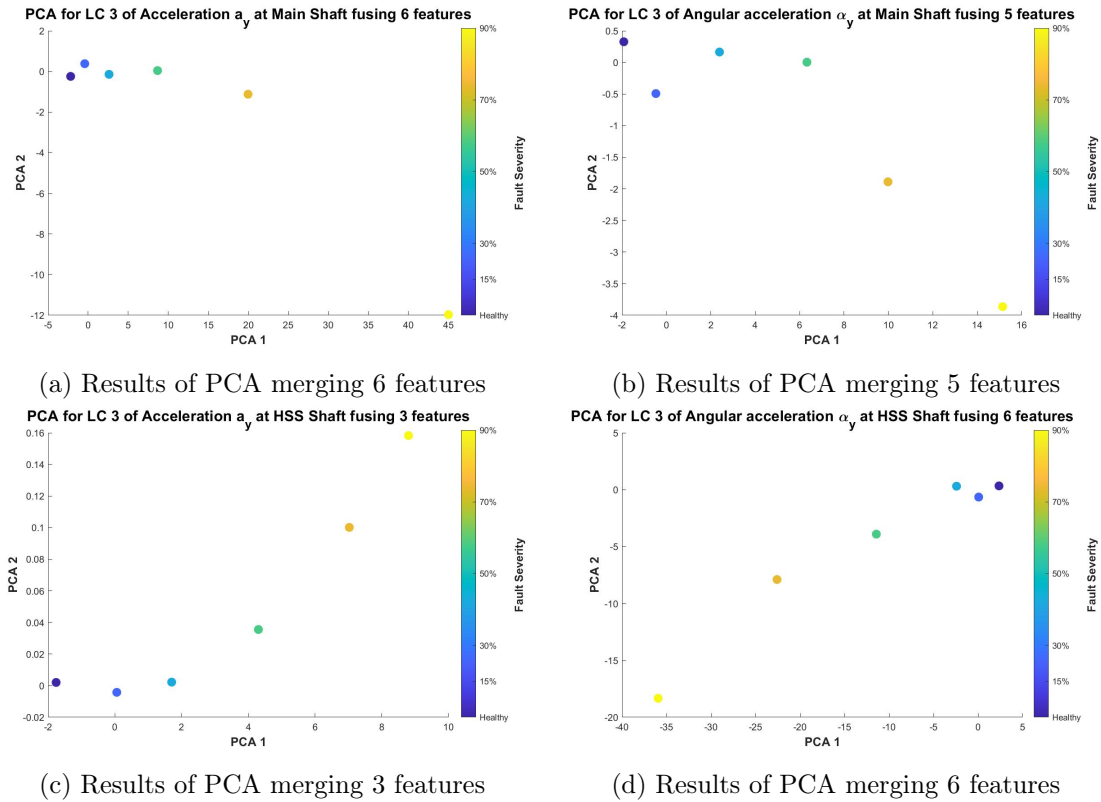
Figure 62: PCA analysis for acceleration $\ddot{y}$ and rotational acceleration $\ddot{\alpha}_y$ in the MS (top figures) and HSS (bottom figures) corresponding to *LC3*

is increasing as the bearing accumulates damage. Therefore, the first principal component is a promising fused health indicator to track the acceleration $\ddot{x}$ at the HSS for increasing bearing damage. In contrast, Figure 61d shows that the first principal component displays a decreasing trend for increasing damage whereas the second principal component gradually increases as damage accentuates. Hence, the second principal component will be used as a health indicator to monitor and predict the rotational acceleration $\ddot{\alpha}_x$ of the HSS. However, its important to note that finding a principal component with increasing trend will not always be possible as seen from Figure 61a which clearly shows that both the first and the second principal component decrease as damage increases. In this situation it is suggest to simply select the one of the two that displays a more monotonic decreasing behaviour.

This process can be visualized more clearly by visualizing each health indicator as a function of damage. Hence, the results of PCA presented in Figure 61, Figure 62 and Figure 63 can be re-arranged and presented as seen in Figure 65, Figure 66 and Figure 68.

Based on the criteria described in this section, the single most suitable principal component is selected for each acceleration signal and is chosen as a unique health indicator for that

(a) Results of PCA merging 7 features

(b) Results of PCA merging 8 features

(c) Results of PCA merging 6 features
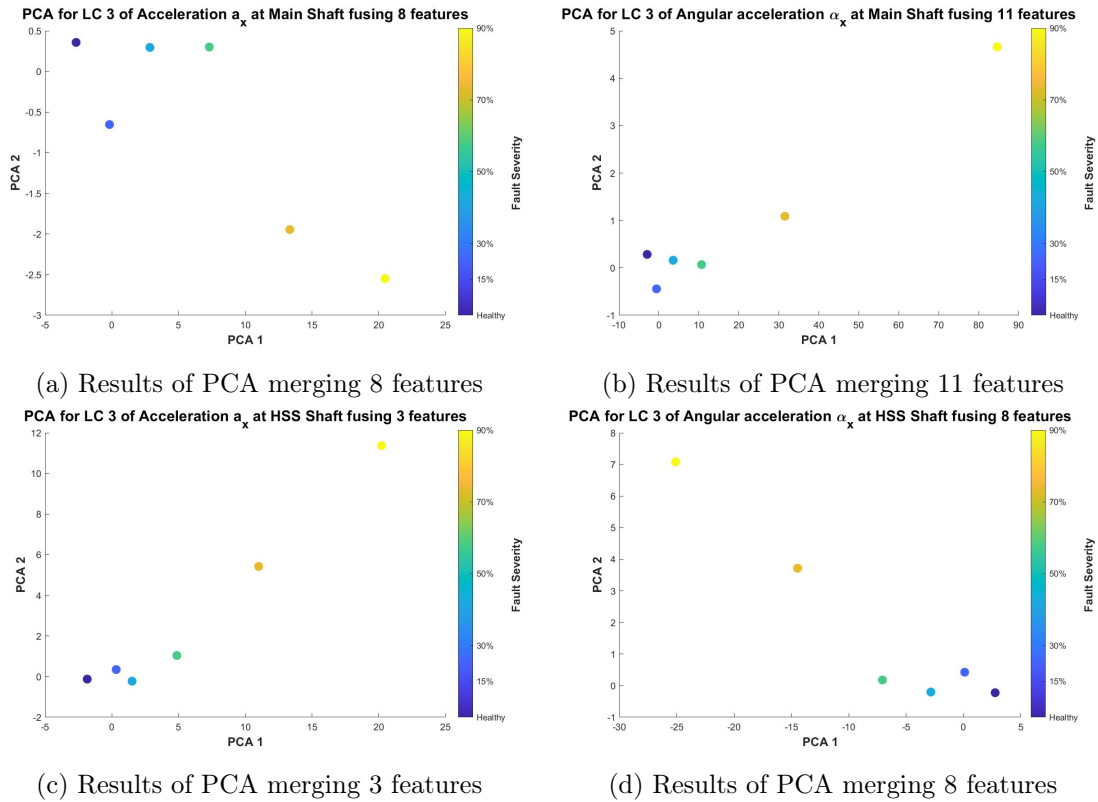
(d) Results of PCA merging 10 features
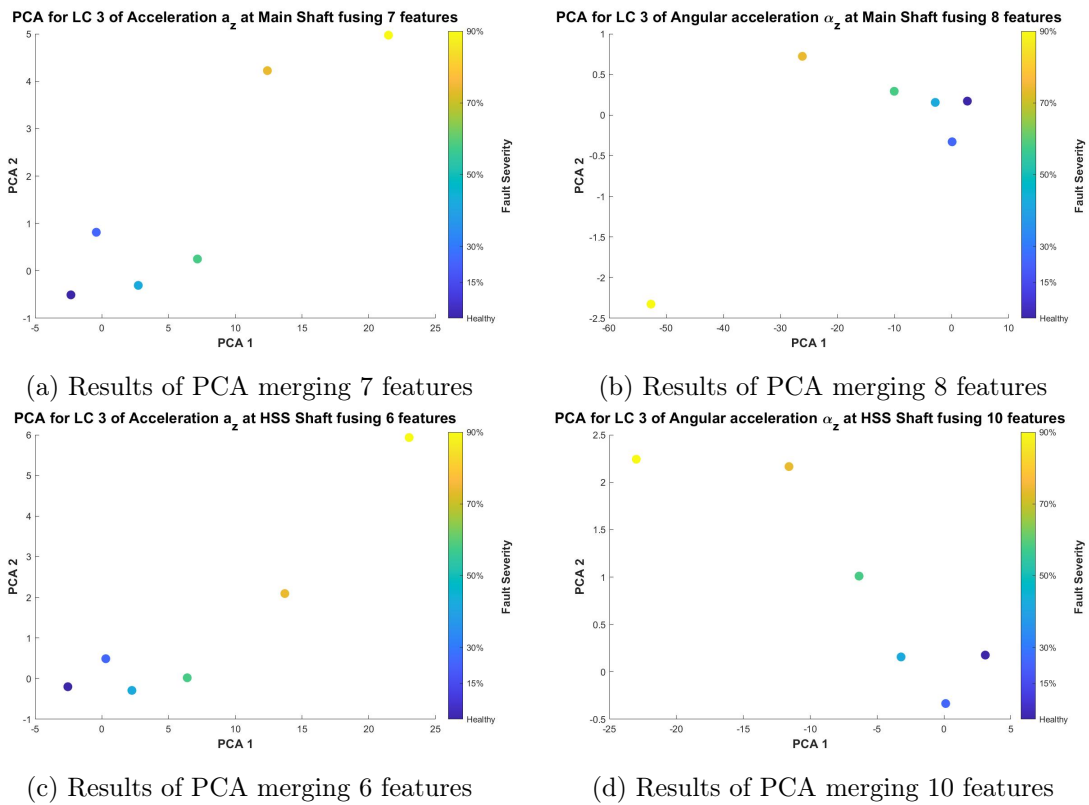
Figure 63: PCA analysis for acceleration $\ddot{z}$ and rotational acceleration $\ddot{\alpha}_z$ in the MS (top figures) and HSS (bottom figures) corresponding to *LC3*
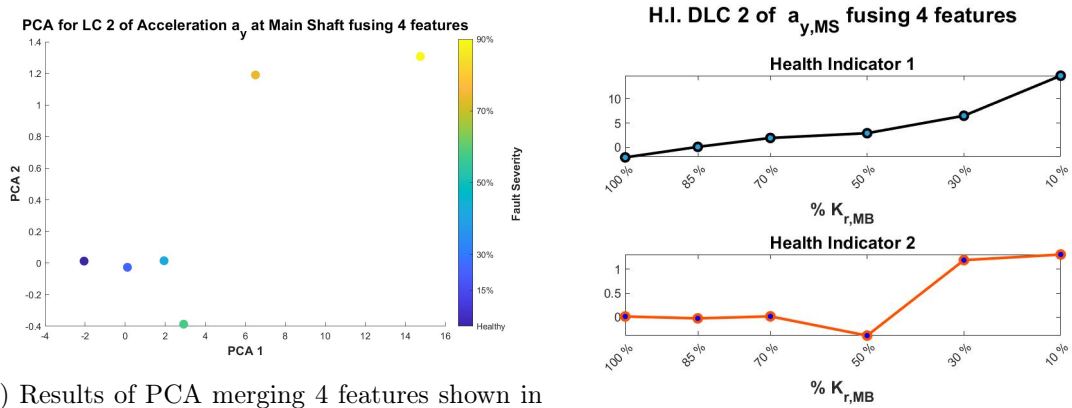
(a) Results of PCA merging 4 features shown in principal component space

(b) Results of PCA as a function of damage
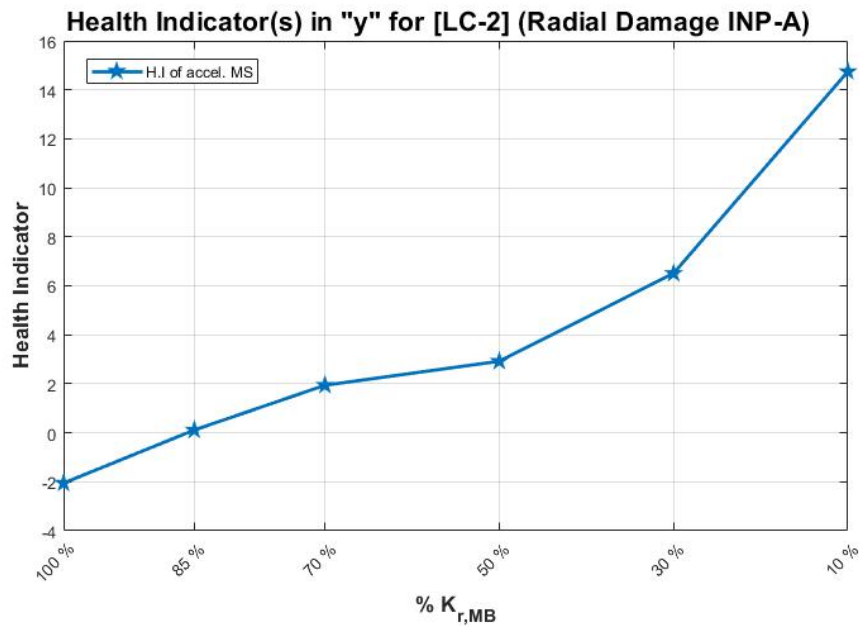
(c) Resulting Health indicator for *LC2*

Figure 64: PCA analysis for acceleration $\ddot{y}$ of the MS and construction of Health Indicator for *LC2*

signal. This workflow can be readily seen from Figure 64 corresponding to *LC2* which was performed by fusing 4 features from the acceleration signal $\ddot{y}$ of the MS. Figure 64a shows the two first principal components plotted in the principal component space, Figure 64b shows the same two principal components as a function of damage to simplify the selection process and Figure 64c illustrates the final selected health indicator which in this case corresponds to the first principal component. As mentioned, this health indicator was the only one obtained for the load case *LC2*.

In a similar manner, the same procedure is followed to ascertain the most convenient Health indicators for the acceleration signals corresponding to *LC3*.
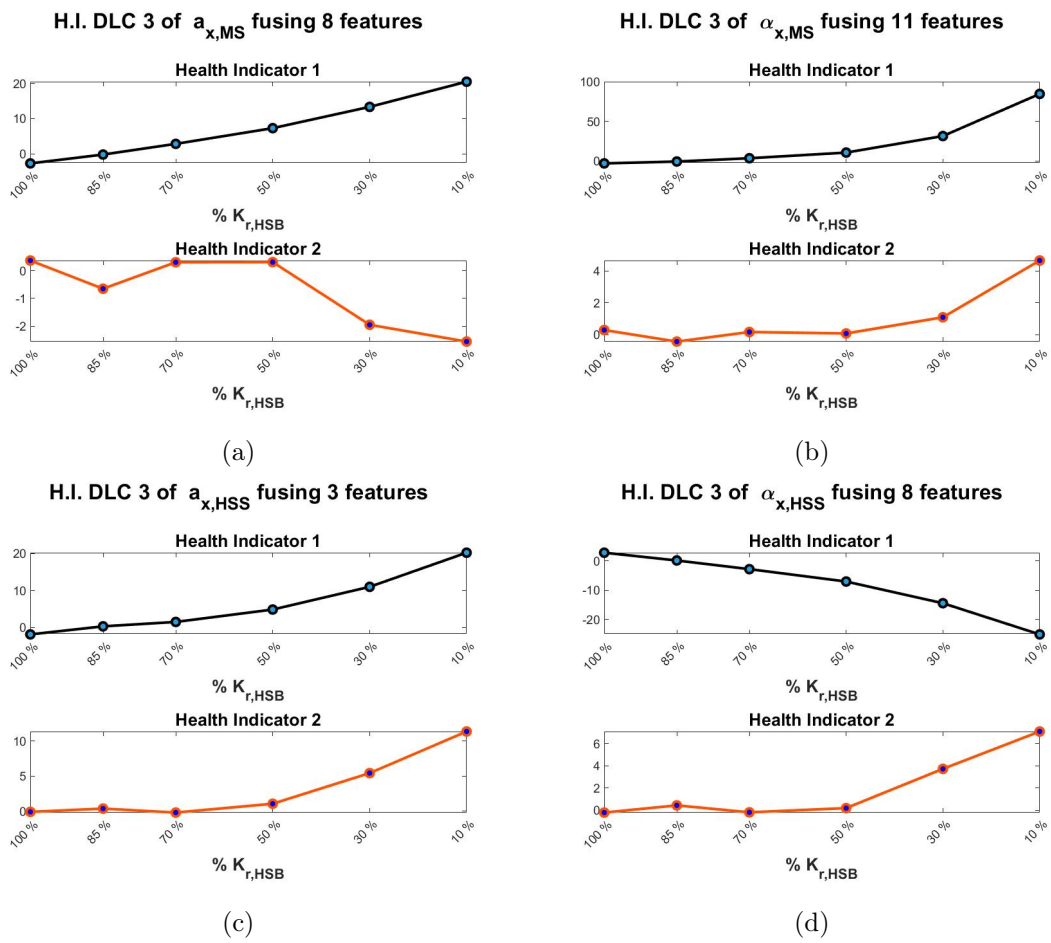
Figure 65: Potential health indicators (H.I) for $\ddot{x}$ and $\ddot{\alpha}_x$ in the MS (a),(b) and HSS (c),(d) corresponding to $LC3$

H.I. DLC 3 of $a_{y,MS}$ fusing 6 features (a)

H.I. DLC 3 of $\alpha_{y,MS}$ fusing 5 features (b)

H.I. DLC 3 of $a_{y,HSS}$ fusing 3 features (c)

H.I. DLC 3 of $\alpha_{y,HSS}$ fusing 6 features (d)
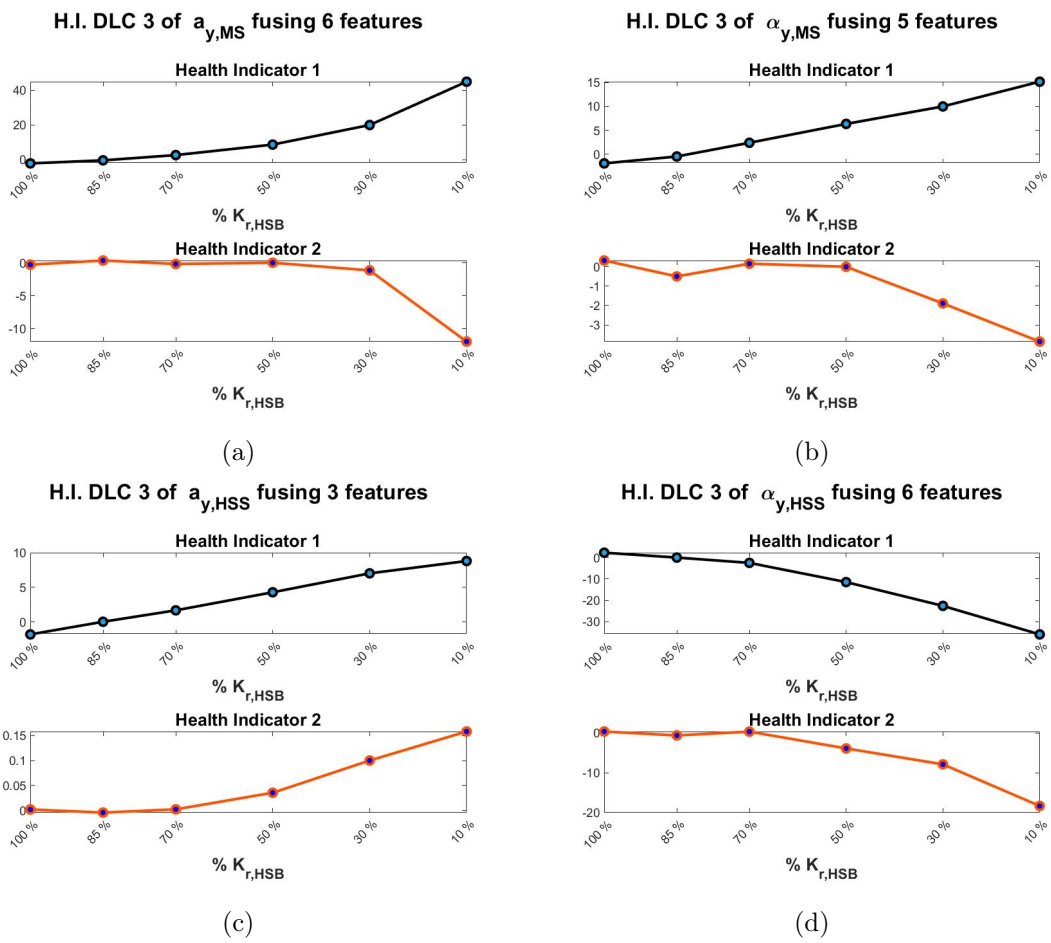
Figure 66: Potential health indicators (H.I) for $\ddot{y}$ and $\ddot{\alpha}_y$ in the MS (a),(b) and HSS (c),(d) corresponding to $LC3$
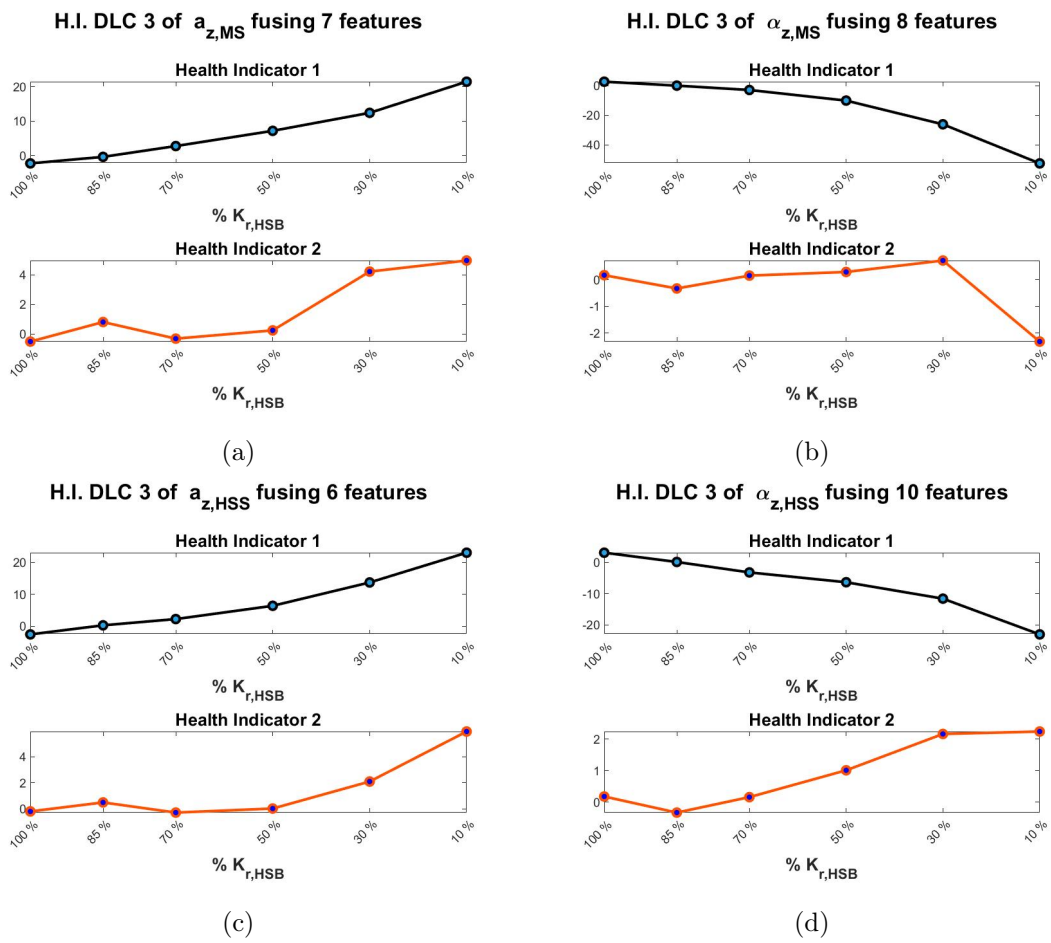
Figure 67: Potential health indicators (H.I) for $\ddot{z}$ and $\ddot{\alpha}_z$ in the MS (a),(b) and HSS (c),(d) corresponding to $LC3$
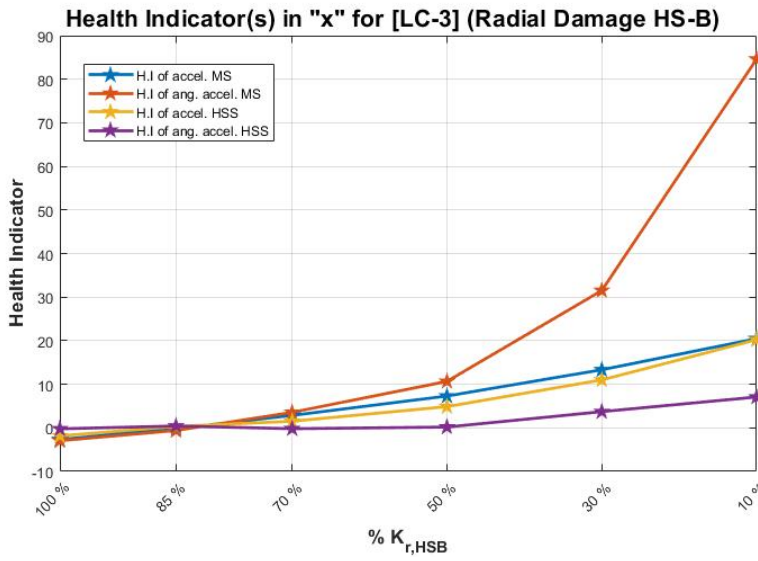
(a) Health indicators for accelerations in x at the MS and HSS $\ddot{x}$, $\ddot{\alpha}_x$
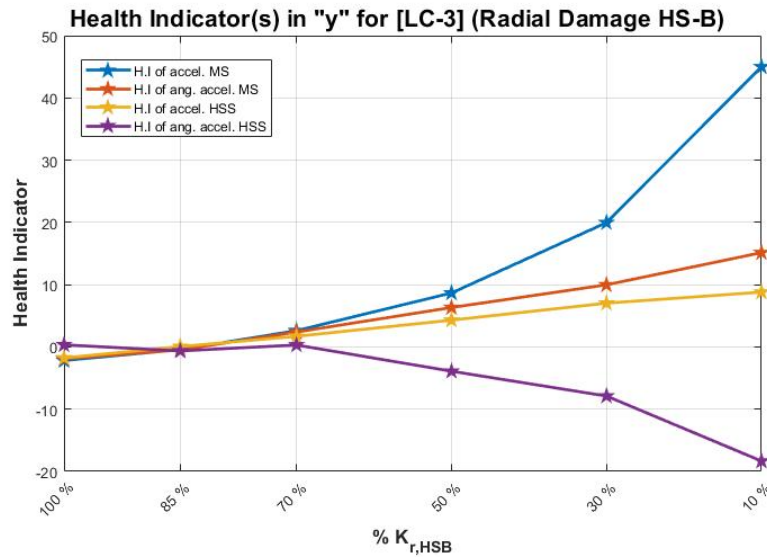
(b) Health indicators for accelerations in y at the MS and HSS $\ddot{y}$, $\ddot{\alpha}_y$
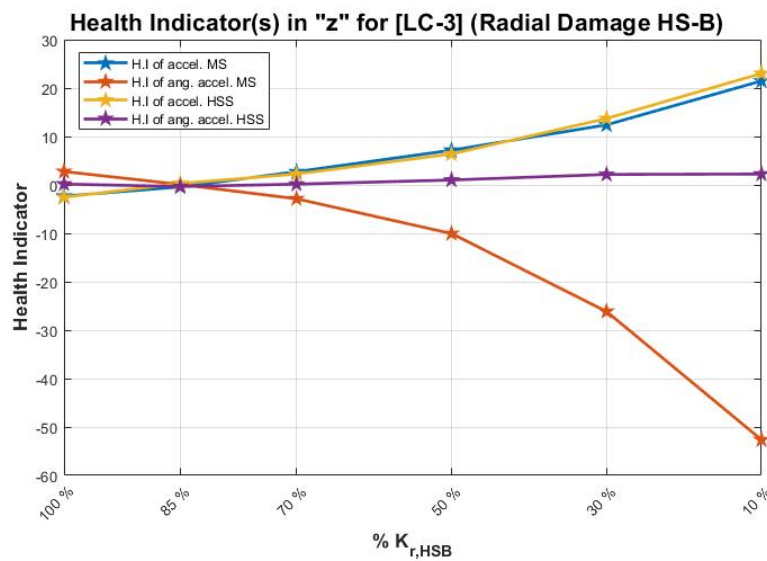
(c) Health indicators for accelerations in z at the MS and HSS $\ddot{z}$, $\ddot{\alpha}_z$

Figure 68: Health indicators for *LC3*

6.5 Outlook for data-driven model

The RUL will be estimated based on the health indicators calculated in the previous selected which resulted from the fusion of conveniently pre-selected statistical indicators.

The advantage of Health Indicators is precisely their ability to describe the process of damage using several quantities extracted from the acceleration signals at the MS and HSS. Consequently, the Health Indicators are used as the prediction variable in the proposed data-driven model. In practice, this means that the RUL can be predicted by extrapolating the trajectory of the Health Indicator values. Hence, it becomes a forecasting task of a time series $y(t)$ where future values are predicted from n past values of that series. In general this can be represented algebraically by Equation 6.24.

$$y(t) = f(y(t-1), \ldots, y(t-n)) \tag{6.24}$$

As shown in Figure 69, for a given indicator -here taken as the fitted health indicator for each acceleration signal- the deterioration process of the component under study can be represented by a continuous function $y(t)$ representing a time series. This time series can be further subdivided in two parts, a first part α indicating a healthy operation of the component and a second stage β corresponding to fault degradation.

Prognosis usually begins when a fault is detected at point A for $t = t_A$. The selected indicator reaches a certain predefined threshold at point B for $t = t_B$. The threshold should be chosen such that the t_B accounts for the logistic time to prepare parts and equipment, the time to wait for a good weather to enable transport, the time to travel to the offshore site and the actual repair and dispatch time.

Ideally, if the total running time - the RUL- between point A to point B can be estimated accurately using only past values of the health indicator covered during period α an optimal maintenance schedule can be set in place.

There are several prediction methods which can be suitable to forecast future values of a given time-series. These methods can be classical and statistical time series forecasting methods which perform well on a wide range of prediction problems provided appropriate data. Some of the most commonly exploited methods are:
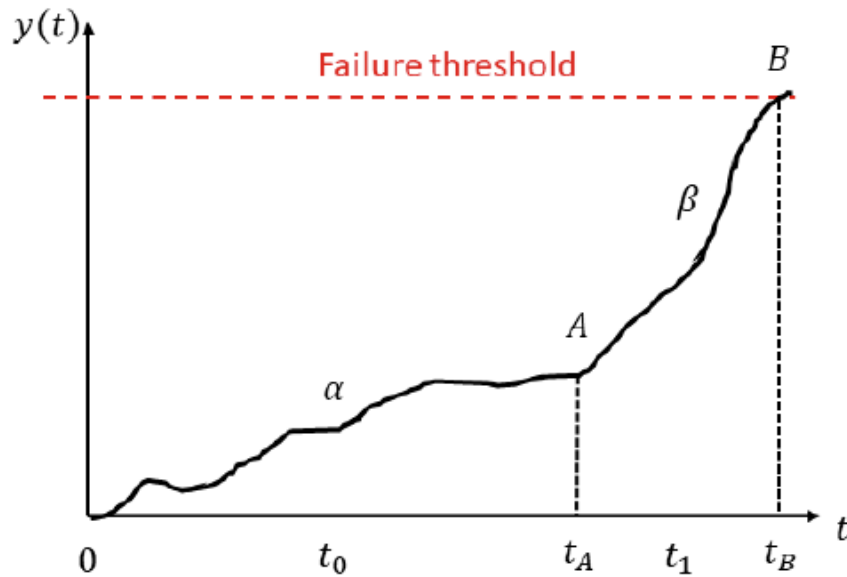
Figure 69: Bearing life process [9]

- Autoregression;

- Moving Average;

- Autoregressive Moving Average;

- Autoregressive Integrated Moving Average (ARIMA);

- Seasonal Autoregressive Integrated Moving-Average (SARIMA);

- Nonlinear Autoregressive exogenous model (NARX).

The next set of tools for time-series prediction are based on dynamic neural networks which are deep neural networks (multilayered neurons) or more commonly shallow neural networks (see subsubsection 3.3.3.1). Whereas the classical methods used for time series prediction such as ARIMA o NARX assume that there is a linear relationship between inputs and outputs, Neural Networks are capable of approximating nonlinear functions without any apriori information about the properties of the data [46]. Neural networks have been succesfully implemented for a variety of WT prognosis tasks such as estimation of RUL of high-speed shaft bearings operating at speeds between 1500 and 1800 RPM [9], estimation of RUL of generator bearings [47], and detecting mechanical faults in a WT using generator current signal analysis (CSA) [38].

Typically, the Artificial Neural Networks (AAN) used to estimate the RUL of the several WT components are feed-forward back-propagation models. During the training process of these models the optimal number of hidden layers, learning rate and algorithm type can be determined by minimizing the error between the target outputs and the model outputs. The so-called feed-forward back-propagation models consist in training an algorithm following two steps: (1) Feeding forward the input values of $y(t)$ and (2) calculate the error and propagate it back to the earlier layers.

The advantage of using neural networks and ANN specifically is that they can be trained to identify complex, nonlinear relationships of non-stationary signals. A prerequisite to successfully implement such methods is that the input data must be adequate and sufficient for prognosis.

Although Health indicators provide good support to bearing prognosis tasks if they reflect the degradation process at these bearings, these indicators must necessarily be expressed as a function of time such that H.I(t). However, the methodology to model damage was based on progressively reducing the stiffness of the bearing where a fault was assumed as explained in section 2.2. Which is equivalent to H.I(K), where $K = K_r^{INPA}$ for *LC2* and $K = K_r^{HSB}$ for *LC3*. This was a convenient approach to modelling damage when relying on data simulated by numerical drivetrain model. The fundamental issue with this methodology is however that a time-dependent relation between bearing stiffness and bearing damage $K \equiv K(t)$ is not available, hence H.I$(t) \neq$ H.I(K).

Since the RUL of a bearing is defined as the total number of revolutions before a failure occurs or the total number of hours that the bearing can run until the first sign of failure develops [48], to fully enable RUL estimation using the constructed H.I an additional time-dependent bearing damage model must be established beforehand such that the condition expressed in Equation 6.25 is satisfied.

$$\text{H.I}(K) = \text{H.I}\left[K(t)\right] \equiv \text{H.I}(t) \tag{6.25}$$

Hence, to fully take advantage of the concept of health indicators these must be constructed for a known discrete or continuous time interval. However, the health indicators that have

been established in the previous section are a function of the evolution in bearing stiffness which poses a decisive obstacle in terms of RUL prediction which can only be overcome through further investigation on the temporal evolution of bearing stiffness for increasing damage.

Another obstacle to address to fully implement the data-driven model is setting an adequate threshold beyond which failure can be assumed. Since the numerical model used throughout this work is able to produce damage data but not data corresponding to actual mechanical failure of the component, a predefined threshold is required indicating unacceptable fault propagation. If $y(t)$ is a well-defined Health Indicator that effectively captures the degradation process, a failure threshold as shown by the red dotted line in Figure 69 is indispensable

A potential solution to establish an adequate threshold with no a priori knowledge on the physics of the system is to make use of the vibration zones defined in several codes such as ISO10816-21 [7]. These predefined limits are referred to as evaluation zones within the standards and they are defined to permit a qualitative assessment of the vibration on a given machine under normal operating conditions. The purpose of these evaluation zones is also to provide a set of guidelines on possible actions the operator should consider. An example of such vibration zones provided in the standards [7] for onshore WTs is given in Figure 70. Although ISO 20816 establishes different categorization and number of zones for specific machine types, they can be broadly divided as follows:

Zone A The vibration of newly commissioned machines normally falls within this zone. The effort required to achieve vibration within zone A can be disproportionate and unnecessary.

Zone B Machines with vibration within this zone are normally considered acceptable for unrestricted long-term operation.

Zone C Machines with vibration within this zone are normally considered unsatisfactory for long-term continuous operation. Generally, the machine may be operated for a limited period in this condition until a suitable opportunity arises for remedial action.

Zone D Vibration values within this zone are normally considered to be of sufficient severity to cause damage to the machine.

Figure 70: ISO 10816-21 Onshore wind turbines with gearbox [7]

Implementing these evaluation zones such as those presented in Figure 70 involves calculating the RMS value of the velocity in [mm/s] at several relevant locations in the gearbox. Naturally, enforcing these evaluation zones within a prognosis model does not exactly result in bearing RUL estimation nor can it overcome the fundamental obstacle related to a lack of time-dependent Health indicators. Instead of the number of hours or cycles to failure, it would however allow WT operators to directly determine the real-time compliance of the monitored assets with recognised standards, ensure safe operation and schedule potential maintenance actions according to ISO guidelines.

A significant advantage of selecting a threshold according to ISO standards is that standards accurately reflect market needs and are based on global expert opinion which permits a strong consensus and high-degree of acceptance by the industry. Incorporating the evalu-

ation zone vibration limits as pre-defined upper limits will also result in a prognosis model that classifies drivetrain vibrations and permissible operating state to criteria from ISO standards. A final relevant advantage of the suggested method is that it would be relatively easy to certify such a prognosis method since the principles behind the model are proven by pre-existing standards.

Chapter 7

Discussion

The fundamental objective of this work has been to determine the Remaining Useful Life of 4 different bearings in a WT drivetrain – 2 bearings supporting the MS and 2 bearings at the HSS - for three load cases representing distinct types of damage. Each load case was partitioned into 5 different damage intensities of increasing severity. The objective of RUL estimation has been approached from two separate prognosis perspectives. The first is a classic prognosis perspective based on the physics-of-failure through the S-N curves by calculating the bearing lifetime [in days] according to the Lundberg and Palmgren theory for increasing damage. The second approach to prognostics was based exclusively on an exhaustive analysis of the acceleration signals to identify damage-induced anomalies in these signals for increasing damage. The raison d'être of the data-driven approach is to investigate if it is possible to detect and predict a bearing fault whilst making no use of the underlying physics that govern the drivetrain. Regardless of the approach, to successfully ascertain an RUL in days it is indispensable to set a pre-defined threshold beyond which the bearing can be assumed to fail.

Although it would be highly desirable to compare the bearing lifetime results obtained according to both of these approaches, prognosis could not be fully implemented for the data-driven approach due to the fact that damage was modelled on the basis of progressively decreasing bearing stiffness to simulate increasing damage. This damage-stiffness relation, which was exploited throughout the thesis, was independent of time. Since a time-dependant bearing stiffness model is indispensable to ascertain a true RUL prediction the data-driven prognosis approach proposed in this work could not culminate in the

number of days to failure of the bearings. This obstacle is closely coupled to the manner in which it was chosen to model bearing damage. This shortcoming essentially stems from a lack of knowledge and to overcome this difficulty the physical time-dependent relation between bearing stiffness and bearing damage must be established beforehand.

Despite the impossibility to directly compare the physics-based model and the data-driven approach a significant number of valuable remarks can be established. These findings are presented in this section and describe how well the three different damage load cases can be treated by a physics-based model and a data-driven approach.

7.1   Load Case 1

The first remark that must be put forth concerning an axial damage at the main up-wind MS bearing is that the simulated damage leads to a drastic increase of axial loads carried by the down-wind MS bearing but does not trigger a significant response in the behaviour of the remaining bearings considered in this thesis. This was seen from a preliminary analysis of the evolution of the force time-series at each of these bearings as well as on the PSD of the translational and rotational accelerations measured at the MS and HSS. The analysis of forces for increasing axial damage at the MS highlighted that the gearbox has a limited capability to transfer a surplus of axial loads down the drivetrain. Furthermore, the increase of axial loads at the affected bearing in the MS had little to no effect on the expected lifetime of this bearing. The variation of lifetime was somewhat more noticeable for the HSS bearing on the generator side but remains relatively low.

The first challenge is, therefore, that a load case with a small observed impact on the analysed drivetrain components will be inherently difficult to detect let alone predict. Accordingly, it was found that neither the physics-based model nor the data-driven model were particularly suitable to detect incipient faults and predict future damage. To understand why evidence of a fault remains relatively hidden, even for severe damage intensities, it is important to keep in mind the inner architecture of the drivetrain and the type of bearings used to support the main shaft. The drivetrain concept modelled in this work used two tapered roller bearings (TRB) as main bearings. These bearings are designed to withstand large axial loads and large radial loads. Additionally, these two bearings are mounted in close proximity to one another with no gears in between. This means that the main shaft behaves in an almost rigid manner and a damage originating at the up-wind

bearing generates vibrations which are directly transmitted to the second main bearing with little impact on the shaft acceleration. Hence, this type of bearing and their layout relative to one another effectively obstructs the propagation of vibrations and complicates detection.

Therefore, the reduced ability to detect fault and predict an axial fault cannot be directly associated to a weakness of the proposed prognosis methods but rather to the good performance of the second main bearing when an axial damage is present at first main bearing. In order to improve diagnostics and prognostics capabilities in such a situation, it may be important to reconsider the approach to model damage. In the present work radial and axial damage were assumed to be uncorrelated which may be a valid assumption when different bearings are responsible for carrying radial and axial loads independently. However, when the main shaft bearings consist of two TRBs, where each bearing carries a combination of both radial and axial forces, assuming uncorrelated damage may lead to unreliable degradation data which will obstruct the possibilities to detect a bearing fault.

Physics-based approach

To successfully determine an RUL a pre-defined failure threshold must be selected. In this work two different thresholds have been established $t_{\mathrm{f},1} = 64$ and $t_{\mathrm{f},2} = 128$ days, the latter being the most conservative. According to the implemented physics-based approach, none of the bearings studied in this work fail for either one of the pre-defined thresholds. As mentioned previously, an axial damage at the up-wind MS bearing induces a significant increase in the axial loads carried by the other MS bearing located down-wind from the damage. Although this severe increase clearly exerts a surplus of axial loads at INP-B this effect does not lead to a noticeable decrease in the bearing's lifetime. The reason for this lies in the expression of P for the calculation of bearing lifetime shown below:

$$L_{10,i} = \left(\frac{C}{P_{\mathrm{eq},i}} \right)^{a} \qquad\qquad P = X \cdot F_r + Y \cdot F_a$$

Since the values of the radial bearing factor X and the axial bearing factor Y, provided by the bearing manufacturer, are $X = 1$ and $Y = 0$ the variations of axial loads F_a are not captured in the expression for P. Hence, despite the pronounced increase of axial loads

experienced at INP-B as a result of an axial damage at INP-A, this redistribution of loads does not influence the bearing's lifetime.

As for the remaining bearings, the fact that bearings of the HSS do not fail aligns with the mild redistribution of loads within the drivetrain observed from the force analysis at these bearings. The decrease of lifetime is significantly more severe for the HSS bearing on the generator side, HS-B, when compared to the MS bearing INP-B. Despite being comparatively higher, the decrease in lifetime of the only affected bearing in the HSS is limited with an increase of 4.88% when the bearing stiffness reaches the most severe damage intensity for $K = 0.10 \cdot K_{\mathrm{x}}^{\mathrm{INPA}}$.

The results from the physics-based model clearly indicate that an axial damage at the MS bearing has little to no impact on the RUL of the MS bearings and a very limited impact on the RUL of one bearing of the HSS.

Data-driven approach

The general methodology to implement a data-driven approach was described in subsection 3.3.3 and the specific data-drive model suggested in this work is extensively discussed in chapter 6. This was done in three subsequent steps: feature extraction, feature selection and feature fusion which culminated in the creation of the so-called Health indicators. According to this methodology, a sufficient number of predictable features must be available prior to creating a Health Indicator which can then be used for prognosis. Although the same 15 features were extracted for all 3 load cases , the feature selection phase culminated in very different results. For load case LC1 feature selection resulted in a lack of relevant features that met the performance requirements adequately. As a consequence, it was not possible to construct Health Indicators for this load case which is a major obstacle in terms of RUL prediction via a purely data-driven model.

This strongly suggests that to successfully approach the prognosis of bearings when the MS bearing suffers an axial damage understanding the physical processes that take place is fundamental to improve the prognosis capabilities. Hence, for the axial damage modelled in *LC1* a deeper understanding of the physics-of-failure associated to this damage is a prerequisite to predict the RUL of drivetrain bearings. That being said, a hybrid prognosis may be considered which uses signal analysis techniques to a certain degree in combination with a physics model. However, signal processing techniques alone will not be successful

in predicting the future condition of this bearing. Furthermore, the physics-based model considered in this work might not be particularly suitable to detect incipient axial damage nor predict the RUL in such a situation. The large increase of loads occurring at the downwind MS bearing INP-B was seen to have no effect whatsoever on the resulting lifetime of this bearing. From the analysis of the evolution of the loads for increasing damage, an increase of approximately 76.5% of axial loads was observed on this bearing compared to the baseline case. However, this drastic increase in loads only resulted in a decrease of -0.26% decrease of the bearings lifetime compared to the healthy drivetrain. Since the axial bearing factor of INP-B is Y=0, the physics-based model assigns a large importance to any variation of radial loads but neglects any deviation in axial loads. This disproportionate importance assigned to radial loads over axial loads potentially undermines RUL prediction when an axial damage is present if radial bearing factor Y and axial bearing factors X are such that $Y >> X$.

Finally, due to the reduced ability to obtain reliable prognosis in the event of an axial damage originating at the MS, load case *LC1* is a clear indication that there is a strong relation between diagnosis and prognosis capabilities. Since detection of this damage was particularly challenging, prognosis was all the more difficult. In order to successfully predict the future state of the bearings it is indispensable to be able to first identify and locate the physical quantities that experience a large variation as damage progresses so as to construct a prognosis algorithm based on the evolution of these physical quantities. In future work it is recommended to pay special attention to the frequency content, peak behaviour, peak magnitude and side-band characteristics at several relevant frequencies susceptible to be excited. Although spectral analysis of the accelerations did not reveal any resonant behaviour corresponding to this load case, a thorough analysis of the loads in the frequency domain may bring further insight. The PSD of axial loads should be investigated for shaft-related frequencies, gear meshing frequencies and other relevant frequencies such as fault frequencies. Tracking the evolution of the spectral energy for increasing damage might be the most reasonable approach to detect this type of fault and establish a prediction on the future operational state of drivetrain bearings.

To summarize, the considered data-driven approach is in fact incompatible for fault detection and fault prognosis of *LC1*. This load case requires an in-depth understanding of the physical processes that take place when an axial damage at the MS occurs and which are

not readily captured by the implemented physics-based model. Hence, both the considered physics-based approach and a data-driven model are not particularly suitable to establish a prognosis algorithm for *LC1*. Ideally, a greater understanding of the underlying physics will improve fault detection of an axial damage. Improving diagnosis capabilities may be particularly beneficial to predictive maintenance in the event of an axial damage at the MS bearing. In fact, for this specific load case, a robust fault detection and appropriate fault diagnosis may very well be a pre-requisite to develop any prognosis capabilities.

7.2   Load Case 2

Results of *LC2* indicate that a radial damage at the MS affects all of the remaining bearings both at the MS and at the HSS. This was seen both in the evolution of force time-series at all bearings as well as on the frequency-domain analysis of acceleration signals. Furthermore, these results strongly imply that gearbox bearings will also exhibit signs of the radial damage originating at the MS. Presumably, these effects may also be present at the generator bearings. Therefore, load case *LC2* highlights that a radial defect in the MS can be detrimental to overall drivetrain health and is likely to influence the behaviour of several other drivetrain components besides the analysed bearings. An interesting remark is that a radial damage at the MS is clearly detectable from spectral analysis. In particular, the evolution of PSD of several acceleration signals show an increase of the energy content at several shaft-related frequencies such as f_{ISS} and f_{HSS} for $\ddot{y}$ at the MS and the HSS. Resonant behaviour is observed at these frequencies with significant variation of peak magnitude. For instance, the increase in energy content escalates dramatically at around f_{ISS} for $\ddot{y}$ at the MS from a peak value of approximately $5 \cdot 10^{-4}$ $\left[\frac{g^2}{Hz}\right]$ for healthy conditions to a peak value over $2 \cdot 10^{-2}$ $\left[\frac{g^2}{Hz}\right]$ when radial bearing stiffness decreases to $0.1 \cdot K_r^{\mathrm{INPA}}$. This represents an increase of 3900%. Additionally, several peak frequency shows a consistent shift towards lower frequencies as damage progresses.

Furthermore, spectral analysis of the acceleration signals reveals that several gear mesh frequencies are excited as damage increases. This phenomenon is commonly referred to frequency modulation and has been pointed out in several works [49], [50]. The meshing frequency modulation phenomenon has been overlooked in the gearbox vibration signals according to [51] [52]. However recent research shows that the presence of this phenomenon can be useful to detect gear and bearing faults which induce resonance frequency bands

as well as planet bearing faults. The spectral analysis results of LC2 clearly indicate that a bearing damage at the MS induces meshing frequency modulation which is in close agreement to [50]

The influence of bearing damage on gear-mesh modulation is all the more relevant in the context of this thesis, where bearings have been modelled rather simply via a stiffness-damping element. Despite the simplified bearing model, a bearing damage of this bearing does result in a realistic excitation of specific meshing modulation regions.

Physics-based approach

According to the results corresponding to *LC2* obtained from the physics-based model a radial damage on the MS bearing drastically decreases the lifetime of all bearings highlighting that the health of MS bearings is critical to overall drivetrain health. A significant reduction in lifetime is seen for all the considered bearings of both the MS and HSS. As a progressive radial damage develops at INP-A this bearing can no longer accommodate radial loads which are transmitted to the second main bearing of the MS. As a consequence, bearing INP-B, directly down-wind from the damaged bearing experiences a harsh decrease of its lifetime as high as 90.31% compared to its healthy state.

Both bearings of the HSS also suffer a severe depletion of their lifetime of 92.66% and 42.43% for HS-A and HS-B, respectively. Bearing HS-A exhibits an increase of 118% of the dynamic equivalent radial load compared to the healthy no-damage case. Accordingly, out of all the bearings under study, the HSS bearing HS-A is the most affected by a radial damage originating in a MS bearing.

These results indicate that the surplus of radial load that cannot be carried by the MS bearings are transmitted into and throughout the gearbox and are effectively propagated towards the HSS.

Data-driven approach

According to the data-driven approach implemented in this work it was possible to construct a single health indicator H.I^{LC2} from the acceleration signal of the MS $\ddot{y}$. Specifically, the health indicator was obtained by fusing 4 ditinct features using the PCA analysis explained in subsection 6.4.1. This in turn means that H.I^{LC2} has the ability to describe the process of damage using several meaningful quantities extracted from the acceleration

signal $\ddot{y}$ at the MS and can be used as a reliable prediction variable in the proposed data-driven model. In practice, this means that the RUL can be predicted by extrapolating the trajectory of H.I$^{\text{LC2}}$.

Furthermore, a radial damage originating at the MS was seen to have a significant effect on several drivetrain components and that the gearbox in particular acts as an amplifier of radial loads contributing to a considerable propagation of these loads in downwind direction from the MS to the HSS. Accordingly, this might benefit the prognostics task from a data-driven perspective since several acceleration signals within the gearbox are likely to exhibit signs of damage which can be used as input in an enhanced prognosis algorithm. In this work only the acceleration signals corresponding to the MS and HSS have been thoroughly investigated. Given the results, however, tracking several additional signals such as accelerations in the planetary stages of the gearbox will presumably improve fault detection and fault prognosis capabilities for this load case.

As stated, the results in the frequency domain corresponding to *LC2* extensively highlight abnormal behaviour. The influence of bearing damage on the modulation of the gear meshing frequencies can be used to further enhance diagnosis capabilities. For instance Wang *et. al.* used this phenomenon for fault diagnosis of the ring gear in planetary WTs [53]. It is interesting to acknowledge that modulation of gear meshing frequencies may serve as the basis of a novel approach to bearing prognosis which has not been developed in this thesis. Since abnormal behaviour related to bearing damage is captured at specific gear meshing frequencies it is deemed a promising opportunity to use this behaviour to construct a data-driven prognosis approach based on the analysis of the frequency content under increasing damage.

7.3   Load Case 3

The design load case that considered a radial damage originating at the bearing of the HSS on the generator side was seen to have a detrimental effect on the remaining useful life of the bearing on the gearbox side in the HSS. When evaluating this load case it is important to take into account the architecture of the drivetrain. In between the two bearings of the HSS sits a pinion gear. When HS-B experiences a depletion of radial stiffness a series of vibrations are transmitted directly to this pinion gear prior to reaching HS-A. The presence and location of this pinion gear allows vibrations to propagate to the gear of the high-speed

shaft and to be transmitted throughout the gearbox, to the intermediate shaft and towards the main shaft in up-wind direction. Although the impact on the lifetime of main shaft bearings was weak the significant effect on the overall gearbox is an advantage in terms of fault diagnosis and prognosis.

Although spectral analysis of *LC3* provided little proof of an ongoing damage at the high-speed shaft and main shaft accelerations, additional sensors at the intermediate-speed and low-speed planetary stage would clearly benefit the detection and prognosis of this damage case. Due to the presence of a gear that effectively transmits vibrations caused by a fault, a clear transmission path for these vibrations exists and should be exploited in future prognosis models.

Physics-based approach

According to the physics-based model, a radial damage at the generator-side HS-B bearing of the HSS modeled by *LC3* only leads to noticeable damage on the the up-wind HSS bearing HS-A. This bearing crosses the most conservative threshold $t_{f,2} = 128$ days and is close to failure according to the less-conservative threshold $t_{f,1} = 64$ days. In fact, the $\text{RUL}^{\text{HSA}}(t_{f,1} = 64days) = 71$ days. Hence, according to the physics-based model this bearing can be expected to fail when the radial stiffness K_r of bearing HS-B approaches a value of $K_r = 0.10 \cdot K_r^{\text{HS-B}}$

The remaining bearings of the MS, INP-A and INP-B experience no variation in their lifetime which remains constant and approximately equal to their lifetime for baseline-healthy conditions. Hence, not even the most conservative threshold value $t_{f,2} = 128$ days is breached by either of the MS bearings.

Data-driven approach

Feature selection for *LC3* culminated in a large group of variables suitable to construct a health indicator. Accordingly, 4 health indicators were put forth for each direction x, y, z: $\text{H.I}_{\text{MS},\ddot{x},\ddot{y},\ddot{z}}^{\text{LC3}}$, $\text{H.I}_{\text{MS},\ddot{\alpha}_x,\ddot{\alpha}_y,\ddot{\alpha}_z}^{\text{LC3}}$ and $\text{H.I}_{\text{HSS},\ddot{x},\ddot{y},\ddot{z}}^{\text{LC3}}$, $\text{H.I}_{\text{HSS},\ddot{\alpha}_x,\ddot{\alpha}_y,\ddot{\alpha}_z}^{\text{LC3}}$ corresponding to translational and rotational accelerations at the MS and the HSS, respectively.

Hence, in total 12 health indicators were created which makes *LC3* an ideal target for a data-driven approach. If an appropriate failure threshold is selected a radial damage at the HSS can presumably be predicted based purely on signal analysis and signal processing

and does not require an in-depth understanding of the physical processes that drive the damage mechanism. Naturally, fixing a reasonable threshold does however require a certain degree of physical knowledge on the acceptable acceleration values based on the historical records. Alternatively, in the absence of a historical dataset a convenient means to set a failure threshold is to select the last value of the health indicator as the threshold.

In comparison with *LC1* and *LC2*, the large number of health indicators make *LC3* the most suitable damage load case to approach purely from a data-driven perspective. Additional remarks on how to compliment and improve the proposed data-driven approach were put forth in section 6.5.

Chapter 8

Conclusions

The work carried out within this thesis has investigated the diagnosis and prognosis of a medium-speed 10-MW drivetrain design using model generated damage data. Each of the simulated load cases introduced in section 2.3 replicates a different type of bearing fault at different locations of the drivetrain. In total three distinct load cases were considered simulating three different types of bearing damage. The primary difference between load cases is that *LC1* and *LC2* reproduce faults in the first up-wind Main Bearing located on the Main Shaft whereas *LC3* replicates a fault on a bearing located on the high-speed shaft. Each load case was partitioned into 5 different damage intensities of increasing severity.

The fundamental goal of this work has been to predict the remaining useful life (RUL) of 4 relevant bearings in the drivetrain for the three considered fault situations. The load cases were analyzed in detail in the time-domain in section 4.1 and in the frequency-domain in section 4.2 so as to understand the behaviour of the drivetrain operating with a faulty bearing and gain insight on the most appropriate approach to detect an incipient fault and predict its evolution. Estimation of bearing RUL has been carried by mobilizing two distinct types of prognosis models: a model based on the physics-of-failure of these bearings presented in chapter 5 and a model based on signal analysis and signal processing of several acceleration signals in chapter 6.

Besides the central objective of bearing RUL prediction, this thesis is also concerned with another underlying but equally important objective: evaluate the ability to construct a prognosis model using only simulated data from a digital twin. Here, the concept of digital twin refers to the numerical drivetrain model that has been used to generate damage-like

data emitted by a faulty bearing. Given the lack of run-to-failure data from wind turbines and the restricted access to condition-monitoring data from real wind turbines it easy to justify efforts that effectively promote the use of numerical twins as a valuable alternative to generate faulty data.

Due to the differences in the nature and location of simulated faults, it should come as no surprise that different approaches to RUL estimation have been necessary to evaluate different types of damage. Since the rotational speed of the high-speed shaft bearing and the speed of the main shaft differ by a factor of 50, the RUL estimation at these distinct locations has resulted in significant differences in prognosis capabilities. Faults at the high-speed shaft are easier to detect than faults originating on lower speed shafts. For example, an imbalance caused by manufacturing defects or shaft misalignment can severely reduce bearing life and trigger unacceptable vibrations. The unbalance force is proportional to ω^2 where ω is the rotating speed of the component. Therefore, as machine speed increases, the effects of imbalance become greater which makes it easier to detect.

The relation between shaft speed where the fault originates and the detection capabilities for that specific fault has been established in this work. This was clear by comparing the relative ease to detect the fault corresponding to *LC3* which affects the high-speed shaft compared to a reduced capacity to detect faults originating in the Main Shaft bearings corresponding to *LC1* and *LC2*. Another relevant difference between *LC1* and *LC2* as opposed to *LC3* is that the first two load cases consider a defect on the first up-wind main shaft bearing which is directly transmitted to the second main shaft bearing located at close proximity and with no gears in between these two bearings. The location of the two main bearings is such that the main shaft behaves in an almost rigid manner which obstructs propagation of vibrations to a large extent. In the case of LC3, the faulty bearing in the high-speed transmits the vibrations to a pinion gear sitting which begins to vibrate and subsequently leads to vibrations in the gear and propagates further into the intermediate shaft and even reaches the Main shaft.

Additionally, it is important to acknowledge that the drivetrain architecture, the type of bearings and their layout has a direct influence on the fault diagnostics and prognostics possibilities. For instance, *LC1* proved that the two tapered roller bearings provided an excellent filter of non-torque loads as an axial damage on the first main bearing was effectively mitigated by the presence of the second main bearing. Although this is positive

from the standpoint of gearbox health and reliability, it posed a challenge to detect and predict this damage.

To improve diagnosis and prognosis, the simulated damage cases must be adjusted to the characteristics of the drivetrain. In the considered drivetrain, the main shaft is supported by two tapered roller bearings which are designed to withstand large axial loads and large radial loads. This means that a radial damage in a tapered roller bearing will lead to a variation of both axial and radial loads and vice-versa. For this specific drivetrain design, modelling a radial damage and an axial damage independently as if no correlation exists will result in unreliable model-generated data that does not capture the coupled axial-radial damage characteristics in tapered roller bearings. Hence, the selected load cases, particularly *LC1*, may not be an adequate choice to replicate damage occurring at tapered roller bearings and the generated-data will undermine fault detection capabilities. The relative distance bearings also plays a role in the detection capability and should be taken into consideration when defining the load cases. In order to detect, localise and find the root cause of a specific fault, the approach to model damage should be based on the type of bearings, bearing configuration and drivetrain architecture.

For each load case, a time-domain analysis was performed on the evolution of loads experienced by 4 different bearings under increasing damage. Besides a preliminary analysis of loads in the time-domain to track the overall drivetrain behaviour and load paths, understanding the frequency distribution of certain acceleration signals was critical to visualize relevant resonant behaviour otherwise hidden in the time-domain. Accordingly, the power spectral density (PSD) was investigated for translational and rotational accelerations for relevant frequencies susceptible to be excited such as shaft-related frequencies, gear meshing frequencies and characteristic fault frequencies as well higher-order harmonics of these frequencies which can also be excited under faulty conditions. These specific frequencies are calculated in section 4.2 and presented in Table 14 and Table 15. Frequency content, peak behaviour, peak location and peak magnitude as well as side-band characteristics were evaluated to enhance fault detection capabilities and progress into fault prognosis. Together with the spectral analysis of Main Shaft and High-Speed Shaft accelerations, the analysis of the load time-series has led to the following observations for each load case.

- The load results corresponding to *LC1* clearly reflect how a local damage in the

up-wind MS bearing directly affects the down-wind MS bearing. Axial damage at
the MS also induces a redistribution of loads at the HSS although the impact of
this response is relatively small. This underlines that the modelled gearbox can
transmit to a certain extent a surplus of axial loads towards other components down-
wind from the faulty MS bearing. As opposed to the clear damage indicators in the
load time-series, an axial damage at the MS goes rather unnoticed in the frequency-
domain. The spectral analysis of this load case was inconclusive and showed no signs
of resonant behaviour or excitation at the shaft-related frequencies, gear meshing or
characteristic fault frequencies. The lack of fault evidence in the spectral analysis of
acceleration signals is related to the bearing configuration supporting the main shaft.
As stated, two tapered roller bearings (TRB) were used mounted in close proximity to
one another. The fact that no anomalies are observed in the main shaft accelerations
is in fact a clear demonstration of a fundamental advantage of using two TRB as
main shaft bearings rather than using traditional drivetrain designs. This work and
more specifically load case *LC1* proves that an axial damage on the first main bearing
leads to an increase of axial loads which are absorbed by the second TRB effectively
keeping shaft vibrations within the acceptable fault-free conditions. Hence, thanks
to this bearing layout, a "purely" axial damage will not easily propagate towards
the gearbox nor other drivetrain components sensitive to axial loads. Results of load
case *LC1* confirms that the two TRB bearings act as a strong filter of non-torque
loads which effectively protects the gearbox from undesired axial loads.

- Spectral and time-domain analysis corresponding to *LC2* revealed indisputable signs
  of abnormal behaviour. Firstly, analysis of load time-series clearly proved that any
  change in the radial stiffness of a main bearing supporting the MS will trigger a
  response that affects all the considered drivetrain bearings both in the MS and in
  the HSS. This response is in the form of a redistribution of radial loads caused by
  the fact that the radial damage at a bearing depletes its ability to carry radial loads
  which must then be transferred to other drivetrain components. Transmission of
  radial loads is noticeable from an early damage stage and a slight decrease of bear-
  ing stiffness rapidly prompts a significant redistribution across the drivetrain and
  the studied bearings begin to exhibit modifications in their load carrying behaviour.
  Spectral analysis reveals an excitation of gear mesh frequencies in the so-called mesh-
  ing frequency modulation. Resonant behaviour is observed at these frequencies with

significant variation in peak magnitude and peak location as damage progresses. Since the HSS bearings are significantly affected by a radial defect originating at the MS, *LC2* effectively demonstrates that other bearings in the drivetrain such as gearbox bearings in the intermediate speed shaft (ISS) will also be affected.

- Loading results in the time-domain corresponding to *LC3* show that as the damaged bearing at the High-Speed Shaft on the generator side gradually loses its ability to carry loads inducing an excess of radial loads partially transmitted to the up-wind High-Speed Shaft bearing on the gearbox side. The presence of a gear in between the two high-speed shaft bearings exacerbates the vibrations caused by the faulty bearing and effectively leads to a backwards propagation from the High-Speed Shaft towards the Main Shaft in upwind direction. Accordingly, a radial damage originating at the High-Speed Shaft is seen to trigger a weak response in the up-wind bearings supporting the main shaft in terms of radial loads. The force time-series response at the Main Shaft is, however, mild and difficult to detect or quantify. Spectral analysis of the accelerations was inconclusive and no major anomalies were detected. Hence, spectral analysis provided no insight on abnormal behaviour at either the MS or the HSS which made it all the more challenging to determine whether a defect at the HSS induces a discernible response at the MS. Similarly to the main shaft bearings, the damaged high-speed shaft bearing considered in *LC3* is also a TRB. Hence, the lack of fault evidence in the spectral analysis of the high-speed shaft accelerations may be another indication that TRB are a good alternative to limit vibrations in the event of damage.

Following from the preliminary analysis in the time-domain and frequency-domain, the prognosis task was approached from two independent perspectives, a physics-based approach and a purely data-driven analysis. Whereas the physics-based model was successfully applied for all three load cases regardless of shaft speed, the data-driven approach suggested in this thesis culminated in very different results depending on the load case. Hence, the applicability of the data-driven prognosis model depends on shaft-speed and the type of bearing fault.

The framework followed to calculate the bearing lifetime according to the Lundberg hypothesis is built on the concept of S-N curves obtained experimentally, this approach is inherently based on physical phenomena and is therefore referred to as a Physics-based

model to bearing RUL prognosis. Prior to predicting the RUL of bearings, a comparative analysis was performed using normalized factor χ_i which represents the variation of the lifetime of each bearing for damage intensity i with respect to the lifetime when that same bearing operates with no drivetrain damage. Naturally, the bearing lifetime corresponding to a healthy drivetrain is that of the baseline simulation. The fault-free lifetime of each bearing according to the physics-based model are presented in Table 24.

	HS-A	HS-B	INP-A	INP-B
days	482.41	139.62	367.03	731.04

Table 24: Bearing lifetime for the baseline simulation corresponding to a healthy drivetrain

Variation of bearing lifetime with respect to baseline lifetime for *LC1*, *LC2* and *LC3* are given in Table 25. Results highlighted in red depict a **decrease** in bearing life time with regard to healthy conditions whereas results highlighted in green correspond to an **increase** in bearing lifetime compared to the baseline simulation where the drivetrain is fully healthy.

According to the implemented procedure to model damage explained in section 2.2, the decrease in bearing stiffness used to replicate damage will reduce the load experienced by the faulty bearing. Its important to note that factor χ_i is inversely proportional to this load and a decrease of the latter will therefore result in an increase of χ_i value. Hence, the lifetime of the faulty bearing increases disproportionately which is unrealistic and non-physical. Accordingly, the results highlighted in grey in Table 25 should be treated with care and should not be misinterpreted as a true increase of the lifetime of the faulty bearings.

LC1				
	HS_A	HS_B	INP_A	INP_B
healthy	0.00%	0.00%	0.00%	0.00%
χ_1	0.17%	-0.51%	-0.02%	-0.03%
χ_2	0.37%	-1.10%	-0.03%	-0.06%
χ_3	0.71%	-2.04%	-0.06%	-0.11%
χ_4	1.12%	-3.28%	-0.10%	-0.17%
χ_5	1.70%	-4.88%	-0.15%	-0.26%

Overall, the drivetrain is significantly more affected by a radial damage than an axial damage (*LC1*), with a radial damage at the MS (*LC2*) being more detrimental to the

LC2				
	HS_A	**HS_B**	**INP_A**	**INP_B**
healthy	0.00%	0.00%	0.00%	0.00%
χ_1	-11.37%	1.99%	10.41%	-7.81%
χ_2	-25.07%	3.83%	26.25%	-18.99%
χ_3	-47.38%	4.25%	71.51%	-40.41%
χ_4	-72.44%	-4.85%	219.52%	-67.26%
χ_5	-92.66%	-42.43%	2305.94%	-90.31%

LC3				
	HS_A	**HS_B**	**INP_A**	**INP_B**
healthy	0.00%	0.00%	0.00%	0.00%
χ_1	10.23%	23.61%	0.40%	0.63%
χ_2	12.82%	62.01%	0.83%	1.33%
χ_3	-8.66%	169.89%	1.44%	2.33%
χ_4	-51.72%	537.77%	1.97%	3.29%
χ_5	-83.10%	4824.28%	1.89%	3.55%

Table 25: Variation of χ at every bearing for increasing damage intensity corresponding to *LC1*, *LC2* and *LC3*

lifetime of the remaining bearings than a radial damage originating in the HSS (*LC3*). A radial damage on the HSS bearing induces a decrease of 83.10% of bearing HS-A whereas a radial damage at MS bearing INP-A leads to a drastic decrease of lifetime of 90.31%, 92.66% and 42.43% compared to healthy state for INP-B, HS-A and HS-B, respectively.

Results corresponding to *LC1* and *LC2* illustrate how a damage originating in the MS bearing will have an impact on the lifetime of bearings both at the MS and HSS, regardless of whether the fault replicates axial or radial damage whereas results corresponding to *LC3* indicate that a radial damage originating in the HSS bearing HS-B leads to a decrease in lifetime of HS-A, the up-wind HSS bearing but no reduction was observed in tha main shaft bearing lifetime. Both *LC1* and *LC2* show that a damage at the MS results in a greater depletion of lifetime of HSS bearings than for the MS bearing INP-B with bearing HS-B being the most vulnerable to axial damage and HS-A to radial damage. Both for *LC2* and *LC3* the bearing on the gearbox side HS-A experiences the greatest decrease in lifetime.

Furthermore, *LC2* demonstrates that the lifetime of bearings inside the gearbox, such as bearings in the intermediate-speed stage, is susceptible to decrease although they haven't been explicitly analyzed in this work. Similarly for *LC3*, as a consequence of radial damage

at HS-B an increase of radial loads transmitted inside the gearbox can be expected to decrease the lifetime of bearings within the gearbox.

Subsequently, prediction of bearing RUL according to the physics-based model was performed by setting two predefined failure thresholds. The wind-wave climate considered in this work is characterised by a unique combination of environmental parameters $U_w - H_s - T_p$ presented in section 5.4. From the joint probability distribution of $U_w - H_s - T_p$ the total number of days the WT can be expected to operate in these conditions was found to be $T = 16$ days. Hence, if the calculated bearing lifetime drops below the limit value T the bearing can be considered to fail. Naturally, the failure threshold was selected higher than the limit value in order to duly prepare for bearing repair, hire crews and vessels, acquire components and ferry them to the offshore site before actual bearing failure occurs. To account for the additional preparation time both thresholds are taken as multiples of T such that $t_{f,1} = 4 \cdot T$ and $t_{f,2} = 8 \cdot T$.

The RUL is then calculated as the intersection between the bearing lifetime (in days) and the predefined thresholds. The results are presented in Table 26 where results highlighted in orange and labelled *Failure* correspond to those bearings where the predicted RUL was lower than the most conservative threshold $t_{f,2} = 8 \cdot T$ and results highlighted in red and labelled as *Severe Failure* represent bearings with a predicted RUL lower than the critical threshold, here taken as $t_{f,1} = 4 \cdot T$

	HS-A	HS-B	INP-A	INP-B
LC1	No failure	No failure		No failure
LC2	31 days	44 days		65 days
LC3	60 days		No failure	No failure

Table 26: Failed bearings according to physics-based model

It is important to keep in mind that the healthy bearing lifetime of the four bearings differs drastically. In particular, the bearing HS-B in the high-speed shaft has an initial lifetime of approximately 140 days when the drivetrain is in healthy conditions as seen in Table 24, a lifetime significantly lower than that of the other bearings. This in turn means that if the failure threshold is set to a very conservative value, the predicted RUL of HS-B will fail almost immediately according to the physical-based model. This implies that the selected threshold value $t_{f,2} = 8 \cdot T$ is an inappropriate choice to evaluate the health of this bearing which may in turn trigger a false alarm. To remedy this, it is important to define the

critical failure threshold uniquely for each bearing such that it accounts for the operational singularities of each bearing type.

The alternative approach to prognostics considered in this thesis involved developing a data-driven model by constructing the so-called health indicators. The first step was to extract a series of statistical and spectral features, also known as condition indicators, for each acceleration signal -translational and rotational acceleration at the MS and at the HSS, for all 3 load cases-. The computed features were selected based on a thorough overview of literature and relevant studies on the diagnosis and prognosis of rotating machinery. Once a fixed number of statistical and spectral indicators were extracted for all signals, the feature selection and feature fusion phases followed discussed in section 6.2 and section 6.3, respectively. This involved identifying the most suitable features for RUL prediction and discarding the rest. Suitable features are those that displayed a consistent and predictable trend as damage increased. This was measured using a feature performance metric known as monotonicity . The most predictable features were pre-selected and fused together by performing a Principal Component Analysis (PCA) as explained in subsection 6.4.1. The results from the feature fusion phase according to the PCA algorithm were then used as Health Indicators which are plotted in subsection 6.4.2.

This procedure was done for each acceleration signal and for each load case. The ability to construct health indicators was directly determined by the feature selection phase which culminated in very different results depending on the load case. Whereas the feature selection phase provided a large amount of quality features for *LC3*, a reduced number of suitable features was found for *LC2*, and of lower quality for RUL prediction. For load case *LC1*, feature selection was even more precarious and no features were found to adequately satisfy the requirement of the monotonicity.

Naturally, in the absence of appropriate features, constructing a health indicator was not possible. Consequently, the possibility to implement a reliable data-driven method using Health Indicators was constricted to *LC3* and, in a lower degree, to *LC2*. The culmination of the data-driven approach is to use the computed Health Indicators as main prediction variables. The advantage of Health Indicators is precisely their ability to mathematically capture the degradation process corresponding to bearing damage. Hence, a direct relation between the value of Health Indicators and degree of damage in the bearing can be

exploited. In practice, this entails predicting the trajectory of the Health Indicator to a certain predefined failure threshold to predict the RUL. Ultimately, the RUL estimation becomes in fact a forecasting task which targets future values of the Health Indicators predicted from past values.

By definition, the RUL of a bearing is the total number of revolutions before a failure occurs or the total number of hours that the bearing can run until the first sign of failure develops. The dependency between damage and time is therefore intrinsic to RUL estimation. The final step to utilize the constructed Health Indicators for RUL prediction, therefore, met a fundamental obstacle. At this point, to fully implement a data-driven solution to estimate bearing life it becomes indispensable to include a time-dependant bearing stiffness model. At the time of writing, a physical or mathematical model that relates the evolution of bearing stiffness with time was not available.

This set back is inherently related to the manner in which it was chosen to model damage throughout this work. Since bearing damage is based on a progressive reduction of that bearing's stiffness, omitting a time-dependent bearing model puts an end to a fully-blown data-driven approach. Although some complimentary remarks to improve the data-driven approach were Additional remarks on how to compliment and improve the proposed data-driven approach were provided in section 6.5, the lack of a time-dependent relation between the evolution of bearing stiffness and damage is the most critical shortcoming to overcome in order to successfully achieve a prediction of bearing RUL. If damage is modelled on the basis of a damage-stiffness relation, an additional relation stiffness-time is indispensable to obtain a true prognosis model.

Despite the limitations of the prognosis methods proposed in this work, the reduced ability to detect and predict faults is highly correlated to the quality of the model-simulated data and should not be seen as a weakness of the prognosis models. The approach to introduce damage in the numerical model will have a paramount importance on the fault detection capabilities. Accordingly, as new drivetrain designs are proposed by the industry the load cases used to replicate damage will need to be specifically selected to account for the inherent properties of the bearing configuration.

A somewhat more subtle but equally important objective of this work has been to investigate the possibilities of using a digital twin to establish a reliable prognosis model. Digital

twins are a convenient tool to simulate degradation data and a much-needed alternative to overcome the shortage of real-life WT CMS data and run-to-failure data. In this work, the simulated data has enabled the creation of a physics-based prognostics model and has set the foundation for a data-driven approach to prognostics. The estimation of RUL of bearings for several bearing faults was successfully obtained exclusively model-generated data. Hence, this academic work has promoted the use of a numerical twin to simulate drivetrain behaviour under faulty conditions and to support research on bearing prognosis.

A final noteworthy contribution of this thesis has been to analyze the behavior of a novel bearing configuration using two tapered roller bearings (TRB) to support the main shaft rather than a combination cylindrical roller bearing and spherical roller bearing used in traditional designs. This bearing configuration is relatively new and is currently gaining traction in large offshore wind turbines. The work carried effectively enables a qualitative analysis of a new generation of medium-speed turbines using two TRB as main bearings. The findings of this thesis, particularly results corresponding to *LC1*, highlights that the two TRB act as a robust filter of non-torque loads which effectively protects the gearbox from undesired axial loads. Consequently, this thesis confirms that using this new bearing configuration based on tapered roller bearings (TRB) exhibits a good resistance to axial damage and has the potential to improve the overall reliability of gearboxes.

Chapter 9

Recommendations

The importance of developing reliable, realistic and cost-effective prognosis models is critical to predict faults, decrease downtime and optimise maintenance schedules. Together, these advantages have the potential to achieve a major cost-reduction which fully justifies extensive research on prognosis models, particularly for vulnerable drivetrain components.

To develop prognosis models academia needs to bypass restricted access to CMS data and the lack of run-to-failure data from real wind farms. Generating useful degradation data is crucial to allow researchers to develop, test and validate prognosis models which can then be presented to the industry. One way to overcome this challenge is to use digital twins to generate simulated faulty data.

To fully take advantage of numerical twins, however, an appropriate methodology to replicate damage at specific components is critical. In this context, exploiting the relation between bearing degradation and bearing stiffness, as was done in this work, is a very convenient manner to rapidly produce model-generated degradation data using only numerical models. In principle this assumption is valid and a degraded bearing will indeed exhibit a deterioration of its mechanical properties -the stiffness among others- which alters its load carrying capacity. Moreover, replicating component damage by modifying component stiffness is a very controllable technique to incrementally simulate a fault at the specific desired locations. To obtain truly useful damage data using bearing stiffness, however, additional efforts must be allocated towards establishing a relation that reflects the time-dependency between the bearing's stiffness and its operational life.

At the time of writing this relation was not known and essentially stems from a lack of knowledge. Any contribution to reduce this knowledge gap will favor prognosis algorithms built on model-generated data. If specific research in the direction of investigating stiffness variation in wind turbine bearings culminates in a time-dependent bearing model, it will certainly benefit prognostics possibilities using exclusively model-generated data. This will promote the use of numerical twins and expedite research on prognosis. In fact, if a relation of this nature is put forth the prognostics of bearing RUL can be effectively approached by the data-driven prognosis model proposed by this work.

Regardless of the implemented prognosis tool, predictive models are characterized by a greater uncertainty such as uncertainties in the determination of loads, of the structure's response as well as uncertainties inherent to the environmental modelling, the global model and its finite element model and uncertainties associated to the drivetrain numerical. Additionally, lack of knowledge such as the interaction between different faults or damage accumulation and propagation mechanisms also results in increased uncertainties. It is important to understand the different sources of uncertainty in failure modelling and research on the quantification of these uncertainties is advisable. It is particularly critical to understand and investigate the influence of uncertainty in the bearing RUL estimation.

This work also found that a radial damage originating on the first main bearing leads to the appearance several gear mesh frequencies in the acceleration signals of multiple shafts inside the gearbox. These gear mesh frequencies were found to be significantly excited as damage increased. This phenomenon, known as frequency modulation, has often been overlooked in gearbox vibration signals but is a clear indicator of incipient damage. Understanding and quantifying the phenomenon of frequency modulation may provide valuable insight on bearing damage and assist the task of prognosis. Accordingly, specific research focusing on gear meshing modulation may be readily justified to enhance bearing health monitoring.

Another important line of research that can greatly contribute to improving this work is to consider radial and axial damage in a bearing as coupled. In this thesis radial and axial damage has been assumed to be decoupled. It is well known that main bearings play a critical role in reducing the non-torque loads entering the gearbox. Accordingly, the type and layout of these bearings will have a considerable impact on how non-torque loads are dealt with. Until recently, the state-of-the-art in drivetrain design involved a 4-point support drivetrain with a first main bearing, a cylindrical roller bearing, used to carry

the radial loads and a second main bearing, a spherical roller bearing, preventing axial loads from entering the gearbox. In this context, decoupling radial and axial damage was a coherent method to replicate damage since the up-wind and down-wind bearings were carrying carrying radial and axial loads separately.

However, this decoupled damage approach is not advisable when the drivetrain operates with two tapered roller bearings since this type of bearing is specifically designed to withstand a combination of large axial and large radial loads. The nature of these bearings means that there will be a strong coupling at any of the main bearings between radial and axial damage which is not captured by assuming load cases that treat axial and radial damage independently. In reality, an axial damage in a tapered roller bearing will lead to a radial response of this bearing and vice-versa. Furthermore, since the 2 main bearings are mounted in close proximity to one another the surplus of loads due to a damage in the up-wind is mostly absorbed by the down-wind bearing which hinders fault detection possibilities based purely on shaft accelerations. To enhance diagnosis and prognosis of the bearings, it is important to capture the several couplings that take place within the drivetrain during the faulty operation. These couplings include a coupling in between different bearings as the loads are transmitted and redistributed throughout several locations in the drivetrain, and in the case of tapered roller bearings, the coupling that exists between a radial and axial damage as well as the coupling in load redistribution that occurs within the two main shaft bearings.

Due to the decoupling of radial an axial damage, for *LC1* the physics-based model was found to overlook the effects on the lifetime of the down-wind main bearing of an axial damage in the up-wind main bearing. Since the axial bearing factor for the second main bearing was equal to zero, the physics-based model failed to account for the large deviation in axial loads whilst assigning a relatively disproportionate importance to the variation in radial loads over axial loads. This shortcoming, however, should not be associated to the physics-based model but to the decoupled axial-radial damage approach. The model-generated data failed to account for the coupled nature of radial and axial stiffness in main shaft bearings which subsequently constrained detection and prognosis using the proposed physics-based model. It is important to keep in mind that the bearing lifetime is related to the variation in bearing loads to the power of 3.33. Any model-generated data that is not able to adequately account for bearing load variations or underestimates such loads

will lead to an overestimation of the lifetime according to the implemented physics-based model.

Given the prominent role tapered roller bearings may be expected to play in a new generation of more reliable large multi-megawatt offshore wind turbine drivetrains, their behaviour needs to be investigated further. As of today the multiple coupled phenomena that exists between these bearings is poorly understood and this knowledge gap must be addressed. An in-depth analysis of the coupled behaviour, load distribution and damage propagation is necessary to improve the model-generated damage data produced by numerical twins. In order to accurately begin to capture the coupling phenomena future work cannot ignore the correlation between axial and radial damage in tapered roller bearings. Lastly, it is fundamental that the manner in which damage is introduced in a numerical model is adapted to each specific drivetrain design, to the type of bearings used and to the inner drivetrain architecture.

Bibliography

[1] Kjetil Uhlen Karl Merz Olimpo Anaya-Lara, John Olav Tande. *Offshore Wind Energy Technology*, chapter 3.

[2] IC isted, howpublished = `https://www.istec.com/en/the-importance-of-condition-monitoring-for-rotating-machinery/`, note = Accessed: 2020-06-29.

[3] Torgeir Moan Shuaishuai Wang, Amir R. Nejad. On initial design and modelling of a 10 mw medium speed drivetrain for offshore wind turbines. *Journal of Physics*.

[4] Lin Li, Zhen Gao, and Torgeir Moan. Joint Distribution of Environmental Condition at Five European Offshore Sites for Design of Combined Wind and Wave Energy Devices. *Journal of Offshore Mechanics and Arctic Engineering*, 137(3), 06 2015. 031901.

[5] Jan Wenske Christian Broer Diego Coronado, Katharina Fischer. Condition monitoring of wind turbines state-of-the-art, user experience and recommendations. Technical report, Fraunhofer Institute for Wind Energy and Energy System Technology.

[6] P. Veers S. Sheng. Wind turbine drivetrain condition monitoring – an overview.

[7] ISO. Iso 10816-21:2015- evaluation of machine vibration by measurements on non-rotating parts — part 21: Horizontal axis wind turbines with gearbox. Technical report, ISO.

[8] Cristian Molina Vicu~na. *Contributions to the analysis of vibrations and acoustic emissions for the condition monitoring of epicyclic gearboxes*. PhD thesis, Faculty of Georesources and Materials Engineering of the RWTH Aachen University.

[9] Xiaochuan Li David Mba Faris Elasha, Suliman Shanbr. Prognosis of a wind turbine gearbox bearing using supervised machine learning. *Sensors*.

[10] Xingyu Zhao Valentin Robu David Flynn Mike Barnes John Keane Goran Nenadic Adrian Stetco, Fateme Dinmohammadi. Machine learning methods for wind turbine condition monitoring: A review. *Renewable Energy*.

[11] OneProd, howpublished = `https://www.oneprod.com/blog/vibration-analysis-basics/`, note = Accessed: 2020-05-26.

[12] Torgeir Moan Amir Rasekhi Nejad, Zhen Gao. On long-term fatigue damage and reliability analysis of gears under wind loads in offshore wind turbine drivetrains. *International Journal of Fatigue*, 61:116 – 128, 2014.

[13] IEC. Iec 61400-25-6 - communications for monitoring and control of wind power plants - logical node classes and data classes for condition monitoring. Technical report, IEC.

[14] Robert Bitsche Taeseong Kim Anders Yde Lars C. Henriksen Anand Natarajan Morten Hansen Christian Bak, Frederik Zahle. Description of the dtu 10 mw reference wind turbine. Technical report, DTU Wind Energy.

[15] Wenfei Xue. Design, numerical modelling and analysis of a spar floater supporting the DTU 10MW wind turbine. Master's thesis, NTNU, Institutt for marin teknikk (NTNU), 2016.

[16] Shuaishuai Wang, Amir R. Nejad, and Torgeir Moan. On design, modelling, and analysis of a 10-mw medium-speed drivetrain for offshore wind turbines. *Wind Energy*, 23(4):1099–1117, 2020.

[17] Roger Bergua. Pure torque drivetrain design. *Gearbox Reliability Collaborative (GRC)*.

[18] Zhongzhe Chen, Shuchen Cao, and Zijian Mao. Remaining useful life estimation of aircraft engines using a modified similarity and supporting vector machine (svm) approach. *Energies*, 11:28, 12 2017.

[19] ISO. Iso 13373-1 - condition monitoring and diagnostics of machines — vibration condition monitoring — part 1: General procedures. Technical report, ISO.

[20] Robert Bond Randall. *Vibration-based condition monitoring: industrial, aerospace and automotive applications*. John Wiley & Sons, 2011.

[21] B. Hendriks K. Harman F. Spinato, M. Wilkinson. Methodology and results of the reliawind reliability field study. In *European Wind Energy Conference*.

[22] C. Crabtree Y. Feng W. Yang, P. Tavner and Y. Qiu. Wind turbine condition monitoring: technical and commercial challenges. *Wind Energy*, 17.

[23] Huageng Luo. Physics-based data analysis for wind turbine condition monitoring. *Clean Energy*.

[24] Dalgobind Mahto Sachin Sharma. Condition monitoring of wind turbines: A review. *International Journal of Scientific Engineering Research*, 4(8).

[25] Manuel Esperon-Miguez Adrian Cubillo, Suresh Perinpanayagam. A review of physics-based models in prognostics: Application to gears and bearings of rotating machinery. *Advances in Mechanical Engineering*.

[26] Harrison H. Chin. Turbine engine hot section prognostics. 2005.

[27] M.R. Hoeprich. Rolling element bearing fatigue damage propagation. *ASME*, 114.

[28] J. Sheldon C.J. Klenke R.F. Orsagh. Prognostics/diagnostics for gas turbine engine bearings. In *Proceedings of the 2003 IEEE aerospace conference*.

[29] F. Di Maio E. Zio E. Fatigue crack growth estimation by relevance vector machine. *Expert Syst Appl*.

[30] N. Paulson F. Sadeghi A. Ghosh. A fracture mechanics approach to simulate subsurface initiated fretting wear. *International Journal of Solids and Structures*, 58.

[31] Robert Bond Randall. *Cepstrum Analysis and Gearbox Fault Diagnosis*. Bruel & Kjaer, 1973.

[32] Nils J. Nilsson. *Introduction to machine learning, an early draft of a proposed textbook*. Department of Computer Science Stanford University, 2005.

[33] S. W. Wegerich J. P. Herzog K. C. Gross, R. M. Singer. Application of a model-based fault detection system to nuclear plant signals. *Argonne National Laboratory*.

[34] Xiyun Yang Peng Guo, David Infield. Wind turbine generator condition-monitoring using temperature trend analysis. *IEEE Transactions on Sustainable Energy*, 3(1):124 – 133, 2012.

[35] Huan Long Jia Xu Ruihua Liu Long Wang, Zijun Zhang. Wind turbine gearbox failure identification with deep neural network. *IEEE Transactions on Industrial Informatics*, 13(3):1360 – 1368, 2016.

[36] Caleb Phillips Rafael Orozco, Shuangwen Sheng. Diagnostic models for wind turbine gearbox components using scada time series data. *IEEE International Conference on Prognostics and Health Management.*

[37] I.C. Konstantakopoulos C.J. Spanos A.M. Agogino D.T.J. O'Sullivan K. Leahy, R.L. Hu. Diagnosing and predicting wind turbine faults from scada data using support vector machines. *IEEE International Conference on Prognostics and Health Management*, 9(1).

[38] Simon J Watson Raed K Ibrahim, Jannis Tautz-Weinert. Neural networks for wind turbine fault detection via current signature analysis. *WindEurope.*

[39] J.J. Cardenas J. Cusido J. Sole-Casals P. Marti-Puig, A. Blanco-M. Effects of the pre-processing algorithms in fault diagnosis of wind turbines. *Environmental Modelling Software.*

[40] H. Zhao and L. Li. Fault diagnosis of wind turbine bearing based on variational mode decomposition and teager energy operator. *IET Renewable Power Generation*, 11(4):453–460, 2017.

[41] W. Musial, S. Butterfield, and B. McNiff. Improving wind turbine gearbox reliability. *European Wind Energy Conference*, 01 2007.

[42] Wei Teng, Xiaolong Zhang, Yibing Liu, and Zhiyong Ma. Prognosis of the remaining useful life of bearings in a wind turbine gearbox. *Energies*, 10:32, 12 2016.

[43] R.B. Randall. The spectral kurtosis: Application to the vibratory surveillance and diagnostics of rotating machines. *Mechanical Systems and Signal Processing*, 20:308–331, 02 2006.

[44] Wahyu Caesarendra and Tegoeh Tjahjowidodo. A review of feature extraction methods in vibration-based condition monitoring and its application for degradation trend estimation of low-speed slew bearing. *Machines*, 5:21, 09 2017.

[45] H. Abdi and L. J. Williams. Principal component analysis. *Wiley Interdisciplinary Reviews: Computational Statistics*, 2:433–459, 09 2010.

[46] Stefan Cristian Ciucu Bodgan Oancea. *Challenges of the Knowledge Society: Time series forecatsing using Neural Networks*. Nicolae Titulescu University Publishing House, 2013.

[47] Hamid Zareipour David Wood Ehsan Mollasalehi Shuangshu Tian-Yan Pei Lixiao Cao, Zheng Qian. Prediction of remaining useful life of wind turbine bearings under non-stationary operating conditions. *energies*, 11(12).

[48] J. Mehnen L. Redding Okoh, R. Roy. Overview of remaining useful life prediction techniques in through-life engineering services. In *Proceedings of the 6th CIRP Conference on Industrial Product-Service Systems*.

[49] Yun Kong, Tianyang Wang, and Fulei Chu. Meshing frequency modulation assisted empirical wavelet transform for fault diagnosis of wind turbine planetary ring gear. *Renewable Energy*, 132:1373 – 1388, 2019.

[50] Amir R. Nejad, Peter Fogh Odgaard, and Torgeir Moan. Conceptual study of a gearbox fault detection method applied on a 5-mw spar-type floating wind turbine. *Wind Energy*, 21(11):1064–1075, 2018.

[51] Kiyohiko Umezawa, Toshio Suzuki, and Taichi Sato. Vibration of power transmission helical gears: Approximate equation of tooth stiffness. *Bulletin of the JSME*, 29(251):1605–1611, 1986.

[52] V Atanasiu and I Doroftei. Dynamic contact loads of spur gear pairs with addendum modifications. *European journal of mechanical and environmental engineering*, 2:21, 2008.

[53] T. Wang, F. Chu, and Q. Han. Fault diagnosis for wind turbine planetary ring gear via a meshing resonance based filtering algorithm. *ISA Transactions*, 67:173–182, 2017.